

ALMA MATER STUDIORUM
UNIVERSITA' DI BOLOGNA

SCHOOL OF ENGINEERING

- Forlì campus -

SECOND CYCLE MASTER'S DEGREE in AEROSPACE
ENGINEERING

Class LM-22

GRADUATION THESIS in Experimental Methods in Aerodynamics

Development and Automatization of a Planar Jet Wind Tunnel for the X-wire Calibration

CANDIDATE:
Mehmet Berkay ERYILDIZ

SUPERVISOR:
Dr. Gabriele Bellani

Academic year 2021/2022

Abstract

The scope of this study is to design an automatic control system and create an automatic x-wire calibrator for a facility named Plane Air Tunnel; whose exit creates planar jet flow. The controlling power state as well as automatic speed adjustment of the inverter has been achieved. Thus, thanks to this study, the wind tunnel can be run with respect to any desired speed and the x-wire can automatically be calibrated at that speed.

To achieve that, VI programming using the LabView environment was learned, to acquire the pressure and temperature, and to calculate the velocity based on the acquisition data thanks to a pitot-static tube. Furthermore, communication with the inverter to give the commands for power on/off and speed control was also done using the LabView VI coding environment. The connection of the computer to the inverter was achieved by the proper cabling using DAQmx Analog/Digital (A/D) input/output (I/O).

Moreover, the pressure profile along the streamwise direction of the plane air tunnel was studied. Pressure tappings and a multichannel pressure scanner were used to acquire the pressure values at different locations. Thanks to that, the aerodynamic efficiency of the contraction ratio was observed, and the pressure behavior was related to the velocity at the exit section.

Furthermore, the control of the speed was accomplished by implementing a closed-loop PI controller on the LabView environment with and without using a pitot-static tube thanks to the pressure behavior information. The responses of the two controllers were analyzed and commented on by giving suggestions.

In addition, hot wire experiments were performed to calibrate automatically and investigate the velocity profile of a turbulent planar jet. To be able to analyze the results, the physics of turbulent planar jet flow was studied. The fundamental terms, the methods used in the derivation of the equations, velocity profile, shear stress behavior, and the effect of vorticity were reviewed.

Thanks to automatic multiple x-wire experiments, it is now easier to form the mean and the fluctuating velocity profiles in two directions in a shorter time. To accomplish that goal, some crucial changes were made to the traversing system to make it fully functional for this purpose.

Acknowledgements

My interest in the aerospace field started when I was a child and decided to become a person contributing to the aviation world. After getting familiar with the branches of aerospace science at university, I was so certain that I am totally devoted to aerodynamics.

My adventure at the University of Bologna was unexpected from many points of view, which lead to me learning a lot. A happy end of this adventure will be reached with this thesis. I hope I have contributed to the people that I have met and learned from.

Firstly, I would like to thank my family, who always supported me and respected my career plans, without letting me down. I cannot ignore their mental support in any way. They always bolster me whenever I tend to fall. All of my successes, if there are any, are for them until the end of my life.

I would like to thank many times my supervisor Prof. Gabriele Bellani for accepting me to the CICLoPE laboratory to write my thesis. I am more than grateful for the time he spent teaching and educating me. I broadened my horizon thanks to his deep knowledge and experience.

I am extremely thankful to my professor, Prof. Alessandro Talamelli for helping me not only in an academic way but also in my life in Forlì. I am so glad that he eased my challenges in the town. I am appreciative of his hospitality.

I feel so lucky that I had a mentor in Ing. Lorenzo Lazzarini, who always answered my questions, and helped me in my tasks although it was not his duty. My thanks to him pales in comparison to the sacrifices he has made.

I sincerely thank my friends, Rithvik, Alex, and Alessio, who I met during my thesis adventure in CICLoPE. They were always there to help me in my times of need. They were always so kind to me, I never felt away from home thanks to their efforts.

I will never forget the team that I met during my studies here. I hope my studies meant something to the CICLoPE laboratory and will be beneficial for someone else.
Cheers.

Table of Contents

Chapter 1: Introduction	1
1.1 Planar Jet Flow	4
Chapter 2: Theoretical Background and Literature Review	7
2.1 Hot Wire Anemometry	7
2.2 Planar Jet Flow	17
Chapter 3: Experimental Setup	25
3.1 Plane Air Tunnel	25
3.1.1 Sliding System	26
3.1.2 Traversing System	28
3.1.3 Inverter and Power System	32
3.2 Data Acquisition and Transmission	34
3.2.1 Sensors	34
3.2.2 Transducers	36
3.2.3 Transmission	38
3.3 Pressure Behavior	39
3.3.1 Offset Compensation	43
3.3.2 Pressure Sampling Time	47
3.3.3 Pressure Sampling Frequency	53
3.4 Inverter Communication	59
3.4.1 On/Off Command Communication	59
3.4.2 Speed Control Communication	61
3.5 Velocity Measurement	62
3.5.1 Pitot-static Tube	62
3.5.2 Inverter Voltage and the Exit Velocity Relation	68
3.5.3 Pressure Tappings	69
3.5.4 PI Control	74
3.6 Hot Wire Experiments	76
3.6.1 Hot Wire Sampling Time	81
3.6.2 Hot Wire Sampling Frequency	89
3.6.3 Single Wire Calibration	93
3.6.4 Traversing System Improvement	95
3.6.5 X-wire Calibration	97
3.6.6 Single Wire Experiments	100
3.6.7 X-wire Experiments	101
3.6.8 Planar Jet Flow Analysis	103

TABLE OF CONTENTS

Chapter 4: Results	105
4.1 Inverter Communication	105
4.2 Pressure Behavior Along the Tunnel	106
4.3 Velocity Measurements	110
4.3.1 PI Control	110
4.4 Hot Wire Experiments	113
4.4.1 Mean Velocity Profile	119
4.4.2 Fluctuating Velocity Profile	126
4.4.3 Reynolds Normal Stress	132
Chapter 5: Discussion	136
5.1 Velocity Measurements by the Pitot-Static Tube and Pressure Tappings	136
5.2 PI control	138
5.3 Pressure behavior	141
5.4 Hot wire experiments	146
5.4.1 Literature comparison	149
Chapter 6: Conclusion	152
Chapter 7: Appendices	157
7.1 Fast fourier transform	157
7.2 VI block diagrams	159
7.2.1 Inverter communication	159
7.2.2 Temperature acquisition	161
7.2.3 Exit velocity calculation	162
7.2.4 Stepper motor	162
7.2.5 PI controller with a pitot-static tube	162
7.2.6 PI controller without a pitot-static tube	163
7.2.7 Pressure acquisition for Scanivalve pressure scanner	163
7.2.8 Hot wire calibration	165
7.2.9 Hot wire experiment	166
7.2.10 X-wire calibraion	168
7.2.11 X-wire experiments	169

List of Figures

1.1	Von Karman vortex shedding appearing on the fluid flow around a cylinder. The direction of the flow is from left, where the cylinder is located, to right. The conditions of the shedding were visualized in different Reynolds number, $Re=150$, $Re=300$ and $Re=4000$, respectively from top to bottom[Alziadeh, 2017].	2
1.2	Basic schematic of a turbulent planar jet flow and fluid dynamics phenomena from its side view. The surrounding air is stationary. The part on the top is the body where the fluid exits from. The 2D coordinate system is visible on top left[Hassan, Guo, and Vlachos, 2019].	5
1.3	Screenshot of a computational fluid dynamics analysis of the turbulent planar jet flow at $Re=12299.9$ for the half geometry to have a less computational effort by using OpenFoam open source code environment. Large eddy simulation with dynamic k equation was preferred. The color map refers to streamwise velocity. The geometry on the left is the half of the plane air tunnel exit section in both z and x axes. The surrounding air is stationary.	6
2.1	Hot wire probe schematic expressing its materials and size [Je-Chin Han, 2020].	7
2.2	Schematic of a hot wire including the coordinate system, angles, and the velocity components. θ shows the pitch angle while the α stands for the yaw angle. Two parallel cylinders that are perpendicular to the y-axis are the probes of the wire, while the wire is connected between their ends [Shekhter, 2011].	12
2.3	Schematic of an x-wire probe side view showing the stem dimensions and the wire orientations on the most left [Je-Chin Han, 2020].	14
2.4	X-wire sensor schematic showing the angles formed by the wire orientations and the coordinate system of the probe. n_1 and n_2 are the normals to wire 1 and wire 2. U is the x component of the flow velocity, \mathbf{V} , while the vertical V is the y component of the flow velocity, \mathbf{V} . θ is the angle between the dominant flow direction and the x-axis of the probe [Bruun, 1996].	15
2.5	Separate schematics of the wires of x-wire to make the velocity components corresponding to each visible. U is the x component of mean velocity while u is the x component of the fluctuating velocity. Fluctuating velocity in the y direction is represented by v	16

2.6 Coordinate system of plane air tunnel. The x-axis is the streamwise direction, the y-axis is the vertical crossflow direction while z-axis is the spanwise direction. 21

2.7 Example of a basic hot wire signal showing instantaneous velocity decomposition into its mean and fluctuating parts [Rathakrishnan, 2020]. 21

2.8 Experimental study of turbulent planar jet flow performed with hot wires. X is the streamwise direction while y is the crosswise direction. In the horizontal axis, non-dimensional quantity η represents the ratio between crosswise distance and streamwise distance from the origin, where x_0 is the virtual origin. In the vertical axis, non-dimensional quantity stands for the ratio between mean velocity magnitude, Q , and mean centerline velocity magnitude, Q_m . Data were obtained at different streamwise locations each corresponding to a different shape on the plot [Heskestad, 1965]. 22

2.9 Visualization of Reynolds Normal Stresses in three directions, where the continuous line stands for R_{uu} , the dashed line shows R_{vv} and the dots represent R_{ww} . The coordinate system is exactly the same as shown in figure 2.6 [STANLEY, SARKAR, and MELLADO, 2002]. 23

2.10 Plot of an experimental result representing the turbulence intensity distribution along the streamwise direction at exit Reynolds number $Re=8000$. Unlike equation 2.66, the effective velocity fluctuation was divided to mean velocity at the exit section without taking the percentage. U_0 is the mean velocity at the exit section, X is the streamwise distance from the exit, u_{rms} is the RMS value of fluctuating velocity and D is the exit section height. Each shape corresponds to a different shape of the exit section. The coordinate system is exactly the same as shown in figure 2.6 [Hashiehbaf and Romano, 2013]. 24

3.1 Side view schematic of Plane Air Tunnel. Flow is generated by a centrifugal blower(A), transferred to the pre-settling chamber(B), and then to the rectangular prism section via two tubes(C). Flow passes through the glass spheres(D) where some of the turbulence is killed. After that, honeycomb(E) helps to straighten the flow. Flow is then forced through a set of screens(F) to decrease the turbulence level again. Contraction(G) accelerates the flow before the exit section. 25

3.2 Plane Air Tunnel perspective view from the exit section, placed on top of a table to maintain the height of the exit. 26

3.3 Sliding mechanism to move the wire holder in streamwise and crosswise direction inside the wake of the turbulent planar jet. The vertical part of the system, which is located close to the table in the picture, is able to move both on the horizontal part that is close to the ground and in the vertical direction. 27

LIST OF FIGURES

3.4 Figure (a) is a data acquisition card for the communication of the sliding mechanism to move the wire holder in the streamwise and crosswise direction inside the wake of the turbulent planar jet. It is connected to the computer via a USB connection. Figure (b) is the cabling for the actuator of the sliding mechanism to move the wire holder in the streamwise and crosswise direction inside the wake of the turbulent planar jet. It is connected to the computer via a USB connection. 27

3.5 Sliding system user interface. X direction is streamwise and z direction is the vertical crosswise direction. The user has to first give the inputs for x and the z direction and then run the code. The sliding system first moves in the streamwise direction and then in the crosswise direction. 28

3.6 Traversing system to calibrate the x-wire at the exit of the plane air tunnel. The system includes a stepper motor (seen on right), metal sticks to hold the stepper motor, transfer the rotation given by the stepper motor, and mount the wire holder on top of it. A wire holder is used to place the wire probe 29

3.7 Figure (a) is the digital output port for the stepper motor cabling. Figure (b) is the power supply to be able to turn on and give the desired input for the stepper motor. The 5 V was used to move the stepper motor while the 24 V is to power the motor.. . . . 30

3.8 Front panel of the stepper motor VI code. As the input, the user has to give millisecond multiple to wait between the steps, lines to communicate for both the direction and the amount, steps desired to move, and the millisecond value of movement. 32

3.9 Siemens Sinamics V20 inverter, changing the voltage or the frequency of the AC motor to control the fan RPM. 33

3.10 Pitot-static tube, measuring total and static pressure to calculate the velocity at a specific location[Gentle, Edwards, and Bolton, 2001]. . . 35

3.11 Basic schematic of a hot wire including its supports[Bruun, 1996]. . . 35

3.12 Thermocouple to sense the temperature at a specific location. . . . 36

3.13 MKS pressure transducers, one is for the ambient pressure measurement and the other is for static and total pressure measurement which is connected to the pitot-static tube. 37

3.14 Electrical diagram of a constant temperature anemometry wheatstone bridge, behaving as the transducer for the hot wire setup. G represents the gain of the amplifier while E stands for voltage and R is used for the resistance [Bruun, 1996]. 38

3.15 DANTEC Dynamics acquisition box, connected to the computer via an ethernet connection, including transducers for the thermocouple and the hot wire. It has six different channels for hot wires with constant temperature anemometry. 38

3.16 NI cDAQ-9189 A/D board for the connection between the DANTEC acquisition box and the computer. Multiple rooms for both Analog/Digital Input/Output. 39

3.17 Pressure tapplings viewed from the exit section. The one on the left is channel 1 just before the contraction and so the exit, while the one after the tubes is channel 5 just after the AC motor and so the inlet. The wind tunnel components are visible between the pressure tapplings. All the pressure tapplings are connected to the pressure scanner with the same type of hose(red) except channel 5(transparent). 40

3.18 Pressure tapplings viewed from the pre-settling chamber. The one on the right is channel 5 just after the AC motor and so the inlet, while the one on the other end is channel 1 just before the contraction and so the exit. The wind tunnel components are visible between the pressure tapplings. All the pressure tapplings are connected to the pressure scanner with the same type of hose(red) except channel 5(transparent). The big circle that the 5th pressure tapping is mounted on is the top of the pre-settling chamber. 40

3.19 Scanivalve DSA3217 pressure scanner having the range of 10''H₂O. There are two cables connected on the side of the scanner, where the one above is for the power supply while the one below is to communicate with the computer. The first four red hoses are connected to the first four pressure tapplings, while the transparent one is connected to the fifth pressure tapping as mentioned before. Extra two red hoses are connected to acquire the pressure values from the pitot-static tube (Channel 6 and 7). It has the REF channel to take the reference to compare the values from numbered channels. 41

3.20 Pressure measurement VI code front panel. It is able to tell the velocity at the exit section both with the data from the pitot-static tube and from pressure tapplings. First, it computes the offset values at zero speed for the two transducers, then subtracts them from the measured values at non-zero speed. The user has to set the sampling rate, sampling time, and ambient pressure for the pitot measurements. On the other hand, just the sampling time has to be written for the Scanivalve since the frequency is set from another front panel shown 3.36. The code makes all the waveforms from each pressure tapping, as well as the pressure drop visible. 42

3.21 Exactly the same front panel to see the pressures and the velocity as discussed in 3.20, just showing the ability to display pressure drop at different speed values on top of each other. 42

3.22 Pressure signal from channel 1 at Re=12328.7 that was obtained by Scanivalve pressure scanner at 270 Hz sampling rate for 300 seconds of sampling time. Blue lines represent the pressure values at the corresponding time value while the red line shows the mean value of the whole time series. 43

3.23 Mensor CPC6000 pressure calibrator. It has 2 channels. It is able to both measure and set the pressure, so it is totally effective in using for calibrating a pressure measurement tool. There is a touchscreen visible on the front side of the calibrator while the pressure channels are located behind. As soon as the desired pressure value to send is set on the calibrator, it starts to stabilize the value by itself and warns the user when it is done. 44

3.24 Behavior of offset for the first experiment. The red colored line represents the offset behavior of channel one at different pressure values while the blue one is channel 2, the green one is channel 3, the yellow one is channel 4, and the black one is channel 5. Each channel’s offset was investigated for a pressure range equal to its operating range. However, since the calibrator can go up to 2450 Pa, the range of channel 5 couldn’t be reached. Offset was taken as the difference between the sent pressure and the read pressure. 45

3.25 The behavior of offset for the second experiment. The red colored line represents the offset behavior of channel one at different pressure values while the blue one is channel 2, the green one is channel 3, the yellow one is channel 4, and the black one is channel 5. Each channel’s offset was investigated for a pressure range equal to its operating range. However, since the calibrator can go up to 2450 Pa, the range of channel 5 couldn’t be reached. Offset was taken as the difference between the sent pressure and the read pressure. To be compared with figure 3.24. 46

3.26 Autocorrelation between the pressure tapping signal samples. The horizontal axis represents the time lag between one sample to another(number of samples) while the vertical axis shows the correlation between those samples. Each filled red circle stands for a correlation value between samples that are corresponding time lag far away from each other. The samples can be said uncorrelated when the autocorrelation goes under the horizontal blue lines. 48

3.27 Autocorrelation between the pressure tapping samples focused between 11500th and 15000th samples. The horizontal axis represents the time lag between one sample to another(number of samples) while the vertical axis shows the correlation between those samples. Each filled red circle stands for a correlation value between samples that are corresponding time lag far away from each other. The samples can be said uncorrelated when the autocorrelation goes under the horizontal blue lines. 48

3.28 The behavior of mean values for eight different trials of sampling time. The whole pressure tapping time series that was obtained with a 270 Hz sampling rate for 300 seconds of sampling time, were divided into portions to see the behavior of the mean value at a corresponding sampling time. The empty circles represent the mean value of a corresponding time series portion. 50

3.29 Percentage range ratios for different sampling time values that were analyzed by dividing the whole pressure tapping time series, obtained with 270 Hz sampling rate for 300 seconds of sampling time, into portions. The empty circles stand for a percentage range ratio of mean values of each time series portion, implying how big the variation of mean values is with respect to the operating pressure range. Sampling time decreases as we go to the right on the horizontal axis. 51

3.30 The variance of vectors that are formed by mean values, where each mean value corresponds to a mean of a pressure tapping time series portion. The empty circles show the variance of mean values of corresponding portions. 52

3.31 Root-mean-square of percentage difference mean value between the real and the pressure tapping time series portions. The empty circles show an RMS % value for corresponding portions. The plot makes visible how effective is the difference between the mean values of the portions and the real mean. 53

3.32 Discrete pressure signal between around 125 s and 140 s sampling time. Filled circles are the pressure values acquired for the corresponding time value. To make it continuous, filled circles are connected to each other. As it is obvious, the number of filled circles gets higher as the pressure value goes towards the mean value. 54

3.33 Plot of pressure deviation from the mean value, which is represented in blue, corresponding to each time value. Signal was obtained by a Scanivalve pressure scanner with a 270 Hz sampling rate for 300 seconds of sampling time. The red line shows the root-mean-square(RMS) value of the fluctuations, to be able to understand its magnitude and effectiveness. 55

3.34 Fast fourier transform coefficients per pressure tapping signal frequency value. 56

3.35 Power spectral density per pressure tapping signal frequency value. 57

3.36 Front panel to change the sampling frequency of Scanivalve, which is provided by Scanivalve company themselves. The address above is the IP address of the computer while the timeout is to stop the code after the desired amount of time. Pressure and temperature values can easily be read from each channel. The 'Clear Ascii Buffer' button should be used if the Ascii table above is wanted to be cleaned. To set the frequency, PERIOD and/or AVG should be changed, by using the command window located just above the 'send (type above)' button. EU has to be set to 1 to deal with engineering units (psi). Moreover, BIN has to be set to 1 if the binary data format is wanted. To see the recent PERIOD, AVG, EU, BIN, and other informational values, the user should click 'send "LIST S"'. 58

3.37 Inverter terminal for on/off command. 0-24V digital input and 0V digital input are separately going into the inverter to take the difference in voltage. 60

3.38 A/D board for on/off. 5V and 0V digital outputs are going out. 60

LIST OF FIGURES

3.39 24 V digital 2 channels power supply in which the right one is currently being used to send 24V input to the inverter to power on/off. The current[Ampers] and the voltage [V] can be set manually by playing with the knob. It has 5 channels for the cables since the ground one can be used for both simultaneously. 60

3.40 Inverter terminal cabling for speed control. Two different 0-10V analog inputs are taken from the A/D to take the difference, where one of them will send 0-10V and the other will send 0V. 61

3.41 A/D board for speed control. Two different 0-10V analog outputs are sent for difference. 61

3.42 Pressure acquisition front panel. The user has to set the ambient pressure [Pa], sampling frequency [Hz], the sampling time [s], and the velocity offset [$\frac{m}{s}$] before running the code. The panel then displays the dynamic pressure [Pa] waveform, flow velocity [$\frac{m}{s}$] with a meter and a waveform graph, the density [$\frac{kg}{m^3}$], mean voltage [V], Reynolds number and elapsed time to acquire the pressure. 64

3.43 Dynamic pressure signal acquired with 100 Hz sampling frequency for 3.2 seconds of sampling time, to see the behavior. Sampling parameters were decided randomly just to see that the code is able to produce a signal in the desired form. The vertical axis is dynamic pressure [Pa] while the horizontal axis is time [s]. 65

3.44 Behavior of dynamic air viscosity with respect to the temperature at a constant atmospheric pressure of 1 atm[Munson, Rothmayer, and Okiishi, 2012]. The temperature range is much wider than the operating range, but they are all included to be parallel with the data provided. Empty circles are the dynamic air viscosity values each corresponding to a temperature value. 66

3.45 Plot to relate the velocity and the voltage, where the circles correspond to data points. The vertical axis is voltage[V] sent by the A/D board and the horizontal axis is velocity [$\frac{m}{s}$] at the exit section that was measured by the pitot-static tube. The voltage step was taken as 0.5V. 68

3.46 A separate investigation of the behavior of pressure at each channel placed at different locations along the plane air tunnel, reported in table 3.5, with respect to changing exit velocity. Each empty circle shows the pressure value for a specific speed value at the exit section. Pressure drop was calculated as the pressure difference between the values from channel 5 and channel 1. 69

3.47 Comparison of velocity values at the exit section that were obtained by pressure tappings and pitot-static tube, **for the first experiment**. The horizontal axis represents velocity values estimated by the pitot-static tube, which uses an MKS pressure transducer. The vertical axis stands for velocity values estimated by using interpolation functions with the pressure values measured by pressure tappings. Each color corresponds to a pressure tapping and pressure drop result. Pressure drop was calculated as the difference between pressure values at channel 5 and channel 1. Each empty circle shows a data point connecting two velocity values. 70

3.48 Relation between velocities that are measured by mks transducer connected to the pitot-static tube and by DSA 3217 pressure scanner that is connected to pressure tappings. p1 represents the results got from channel 1 and the same is valid for all p's. pdrop is the difference between the pressure at channel 5 and the pressure at channel 1. Four different plots where each was got from a different experiment, repeated to be consistent. 71

3.49 Percentage deviation of velocity values that were obtained by pressure tappings, plotted in the vertical axis, from the velocity values that were obtained by the pitot-static tube, reported in the horizontal axis, **for the first experiment**. Data were obtained for pressure drop and different channels placed along the streamwise direction of the plane air tunnel, reported in table 3.5. Each empty circle corresponds to a data point. Pressure drop was calculated as the difference between pressure values at channel 5 and channel 1. 72

3.50 Percentage deviation of velocity values that were obtained by pressure tappings, plotted in the vertical axis, from the velocity values that were obtained by the pitot-static tube, reported in the horizontal axis, **for the second experiment**. Data were obtained for pressure drop and different channels placed along the streamwise direction of the plane air tunnel, reported in table 3.5. Each empty circle corresponds to a data point. Pressure drop was calculated as the difference between pressure values at channel 5 and channel 1. 72

3.51 Percentage deviation of velocity values that were obtained by pressure tappings, plotted in the vertical axis, from the velocity values that were obtained by the pitot-static tube, reported in the horizontal axis, **for the third experiment**. Data were obtained for pressure drop and different channels placed along the streamwise direction of the plane air tunnel, reported in table 3.5. Each empty circle corresponds to a data point. Pressure drop was calculated as the difference between pressure values at channel 5 and channel 1. 73

3.52 Percentage deviation of velocity values that were obtained by pressure tappings, plotted in the vertical axis, from the velocity values that were obtained by the pitot-static tube, reported in the horizontal axis, **for the fourth experiment**. Data were obtained for pressure drop and different channels placed along the streamwise direction of the plane air tunnel, reported in table 3.5. Each empty circle corresponds to a data point. Pressure drop was calculated as the difference between pressure values at channel 5 and channel 1. 73

3.53 Magnitude of difference between the speed values estimated by pressure tappings and by pitot-static tube, at the exit section for four different experiments. Each color corresponds to a pressure tapping and pressure drop while each empty circle shows a data point. Pressure drop was calculated as the difference between pressure values at channel 5 and channel 1. 74

3.54 Front panel of the program in which the user introduces the hot wire connection to the acquisition board. There are 7 channels visible, 0 is for the thermocouple and 1-6 are for the hot wires. The user should select the number of the module in "CTA module no." and click ok. 77

3.55 Front panel of the program in which the user adjusts the overheat for the hot wire experiment. Measured quantities are the ambient temperature, wire resistance, leads resistance, support resistance, cable resistance, cold cable resistance, and wire temperature. User should click "measure temperature", "measure temperature", "set decade" and "ok". 78

3.56 Front panel of the program in which the user simply tells the system to operate the CTA setup. The user should first click the switch above "operate" and see the green light next to "operate" and then "ok" to finish this step. 79

3.57 Front panel of the program in which the user sets the parameters for conditioning the hot wire signal. The high-pass filter, low-pass filter, gain, and the offset for the voltage signal are set with this front panel. The user should adjust the required parameters and click "ok". 80

3.58 Front panel of the program in which the user tests the response of the hot wire by sending an input voltage value and observing the behavior. Frequencies of the AC test and the sampling can be changed. The vertical axis is voltage [V] and the horizontal axis is time [s]. Bridge compensations like gain, offset and the bridge can be set. The user should first click "one shot" and then "ok". 81

3.59 Voltage signal at $\frac{x}{d} = 5$ at exit Reynolds number $Re=8000$ that was obtained by NI DAQ acquisition board at 20000 Hz sampling rate for 100 seconds of sampling time. Blue lines represent the pressure values at the corresponding time value while the red line shows the mean value of the whole time series. 82

LIST OF FIGURES

3.60 Autocorrelation between the hot wire voltage samples. The horizontal axis represents the time lag between one sample to another (number of samples) while the vertical axis shows the correlation between those samples. Each filled red circle stands for a correlation value between samples that are corresponding time lag far away from each other. The samples can be said uncorrelated when the autocorrelation goes under the horizontal blue lines 83

3.61 The autocorrelation of hot wire signal that is zoomed between specific values to analyze it in more detail. 84

3.62 Behavior of mean values for eight different trials of sampling time. The whole hot wire voltage time series that was obtained with a 20000 Hz sampling rate for 100 seconds of sampling time, were divided into portions to see the behavior of the mean value at a corresponding sampling time. The empty circles represent the mean value of a corresponding time series portion. 85

3.63 Percentage range ratios for different sampling time values that were analyzed by dividing the whole hot wire voltage time series, obtained with a 20000 Hz sampling rate for 100 seconds of sampling time, into portions. The empty circles stand for a percentage range ratio of mean values of each time series portion, implying how big the variation of mean values is with respect to the operating pressure range. Sampling time decreases as we go to the right on the horizontal axis. 86

3.64 Variance of vectors formed by mean values, where each mean value corresponds to a mean of a hot wire voltage time series portion. The empty circles show the variance of mean values of corresponding portions. 87

3.65 Root-mean-square of percentage difference mean value between the real and the hot wire voltage time series portions. The empty circles show an RMS % value for corresponding portions. The plot makes visible how effective is the difference between the mean values of the portions and the real mean. 88

3.66 Plot of voltage deviation from the mean value at $Re= 8000$ the exit section, which is represented in blue, corresponding to each time value. Signal was obtained by NI DAQ acquisition board with 20000 Hz sampling rate for 100 seconds of sampling time. The red line shows the root-mean-square(RMS) value of the fluctuations, to be able to understand its magnitude and effectiveness. RMS value was analyzed since the mean value of the fluctuations gives 0, as expected. 90

3.67 Fast fourier transform coefficients per hot wire signal frequency value that was computed with respect to the formulation discussed in section 3.3.3. 91

3.68 Power spectral density per hot wire signal frequency value that was computed with respect to the formulation discussed in section 3.3.3. The number of bins was selected as 2×10^6 92

LIST OF FIGURES

3.69	Hot wire calibration front panel in which the user can set pressure sampling time, ambient pressure, hot wire sampling rate, hot wire sampling time, maximum speed, speed step, and the starting speed. VI shows the hot wire voltage signal, calibration plot, dynamic pressure, density, hot wire mean voltage, current velocity, elapsed time for the hot wire acquisition, and temperature. The user should set on/off to true before running the VI.	94
3.70	Engineering drawing of the part designed to fix one end of the traversing system. All the units are in mm.	95
3.71	Engineering drawing of the part designed to hold the x-wire during the calibration. All the units are in mm.	96
3.72	The product of the 3D printing process to fix one end of the traversing system for the calibration process. The part helps to fix the one end of the traversing system on the y-axis to ensure the rotation given by the stepper motor. Three legs of the part are plugged into the traversing system after drilling the holes. The material of the particle is plastic.	97
3.73	Printed product of the x-wire holder design for the calibration process. X-wire probe is plugged in inside the holder to demonstrate the usage. X-wire is supposed to be plugged in on the right end of the probe shown in the picture. The upper two holes can be used to fix the wire probe to ensure that its location will not change during the experiments. The material of the particle is plastic.	97
3.74	X-wire picture including the wires, probes, stem, and the dots on the stem to give a reference to the user for the proper orientation.	98
3.75	X-wire calibration front panel in which the user can set pressure sampling time, ambient pressure, hot wire sampling rate, hot wire sampling time, maximum speed, speed step, the starting speed, angle step and the maximum step corresponding to the maximum angle desired to be reached. VI shows the two hot wire voltage signals, calibration plot, dynamic pressure, density, temperature, the two hot wire mean voltage values and the current velocity. The user should set on/off to true before running the VI.	99
3.76	Hot wire experiment front panel in which the user can set the desired speed at the exit section, diameter step, and the last location in both stepwise and crosswise direction, hot wire sampling time and rate, pressure sampling time, and ambient pressure. VI is capable of informing the user if the offset is calculated, offset dynamic pressure, dynamic pressure, temperature, dynamic viscosity, density, Reynolds number, hot wire mean voltage, hot wire voltage signal, and the time series. The user should set on/off to true before running the VI.	100
3.77	Engineering drawing of the part designed to mount the x-wire on the sliding system for the experiments. All the units are in mm.	102

LIST OF FIGURES

3.78 VI code for fully automatic x-wire experiments with the help of the sliding system. The user should first provide the inputs for the diameter step in the streamwise direction, diameter step in the crosswise direction, last diameter location in both directions, pressure sampling time, ambient pressure, hot wire sampling time, and the hot wire sampling rate before running the code. Measured quantities are the voltages from two wires, temperature, and dynamic pressure. The VI starts to acquire once the offset is calculated. 102

4.1 On/off command front panel where the user should use the boolean switch to power on/off the inverter. The error box on the right is there in case of any unknown error appears. If the user wants to halt the loop, it is enough to click "STOP". 105

4.2 Inverter speed control front panel. The user sets the voltage either by the knob or by the digital numeric input below the knob, from the computer to control the speed of the inverter. The maximum voltage of 10V corresponds to a speed around $51 \frac{m}{s}$ at the exit section. The "STOP" button is to stop the loop. 106

4.3 Pressure drop along PAT. Each color stands for an exit velocity and each empty circle shows the pressure value at the corresponding channel located at different locations along the plane air tunnel, reported in table 3.5. The data were obtained from DSA 3217 pressure scanner. 106

4.4 The behavior of pressure at each channel placed at different locations along the plane air tunnel, reported in table 3.5, with respect to changing exit velocity. Each color corresponds to a channel while each empty circle shows the pressure value for a specific speed value at the exit section. 107

4.5 The behavior of pressure drop with respect to changing exit velocity. Pressure drop was calculated as the pressure difference between the 5th and 1st channels, where the numbers standing for the pressure tapping locations were reported in table 3.5. Each empty circle shows the pressure drop value for a specific speed value at the exit section. . 108

4.6 Plot of static pressure just before the contraction section and the dynamic pressure at the exit section at different exit section velocities. Each empty circle corresponds to a data point. 109

4.7 Plot of difference between static pressure at the settling chamber and the dynamic pressure at the exit section at different exit section velocities. Each empty circle corresponds to a data point. 110

4.8 PI controller front panel using a pitot-static tube. The user has to set the ambient pressure, velocity offset, and sampling time before running the code. The sampling frequency was taken as 100 Hz which is not required to be entered every time. Moreover, the user also has to set proportional gain and integral gain, which means the behavior of the response can be controlled by the user. 111

4.9 Response plot of the PI controller that was created with a pitot-static tube. The vertical axis represents the speed $[\frac{m}{s}]$ at the exit section while the horizontal one stands for the time[s]. Circles are data points where the speed was measured and reported. Moreover, the black line shows the behavior of the desired speed $[\frac{m}{s}]$ set by the user, on the other hand, the red line corresponds to the current speed $[\frac{m}{s}]$ measured at the exit section after the user sets the desired speed. . . . 111

4.10 PI controller front panel without using a pitot-static tube. The user has to set the ambient pressure, velocity offset, and sampling time before running the code. Moreover, the user also has to set proportional gain and integral gain, which means the behavior of the response can be controlled by the user. 112

4.11 Response plot of the PI controller that was created without a pitot-static tube. The vertical axis represents the speed $[\frac{m}{s}]$ at the exit section while the horizontal one stands for the time[s]. Circles are data points where the speed was measured and reported. Moreover, the black line shows the behavior of the desired speed $[\frac{m}{s}]$ set by the user, on the other hand, the red line corresponds to the current speed $[\frac{m}{s}]$ measured at the exit section after the user sets the desired speed. 113

4.12 Hot wire calibration curve obtained at the exit section of plane air tunnel. Each empty circle corresponds to a data point. 114

4.13 Velocity behavior of the planar jet flow at $\frac{x}{d} = 10, \frac{y}{d} = 0$ and with exit section Reynolds number, $Re=8000$. The plot was obtained thanks to the hot wire voltage signal and the calibration function relating the velocity to the voltage. The acquisition was performed for 100 seconds at a sampling rate of 20 kHz. 115

4.14 Fluctuating velocity behavior of the planar jet flow at $\frac{x}{d} = 10, \frac{y}{d} = 0$ and with exit section Reynolds number, $Re=8000$. The plot was obtained thanks to the hot wire voltage signal and the calibration function relating the velocity to the voltage and the formula represented in equation 2.64. The acquisition was performed for 100 seconds at a sampling rate of 20 kHz. 116

4.15 Look-up table obtained by reporting the mean voltage values of two wires at the corresponding velocity and the angle values. E1 is the mean voltage value of wire 1 while the mean voltage of wire 2 is denoted as E2. 117

4.16 The surface formed by the data points at which the voltage values from the calibration correspond to a streamwise velocity calculated by the equation 3.32. The grid was created with 1001 points. 118

4.17 Surface formed by the data points at which the voltage values from the calibration correspond to a crosswise velocity calculated by the equation 3.32. The grid was created with 1001 points. 118

LIST OF FIGURES

- 4.18 3D plot of mean streamwise velocity profiles measured at different streamwise locations with single hot wire at exit Reynolds number $Re=12235.8$. Each empty circle corresponds to a data point. Dimensions both crosswise and streamwise are normalized with the exit section length, which is represented by "d". The acquisition for a wire was performed for 40 s having a sampling rate of 10 kHz. 121
- 4.19 2D plot of mean streamwise velocity profiles measured at different streamwise locations with single hot wire at exit Reynolds number $Re=12235.8$. Each empty circle corresponds to a data point. Dimensions both crosswise and streamwise are normalized with the exit section length, which is represented by "d". The acquisition for a wire was performed for 40 s having a sampling rate of 10 kHz. 122
- 4.20 3D plot of mean streamwise velocity profiles measured at different streamwise locations with x-wire at exit Reynolds number $Re=11506.6$. Each empty circle corresponds to a data point. Dimensions both crosswise and streamwise are normalized with the exit section length, which is represented by "d". The acquisition for a wire was performed for 40 s having a sampling rate of 10 kHz. 123
- 4.21 2D plot of mean streamwise velocity profiles measured at different streamwise locations with x-wire at exit Reynolds number $Re=11506.6$. Each empty circle corresponds to a data point. Dimensions both crosswise and streamwise are normalized with the exit section length, which is represented by "d". The acquisition for a wire was performed for 40 s having a sampling rate of 10 kHz. 124
- 4.22 3D plot of mean crosswise velocity profiles measured at different streamwise locations with x-wire at exit Reynolds number $Re=12833.47$. Each empty circle corresponds to a data point. Dimensions both crosswise and streamwise are normalized with the exit section length, which is represented by "d". The acquisition for a wire was performed for 40 s having a sampling rate of 10 kHz. 125
- 4.23 2D plot of mean crosswise velocity profiles measured at different streamwise locations with x-wire at exit Reynolds number $Re=12833.47$. Each empty circle corresponds to a data point. Dimensions both crosswise and streamwise are normalized with the exit section length, which is represented by "d". The acquisition for a wire was performed for 40 s having a sampling rate of 10 kHz. 126
- 4.24 3D plot of fluctuating streamwise velocity profiles measured at different streamwise locations with single hot wire at exit Reynolds number $Re=12235.8$. Each empty circle corresponds to a data point. Dimensions both crosswise and streamwise are normalized with the exit section length, which is represented by "d". The acquisition for a wire was performed for 40 s having a sampling rate of 10 kHz. 127

LIST OF FIGURES

4.25 2D plot of fluctuating streamwise velocity profiles measured at different streamwise locations with single hot wire at exit Reynolds number $Re=12235.8$. Each empty circle corresponds to a data point. Dimensions both crosswise and streamwise are normalized with the exit section length, which is represented by "d". The acquisition for a wire was performed for 40 s having a sampling rate of 10 kHz. 128

4.26 3D plot of fluctuating streamwise velocity profiles measured at different streamwise locations with x-wire at exit Reynolds number $Re=11506.6$. Each empty circle corresponds to a data point. Dimensions both crosswise and streamwise are normalized with the exit section length, which is represented by "d". The acquisition for a wire was performed for 40 s having a sampling rate of 10 kHz. 129

4.27 2D plot of fluctuating streamwise velocity profiles measured at different streamwise locations with x-wire at exit Reynolds number $Re=11506.6$. Each empty circle corresponds to a data point. Dimensions both crosswise and streamwise are normalized with the exit section length, which is represented by "d". The acquisition for a wire was performed for 40 s having a sampling rate of 10 kHz. 130

4.28 3D plot of mean streamwise velocity profiles measured at different streamwise locations with x-wire at exit Reynolds number $Re=12833.47$. Each empty circle corresponds to a data point. Dimensions both crosswise and streamwise are normalized with the exit section length, which is represented by "d". The acquisition for a wire was performed for 40 s having a sampling rate of 10 kHz. 131

4.29 3D plot of mean streamwise velocity profiles measured at different streamwise locations with x-wire at exit Reynolds number $Re=12833.47$. Each empty circle corresponds to a data point. Dimensions both crosswise and streamwise are normalized with the exit section length, which is represented by "d". The acquisition for a wire was performed for 40 s having a sampling rate of 10 kHz. 132

4.30 Variation of Reynolds normal stresses along the crosswise direction at different streamwise locations. Each empty circle corresponds to a data point. Experiments were conducted with the single hot wire at 10 kHz for 40 seconds at the exit section Reynolds number $Re=12235.8$. 133

4.31 Variation of Reynolds normal stresses along the centerline at different streamwise locations. Each empty circle corresponds to a data point. Experiments were conducted with the single hot wire at 10 kHz for 40 seconds at the exit section Reynolds number $Re=12235.8$ 134

4.32 Variation of Reynolds normal stresses, normalized by the squared centerline velocity at the corresponding location, along the crosswise direction at different streamwise locations. Each empty circle corresponds to a data point. Experiments were conducted with the single hot wire at 10 kHz for 40 seconds at the exit section Reynolds number $Re=12235.8$ 135

LIST OF FIGURES

5.1 Response plots from two different control loops, where one is with the pitot-static tube at the exit section and the other is without the pitot-static tube. Empty circles correspond to a data point where each stands for a different type of speed at the exit section. 140

5.2 Percentage pressure drop calculated at different exit section velocity values. Pressure drop is the difference between the pressure at the pre-settling chamber and the settling chamber just before the contraction part. Each empty circle corresponds to a data point. 142

5.3 Pressure drop along the honeycomb for different speed values at the exit section of the plane air tunnel. Each empty circle corresponds to a data point. 143

5.4 Percentage static pressure decrement along the contraction part for different exit section velocity values. Each empty circle corresponds to a data point. 145

5.5 Similarity between the static pressure at the settling chamber and the static pressure drop along the contraction part. Each empty circle corresponds to a data point. 146

5.6 Normalized mean velocity profile variation along the streamwise direction. The horizontal axis shows the normalized velocity where the U_c refers to the centerline mean velocity. Each symbol corresponds to a data point. The data points marked with the "o" belong to x-wire while the ones shown with "*" are from the single wire experiments. 147

5.7 Normalized fluctuating velocity profile variation along the streamwise direction. The horizontal axis shows the normalized velocity where the u_{rmsc} refers to the centerline fluctuating velocity. Each symbol corresponds to a data point. The data points marked with the "o" belong to x-wire while the ones shown with "*" are from the single wire experiments. 148

5.8 Normalized fluctuating velocity by the centerline velocity at $y/d=0$ plotted at different streamwise locations. Each symbol corresponds to a data point. The data points marked with the "o" belong to x-wire while the ones shown with "*" are from the single wire experiments. . 149

5.9 Comparison between the literature(left)[Heskestad, 1965] and the experimental results(right) for the mean velocity value normalized by the mean centerline velocity value at the corresponding streamwise location. The horizontal axis is the ratio between the crosswise and the streamwise direction while the vertical axis is the normalized velocity. 150

5.10 Comparison between the literature(left)[Hashiehbfaf and Romano, 2013] and the experimental results(right) for the fluctuating velocity value normalized by the mean exit velocity value at the corresponding streamwise location. The horizontal axis is the streamwise location while the vertical axis is the normalized velocity, also called turbulent intensity. Each empty circle corresponds to a data point on the right. 151

7.1 On/off command VI code 159

7.2 Inverter control VI code 159

LIST OF FIGURES

7.3	Pressure acquisition VI code for mks transducer	160
7.4	Pressure acquisition VI code for mks transducer	160
7.5	Temperature acquisition VI code	161
7.6	Inner loop of temperature acquisition VI code	161
7.7	Velocity calculation VI code	162
7.8	Block diagram of the VI to control the rotation of the stepper motor used for the traversing system for x-wire calibration.	162
7.9	PI controller with a pitot-static tube VI code	162
7.10	PI controller without a pitot-static tube VI code	163
7.11	Adjustable frequency pressure scanner VI	163
7.12	Pressure scanner block diagram 1	164
7.13	Pressure scanner block diagram 2	164
7.14	Pressure scanner block diagram 3	165
7.15	Hot wire calibration fully automatic VI block diagram 1	165
7.16	Hot wire calibration fully automatic VI block diagram 2	166
7.17	Hot wire experiment fully automatic VI block diagram 1	166
7.18	Hot wire experiment fully automatic VI block diagram 1	167
7.19	Hot wire experiment fully automatic VI block diagram 3	167
7.20	X-wire wire calibration fully automatic VI block diagram 1	168
7.21	X-wire wire calibration fully automatic VI block diagram 2	168
7.22	X-wire wire calibration fully automatic VI block diagram 3	169
7.23	X-wire experiment fully automatic VI block diagram 1	169
7.24	X-wire experiment fully automatic VI block diagram 2	170
7.25	X-wire experiment fully automatic VI block diagram 3	170

List of Tables

3.1	Microstep setting for the stepper motor. Shows the setting that has to be done by the switches, to have the desired number of steps for 60° rotation. It determines the resolution of the stepper motor.	31
3.2	Current setting of the stepper motor. Switches should be arranged in a corresponding way to the current value used for the motor.	31
3.3	Properties of fan used in plane air tunnel to provide the flow rate into it.	32
3.4	Properties of AC motor used in plane air tunnel to provide the rotation for the fan.	33
3.5	Locations of pressure tapplings. They are sequenced from the beginning (5 th channel) to the end (1 st channel). Channel 1 is the one that is the closest to the exit, while channel 5 is the one that is closest to the AC motor. There are wind tunnel components between the channels, to analyze the pressure drop between them.	39
3.6	Percentage range ratio for channels indicating how big the offset values for different pressure values of each channel with respect to the operating pressure range obtained during the first experiment. Calculated by using equation 3.3.	46
3.7	Percentage range ratio for channels indicating how big the offset values for different pressure values of each channel with respect to the operating pressure range obtained during the second experiment. Calculated by using equation 3.3. To be compared with table 3.6.	47
3.8	Sampling time values for the corresponding number of portions that the whole pressure voltage time series was divided to.	49
3.9	Potential pressure sampling time values for the pressure scanner DSA 3217.	53
3.10	Pressure acquisition parameters decided for pressure scanner DSA 3217 after analyzing all related methods.	57
3.11	Commands to change the sampling frequency of Scanivalve.	59
3.12	Boolean values for on/off command. To power on the inverter, the true command should be sent, so the boolean should be switched to light up green. To power off the inverter, the false command should be sent, so the boolean shouldn't light up.	61
3.13	Pressure acquisition sampling parameters, decided arbitrarily for now just to be able to create a working acquisition VI code and analyze the pressure signal.	63

LIST OF TABLES

3.14	Fourth-order polynomial interpolations that were performed with respect to the curve represented in figure 3.46. Pressure drop was calculated as the pressure difference between the values from channel 5 and channel 1. Interpolated functions will be used to estimate the exit velocity by measuring the pressure values at channels.	70
3.15	PI gain table that was set iteratively by trial and fail method for the case with the pitot-static tube.	75
3.16	PI gain table that was set iteratively by trial and fail method for the case without the pitot-static tube.	76
3.17	Sampling time values for the corresponding number of portions that the whole hot wire voltage time series was divided to.	85
3.18	Potential hot wire sampling time values for the NI DAQ acquisition board. The values were obtained by different methods discussed in part 3.3.2.	88
3.19	Sampling parameters selected for the hot wire acquisition.	93
3.20	Speed values chosen for the x-wire calibration.	99
3.21	Angle values are chosen for the x-wire calibration.	99
4.1	Comparison of resolutions of two different range MKS transducers, which were calculated by using equation 3.2.	112
4.2	Sampling parameters preferred during the hot wire experiments. . . .	114
4.3	Points at which the hot wire measurements were performed. x/d is the normalized distance in streamwise directions and the y/d is the normalized distance in the crosswise direction.	120
5.1	PI gain table that was set iteratively by trial and fail method. . . .	138
5.2	Resolution, minimum detectable pressure value in Pascals, values by two different pressure transducers where one was used for the pitot-static tube (MKS) and the other was used for pressure tappings (DSA 3217).	141
5.3	Porosity values for three different wind tunnel components.	143
5.4	Sampling parameters for the hot wire experiments	146

Nomenclature

Abbreviations

A/D : Analog/Digital

AC : Alternating current

AVG : Average

CCA : Constant current anemometry

CICLoPE : The Centre for International Cooperation in Long Pipe Experiments

CTA : Constant temperature anemometry

DR : Dynamic range

FFT : Fast fourier transform

I/O : Input/Output

NI : National instruments

PAT : Plane air tunnel

PI : Proportional integral

PLC : Programmable logic controller

PSD : Power spectral density

RMS : Root-mean-square

RPM : Revolutions per minute

VFD : Variable frequency driver

VI : Virtual instrument

Greek letters

α : Directional dependency or overheat ratio

β : Thermal expansion coefficient or porosity or temperature coefficient of resistance

δU : Uncertainty

ϵ : Emissivity of the wire surface

λ : Bulk viscosity coefficient

NOMENCLATURE

μ : Dynamic viscosity or mean value

μ : Kinematic viscosity

ρ : Fluid density

σ : Stefan-Boltzmann constant

τ_{ii} : Normal stress in i direction

τ_{ij} : Shear stress in ij direction

θ : Flow angle

Mathematical operations

Δ : Difference

$\frac{D}{Dt}$: Total derivative

$\nabla \cdot x$: Divergence of x

Notations

\dot{m} : Mass flow rate

\dot{q} : Heat flux

\bar{x} : Mean x value

x' : Fluctuating x value

A : Section area

a : Speed of sound

A_c : Free tunnel crosssectional area

A_t : Total tunnel crosssectional area

C_i : Fitting coefficients

C_p : Specific heat capacity

C_w : Wire heat capacity

E : voltage thermal energy stored by the wired

f_s : Sampling frequency

g : Gravitational acceleration

H : Heat transferred to surroundings

NOMENCLATURE

h :	Convective heat transfer coefficient or hot wire spanwise(pitch) velocity correction factor
I :	Current
k :	Conductive heat transfer coefficient or hot wire cross-wise(yaw) velocity correction factor
N :	Number of samples or number of bits
N_b :	Number of frequency bins
p_1 :	1 st pressure tapping
p_2 :	2 nd pressure tapping
p_3 :	3 rd pressure tapping
p_4 :	4 th pressure tapping
p_5 :	5 th pressure tapping
p_0 :	Stagnation pressure
$p_{dynamic}$:	Dynamic pressure
p_{static} :	Static pressure
p_{total} :	Total pressure
p_{drop} :	Pressure drop
R :	Specific gas constant
R_f :	Wire resistance at flow temperature
R_w :	Wire resistance
R_{ii} :	Reynolds normal stress in i direction
R_{ij} :	Reynolds shear stress in ij direction
T_f :	Flow temperature
T_s :	Surroundings temperature
T_w :	Wire temperature
t_s :	Sampling time
Tu :	Turbulence intensity
U_{eff} :	Effective velocity
U_{range} :	Range of the signal value

NOMENCLATURE

W : Power generated by joule heating

X_N : Normal component of parameter x

X_T : Tangential component of parameter x

x_{rms} : RMS x value

Non-dimensional parameters

Gr : Grashof number

M : Mach number

Nu : Nusselt number

Pr : Prandtl number

Re : Reynolds number

1

Introduction

Although only some scientists are aware of it, fluids are everywhere, even though they are not visible, since they can be in the form of liquids and gases. Assuming that the surrounding fluid is stationary, as an object moves, a certain fluid flow starts to occur around the object since it disturbs the surrounding fluid volume inserting forces into the fluid, thus feeling the reaction forces from the fluid. The subdiscipline that studies the movement of fluids is called "fluid dynamics". Fluid dynamics is one of the main branches of fluid mechanics [Jones, 2019]. In addition, more specifically, the subdiscipline that deals with the motion of air and other gaseous fluids, and the forces acting on the body by these fluids, is called "aerodynamics" [NASA, 2011]. As one can immediately guess, there are infinitely many cases in that a fluid can move, in terms of direction, rotation, speed, geometry, etc. where each results in a different condition that should be analyzed by a corresponding specific technique.

There are two ways to analyze the behavior of a fluid movement, which are called experimental and computational. In computational fluid dynamics, fluid flow is fully solved by the governing equations, which are mass conservation, momentum conservation, and energy conservation [Wendt, 2008]. On the other hand, experimental fluid dynamics analyses the fluid flow straight in the field by using specific techniques and materials, either by creating the same conditions of the flow in the lab or by implementing the techniques directly in the real flow case. In this study, experimental methods were used to analyze a certain type of fluid flow.

Experiments in aerodynamics are needed when the system is too complex to trust the computational methods, when equations and/or solutions are not known or are not reliable for a specific case, and when there is a need to validate or find new laws, equations, and/or models. To accomplish accurate results, all and only related conditions should be provided for the experiment.

One of the most important classifications of a flow, being laminar or turbulent, determines the level of difficulty in investigating the flow characteristics either experimentally or computationally. In laminar flow, the fluid moves smoothly in parallel layers with no disruption between the layers [SimScale, 2021]. Thus, the investigation of flow properties is way easier due to a clear pattern. On the other hand, a flow can be said to be turbulent when there is not a certain pattern since it is chaotic, including eddies and vortices [Mathieu and Scott, 2000].

A turbulent flow is multi-scale, non-deterministic in both time and space, has a high Reynolds number, stochastic, 3D and contains small-scale random vorticity and

instabilities. Thus, it requires a very large number of data points in the domain to be able to catch most of the details. Although it is not yet completely determined, the flow can be estimated as being laminar or turbulent by computing the Reynolds number[Banerjee, 2014]. The following figure 1.1 shows the effect of the Reynolds number on the flow behavior around a cylinder.

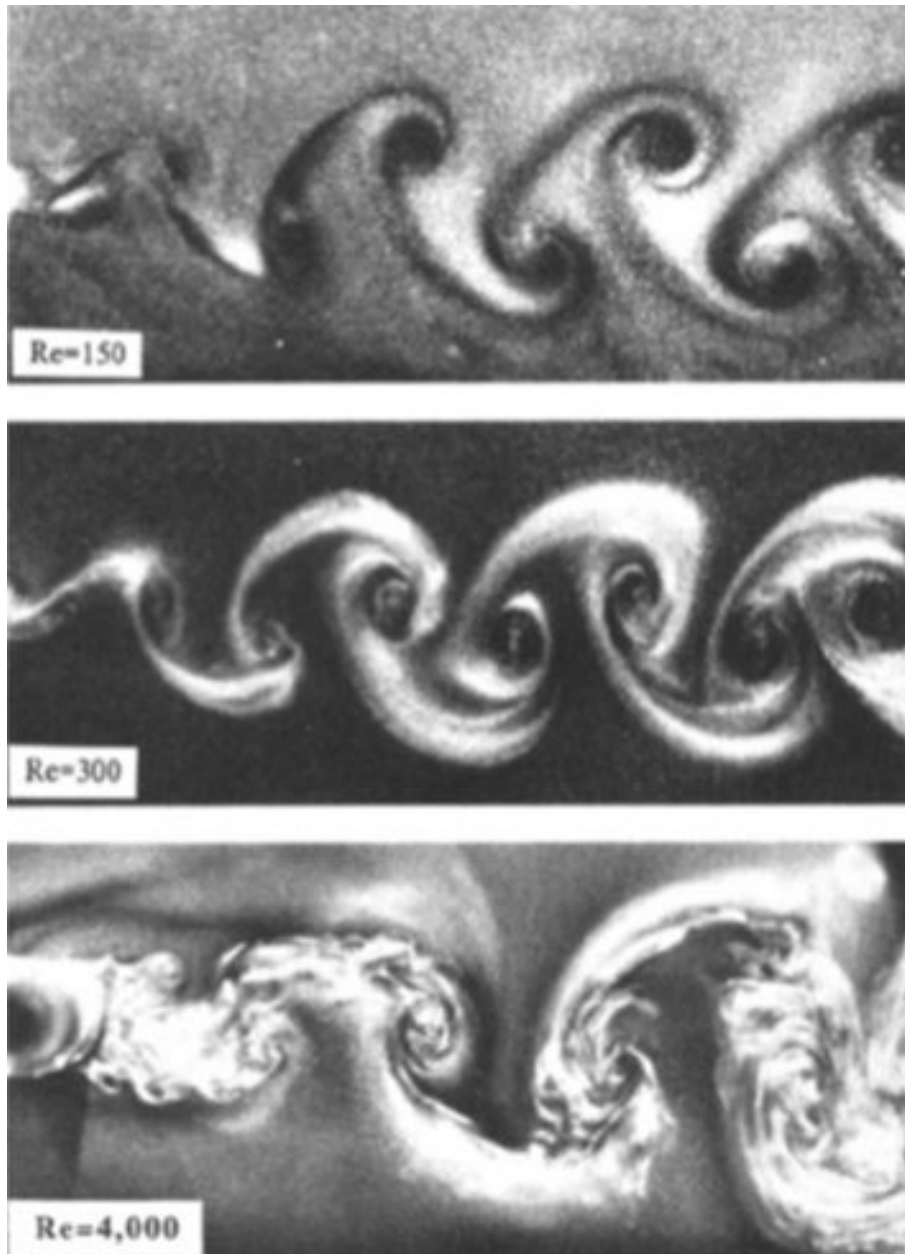


Figure 1.1: Von Karman vortex shedding appearing on the fluid flow around a cylinder. The direction of the flow is from left, where the cylinder is located, to right. The conditions of the shedding were visualized in different Reynolds number, $Re=150$, $Re=300$ and $Re=4000$, respectively from top to bottom[Alziadeh, 2017].

All turbulent fluid flows are composed of certain behavior of variables such as velocity, temperature, pressure, vorticity, etc., which they are classified with respect

to. Any of these instantaneous quantities can be decomposed into two components, which are known as the mean value and the fluctuating value. The mean part of the quantity is nothing but the time-averaged value while the deviations from the mean value are called fluctuations (see fig 2.6). Fluctuations are the most powerful indications of the intensity of the turbulence level of the flow. Depending on the quantity, the fluctuations are usually very high frequency [“Measuring Turbulent Flows”, 2022]. In this study, the aim is to make the proper tool ready for the velocity measurements in a long pipe flow. Therefore, the method for the experimental study should be decided wisely in a way that the equipment is capable of capturing enough information despite the extremely high frequency fluctuating velocity.

Introducing hot wire anemometry, one of the fastest measurement techniques in experimental aerodynamics, it was made possible to investigate turbulent flows thanks to its temporal resolution. It requires a very short time to respond to a change in the measured quantity, resulting in the possibility to catch the fluctuations. Hot wire anemometry is a single-point measurement technique, which requires a special calibration to relate the wire voltage to the velocity of the flow. While a single wire is usually preferred only for one component measurements, an x-wire is used for two-component studies and the 3D measurements are performed with the triaxial probes. This study focused on the x-wire experiments since two-component measurements are aimed inside the long pipe flow.

However, in turbulent pipe flow, since the speed is not constant and the random fluctuations are in 3D affecting the response of the hot wire due to its directional sensitivity, it is not really the best way to perform the calibration. Hence, the jet flow was preferred to calibrate the hot wire because it has a potential core, in which the flow speed is constant and fluctuation-free.

A jet flow, which will be introduced more in detail in section 1.1, is a type of flow in which it maintains the inlet speed inside a region, called the potential core before it becomes turbulent. Then, the flow becomes fully turbulent as the vortices grow. The most common type of jet flow is a round jet, whose exit is a circle. Round jets are usually used to calibrate only one wire since their potential core is not big enough. However, in turbulence studies, the use of more than one wire is necessary to reach the fluctuation correlations at different points. For that reason, the planar jet, which has a rectangular exit section, was preferred to calibrate more than one wire simultaneously, as it has a bigger potential core along its spanwise direction (see fig 2.7).

If the calibration of an x-wire is not performed clear of errors, the results are not reliable at all, even though the experiments were conducted free from disturbances. During the calibration, there are two main sources of errors, which are man-made and system-induced. Problems that can be caused by the user could be the manual speed and angle settings. According to that, this study concentrated on possible ways of automatizing the calibration to avoid man-made sources of errors. The aim is to develop a setup that lets the user calibrate a hot wire fully automatically, including powering on/off the wind tunnel, adjusting its speed, and the angle of the wire in case of x-wire calibration. Moreover, since the hot wires are highly sensitive to any flow around, the studies refrained from using the pitot-static tube to exclude another source of flow disturbance during the multiple wire calibration. In this

way, a single and an x-wire calibration can easily be performed free from man-made disturbances and it avoids excessive time and effort wasted during the calibrations.

1.1 Planar Jet Flow

A jet flow, as it sounds highly intuitive, is a flow case in which the fluid is leaving a body from its exit to a free space. For example, the exhaust gas leaving a car's exhaust creates a jet flow. There are two different main types of jet flows. One of them is a round jet, as in the car exhaust example. In a round jet, the shape of the body exit section is round which creates spreading in all directions. On the other hand, the other type of jet flow, the planar jet flow was formed by a body exit shape that is rectangular, meaning that it is much longer in one direction compared to another. These type of flows are called planar jet flows since it creates a plane after the exit due to the rectangular shape of the exit. In figure 3.2, the exit section of the plane air tunnel is visible. Both of the jet flows have a dominant streamwise fluid flow which results in spreading in other directions due to the turbulence[WU et al., 2013].

The planar jet flow is a type of free shear flow, which is firstly investigated by Schlichting[WU et al., 2013]. After his numerical studies, it became one of the significant questions in fluid dynamics, and then the first experimental study was performed by Forthman in which he measured and reported the mean velocity profile of a planar jet[WU et al., 2013]. As time goes and the questions arises, lots of scientists started contributing to the literature both experimentally and numerically.

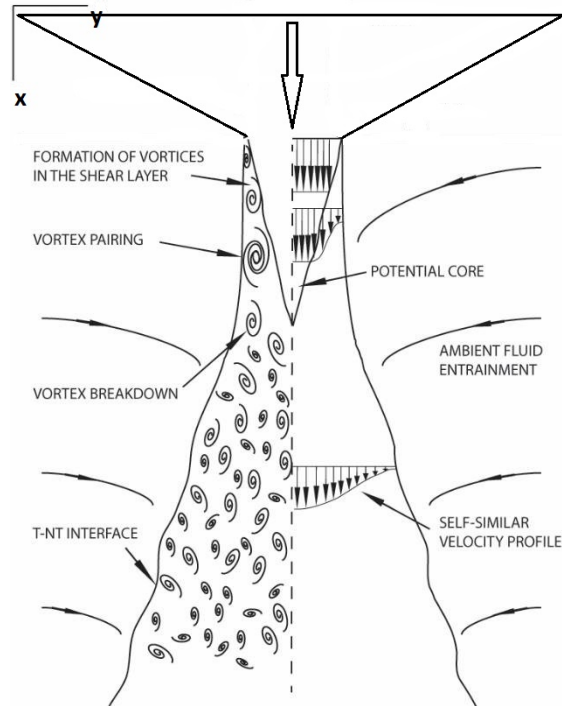


Figure 1.2: Basic schematic of a turbulent planar jet flow and fluid dynamics phenomena from its side view. The surrounding air is stationary. The part on the top is the body where the fluid exits from. The 2D coordinate system is visible on top left[Hassan, Guo, and Vlachos, 2019].

Figure 1.2 above shows the basic schematic of a turbulent planar jet flow from its side view. The layer separating the moving air and the surrounding stationary air is called as "Viscous Super Layer". Its mean thickness is in the order of Kolmogorov's scale[Taveira and Silva, 2014].

After leaving the body, the flow becomes a free shear flow since there appear the shear forces between the moving air and the stationary air surrounding the exit. These shear forces result in "Kelvin-Helmoltz instability", where small-scale perturbations draw kinetic energy from the mean flow[Gramer, Gramer@noaa, and Gov, 2007]. As it can be understood from the picture, as soon as the fluid leaves the body, a region called as "potential core" appears, at which the inlet velocity remains constant and uniform inside, without being affected by the vortices between the shear layer and the core[Kashi, Weinberg, and Haustein, 2018]. The formation of vortices in the shear layer starts just outside the potential core, pressing the region inside. Thus, the potential core cannot remain rectangular but it spreads along the streamwise direction with a decreasing height until the region loses its uniform undisturbed inlet velocity. Then, those small vortices start to grow at the nozzle, and they are carried with the flow in the streamwise direction. Those growing vortices interrupt the jet area. Hence, the jet is collapsed and becomes fully turbulent.

A turbulent planar jet flow is a coherent turbulent structure in which there is an organized component of vorticity being phase-correlated over the entire space of the structure. Thus, time-averaged statistics can be applied to investigate the behavior of the structure.

Another outcome of the shear forces is entrainment into the jet area. Entrainment

is the phenomenon of the fact that the fluid outside the jet region enters inside. Due to that entrance of the external fluid, the height of the jet region increases, which is called spreading, as the mean velocity decreases [Enjalbert, Galley, and Pierrot, 2009]. Therefore, the shape of a turbulent jet flow is derived from the shear forces due to the pressure difference between the flow inside the jet region and the surrounding air. As well as figure 1.2, figure 1.3 also represents the increasing height of the jet area while the speed along the streamwise direction is decreasing. The height that is visible in figure 1.3 refers to "half-width" since is half of the distance between the upper and lower boundaries of the jet area. The spreading rate is measured by analyzing the change in half-width with respect to streamwise direction. Furthermore, the turbulent planar jet flow is assumed to be identical in the plane direction (xz plane), and there is no spreading in that direction.

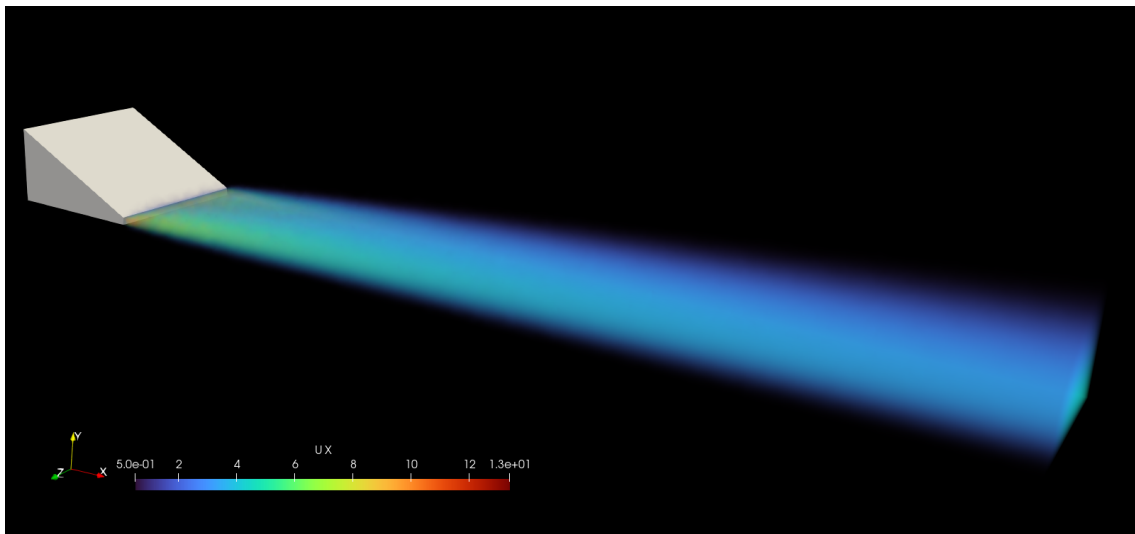


Figure 1.3: Screenshot of a computational fluid dynamics analysis of the turbulent planar jet flow at $Re=12299.9$ for the half geometry to have a less computational effort by using OpenFoam open source code environment. Large eddy simulation with dynamic k equation was preferred. The color map refers to streamwise velocity. The geometry on the left is the half of the plane air tunnel exit section in both z and x axes. The surrounding air is stationary.

As the flow develops, the velocity profile is said to become self-similar and it stops changing after a relatively long distance from the potential core in a streamwise direction. From that point, the flow can be said to be fully-developed.

Theoretical Background and Literature Review

2.1 Hot Wire Anemometry

Hot wires are widely used sensors to measure the temperature and the velocity in gas, liquid, or two-phase flows. They have a very good frequency response relative to its main competitors (Laser Doppler Anemometry - LDA), letting it provide high sampling rate measurements. Hot wires are very small piece of sensors which has a diameter of around $5 \mu\text{m}$ and a length of 0.1 mm to 3 mm [Morris and Langari, 2012]. Tungsten and platinum are the most preferred materials for hot wires since they can provide a high-temperature coefficient of resistance [Shekhter, 2011]. Following figure 2.1 shows the shape of a hot wire probe which is made of tungsten and platinum [Je-Chin Han, 2020]

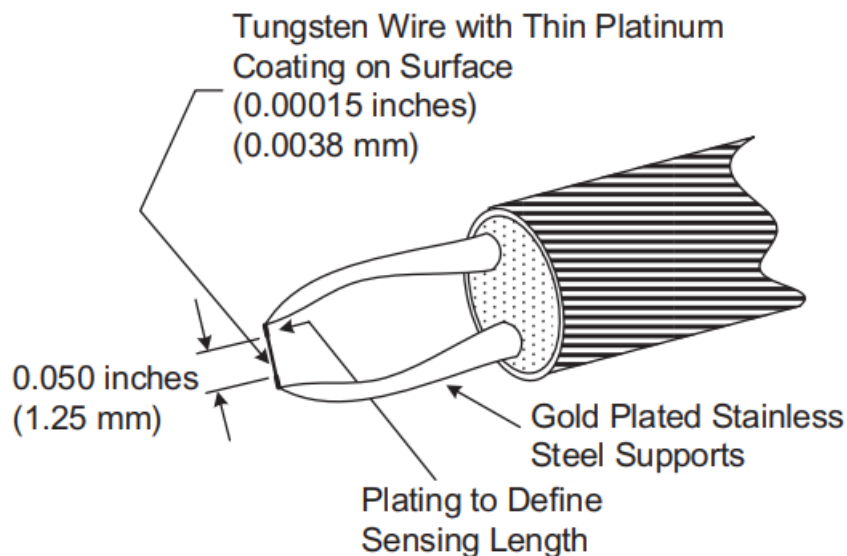


Figure 2.1: Hot wire probe schematic expressing its materials and size [Je-Chin Han, 2020].

The working principle of the hot wire anemometry is based on two facts; the heat transfer between the surrounding and the wire itself, and the electrical resistance of a

metal conductor is a function of its temperature [George, 1985]. As a circuit element, hot wires have their own resistance, which changes with the varying temperature of the wire. Considering a wire that is heated by a passage of current on the circuit that it is connected to and is placed somewhere in space. If there is no flow, the wire equates its temperature by dissipating heat to the surrounding. On the other hand, if there is a fluid flow with nonzero velocity, the heat transfer coefficient changes, resulting in the alteration of heat dissipation. Then, new heat dissipation causes a new wire temperature and so the change in its resistance. Since the wire is connected to a circuit having its own voltage and current values, the effect of resistance change can easily be seen by analyzing the voltage and/or current values instantaneously, hence the behavior of velocity or temperature can be investigated.

As it can be understood from the discussion above, in hot wire anemometry, hot wire senses the changes in the flow, behaving as a sensor, and then the circuit that it is connected to transforms these changes into a certain form of a signal, acting as the transducer of the system.

The governing equation of a hot wire anemometry [Bruun, 1996] is written as

$$\boxed{\frac{DE}{Dt} = W - H}, \quad (2.1)$$

$$E = C_w T_s, \quad (2.2)$$

$$W = I^2 R_w, \quad (2.3)$$

where

E = thermal energy stored by the wire [J],

W = power generated by joule heating [W],

H = heat transferred to surroundings [J],

C_w = wire heat capacity [$\frac{J}{K}$],

T_s = surroundings temperature [K],

I = current [A],

R_w = wire resistance [Ω].

When the equilibrium is reached, power generated by joule heating, W , and heat transferred to surroundings, H becomes equal to each other. Moreover, heat can be transferred in three ways; convection to fluid flow, conduction to probes, and radiation to surroundings [Bergman, Bergman, Incropera, DeWitt, and Lavine, 2011], which can be represented as follows. Equation 2.4 represents the heat transferred by conduction while the equation 2.5 stands for the heat transferred by convection and the equation 2.6 shows the formula for heat transfer by radiation [Patil, Radle, and Shome, 2015].

$$\dot{q}_k = kA \frac{T_w - T_f}{L}, \quad (2.4)$$

$$\dot{q}_c = hA(T_w - T_f), \quad (2.5)$$

$$\dot{q}_r = \epsilon\sigma A(T_w^4 - T_f^4), \quad (2.6)$$

$$H = \sum \dot{q}_k + \dot{q}_c + \dot{q}_r, \quad (2.7)$$

where

- k = conductive heat transfer coefficient,
- A = surface area of the wire subjected to heat transfer,
- T_w = wire temperature,
- T_f = flow temperature,
- L = length scale,
- h = convective heat transfer coefficient,
- ϵ = emissivity of the wire surface,
- σ = Stefan-Boltzmann constant.

By assuming that the wire is long enough and the wire temperature is uniform, conductive heat transfer to the supports can be neglected. Moreover, possessing high enough flow velocity and $\frac{l}{d} > 200$ allows the radiation to the surroundings and the free convection to the flow to be negligible. Thus, the heat transferred by the wire can be written down as

$$H = \sum \dot{q}_c, \quad (2.8)$$

where \dot{q}_c represents only the forced convection by the flow.

Since only the convective heat transfer is being dealt with, introducing a non-dimensional heat transfer coefficient by the convection, the Nusselt number, will help in a way that the voltage of the circuit can be related to the flow velocity.

$$Nu = \frac{hd}{k}, \quad (2.9)$$

where

d = wire diameter.

Nusselt number is defined as the ratio of convective heat transfer to conductive heat transfer [Astakhov, 2012], so equation 2.9 can easily be derived by dividing equation 2.5 to 2.4. Then, assuming the equilibrium condition is reached so the power generated by joule heating, W becomes equal to the heat transferred to surroundings, H as follows

$$hA(T_w - T_f) = I^2 R_w, \quad (2.10)$$

substituting the formula for cylinder surface area and the Nusselt number definition into equation 2.10

$$Nu(\pi k L)(T_w - T_f) = I^2 R_w, \quad (2.11)$$

To relate the voltage value of the circuit to the flow velocity, the Nusselt number should be written as a function of velocity. There are several empirical formulas relating the Nusselt number to the velocity, geometry, and temperature of the flow. Actually, the Nusselt number dependency can be formulated as [Astakhov, 2012],[Sheikholeslami and Ganji, 2017]

$$Nu = Nu(Re, Pr, Gr, M, \alpha, \gamma, \frac{T_w - T_f}{T_f}), \quad (2.12)$$

where

$$Gr = \frac{gL^3\beta\Delta T}{\nu^2}, \quad (2.13)$$

$$Gr = \frac{Buoyancy\ forces}{Viscous\ forces}, \quad (2.14)$$

$$Pr = \frac{\mu c_p}{k}, \quad (2.15)$$

$$Pr = \frac{Momentum\ diffusivity}{Thermal\ diffusivity}, \quad (2.16)$$

$$M = \frac{V}{a}, \quad (2.17)$$

$$M = \frac{Flowspeed}{Speed\ of\ sound}, \quad (2.18)$$

α	and	γ	= directional dependency,
g			= gravitational acceleration [$\frac{m}{s}$],
L			= representative length [m],
β			= thermal expansion coefficient [K^{-1}],
Δ			= temperature difference between the wire and the fluid bulk temperature [K],
ν			= kinematic viscosity [$\frac{m^2}{s}$],
μ			= dynamic viscosity [$\frac{Ns}{m^2}$],
c_p			= specific heat [$\frac{J.kg}{K}$],
k			= thermal conductivity [$\frac{W}{m.K}$],
V			= flow speed [$\frac{m}{s}$],
a			= speed of sound [$\frac{m}{s}$].

As one can understand, the Grashof number, Gr is the non-dimensional quantity representing the free convection due to buoyancy forces [Shires, 2011]. As it was mentioned before, by assuming that $\frac{l}{a} > 200$ and

$$Re > Gr^{\frac{1}{3}}, \quad (2.19)$$

Grashof number dependency of Nusselt number can be neglected. Moreover, since the flow is not in sonic conditions, and it is orthogonal to the hot wire placed in the flow, it can be said that the Nusselt number is the function of only

$$Nu = Nu(Re, Pr, \frac{T_w - T_f}{T_f}). \quad (2.20)$$

Thus, one of the most widely used empirical formulas formed by [Kramers, 1946] is represented as

$$Nu = 0.42Pr^{0.20} + 0.57Pr^{0.33}Re^{0.50}. \quad (2.21)$$

Since the change in temperature of the wire is proportional to the change in its resistance, the temperature difference in equation 2.11 can be replaced by the resistance difference and then the following equation relating the electrical quantities to the flow velocity can be obtained [George, 1985].

$$\boxed{\frac{I^2 R_w}{R_w - R_f} = A + B < U >^{0.5}}, \quad (2.22)$$

where

$$A = 0.42 \frac{(\pi k L)}{\beta} Pr^{0.20}, \quad (2.23)$$

$$B = 0.57 \frac{(\pi k L)}{\beta} Pr^{0.33} \left(\frac{d}{\nu}\right)^{0.5}, \quad (2.24)$$

R_f = wire resistance at flow temperature [Ω],

β = temperature coefficient of resistance,

d = wire diameter [m].

Having derived the equation to relate the resistance and voltage to the flow velocity, it must be strictly known that these relations 2.23 and 2.24 are **not** used practically. Coefficients A and B are determined by a special method of calibration depending on the flow case, which was discussed in section 3.6.

There are two different main applications of hot wire anemometry, which are named constant current anemometry (CCA) and constant temperature anemometry (CTA). In constant current anemometry, a change in flow velocity results in a temperature variation in the wire, which lets its resistance alter, and so does the current in the circuit. Then, the change in current is measured and set back to the previous value by changing the voltage with an amplifier. Hence, the current of the circuit is kept constant. The frequency response is set by the geometrical properties of the wire. Moreover, burnout is one of the most common problems that can be faced in CCA since the current is kept constant although the temperature of the wire is increasing [Zhao et al., 2021].

The type of hot wire anemometry application that was preferred for this study is CTA, since its frequency response is much better than CCA, and velocity is a rapidly changing quantity. In constant temperature anemometry, variation in resistance of the wire is due to the flow velocity change followed by the change in the wire temperature. Resistance alteration forces the current to change, the amplifier senses the change in current and sets it back to keep the resistance constant. In this way, the temperature of the wire is kept constant. The electrical circuit performing these operations consists of a wheatstone bridge which can be seen in figure 3.14. The frequency response is set by the electrical configuration of the feedback loop.

An important quantity to represent the wire sensitivity to velocity fluctuations is the overheat ratio, α that is represented below in equation 2.25 [Farouk, Lin, and Lei, 2010]

$$\alpha = \frac{T_w - T_f}{T_f}. \quad (2.25)$$

As the difference between the wire temperature and the flow temperature increases, the hot wire becomes more sensitive to velocity fluctuations. Thus, the higher the overheat ratio the better velocity fluctuation measurements. It is crucial to keep the flow temperature, T_f constant during the experiments, but it may not be highly possible if the wind tunnel is an open loop. In that case, certain corrections, that were discussed in section 3.6, for the temperature difference must be done while calibrating the wire for the recent flow condition.

Another investigation to understand the response of a hot wire is on its directional sensitivity. As it was mentioned before, the hot wire is placed orthogonal to the known direction of the flow to ensure that the measured velocity is the streamwise velocity. However, by looking at the figure 2.2 below, one can immediately say that the problems will certainly arise since the response of the hot wire is almost equal in x and z directions so it is hard to understand which one is being measured.

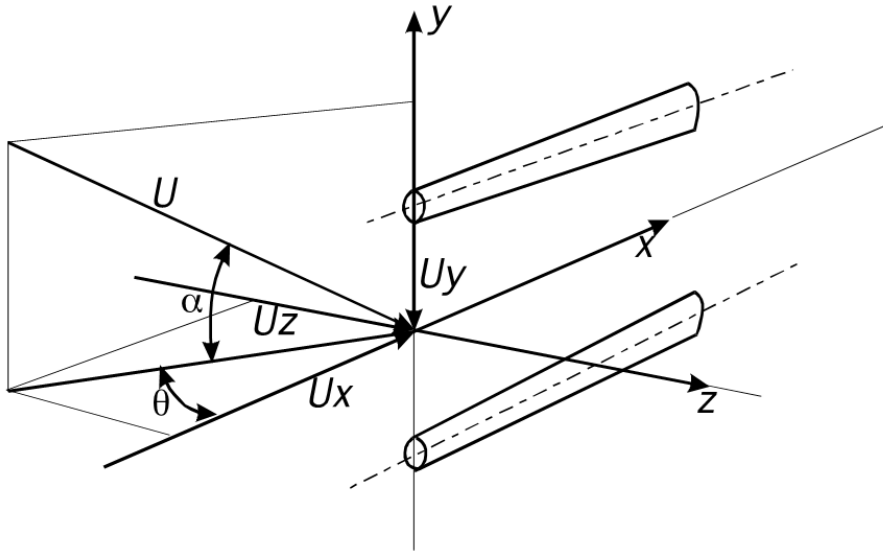


Figure 2.2: Schematic of a hot wire including the coordinate system, angles, and the velocity components. θ shows the pitch angle while the α stands for the yaw angle. Two parallel cylinders that are perpendicular to the y-axis are the probes of the wire, while the wire is connected between their ends [Shekhter, 2011].

Thus, an equation [Je-Chin Han, 2020] to express the output velocity of the hot wire can be written as

$$U_{eff}^2 = U_x^2 + k^2 U_y^2 + h^2 U_z^2, \quad (2.26)$$

where

U_{eff} = effective velocity sensed by hot wire [$\frac{m}{s}$],
 U_x = flow velocity in streamwise direction [$\frac{m}{s}$],
 U_y = flow velocity in cross-wise direction [$\frac{m}{s}$],
 U_z = flow velocity in spanwise direction [$\frac{m}{s}$],
 k = hot wire cross-wise(yaw) velocity correction factor,
 h = hot wire spanwise(pitch) velocity correction factor.

Velocity correction factors, k, and h can empirically be determined by knowing the real velocity and the velocity estimated by hot wire at the corresponding axis. According to [Je-Chin Han, 2020], k varies between $0 < k < 0.2$ while h generally takes a value in the interval of $1 < h < 1.2$. As the ratio of hot wire length to diameter, $\frac{l}{d}$ increases, k decreases. Moreover, if the wire is placed correctly, mean velocities in spanwise and cross-wise directions are equal to zero, meaning that the effective velocity can be represented as

$$U_{eff}^2 = (\bar{U}_x + u_x)^2 + k^2 u_y^2 + h^2 u_z^2, \quad (2.27)$$

where

\bar{U}_x = mean velocity in streamwise direction [$\frac{m}{s}$],
 u_x = fluctuating velocity in streamwise direction [$\frac{m}{s}$],
 u_y = fluctuating velocity in cross-wise direction [$\frac{m}{s}$],
 u_z = fluctuating velocity in spanwise direction [$\frac{m}{s}$].

Applying Taylor series expansion and knowing that

$$\bar{U}_x \gg |u_x|, |u_y|, |u_z|, \quad (2.28)$$

effective velocity is reduced to

$$\boxed{U_{eff} = \bar{U}_x + u_x}. \quad (2.29)$$

A two wires probe, x-wire is one of the tools that allows one to measure the quantities in two directions unlikely to a single wire. In x-wire configuration, two wires are placed orthogonal to each other like an X shape as can be seen in the following figure 2.3

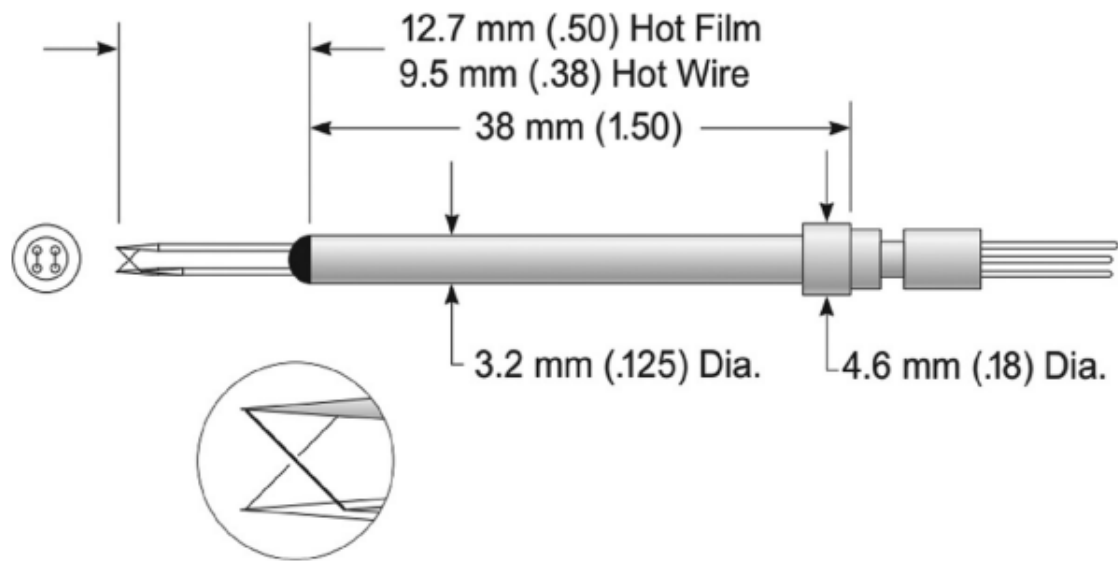


Figure 2.3: Schematic of an x-wire probe side view showing the stem dimensions and the wire orientations on the most left [Je-Chin Han, 2020].

Wires are mounted with 90° between each other so that the angle between each wire and the dominant flow direction is 45° . Side view schematic of an x-wire sensor is visible in figure 2.4 below

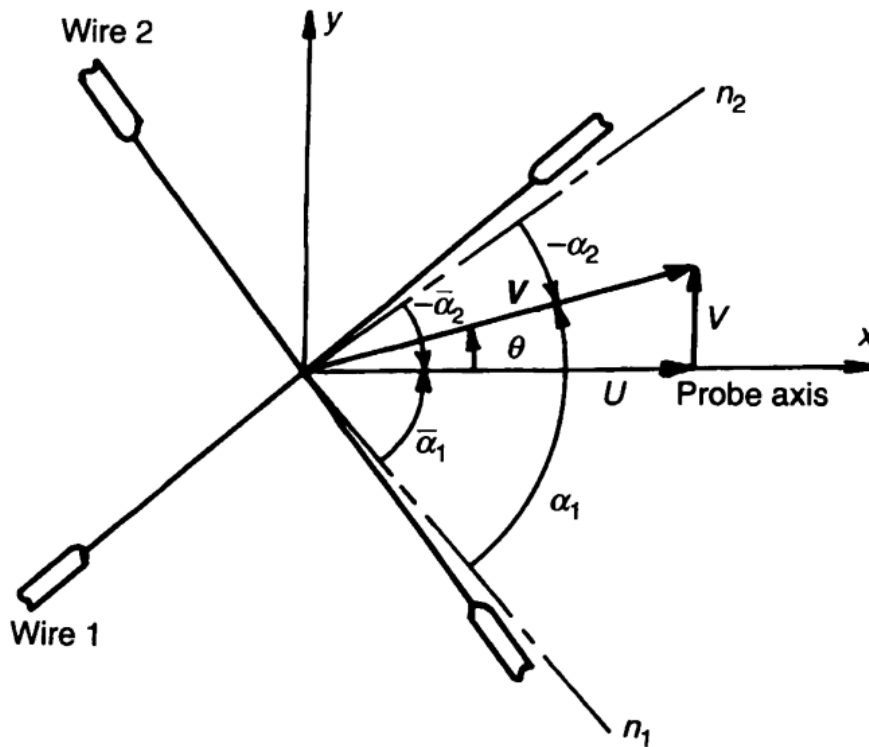


Figure 2.4: X-wire sensor schematic showing the angles formed by the wire orientations and the coordinate system of the probe. n_1 and n_2 are the normals to wire 1 and wire 2. U is the x component of the flow velocity, \mathbf{V} , while the vertical V is the y component of the flow velocity, \mathbf{V} . θ is the angle between the dominant flow direction and the x-axis of the probe [Bruun, 1996].

The x-wire should be placed in a way that $\theta = 0^\circ$, then the flow angle and the two components of the velocity can easily be determined by investigating the voltage values coming from two wires, concerning the response of the x-wires. The velocity can be divided into two components for each wire as follows

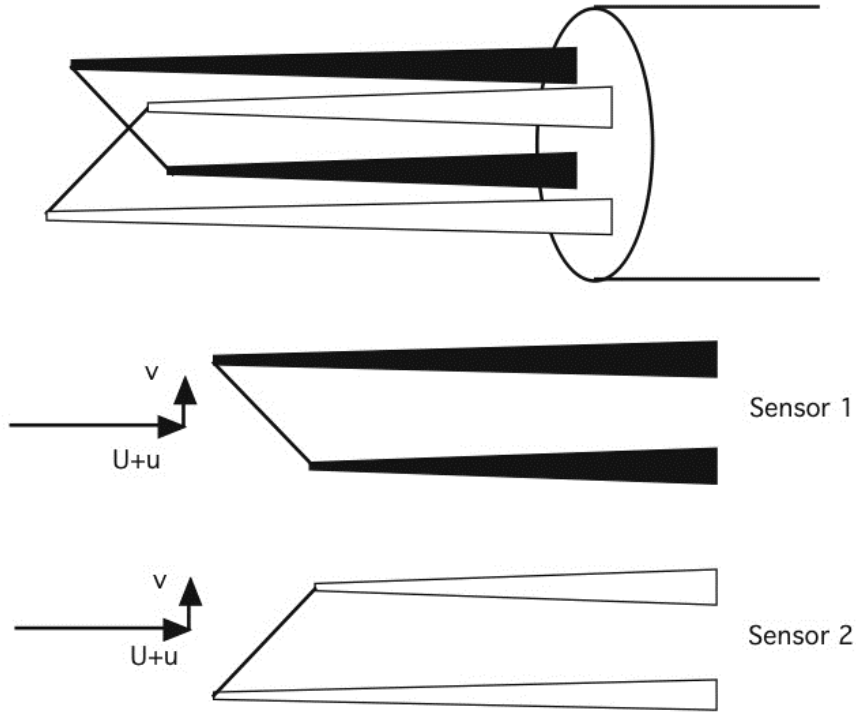


Figure 2.5: Separate schematics of the wires of x-wire to make the velocity components corresponding to each visible. U is the x component of mean velocity while u is the x component of the fluctuating velocity. Fluctuating velocity in the y direction is represented by v .

$$U_{N1} = \frac{U + u + v}{\sqrt{2}}, \quad (2.30)$$

$$U_{T1} = \frac{U + u - v}{\sqrt{2}}, \quad (2.31)$$

$$U_{N2} = \frac{U + u - v}{\sqrt{2}}, \quad (2.32)$$

$$U_{T2} = \frac{U + u + v}{\sqrt{2}}, \quad (2.33)$$

where

U_{Ni} = velocity normal to wire i ,

U_{Ti} = velocity tangent to wire i .

Then, the effective cooling velocity of the two wires [Burattini, 2008] can be written as

$$U_{eff1}^2 = U_{N1}^2 + k^2 U_{T1}^2 = \frac{1}{2} [(U + u + v)^2 + k^2 (U + u - v)^2 + 2h^2 w^2], \quad (2.34)$$

$$U_{eff2}^2 = U_{N2}^2 + k^2 U_{T2}^2 = \frac{1}{2} [(U + u - v)^2 + k^2 (U + u + v)^2 + 2h^2 w^2], \quad (2.35)$$

Then, the mean and the fluctuating velocity can be formulated as

$$U_{xprobe} = \frac{U_{eff1} + U_{eff2}}{\sqrt{2(1+k^2)}} = U[1 + \frac{u}{U} + \frac{k^2 v^2 + h^2 w^2}{(1+k^2)U^2} + h.o.t.], \quad (2.36)$$

$$v_{xprobe} = \frac{U_{eff1} - U_{eff2}}{\sqrt{2(1+k^2)}} = v \frac{1-k^2}{1+k^2} + O(vw^2, v^3). \quad (2.37)$$

In real life, while conducting an x-wire experiment, instead of using the equations reported above, calibration is preferred to analyze the response of the x-wire to be safer and more practical. The calibration procedure of the x-wire is discussed in section 3.6.5

2.2 Planar Jet Flow

As introduced in section 1.1, planar jet flow is a free shear flow that is produced by a rectangular orifice of an open loop blower plane air tunnel. Governing equations [Anderson, 1992] to investigate the viscous fluid flow in the non-conservation form are

$$\frac{D\rho}{Dt} + \rho \nabla \cdot V = 0, \quad (2.38)$$

$$\rho \frac{Du}{Dt} = -\frac{\partial p}{\partial x} + \frac{\partial \tau_{xx}}{\partial x} + \frac{\partial \tau_{yx}}{\partial y} + \frac{\partial \tau_{zx}}{\partial z} + \rho f_x, \quad (2.39)$$

$$\rho \frac{Dv}{Dt} = -\frac{\partial p}{\partial y} + \frac{\partial \tau_{yx}}{\partial x} + \frac{\partial \tau_{yy}}{\partial y} + \frac{\partial \tau_{zy}}{\partial z} + \rho f_y, \quad (2.40)$$

$$\rho \frac{Dw}{Dt} = -\frac{\partial p}{\partial z} + \frac{\partial \tau_{xz}}{\partial x} + \frac{\partial \tau_{yz}}{\partial y} + \frac{\partial \tau_{zz}}{\partial z} + \rho f_z, \quad (2.41)$$

$$\begin{aligned} \rho \frac{D}{Dt} \left(e + \frac{V^2}{2} \right) &= \rho \dot{q} + \frac{\partial}{\partial x} \left(k \frac{\partial T}{\partial x} \right) + \frac{\partial}{\partial y} \left(k \frac{\partial T}{\partial y} \right) + \frac{\partial}{\partial z} \left(k \frac{\partial T}{\partial z} \right) \\ &\quad - \frac{\partial u p}{\partial x} - \frac{\partial v p}{\partial y} - \frac{\partial w p}{\partial z} + \frac{\partial u \tau_{xx}}{\partial x} + \frac{\partial u \tau_{yx}}{\partial y} + \frac{\partial u \tau_{zx}}{\partial z} \\ &\quad + \frac{\partial v \tau_{xy}}{\partial x} + \frac{\partial v \tau_{yy}}{\partial y} + \frac{\partial v \tau_{zx}}{\partial z} + \frac{\partial w \tau_{xz}}{\partial x} + \frac{\partial w \tau_{yz}}{\partial y} + \frac{\partial w \tau_{zz}}{\partial z} + \rho \vec{f} \cdot \vec{V}, \end{aligned} \quad (2.42)$$

where

$\frac{D}{Dt}$	= total derivative,
ρ	= fluid density ,
$\nabla \cdot x$	= divergence of x,
\vec{V}	= velocity,
p	= pressure,
u	= velocity in x direction,
v	= velocity in y direction,
w	= velocity in z-direction,
τ_{ii}	= normal stress in i direction,
τ_{ij}	= shear stress in ij direction,
f_i	= body force per unit mass acting on the fluid element in i direction,
T	= temperature,
e	= internal energy per unit mass,
\dot{q}	= the heat transferred by thermal conduction into the moving fluid element,
k	= thermal conductivity,
$\frac{V^2}{2}$	= kinetic energy per unit mass.

The equations 2.38, 2.39, 2.40, 2.41 and 2.42 are called as Navier Stokes equations that are used to analyse the behavior of a fluid flow in non-conservative form. The non-conservation form of the equations was obtained thanks to the fundamental physical principles applied to a moving fluid element. On the other hand, the conservation form of the equations can be obtained from finite control volume fixed in space [Hall, 2021b].

Firstly, equation 2.38 is the continuity equation that was derived from the conservation of mass, saying that the mass of the fluid is conserved over time over a finite volume in space. Secondly, equations 2.39, 2.40 and 2.41 are momentum equations, which are used to ensure that the momentum is conserved in x, y and z directions, respectively. Lastly, equation 2.42 is the last governing equation that is used to show that the energy is conserved.

To have the conservation form of the governing equations, the equations should be modified for a finite volume fixed in space. Firstly, the integral definition over the control volume was applied to the continuity equation. Moreover, using the definition of the substantial derivative and then applying the divergence definition and the derivative rules to the non-conservative equations results in the conservation form of the momentum and energy equations. Following equations 2.43, 2.44, 2.45, 2.46 and 2.47 are the conservation form of the governing equations.

$$\frac{\partial \rho}{\partial t} + \nabla \cdot (\rho \vec{V}) = 0, \quad (2.43)$$

$$\frac{\partial(\rho u)}{\partial t} + \nabla \cdot (\rho u \vec{V}) = -\frac{\partial p}{\partial x} + \frac{\partial \tau_{xx}}{\partial x} + \frac{\partial \tau_{yx}}{\partial y} + \frac{\partial \tau_{zx}}{\partial z} + \rho f_x, \quad (2.44)$$

$$\frac{\partial(\rho v)}{\partial t} + \nabla \cdot (\rho v \vec{V}) = -\frac{\partial p}{\partial y} + \frac{\partial \tau_{yx}}{\partial x} + \frac{\partial \tau_{yy}}{\partial y} + \frac{\partial \tau_{zy}}{\partial z} + \rho f_y \quad (2.45)$$

$$\frac{\partial(\rho w)}{\partial t} + \nabla \cdot (\rho w \vec{V}) = -\frac{\partial p}{\partial z} + \frac{\partial \tau_{xz}}{\partial x} + \frac{\partial \tau_{yz}}{\partial y} + \frac{\partial \tau_{zz}}{\partial z} + \rho f_z, \quad (2.46)$$

$$\begin{aligned}
 \frac{\partial}{\partial t}[\rho(e + \frac{V^2}{2})] + \nabla \cdot [\rho(e + \frac{V^2}{2}\vec{V})] = \rho\dot{q} + \frac{\partial}{\partial x}(k\frac{\partial T}{\partial x}) + \frac{\partial}{\partial y}(k\frac{\partial T}{\partial y}) + \frac{\partial}{\partial z}(k\frac{\partial T}{\partial z}) \\
 - \frac{\partial up}{\partial x} - \frac{\partial vp}{\partial y} - \frac{\partial wp}{\partial z} + \frac{\partial u\tau_{xx}}{\partial x} + \frac{\partial u\tau_{yx}}{\partial y} + \frac{\partial u\tau_{zx}}{\partial z} \\
 + \frac{\partial v\tau_{xy}}{\partial x} + \frac{\partial v\tau_{yy}}{\partial y} + \frac{\partial v\tau_{zx}}{\partial z} + \frac{\partial w\tau_{xz}}{\partial x} + \frac{\partial w\tau_{yz}}{\partial y} + \frac{\partial w\tau_{zz}}{\partial z} + \rho\vec{f} \cdot \vec{V}.
 \end{aligned} \tag{2.47}$$

Furthermore, the normal and the shear stresses can be expressed as [Anderson, 1992]

$$\tau_{xx} = \lambda\nabla \cdot \vec{V} + 2\mu\frac{\partial u}{\partial x}, \tag{2.48}$$

$$\tau_{yy} = \lambda\nabla \cdot \vec{V} + 2\mu\frac{\partial v}{\partial y}, \tag{2.49}$$

$$\tau_{zz} = \lambda\nabla \cdot \vec{V} + 2\mu\frac{\partial w}{\partial z}, \tag{2.50}$$

$$\tau_{xy} = \tau_{yx} = \mu(\frac{\partial u}{\partial y} + \frac{\partial v}{\partial x}), \tag{2.51}$$

$$\tau_{xz} = \tau_{zx} = \mu(\frac{\partial u}{\partial z} + \frac{\partial w}{\partial x}), \tag{2.52}$$

$$\tau_{yz} = \tau_{zy} = \mu(\frac{\partial v}{\partial z} + \frac{\partial w}{\partial y}), \tag{2.53}$$

where,

μ = molecular viscosity coefficient,

λ = bulk viscosity coefficient,

$$\lambda = -\frac{2}{3}\mu. \tag{2.54}$$

Thus, by inserting definitions of stresses into momentum equations, governing equations can be written in the form of

$$\frac{\partial \rho}{Dt} + \nabla \cdot (\rho\vec{V}) = 0, \tag{2.55}$$

$$\begin{aligned}
 \frac{\partial(\rho u)}{\partial t} + \frac{\partial(\rho u^2)}{\partial x} + \frac{\partial(\rho uv)}{\partial y} + \frac{\partial(\rho uw)}{\partial z} = -\frac{\partial p}{\partial x} + \frac{\partial}{\partial x}(\lambda\nabla \cdot \vec{V} + 2\mu\frac{\partial u}{\partial x}) \\
 + \frac{\partial}{\partial y}[\mu(\frac{\partial u}{\partial y} + \frac{\partial v}{\partial x})] + \frac{\partial}{\partial z}[\mu(\frac{\partial u}{\partial z} + \frac{\partial w}{\partial x})] + \rho f_x,
 \end{aligned} \tag{2.56}$$

$$\begin{aligned}
 \frac{\partial(\rho v)}{\partial t} + \frac{\partial(\rho uv)}{\partial x} + \frac{\partial(\rho v^2)}{\partial y} + \frac{\partial(\rho vw)}{\partial z} = -\frac{\partial p}{\partial y} + \frac{\partial}{\partial x}[\mu(\frac{\partial u}{\partial y} + \frac{\partial v}{\partial x})] \\
 + \frac{\partial}{\partial y}(\lambda\nabla \cdot \vec{V} + 2\mu\frac{\partial v}{\partial y}) + \frac{\partial}{\partial z}[\mu(\frac{\partial v}{\partial z} + \frac{\partial w}{\partial y})] + \rho f_y,
 \end{aligned} \tag{2.57}$$

$$\begin{aligned} \frac{\partial(\rho w)}{\partial t} + \frac{\partial(\rho u w)}{\partial x} + \frac{\partial(\rho v w)}{\partial y} + \frac{\partial(\rho w^2)}{\partial z} &= -\frac{\partial p}{\partial z} + \frac{\partial}{\partial x} \left[\mu \left(\frac{\partial u}{\partial z} + \frac{\partial w}{\partial x} \right) \right] \\ &+ \frac{\partial}{\partial y} \left[\mu \left(\frac{\partial v}{\partial z} + \frac{\partial w}{\partial y} \right) \right] + \frac{\partial}{\partial z} (\lambda \nabla \cdot \vec{V} + 2\mu \frac{\partial u}{\partial z}) + \rho f_z, \end{aligned} \quad (2.58)$$

$$\begin{aligned} \rho \frac{De}{Dt} &= \rho \dot{q} + \frac{\partial}{\partial x} \left(k \frac{\partial T}{\partial x} \right) + \frac{\partial}{\partial y} \left(k \frac{\partial T}{\partial y} \right) + \frac{\partial}{\partial z} \left(k \frac{\partial T}{\partial z} \right) - p \left(\frac{\partial u}{\partial x} - \frac{\partial v}{\partial y} - \frac{\partial w}{\partial z} \right) \\ &+ \lambda \left(\frac{\partial u}{\partial x} - \frac{\partial v}{\partial y} - \frac{\partial w}{\partial z} \right)^2 + \mu \left[2 \left(\frac{\partial u}{\partial x} \right)^2 + 2 \left(\frac{\partial v}{\partial y} \right)^2 + 2 \left(\frac{\partial w}{\partial z} \right)^2 + \left(\frac{\partial u}{\partial y} + \frac{\partial v}{\partial x} \right)^2 \right. \\ &\quad \left. + \left(\frac{\partial u}{\partial z} + \frac{\partial w}{\partial x} \right)^2 + \left(\frac{\partial v}{\partial z} + \frac{\partial w}{\partial y} \right)^2 \right]. \end{aligned} \quad (2.59)$$

Since the density is assumed to be constant in both time and space, the hypothesis of incompressibility can be shown as

$$\frac{\partial \rho}{\partial t} = \frac{\partial \rho}{\partial x} = \frac{\partial \rho}{\partial y} = \frac{\partial \rho}{\partial z} = 0. \quad (2.60)$$

Thus, the continuity and momentum equations can be modified for the incompressible flow case [Quartapelle, 2013] as

$$\boxed{\nabla \cdot u = 0}, \quad (2.61)$$

$$\boxed{\frac{\partial u}{\partial t} + (u \cdot \nabla)u = -\frac{1}{\rho} \nabla P + \nu \nabla^2 u}, \quad (2.62)$$

where

ν = kinematic fluid viscosity.

Since the energy equation is completely decoupled from Navier Stokes if the viscosity is said to be independent of temperature [COMSOL, 2018], it can be written as

$$\boxed{\rho C_p \frac{\partial T}{\partial t} + \rho C_p u \cdot \nabla T = \nabla \cdot (k \nabla T) + \dot{q}}, \quad (2.63)$$

where

C_p = specific heat capacity.

The governing equations to analyze the fluid flow briefly explained above have to be implemented on the planar jet flow whose coordinate system is shown in figure 2.6.

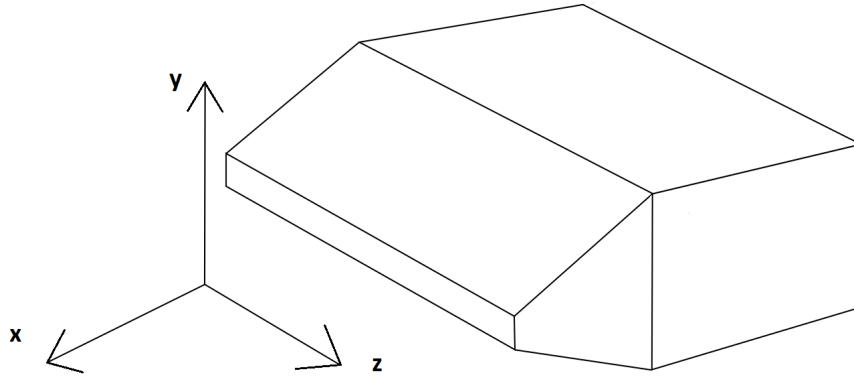


Figure 2.6: Coordinate system of plane air tunnel. The x-axis is the streamwise direction, the y-axis is the vertical crossflow direction while z-axis is the spanwise direction.

To investigate the physics of the turbulent planar jet flow, one of the fundamental steps to perform is estimating the velocity field. Unlike the laminar flow, the velocity is not constant in time if the flow is turbulent, but it shows high-frequency fluctuations in magnitude. Thus, any instantaneous velocity can be decomposed into two components as follows

$$V = \bar{V} + v', \quad (2.64)$$

where

- V = instantaneous velocity in 3D,
- \bar{V} = time-averaged velocity in 3D,
- v' = fluctuating velocity in 3D.

Considering that a velocity measurement was done at a point for 5 seconds. The velocity magnitude will not stay constant as a straight line but will have random oscillations in magnitude. In this case, the mean of the velocity time series results in the time-averaged velocity, \bar{V} , while the difference between the mean value and an instantaneous velocity value at a given time is the fluctuating velocity, v' . The decomposition is shown in following figure 2.7 taken from [Rathakrishnan, 2020].

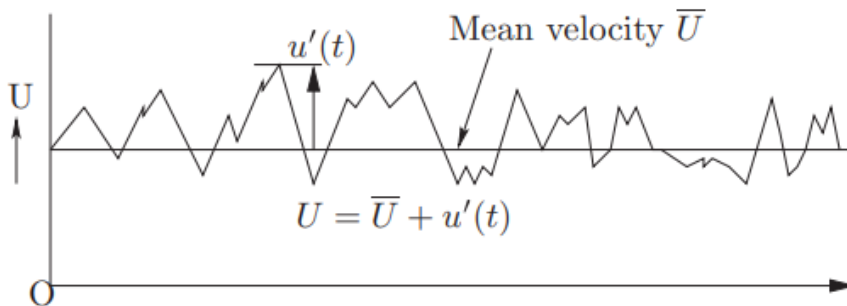


Figure 2.7: Example of a basic hot wire signal showing instantaneous velocity decomposition into its mean and fluctuating parts [Rathakrishnan, 2020].

By estimating the velocity field with respect to non-dimensional quantities, results are transformed into a universal form. For example, the following figure 2.8 was taken from a hot wire experiment on a turbulent planar jet that was performed by [Heskestad, 1965].

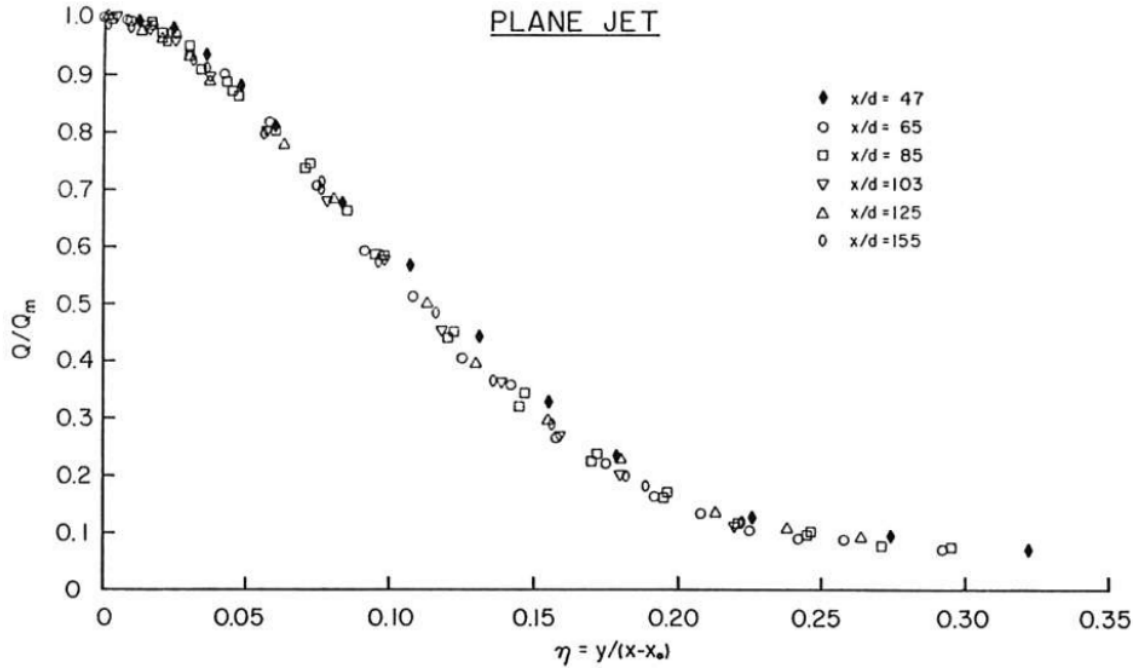


Figure 2.8: Experimental study of turbulent planar jet flow performed with hot wires. X is the streamwise direction while y is the crosswise direction. In the horizontal axis, non-dimensional quantity η represents the ratio between crosswise distance and streamwise distance from the origin, where x_0 is the virtual origin. In the vertical axis, non-dimensional quantity stands for the ratio between mean velocity magnitude, Q , and mean centerline velocity magnitude, Q_m . Data were obtained at different streamwise locations each corresponding to a different shape on the plot [Heskestad, 1965].

Moreover, by applying velocity and pressure decomposition, as shown in figure 2.64, to the Navier Stokes equations and Reynolds-averaging the whole equations, the terms called "Reynolds Stresses" are obtained [AMSO, 2012]. The form of the Reynolds Stresses is shown as follows

$$R_{ij} = \overline{u'_i u'_j} \quad (2.65)$$

Reynolds stresses represent the mean force per unit area imposed by the turbulent fluctuations on the mean flow [AMSO, 2012]. Following figure 2.9 [STANLEY, SARKAR, and MELLADO, 2002] shows the distribution of Reynolds Stresses in a planar jet.

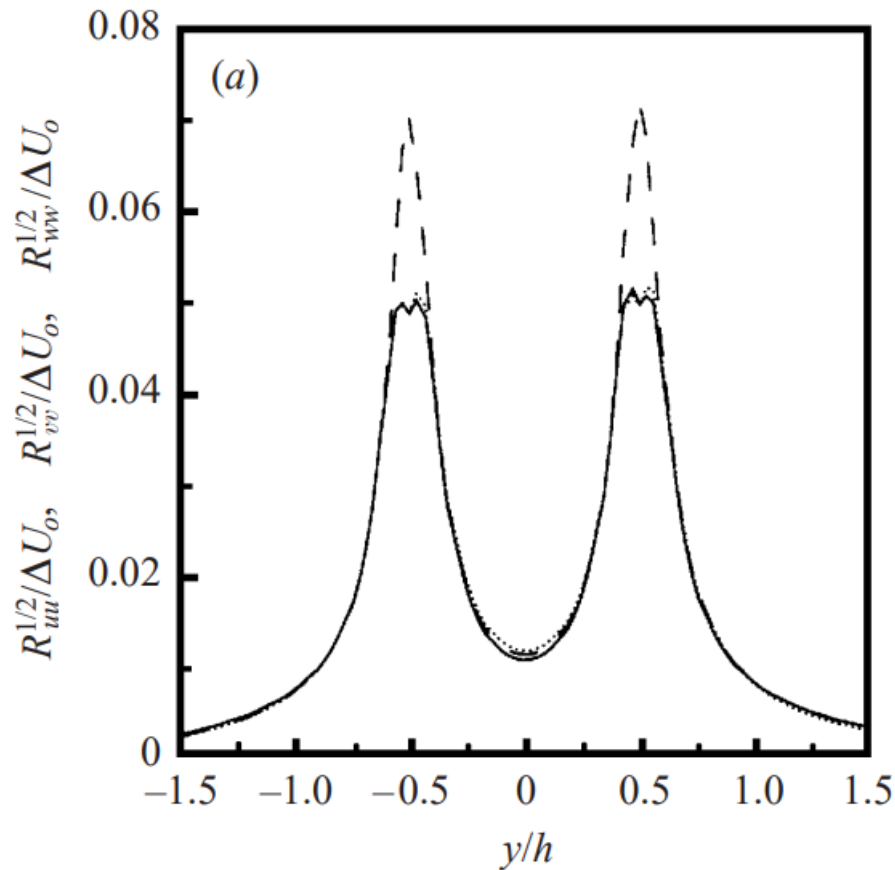


Figure 2.9: Visualization of Reynolds Normal Stresses in three directions, where the continuous line stands for R_{uu} , the dashed line shows R_{vv} and the dots represent R_{wv} . The coordinate system is exactly the same as shown in figure 2.6 [STANLEY, SARKAR, and MELLADO, 2002].

Defining another parameter, percentage turbulence intensity, Tu which allows a better understanding of the fluctuations' behavior can be done as

$$Tu\% = \frac{u'_{rms}}{U} \times 100. \quad (2.66)$$

As can easily be seen from the equation above, turbulence intensity is calculated as the ratio of the RMS value of fluctuating velocity to the mean velocity at the same location. By investigating the turbulence intensity in streamwise, crosswise, and spanwise directions in the planar jet, fluctuations inside the wake can easily be identified. For example, the following figure 2.10 is a result of an experimental campaign taken from [Hashiehbf and Romano, 2013], showing the turbulence intensity distribution along the streamwise direction.

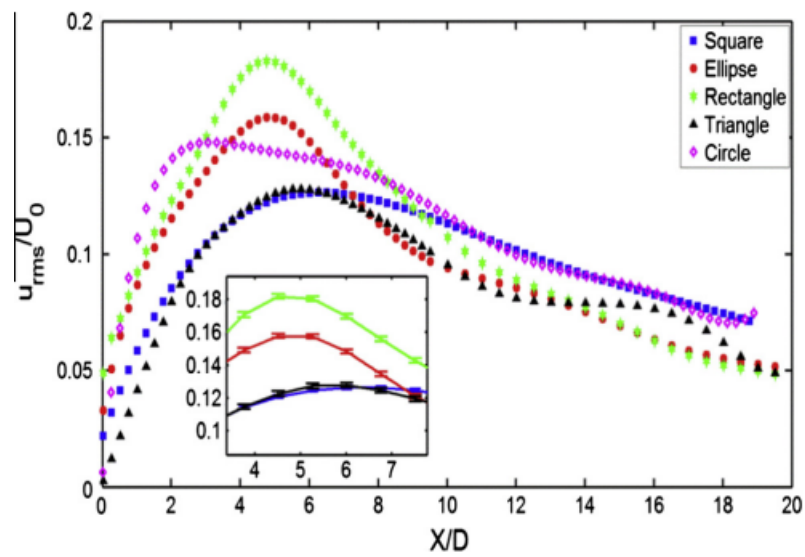


Figure 2.10: Plot of an experimental result representing the turbulence intensity distribution along the streamwise direction at exit Reynolds number $Re=8000$. Unlike equation 2.66, the effective velocity fluctuation was divided to mean velocity at the exit section without taking the percentage. U_0 is the mean velocity at the exit section, X is the streamwise distance from the exit, u_{rms} is the RMS value of fluctuating velocity and D is the exit section height. Each shape corresponds to a different shape of the exit section. The coordinate system is exactly the same as shown in figure 2.6 [Hashiehbab and Romano, 2013].

Figures 2.8, 2.9, 2.10 and others were used to compare the data obtained by this study and the literature. Other parameters to characterize the turbulent planar jet were discussed in section 3.6.8.

3

Experimental Setup

3.1 Plane Air Tunnel

The PAT is an open-loop blowing wind tunnel that was designed for investigating the planar jet flow. The setup consists of several different parts as a motor, pre-settling chamber, plastic hoses, flow conditioners, and a nozzle. Figure 3.1 shows the basic schematic of the wind tunnel.

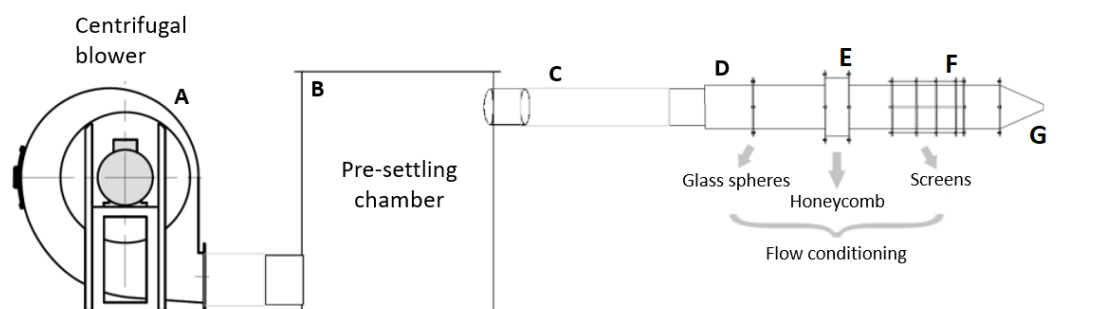


Figure 3.1: Side view schematic of Plane Air Tunnel. Flow is generated by a centrifugal blower(A), transferred to the pre-settling chamber(B), and then to the rectangular prism section via two tubes(C). Flow passes through the glass spheres(D) where some of the turbulence is killed. After that, honeycomb(E) helps to straighten the flow. Flow is then forced through a set of screens(F) to decrease the turbulence level again. Contraction(G) accelerates the flow before the exit section.

As it can easily be seen in the figure 3.1, there is a three-phase AC motor acting as a centrifugal blower, which gives the input air to the tunnel. Perturbations caused by the fans were decreased by using a pre-settling chamber. The air coming out of the pre-settling chamber is transferred to the stagnation chamber via two hoses symmetrically. The stagnation chamber includes glass spheres, honeycomb, and three screens which all can be used for flow conditioning. A significant amount of pressure drop is achieved along the stagnation chamber. After all, the last part of the PAT is a nozzle, where the flow accelerates and exits the wind tunnel. The contraction ratio of the nozzle is 9:1, which let the speed up and kills some parts of

the turbulence. The exit section is 2 cm in height and 45 cm in width, leading to a planar turbulent jet flow. The following figure 3.2 shows the picture of the PAT including the pre-settling chamber, that was taken from the exit section.

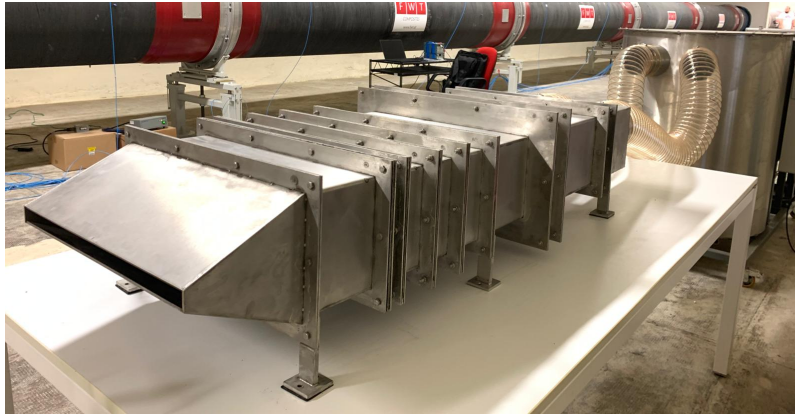


Figure 3.2: Plane Air Tunnel perspective view from the exit section, placed on top of a table to maintain the height of the exit.

As in most of the open loop blowing wind tunnels, the PAT does not have a diffuser and the test section is in ambient pressure. One of the drawbacks of PAT is the fact that the test section is affected by external disturbances.

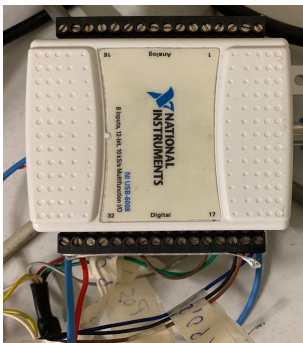
3.1.1 Sliding System

To be able to move the hot wire inside the wake of the turbulent planar jet, a sliding system was used. The system is able to move the hot wire in both crosswise and streamwise directions, and it is not able to move the wire in the plane direction, z axis. Movement in the z -axis is not needed since the turbulent planar jet is assumed to be homogeneous in the z -direction. The picture of the sliding system can be seen in figure 3.3 below.

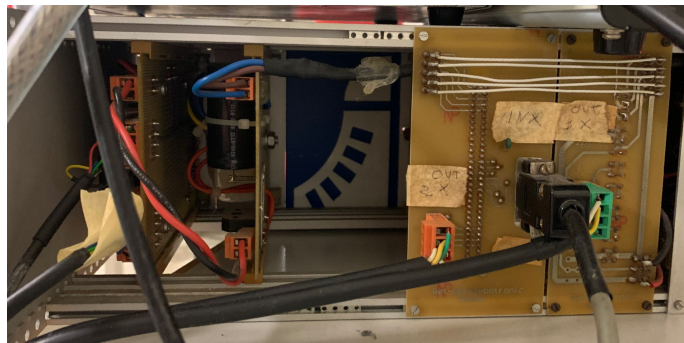


Figure 3.3: Sliding mechanism to move the wire holder in streamwise and crosswise direction inside the wake of the turbulent planar jet. The vertical part of the system, which is located close to the table in the picture, is able to move both on the horizontal part that is close to the ground and in the vertical direction.

Since the system is desired to be controlled by the LabView environment, proper cabling should have been done. As can be seen in figure 3.4, a National Instruments driver was used to provide the communication between the computer and the sliding system board. The circuit board works with the usual city electricity.



(a) Driver



(b) Circuit Board

Figure 3.4: Figure (a) is a data acquisition card for the communication of the sliding mechanism to move the wire holder in the streamwise and crosswise direction inside the wake of the turbulent planar jet. It is connected to the computer via a USB connection. Figure (b) is the cabling for the actuator of the sliding mechanism to move the wire holder in the streamwise and crosswise direction inside the wake of the turbulent planar jet. It is connected to the computer via a USB connection.

Basically, the user gives the required input on the computer, the driver transfers

the input to the sliding system board, and they are transmitted to the sliding system itself after being computed by the board seen in figure 3.4 (b).

The user can remotely control the sliding system by using a very simple VI code, whose front panel can be seen in the figure 3.5 below

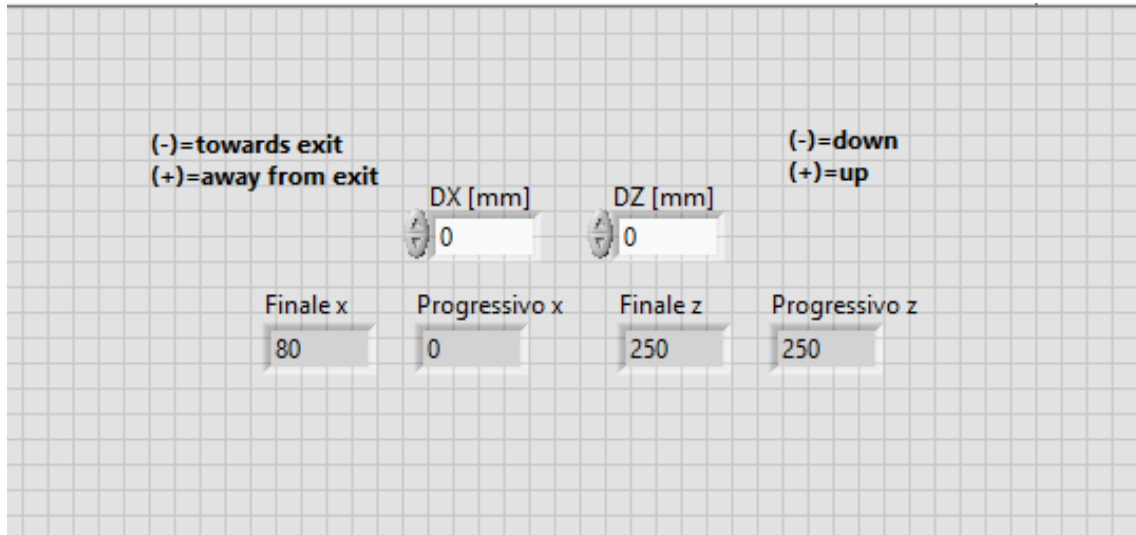


Figure 3.5: Sliding system user interface. X direction is streamwise and z direction is the vertical crosswise direction. The user has to first give the inputs for x and the z direction and then run the code. The sliding system first moves in the streamwise direction and then in the crosswise direction.

3.1.2 Traversing System

A traversing system, which is visible in the figure 3.6 below, was designed to be able to accurately calibrate the x-wire. As it can be understood from the figure, it has a stepper motor giving the rotation to the horizontal stick on which the x-wire holder is mounted. The horizontal stick is connected to a metal connector which behaves like a bridge between the horizontal stick and the stepper motor. Moreover, the horizontal stick can be mounted at different locations on the stick holder. The wire probe is placed on the wire holder in a way that the two wires will be exactly at the center of rotation of the stepper motor to ensure that the given angle is the same for the x-wire.



Figure 3.6: Traversing system to calibrate the x-wire at the exit of the plane air tunnel. The system includes a stepper motor (seen on right), metal sticks to hold the stepper motor, transfer the rotation given by the stepper motor, and mount the wire holder on top of it. A wire holder is used to place the wire probe .

To use the stepper motor by controlling it via the computer, specific cabling was performed. Firstly, the 24 V channel of the power supply, which can be seen in figure 3.7 (b), was used to power the stepper motor. Secondly, the 5 V channel was used to give the movement to the motor, indicating the direction for both (-) and (+) rotations, which were connected also to the digital output port of the cDAQ-9189 board to take the input from the user, as it can be seen in the figure 3.7 (a).



(a) Digital port



(b) Power supply

Figure 3.7: Figure (a) is the digital output port for the stepper motor cabling. Figure (b) is the power supply to be able to turn on and give the desired input for the stepper motor. The 5 V was used to move the stepper motor while the 24 V is to power the motor..

To transfer the inputs from the user, the NI cDAQ-9189 board, and the power supply, a driver was used. The tables represented below show the settings for the switches on the driver, to be able to use the stepper motor in the desired way.

Microstep setting				
Steps per revolution	Switch			
	5	6	7	8
400	off	on	on	on
800	on	off	on	on
1600	off	off	on	on
3200	on	on	off	on
6400	off	on	off	on
12800	on	off	off	on
25600	off	off	off	on
1000	on	on	on	off
2000	off	on	on	off
4000	on	off	on	off
5000	off	off	on	off
8000	on	on	off	off
10000	off	on	off	off
20000	on	off	off	off
25000	off	off	off	off

Table 3.1: Microstep setting for the stepper motor. Shows the setting that has to be done by the switches, to have the desired number of steps for 60° rotation. It determines the resolution of the stepper motor.

Current setting			
Current	Switch		
	1	2	3
1 A	on	on	on
1.46 A	off	on	on
1.91 A	on	off	on
2.37 A	off	off	on
2.84 A	on	on	off
3.31 A	off	on	off
3.76 A	on	off	off
4.2 A	off	off	off

Table 3.2: Current setting of the stepper motor. Switches should be arranged in a corresponding way to the current value used for the motor.

In this study, the number of steps was decided to be 400 for a rotation of 360°. Thus, the resolution of the stepper motor can be calculated as

$$1 \text{ step} = \frac{360}{400} = 0.9^\circ.$$

Having appropriately performed all the cabling, the motor is ready to go. The user can easily control the stepper motor by using a VI code, whose user interface is shown in the figure 3.8 below, by giving the required inputs of millisecond multiple to wait between the steps, lines to communicate for both the direction and the amount, steps desired to move and the millisecond value of movement. After all, the user should just run the code.

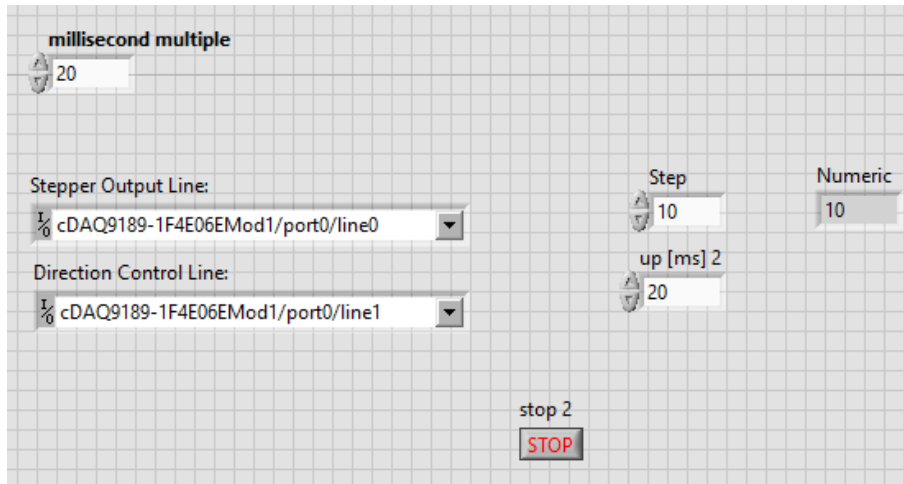


Figure 3.8: Front panel of the stepper motor VI code. As the input, the user has to give millisecond multiple to wait between the steps, lines to communicate for both the direction and the amount, steps desired to move, and the millisecond value of movement.

3.1.3 Inverter and Power System

The PAT wind tunnel is powered by a three-phase AC motor, whose properties are shown in the table 3.4, having a frequency of 50 Hz and voltage of 400/690 V. The power generated by the motor is transmitted to a fan by a shaft. The properties of the fan can be seen in the table 3.3

Brand	Off CIESE
Model	MAR/S 502
Number	2020 - 020559
Weight [kg]	98
Power [kW]	5.5
Frequency [Hz]	50
Voltage [V]	400/690
RPM	2800

Table 3.3: Properties of fan used in plane air tunnel to provide the flow rate into it.

The rotating fan produces the blowing wind inside the tunnel, which is pushed through the tubes into the pre-settling chamber. The speed control of the AC motor is achieved by using a variable frequency driver, which is also called an inverter.

Brand	WM Motors
Model	IE2
Number	60034-1
Phase	3
Number	2020 - 020559
Weight [kg]	45
Power [kW]	5.5 or 6.6
Frequency [Hz]	50 or 60
Voltage [V]	400/690 or 480/831
RPM	2800
Current [A]	10.4/6

Table 3.4: Properties of AC motor used in plane air tunnel to provide the rotation for the fan.

An inverter is a tool that allows the user to change the frequency of city electricity so that the motor rpm changes. Changing the rpm of the motor results in a change in fan rpm, which ends up altering the velocity of the flow inside the wind tunnel. Specifically, Siemens Sinamics V20 inverter was used for the speed control of the AC motor, which provides three-phase AC 400-480 V input and has a 7.5 hp motor. Moreover, the inverter is capable of dealing with frequency values up to 599 Hz [Siemens, 2013]. The front face of the inverter can be seen in figure 3.9.

SIEMENS



Figure 3.9: Siemens Sinamics V20 inverter, changing the voltage or the frequency of the AC motor to control the fan RPM.

V20 inverter offers different types of communication with multiple sources. Usually, a programmable logic controller is preferred to communicate with an inverter using the computer as the source. However, the PLC requires its programming, and also it means that there will be one more tool inside the communication chain, resulting in lower efficiency and more disturbances and noise. A better way would be to communicate the inverter with a computer via a serial connection, which results in fewer disturbances and noise. In this study, the control of V20 via an ethernet connection from a computer was achieved by the use of an A/D input/output NI cDAQ-9189 board, whose specifications will be discussed in section 3.2.

3.2 Data Acquisition and Transmission

The process including the sampling of the analog signals to have them in digital form is called data acquisition. Acquiring the data has a very essential role for demonstration, storage and analysis purposes[Smith, 2020]. To acquire the desired data from the test section, there must be a unique setup composed of different tools, machines, and cables between them. After all, acquired data is transmitted to the computer to be able to process the results.

Sensors are the first elements of the acquisition chain. They are expected to change their status with respect to the change in the parameters that they are designed to measure. The next member of the chain is the transducer. A transducer transforms the status change of a sensor into an output signal by converting one energy to another. The signal is not necessary, but generally continuous and electrical. After having the analog signal of the measured quantity, data conversion is done from analog signal to digital signal by the acquisition system, concerning the proper values of sampling rate and time.

The last step is to transfer the acquired data to the computer. There are multiple ways of transmitting the data from the acquisition board to a computer. In this project, the connection was provided by the ethernet for the hot wires and the pressure. On the other hand, a serial connection was preferred for the temperature data transmission.

3.2.1 Sensors

The variance in sensors' status lets the system know that the quantity required to be measured has changed. There are three different types of sensors being used in the PAT setup. One of them is a well-known sensor for mean velocity measurements, which is a pitot-static tube. It changes the pressure with respect to the speed variance in the flow. In figure 3.10, a drawing of a pitot-static tube is shown. A pitot-static tube measures both static and total pressure, then it allows us to calculate the mean velocity by having the local dynamic pressure.

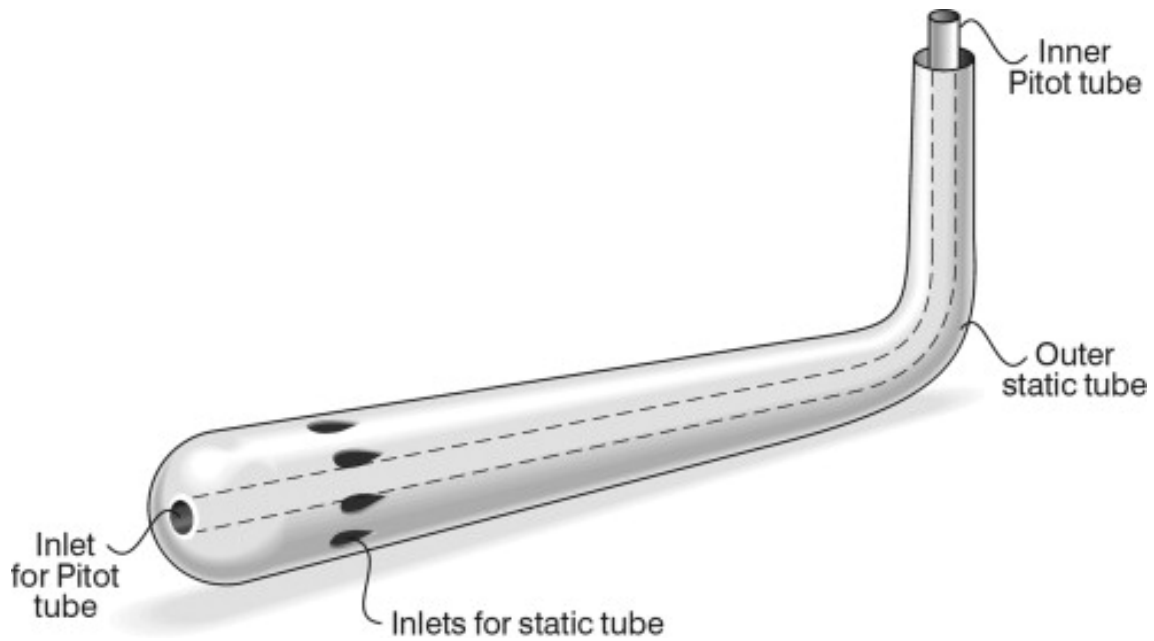


Figure 3.10: Pitot-static tube, measuring total and static pressure to calculate the velocity at a specific location[Gentle, Edwards, and Bolton, 2001].

Secondly, figure 3.11 represents the hot wire[Bruun, 1996] that is being used to measure not only the mean velocity but also the velocity fluctuations in this setup. The hot wire changes its temperature as a result of a speed change in the flow. A hot wire is connected to a circuit, ie. a wheatstone bridge, which behaves as a transducer, in which the temperature variance in the hot wire corresponds to voltage fluctuations.

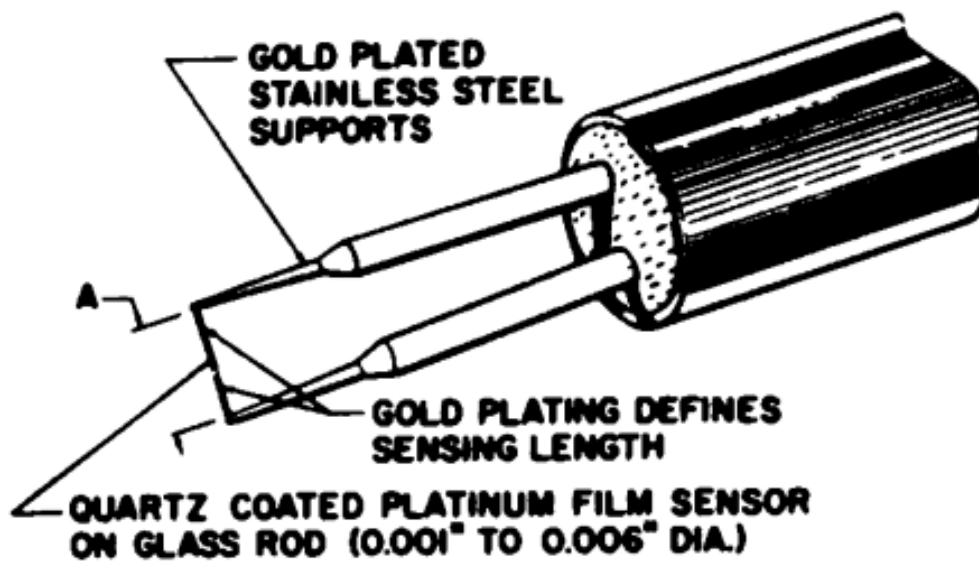


Figure 3.11: Basic schematic of a hot wire including its supports[Bruun, 1996].

Finally, a thermocouple can be seen in the figure 3.12 Thermocouple is used to measure the local temperature. A junction is formed by two different metals joined together to sense the temperature difference. Any temperature change at the joint point corresponds to a voltage value in the electrical circuit that the thermocouple is connected. Therefore, the local temperature can be decided by analyzing the voltage behavior for a certain time.



Figure 3.12: Thermocouple to sense the temperature at a specific location.

3.2.2 Transducers

Transducers are other important members which convert the status change of the sensors to an output signal. They allow the user to be able to understand the behavior of the measured quantity instantly, by looking at the corresponding output signal. There are different types of transducers that are designed for particular operations. One of the most common transducers is shown in figure 3.13, pressure transducers. Two identical pressure transducers were used for the setup, where one measures atmospheric pressure, and the other measures dynamic pressure. The static and the total pressure ports of the pitot-static tube are connected to a pressure transducer to be able to calculate the dynamic pressure locally. Then, MKS transducers give the voltage versus time as the output signal, with respect to the dynamic pressure change.



Figure 3.13: MKS pressure transducers, one is for the ambient pressure measurement and the other is for static and total pressure measurement which is connected to the pitot-static tube.

There are two types of MKS transducers used for the experiments in the PAT setup. One of them has a reference of 2 Torr, and the other has 10 Torr. Since the output voltage values directly correspond to Torr values, pressure in the unit of Pascal can be easily obtained as

$$1 \text{ Torr} = 133.32 \text{ Pa.} \quad (3.1)$$

Moreover, according to the user manual provided by MKS Instruments [MKS Instruments, 1999], the resolution of a transducer is given as in equation 3.3, where the resolution means the minimum detectable value of a given quantity.

$$\text{Resolution} = 1 \times 10^{-5} FS, \quad (3.2)$$

where,

FS = Full-scale range of the transducer.

Secondly, there are 2 different methodologies of conducting a hot wire experiment, constant current anemometry, and constant temperature anemometry. Since the frequency response of CTA is much higher than the one of CCA, cta was preferred for the velocity measurements, where the fluctuations have a much higher frequency. Thus, figure 3.14 represents the so-called wheatstone bridge which behaves as the transducer of a hot wire working with constant temperature[Bruun, 1996].

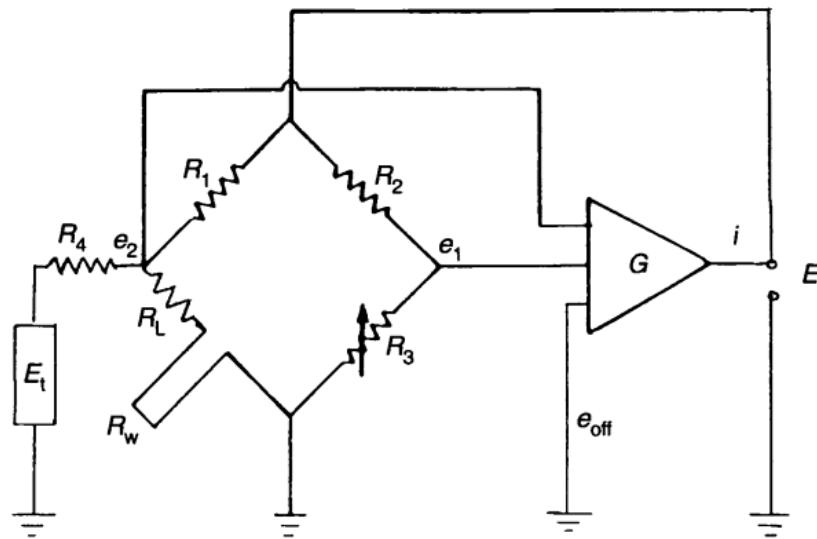


Figure 3.14: Electrical diagram of a constant temperature anemometry wheatstone bridge, behaving as the transducer for the hot wire setup. G represents the gain of the amplifier while E stands for voltage and R is used for the resistance [Bruun, 1996].

The transducers of both thermocouple and hot wire are located inside the Dantec Dynamics anemometer system box, which can be seen in figure 3.15. As it can easily be observed from the figure, the port on the left is reserved for thermocouple values while the others are for hot wires.



Figure 3.15: DANTEC Dynamics acquisition box, connected to the computer via an ethernet connection, including transducers for the thermocouple and the hot wire. It has six different channels for hot wires with constant temperature anemometry.

3.2.3 Transmission

To transmit the output signal of the hot wires and the pressure voltage to the computer to display, analyze and save it, an A/D input/output board was used,

which communicates with the computer via an ethernet connection. As it can be understood from the figure 3.16, it has 8 different mods and multiple channels in each mod. A/D board takes the signal outputs from the Dantec system box as input and transfers them to the computer via an ethernet connection.

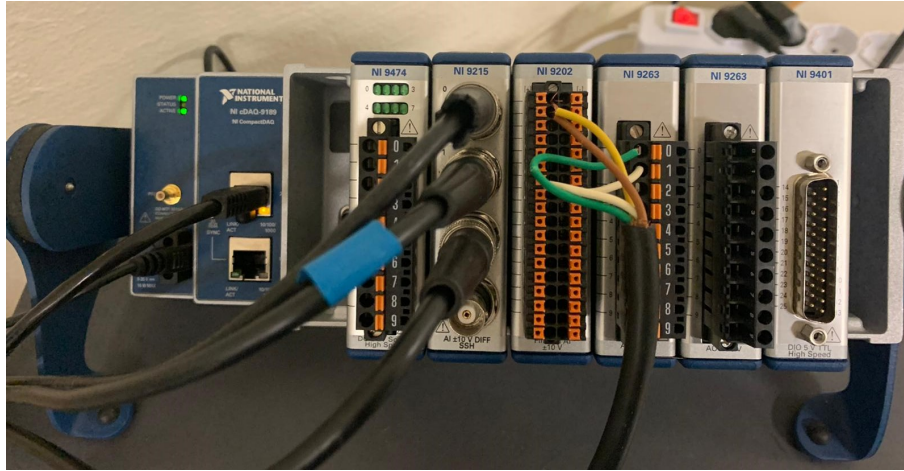


Figure 3.16: NI cDAQ-9189 A/D board for the connection between the DANTEC acquisition box and the computer. Multiple rooms for both Analog/Digital Input/Output.

Moreover, a serial connection between the transducer and the computer was set to transmit the temperature data.

3.3 Pressure Behavior

Pressure behavior along the PAT was investigated to be able to have speed control without using a pitot-static tube at the exit section and to comment on the tunnel efficiency.

Pressure tappings were mounted at the channels that were created at five different locations which are listed in the following table;

Channel 1	Just before the contraction
Channel 2	Just before the screens
Channel 3	Just before the honeycomb
Channel 4	Just before the glass spheres
Channel 5	At the pre-settling chamber

Table 3.5: Locations of pressure tappings. They are sequenced from the beginning (5th channel) to the end (1st channel). Channel 1 is the one that is the closest to the exit, while channel 5 is the one that is closest to the AC motor. There are wind tunnel components between the channels, to analyze the pressure drop between them.

Locations of the tappings can clearly be seen on the figures 3.17 and 3.18 below.

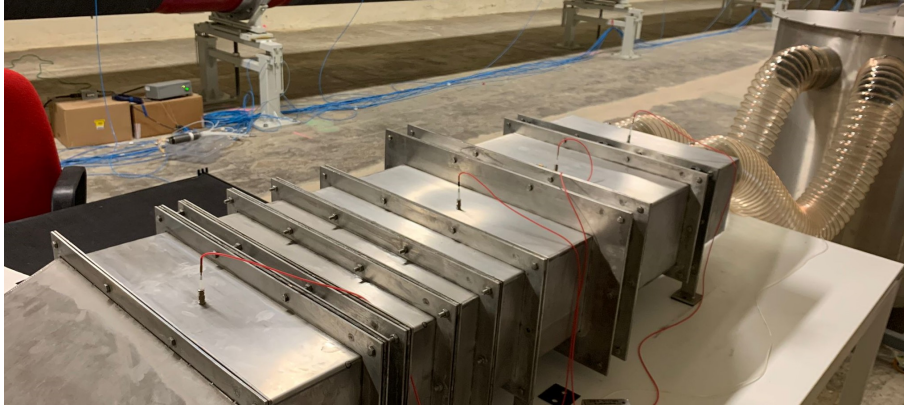


Figure 3.17: Pressure tapings viewed from the exit section. The one on the left is channel 1 just before the contraction and so the exit, while the one after the tubes is channel 5 just after the AC motor and so the inlet. The wind tunnel components are visible between the pressure tapings. All the pressure tapings are connected to the pressure scanner with the same type of hose(red) except channel 5(transparent).

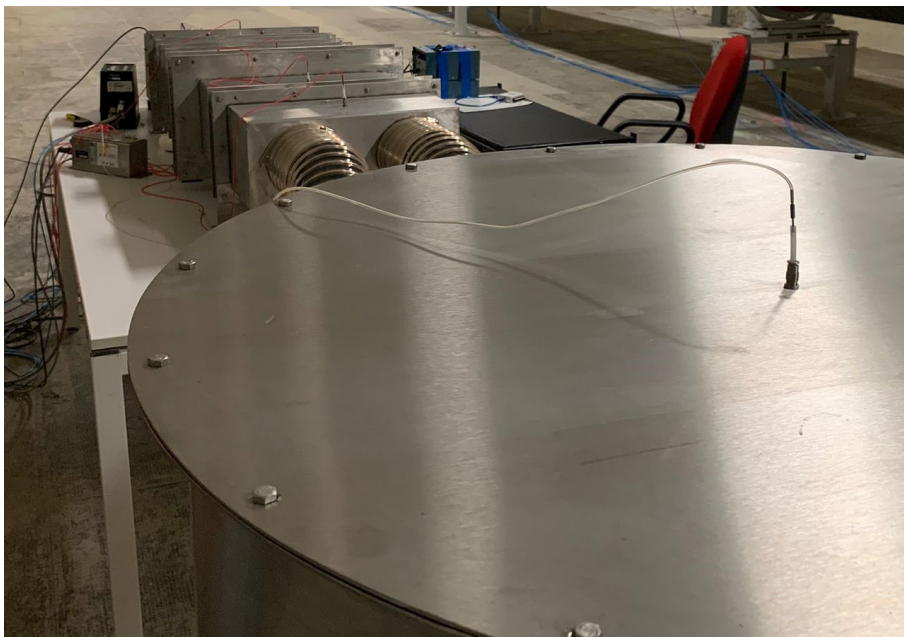


Figure 3.18: Pressure tapings viewed from the pre-settling chamber. The one on the right is channel 5 just after the AC motor and so the inlet, while the one on the other end is channel 1 just before the contraction and so the exit. The wind tunnel components are visible between the pressure tapings. All the pressure tapings are connected to the pressure scanner with the same type of hose(red) except channel 5(transparent). The big circle that the 5th pressure tapping is mounted on is the top of the pre-settling chamber.

To be able to acquire the pressure values from five different channels simultaneously, a multi-channel pressure transducer Scanivalve DSA3217 was used. The picture of the scanner is shown in figure 3.19. The scanner has the range of $10''H_2O$, which is equal to 2490.89 Pa. The two extra channels in the figure 3.19 were connected to the static pressure and total pressure channels of the pitot-static tube just

for testing the device and comparing the results with the MKS Baratron 100 Torr = 13332.24 Pa transducer. According to the user manual [Corp., 2016] of the pressure transducer, the number of bits that it can work with is 16, so the resolution of the transducer can be calculated by using equation 5.2 as follows

$$\frac{2490.89}{2^{16} - 1} = 0.04 \text{ Pa.}$$



Figure 3.19: Scanivalve DSA3217 pressure scanner having the range of $10''H_2O$. There are two cables connected on the side of the scanner, where the one above is for the power supply while the one below is to communicate with the computer. The first four red hoses are connected to the first four pressure tapplings, while the transparent one is connected to the fifth pressure tapping as mentioned before. Extra two red hoses are connected to acquire the pressure values from the pitot-static tube (Channel 6 and 7). It has the REF channel to take the reference to compare the values from numbered channels.

A VI code, whose front panel and the block diagram can be seen in figures 3.20, 7.12, 7.13, 7.14 was created using the LabView environment, with which the user is fully able to see the offset at each channel and to control the sampling time, sampling frequency and the flow speed at the exit section.

CHAPTER 3. EXPERIMENTAL SETUP

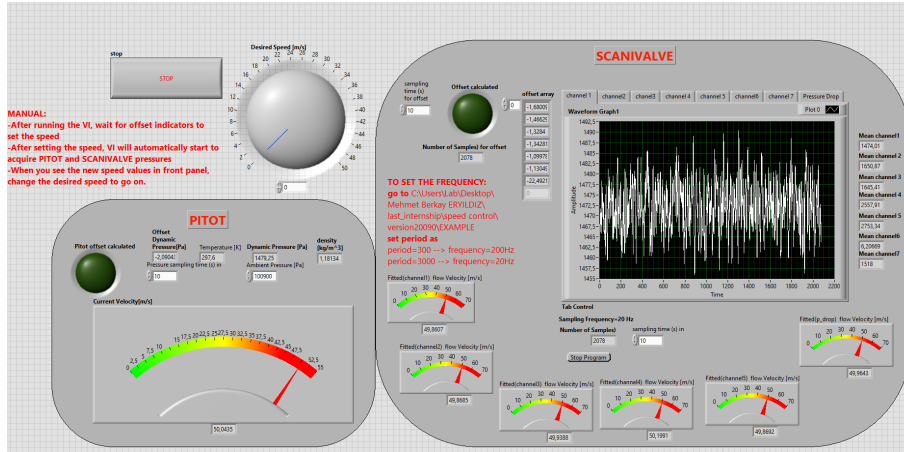


Figure 3.20: Pressure measurement VI code front panel. It is able to tell the velocity at the exit section both with the data from the pitot-static tube and from pressure tappings. First, it computes the offset values at zero speed for the two transducers, then subtracts them from the measured values at non-zero speed. The user has to set the sampling rate, sampling time, and ambient pressure for the pitot measurements. On the other hand, just the sampling time has to be written for the Scanivalve since the frequency is set from another front panel shown 3.36. The code makes all the waveforms from each pressure tapping, as well as the pressure drop visible.

As it can be understood from the front panel and the block diagram, the code is fully able to acquire the pressure values from both the MKS transducer and the Scanivalve scanner, then calculate the speed at the exit section, and save them into a file for comparison. The speed values computed by pressure tappings were related by an experimental interpolation that will be discussed in section 3.5.3. Moreover, the user is able to see the pressure drop along the PAT for different speeds scaled for the highest range as represented in the figure 3.21 below.

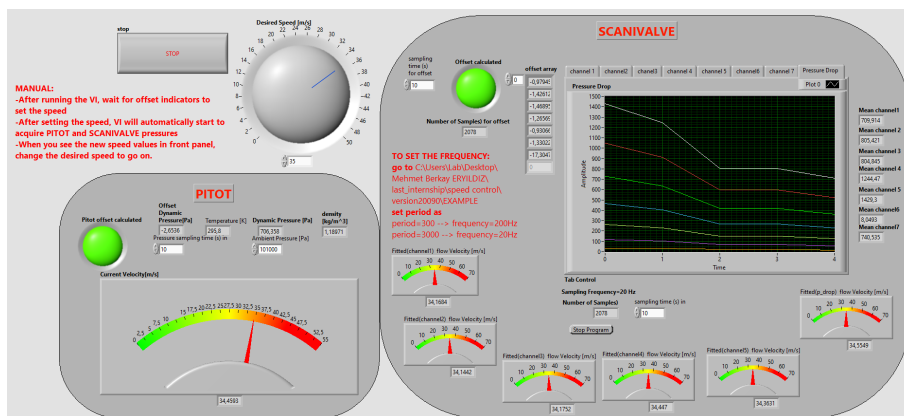


Figure 3.21: Exactly the same front panel to see the pressures and the velocity as discussed in 3.20, just showing the ability to display pressure drop at different speed values on top of each other.

Following figure 3.22 is the pressure signal acquired at the first pressure tapping before the contraction part, with a rate of 270 Hz for 300 seconds when the Reynolds number is $Re=12328.7$.

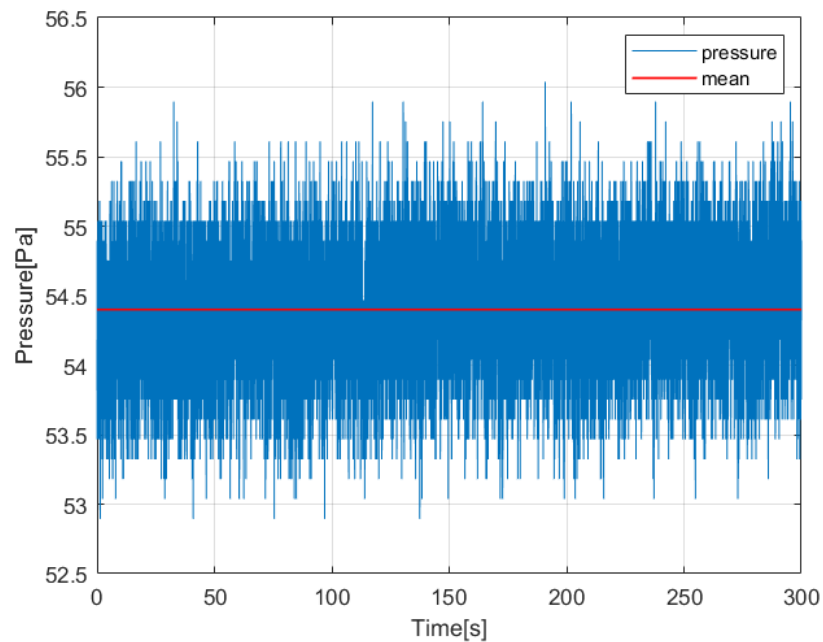


Figure 3.22: Pressure signal from channel 1 at $Re=12328.7$ that was obtained by Scanivalve pressure scanner at 270 Hz sampling rate for 300 seconds of sampling time. Blue lines represent the pressure values at the corresponding time value while the red line shows the mean value of the whole time series.

3.3.1 Offset Compensation

Since there is a certain offset value realized at each channel, first a pressure calibrator was used to see the behavior of the offset value. The calibrator Mensor CPC6000, shown in figure 3.23 sends a known pressure value to the related channel which we can read the value given by the transducer by using the LabView code.



Figure 3.23: Mensor CPC6000 pressure calibrator. It has 2 channels. It is able to both measure and set the pressure, so it is totally effective in using for calibrating a pressure measurement tool. There is a touchscreen visible on the front side of the calibrator while the pressure channels are located behind. As soon as the desired pressure value to send is set on the calibrator, it starts to stabilize the value by itself and warns the user when it is done.

By reading the input pressure from the calibrator screen and the output pressure value from the LabView for the transducer, it is easy to observe the behavior of the offset for different pressure values.

The following figure 3.24 represents the behavior of the offset for different pressure values.

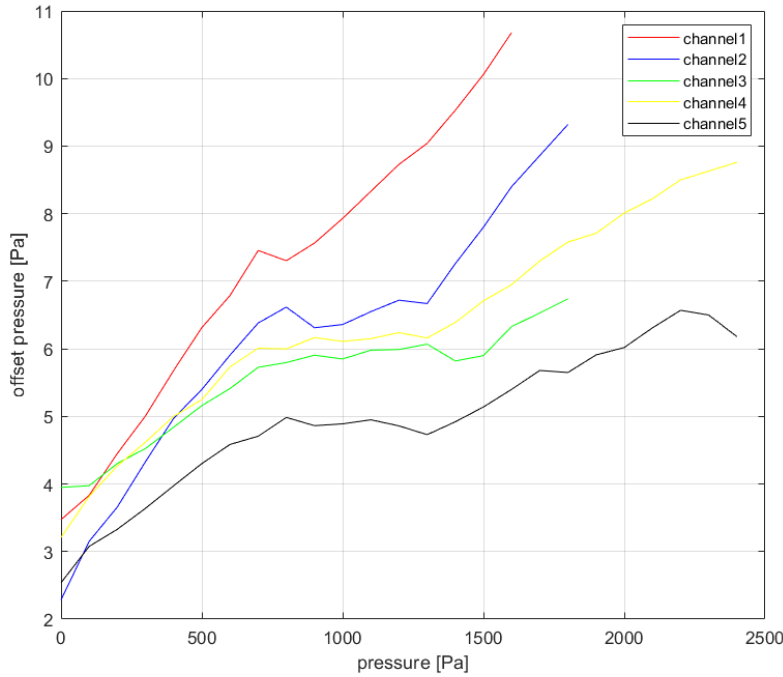


Figure 3.24: Behavior of offset for the first experiment. The red colored line represents the offset behavior of channel one at different pressure values while the blue one is channel 2, the green one is channel 3, the yellow one is channel 4, and the black one is channel 5. Each channel's offset was investigated for a pressure range equal to its operating range. However, since the calibrator can go up to 2450 Pa, the range of channel 5 couldn't be reached. Offset was taken as the difference between the sent pressure and the read pressure.

Although the offset value seems to be varying in huge amounts, the variation is extremely small compared to the pressure operation range. To analyze the offset variation with respect to the operation range, the equation 3.3 below was used to have it as a percentage.

$$\text{Range ratio}\% = \frac{\max(\text{offset}) - \min(\text{offset})}{\max(\text{pressure}) - \min(\text{pressure})} \times 100, \quad (3.3)$$

where:

offset = vector formed by offset values,
 pressure = vector formed by pressure values.

Then, the percentage range ratios were decided as they are listed in table 3.6

Channel number	Percentage range ratio %
1	0.45
2	0.39
3	0.16
4	0.23
5	0.17

Table 3.6: Percentage range ratio for channels indicating how big the offset values for different pressure values of each channel with respect to the operating pressure range obtained during the first experiment. Calculated by using equation 3.3.

Furthermore, to be on the safe side and to understand if the behavior changes, the same experiment was repeated and the values were reported. Figure 3.25 shows the offset values, which looks similar to figure 3.24.

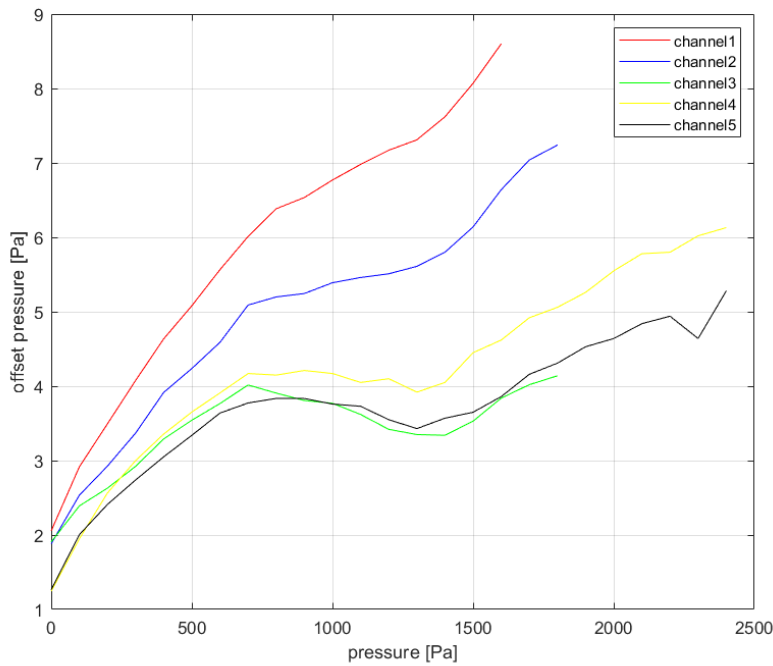


Figure 3.25: The behavior of offset for the second experiment. The red colored line represents the offset behavior of channel one at different pressure values while the blue one is channel 2, the green one is channel 3, the yellow one is channel 4, and the black one is channel 5. Each channel’s offset was investigated for a pressure range equal to its operating range. However, since the calibrator can go up to 2450 Pa, the range of channel 5 couldn’t be reached. Offset was taken as the difference between the sent pressure and the read pressure. To be compared with figure 3.24.

Reporting the percentage range ratios for different channels again in the table 3.7, it is obvious that the offset behavior improves. Thus, it can easily be said that the offset becomes closer to being constant as the Scanivalve scanner is being used.

Channel number	Percentage range ratio %
1	0.41
2	0.29
3	0.12
4	0.20
5	0.16

Table 3.7: Percentage range ratio for channels indicating how big the offset values for different pressure values of each channel with respect to the operating pressure range obtained during the second experiment. Calculated by using equation 3.3. To be compared with table 3.6.

Therefore, taking into account that both the percentage range ratios are very small and they become smaller as the transducer is used, it was decided to consider the offset value as constant. To ensure that the offset is close to staying constant, the transducer is powered on while there is a flow with non-zero velocity and a warm-up acquisition was performed for 1 hour at the beginning of each experiment. Hence, to deal with the offset, the pressure values were acquired when the flow velocity is zero inside, then they are subtracted from the values acquired at different speeds.

3.3.2 Pressure Sampling Time

To set the sampling time of the pressure signal, it was acquired for 300 seconds, which is relatively a long time, with the sampling frequency of 270 Hz, shown in figure 3.22. Two different methods were followed to decide the sampling time, which are not totally different from each other.

One way is the autocorrelation of the pressure values. The autocorrelation function calculates the correlation between the signal values that are k time periods apart from each other[“Sample autocorrelation”, 2022]. The formula to compute the autocorrelation is

$$r_k = \frac{c_k}{c_0}. \quad (3.4)$$

where:

$$c_k = \frac{1}{T} \sum_{t=1}^{T-k} (y_t - \bar{y})(y_{t+k} - \bar{y}), \quad (3.5)$$

T = sampling time[s],

y = pressure time series,

k = time lag between the samples[s],

r_k = correlation between the samples,

c_0 = sample variance of the time series[Pa].

The following figure 3.26 represents the autocorrelation function plot for a different time lag between the samples that was computed by the formula represented before.

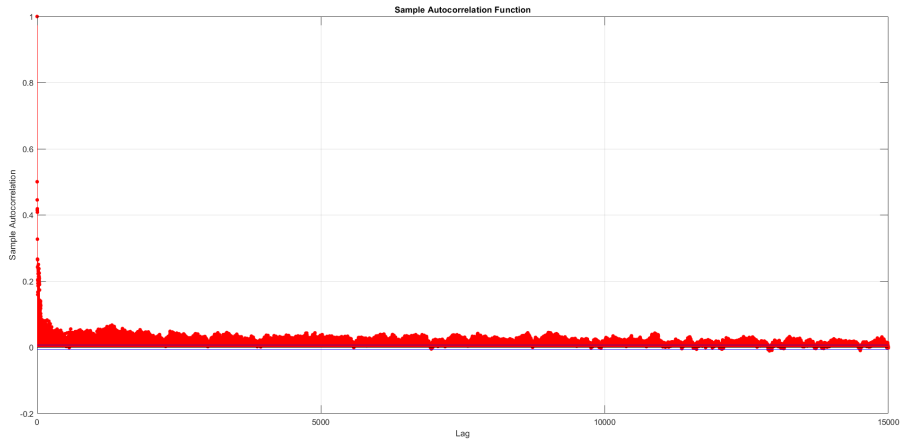


Figure 3.26: Autocorrelation between the pressure tapping signal samples. The horizontal axis represents the time lag between one sample to another (number of samples) while the vertical axis shows the correlation between those samples. Each filled red circle stands for a correlation value between samples that are corresponding time lag far away from each other. The samples can be said uncorrelated when the autocorrelation goes under the horizontal blue lines.

Autocorrelation was performed for 15000 samples since the correlation was expected to be lost after almost 40 seconds due to the physics of the pressure signal. Figure 3.26 shows a certain trend in the correlation of the samples as they become far away from each other. The blue horizontal lines represent the level of correlation below which the samples can be assumed non-correlated. The correlation becomes genuinely small after the 11000th sample as is obvious in the figure 3.26. Since it is not completely visible, figure 3.27 makes the trend more visible close to the portion where the correlation is almost lost.

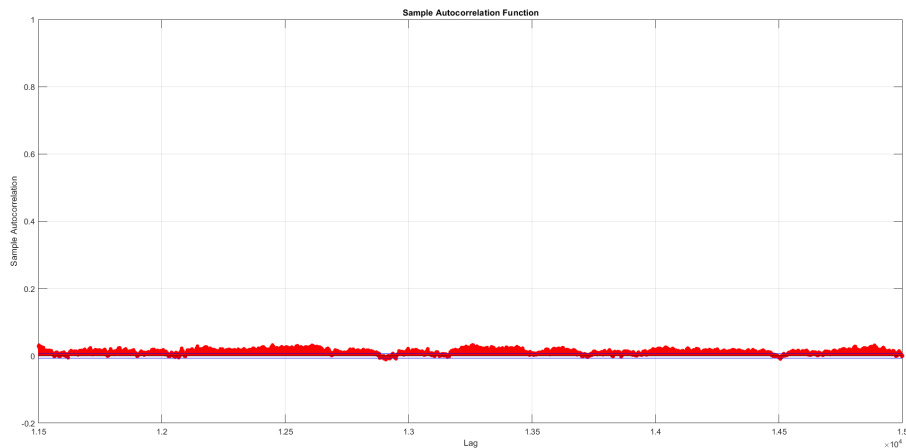


Figure 3.27: Autocorrelation between the pressure tapping samples focused between 11500th and 15000th samples. The horizontal axis represents the time lag between one sample to another (number of samples) while the vertical axis shows the correlation between those samples. Each filled red circle stands for a correlation value between samples that are corresponding time lag far away from each other. The samples can be said uncorrelated when the autocorrelation goes under the horizontal blue lines.

Thus, it can be said that the signal loses its correlation at the 11500th sample,

then calculating the time as

$$t = N/f_s. \quad (3.6)$$

where:

t = time to be decided[s],
 N = number of samples,
 f_s = sampling frequency.

which results in

$$t = 11500/270 = 42.59 \text{ s.}$$

Thus, the sampling time for the pressure signal can be decided to be 43 seconds.

The other way to determine the sampling time is to check the variation of the mean value after dividing the samples into portions. The pressure signal that was obtained by 300 seconds of acquisition with 270 Hz of frequency was divided into up to nine portions to check the behavior of the mean value at each portion. Hence, there are eight different vectors composed of mean values, each has the length of the number of portions that the time series was divided into. The desired condition of the mean values is to have them closest to the mean value of the whole time series, 54.4221 Pa, while their variance is relatively low. The following table 3.8 shows sampling time values for the corresponding number of portions that the whole time series was divided into.

Portions	Sampling time [s]
2	150
3	100
4	75
5	60
6	50
7	42.86
8	37.50
9	33.33

Table 3.8: Sampling time values for the corresponding number of portions that the whole pressure voltage time series was divided to.

To compare the behavior of the mean values for different sampling times, the first thing to do was decided as the percentage range ratio analysis. The percentage range was computed as

$$\text{Range ratio}\% = \frac{\max(m) - \min(m)}{\max(\text{pressure}) - \min(\text{pressure})} \times 100, \quad (3.7)$$

where:

m = vector composed by mean values for each portion,
 pressure = pressure time series vector.

Performing the variation as the second method, the following figure 3.28 shows the behavior of the mean values for each portion.

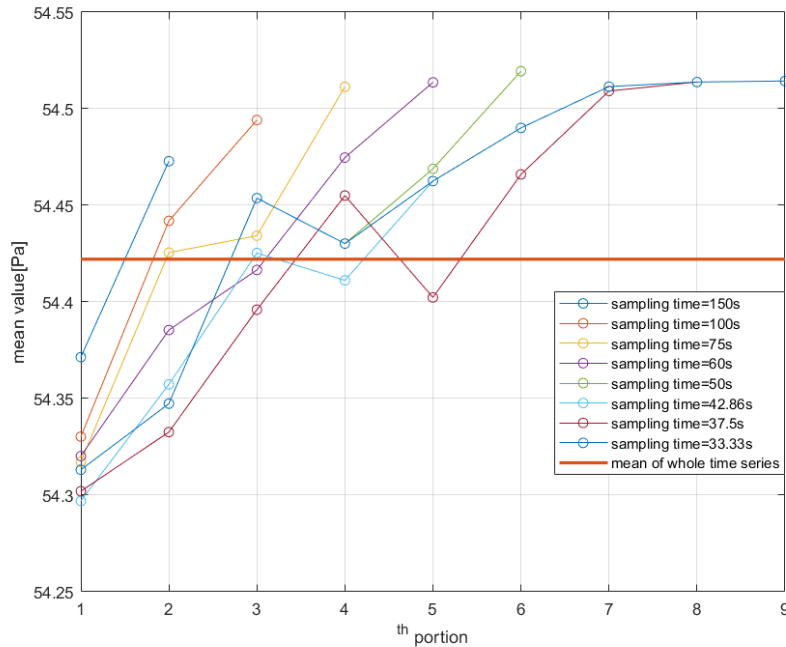


Figure 3.28: The behavior of mean values for eight different trials of sampling time. The whole pressure tapping time series that was obtained with a 270 Hz sampling rate for 300 seconds of sampling time, were divided into portions to see the behavior of the mean value at a corresponding sampling time. The empty circles represent the mean value of a corresponding time series portion.

Following figure 3.29 shows the trend created by the range ratios each corresponding to a different sampling time

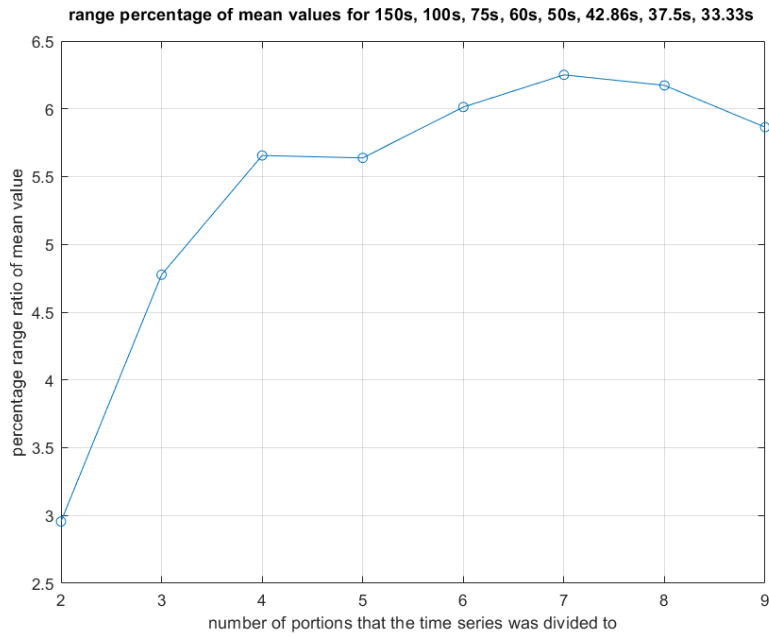


Figure 3.29: Percentage range ratios for different sampling time values that were analyzed by dividing the whole pressure tapping time series, obtained with 270 Hz sampling rate for 300 seconds of sampling time, into portions. The empty circles stand for a percentage range ratio of mean values of each time series portion, implying how big the variation of mean values is with respect to the operating pressure range. Sampling time decreases as we go to the right on the horizontal axis.

As it can clearly be seen from the figure 3.29, there is an increasing trend for the percentage range as the sampling time decreases. Thus, it means that the range values at each portion of the time series become more non-deterministic as the window of the portion gets smaller. Since 6.5% is an acceptable ratio for the range variation and there is a decreasing trend, 33.33 seconds of sampling time was considered to be enough in terms of the mean value variation.

Secondly, the variance of each mean value vector was computed. Variance is the measurement of how spread the values of a series. The formula is written as

$$V = \frac{1}{N-1} \sum_{i=1}^N |m_i - \mu|^2, \quad (3.8)$$

where:

- m = vector consists of mean values of each portion,
- μ = mean value of the vector,
- N = length of the vector.

Following figure 3.30 represents the variance of the vectors composed of mean values, for different numbers of portions.

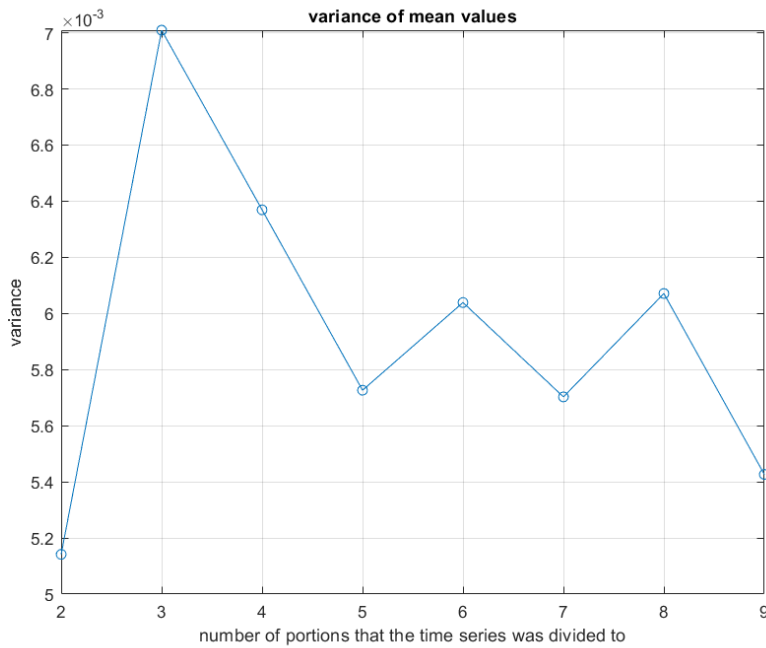


Figure 3.30: The variance of vectors that are formed by mean values, where each mean value corresponds to a mean of a pressure tapping time series portion. The empty circles show the variance of mean values of corresponding portions.

Obviously, figure 3.30 validates the selection of sampling time as 33.33 seconds, since its variance value is the one that is closest to the variance of 150 seconds sampling time portions. Moreover, the decreasing trend is highly visible in the plot.

Thirdly, and most importantly, percentage values of the difference between the mean value of the entire time series and the mean values corresponding to each portion were computed. To normalize the difference vectors each having a different length, their root-mean-square value was computed to see the effective values. The formula that was used to calculate the percentage difference is

$$\text{difference}\% = \frac{\text{abs}(m - \mu)}{\mu} \times 100. \quad (3.9)$$

Moreover, the root-mean-square value of each difference vector was calculated as

$$RMS = \sqrt{\frac{\sum_{i=1}^N m_i^2}{N}}. \quad (3.10)$$

Then, the following plot was obtained to compare the RMS values.

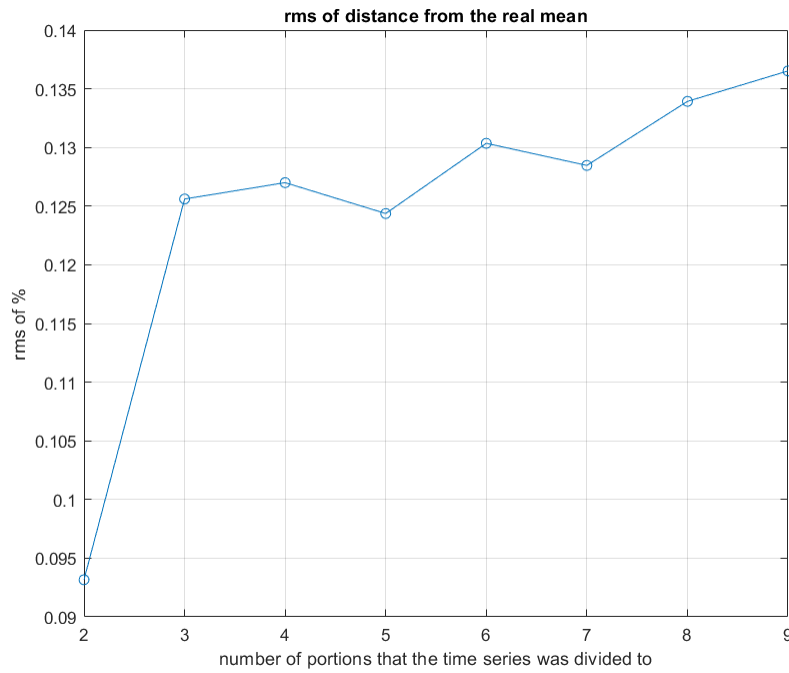


Figure 3.31: Root-mean-square of percentage difference mean value between the real and the pressure tapping time series portions. The empty circles show an RMS % value for corresponding portions. The plot makes visible how effective is the difference between the mean values of the portions and the real mean.

As it is totally clear in the plot, the difference between the mean values goes up to 0.1365 % when the sampling time decreases until 33.33 seconds. Since 0.1365 % difference is fully acceptable, sampling time can be decided as 33.33 seconds for this analysis also.

To sum up, the following table 3.9 lists the potential sampling time values selected by different methodologies.

Autocorrelation studies	42.59 s
Percentage range studies	33.33 s
Variance studies	33.33 s
Percentage difference studies	33.33 s

Table 3.9: Potential pressure sampling time values for the pressure scanner DSA 3217.

Thus, to be on the safe side and not miss any significant detail of the pressure signal, the sampling time was decided as 43 seconds.

3.3.3 Pressure Sampling Frequency

To catch enough details in pressure behavior, an appropriate sampling frequency[Hz] should be decided. According to Nyquist Theorem[Colarusso, Kidder, Levin, and

Neil Lewis, 1999], the sampling frequency should be greater than or equal to two times the maximum frequency of the related signal, so as to not have the aliasing error which appears due to undersampling. Thus, first of all, the pressure signal was acquired with the maximum possible rate for a long possible time. Then, to be able to decide the maximum frequency, the time series pressure signal was transferred to the frequency domain to investigate the power spectral density.

The power spectral density was calculated through the fast fourier transform, which is a method to compute the discrete fourier transform. Discrete fourier transform is used in discrete time series signals to transform the time domain into the frequency domain. In figure 3.32, it was made highly visible the fact that the time series is discrete.

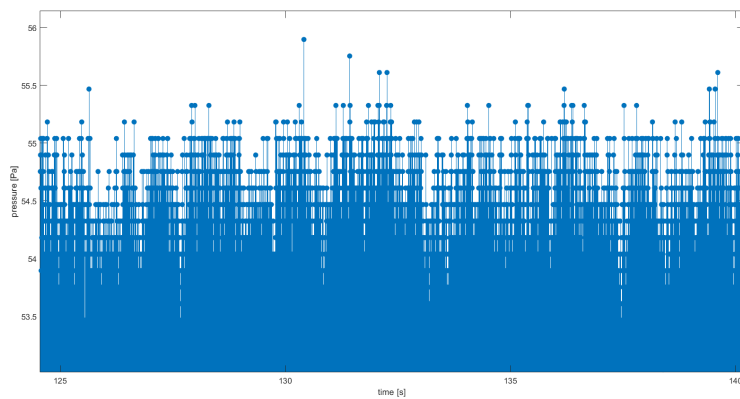


Figure 3.32: Discrete pressure signal between around 125 s and 140 s sampling time. Filled circles are the pressure values acquired for the corresponding time value. To make it continuous, filled circles are connected to each other. As it is obvious, the number of filled circles gets higher as the pressure value goes towards the mean value.

Starting from the beginning, the formula to calculate the fourier transform, which is used for continuous time series signals, is represented in section 7.1.

Since it was observed that the fast fourier transform analysis is not informative enough for the whole pressure time series signal, it was performed for the deviation from the mean voltage value.

Thus, a first look at the waveform of the fluctuating voltage at exit section $Re=12328.7$ can easily be made in the following figure 3.33.

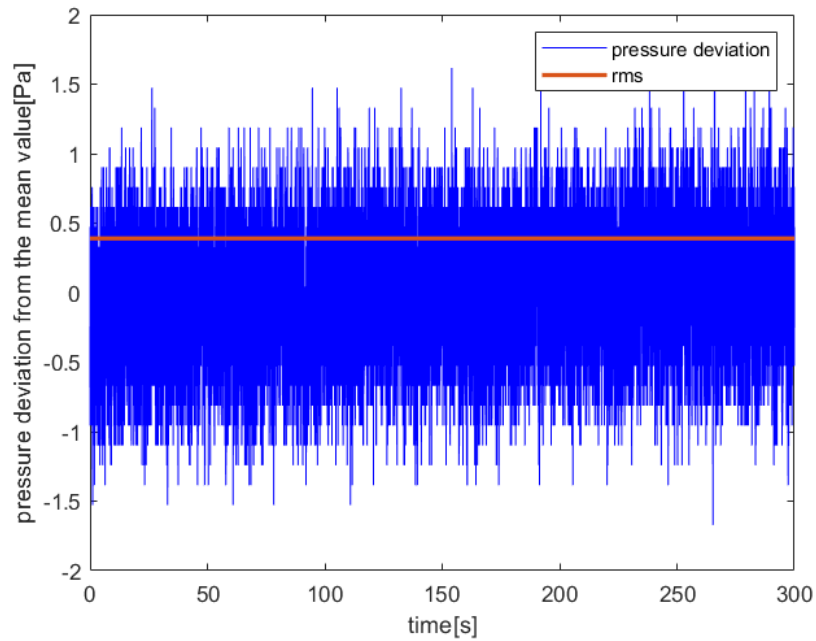


Figure 3.33: Plot of pressure deviation from the mean value, which is represented in blue, corresponding to each time value. Signal was obtained by a Scanivalve pressure scanner with a 270 Hz sampling rate for 300 seconds of sampling time. The red line shows the root-mean-square(RMS) value of the fluctuations, to be able to understand its magnitude and effectiveness.

The fast fourier transform coefficients were plotted for the frequency as can be seen in the figure 3.34

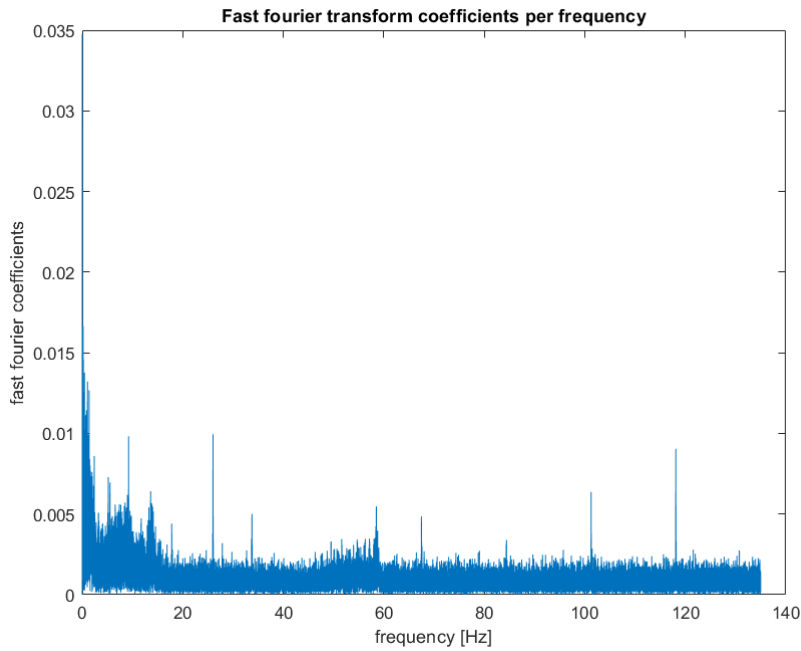


Figure 3.34: Fast fourier transform coefficients per pressure tapping signal frequency value.

Because the fast fourier transform coefficients have both imaginary and real parts, which may result in some negative values, absolute values were taken. As it can clearly be seen from the figure 3.34, the behavior of the coefficients is not crystal clear and may result in inaccurate comparisons of two different signals with different lengths. Thus, power spectral density was computed as

$$PSD = \hat{f} \text{conj}(\hat{f}) / N_b, \quad (3.11)$$

where:

- PSD = power spectral density,
- N_b = number of frequency bins,
- $\text{conj}(\hat{f})$ = conjugate of \hat{f} .

Power spectral density is the indicator of the power content of the time series corresponding to the frequencies of the waveforms inside the series [DEMPSTER, 2001]. However, due to the limitation on sampling frequency by the pressure scanner and the physics of the pressure signal, PSD density was not a sign to comment on the frequency of the pressure signal. Thus, the operations were performed for the fluctuations of the signal, which are represented as

$$P(t) = \bar{P} + p', \quad (3.12)$$

where:

- $P(t)$ = instantenous pressure signal,
- \bar{P} = mean pressure value,
- p' = fluctuating pressure value.

The following plot 3.35 was created to analyze the power and frequency content of the signal

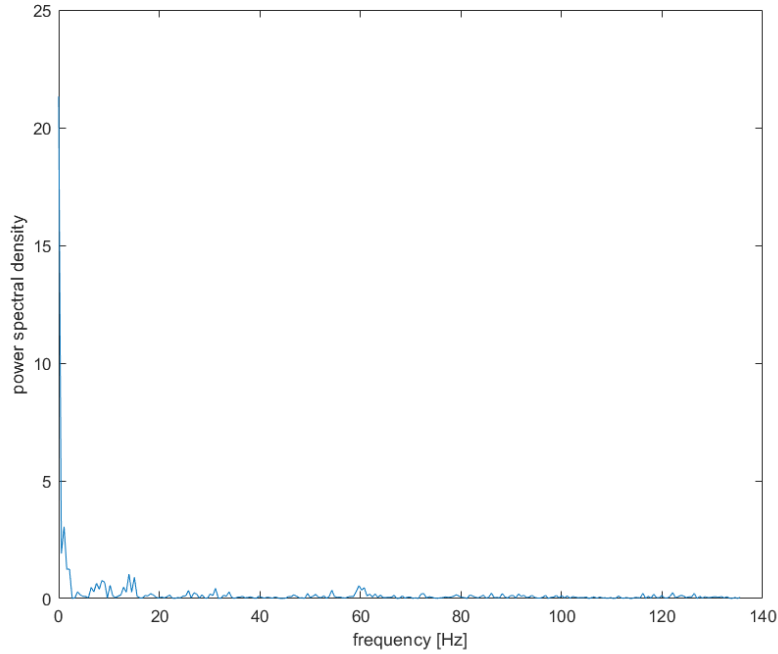


Figure 3.35: Power spectral density per pressure tapping signal frequency value.

As it can easily be understood from the plot above, the power content of the signal is the highest at 0 Hz and starts to decrease drastically after the first peak. The last valuable peak is at 14 Hz. Hence, the sampling frequency for the pressure scanner was determined as 28 Hz by taking into account the Nyquist criterion [Colarusso et al., 1999]. All in all, the following table represents the values decided to acquire the pressure

Sampling frequency	28 Hz
Sampling time	43 s

Table 3.10: Pressure acquisition parameters decided for pressure scanner DSA 3217 after analyzing all related methods.

After deciding the sampling frequency, Scanivalve requires a specific way to set the desired frequency for the pressure acquisition. The formula for the sampling frequency is

$$\text{Frequency} = \frac{1}{\text{Period} \times 16 \times \text{Average}}, \quad (3.13)$$

where the period represents the interval between channel samples, in microseconds [μs] and can get a value between

Variable	Command
Period	SET PERIOD X
Average	SET AVG X

Table 3.11: Commands to change the sampling frequency of Scanivalve.

where:

X = desired value inside the interval.

3.4 Inverter Communication

The first command is to power on/off the inverter by just using the front panel of the program, before setting the velocity of the flow.

Secondly, set the exit velocity to the desired value, a proper inverter communication should be done. Since the inverter cannot directly change the velocity of the flow, a relation between the inverter input/output (voltage in this case) and the exit velocity should be created. After giving the voltage input to the inverter, it has to be ensured that the desired velocity at the exit section of the PAT is reached.

3.4.1 On/Off Command Communication

A serial connection between the A/D board and the inverter was provided. One of the cables was connected to the digital output of the A/D board and to the 24 V digital input of the inverter while another cable was connected to the ground digital output of the A/D board and to the 0 V digital input of the inverter to have the voltage difference between the inputs.

Moreover, since the A/D board is not able to give the required 24 V digital output to the inverter, an external power supply was needed. Thus, the plus (+) node of the power supply was connected to the voltage supply digital output channel while the minus (-) node is connected to the ground digital output channel on the A/D board. The digital power supply, cabling of the inverter and the A/D board for on/off command are shown on the figures 3.39, 3.37 and 3.38, respectively.

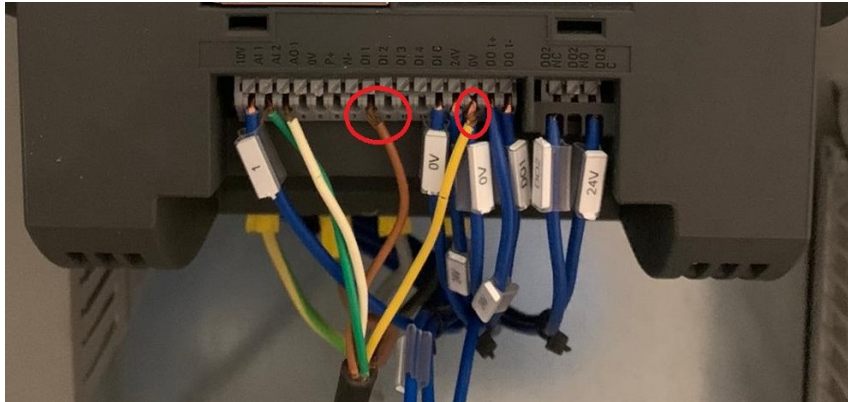


Figure 3.37: Inverter terminal for on/off command. 0-24V digital input and 0V digital input are separately going into the inverter to take the difference in voltage.



Figure 3.38: A/D board for on/off. 5V and 0V digital outputs are going out.



Figure 3.39: 24 V digital 2 channels power supply in which the right one is currently being used to send 24V input to the inverter to power on/off. The current[Ampers] and the voltage [V] can be set manually by playing with the knob. It has 5 channels for the cables since the ground one can be used for both simultaneously.

A VI code, which can be seen in figure 7.1 using the LabView environment was created to be able to give the command to the inverter. While designing the VI code, a digital output channel was created before starting the task. Then, a digital boolean data was written by using the "DAQmx Write" block, where the two different commands will be as listed on the table 3.12

On command	Off command
True	False

Table 3.12: Boolean values for on/off command. To power on the inverter, the true command should be sent, so the boolean should be switched to light up green. To power off the inverter, the false command should be sent, so the boolean shouldn't light up.

3.4.2 Speed Control Communication

A serial connection between the A/D board and the inverter was provided. One of the cables was connected to the 10 V analog output of the A/D board and to the 10 V analog input of the inverter while another cable was connected to the 0 V analog output of the A/D board and the 0 V analog input of the inverter to have the voltage difference between the cables. The cablings of the inverter and the A/D board are shown in figure 3.40 and figure 3.41, respectively.

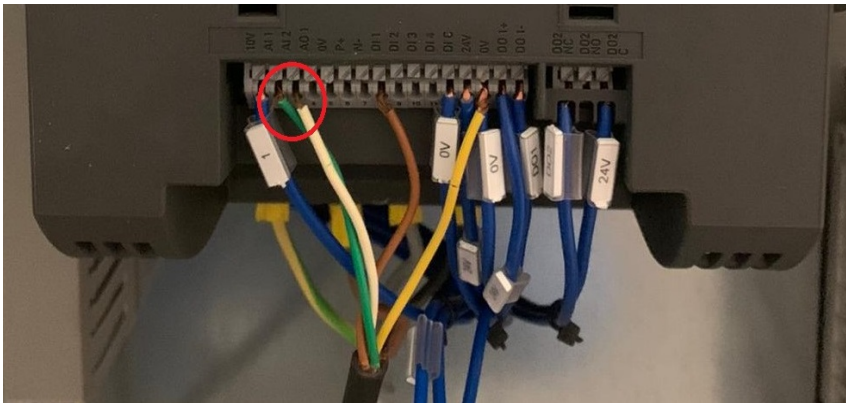


Figure 3.40: Inverter terminal cabling for speed control. Two different 0-10V analog inputs are taken from the A/D to take the difference, where one of them will send 0-10V and the other will send 0V.

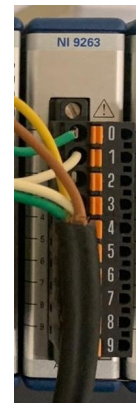


Figure 3.41: A/D board for speed control. Two different 0-10V analog outputs are sent for difference.

Furthermore, a VI code can be seen in the figure 7.2, which was created to give the desired voltage input to the A/D board which is expected to send the information to the inverter.

As can clearly be seen in both figures 3.41 and 7.2, the physical channel for voltage output, Mod5/ao0, was identified for giving the control input to the inverter. After creating the channel, the task was launched by the "start task" VI block. Inside a while loop, the user continuously gives the desired voltage input, which is sent to the inverter by a "write" block. The last block is to clear the task after the while loop is terminated, which can only be done by pressing the "stop" button.

Moreover, to let the inverter take the input not from its buttons, but from its terminal, specific programming was done on the inverter using its own buttons and screen. The following sequence tells the procedure step by step;

1. Do a single short press on the M button.
2. Select the P0010 menu and set it to 30 to start the factory reset.
3. Select the P0970 menu and set it to 21.
4. Press the M button until the inverter shows alternating frequency between 5 Hz and 0 Hz.
5. Do a single long press on the M button until it displays the P0100 menu.
6. Select the P0100 menu and set it to 0 to set the motor frequency which is 50 Hz.
7. Select the P0304 menu and set it to 400 since it is the voltage value of the motor.
8. Do a single short press on M and select Cn002 to set the parameters for "control from terminals", and press the OK button until there is a minus sign visible on the left.
9. Do a single short press on the M button and set it to 0 to have default settings.
10. Do a single short press on the M button.
11. Do a single long press on the M button until the default 0 Hz frequency value is displayed on the screen.
12. Do a single short press on M until the P0970 menu is visible.
13. Select the P0003 menu and set it to 3 for the expert access level .
14. Select the P0010 menu and set it to 1 for quick commissioning.
15. Select the P0700 menu and set it to 2 to set the terminal as the command source.
16. Select the P3900 menu and set it to 2 to end the quick commissioning.
17. Select the P2010 menu and set it to 6 to have 9600 bps.
18. Select the P2010 menu and set it to 6 to have 9600 bps.

3.5 Velocity Measurement

The velocity at the desired section can be measured by acquiring the pressure and the temperature to use them with the ideal gas law and Bernoulli's principle. The sampling rates and the sampling times should be set carefully to have an accurate result.

3.5.1 Pitot-static Tube

Being one of the most fundamental ways of measuring the speed in fluid dynamics, a pitot-static tube was preferred as one of the two methods to estimate the velocity at a given location. As was discussed before, a pitot-static tube measures both the total pressure and the static pressure, then calculates the velocity by using the dynamic pressure. To do that, the pressure and temperature acquisition process should be investigated.

Pressure Acquisition

Likely to inverter communication, a VI code was created to acquire the dynamic pressure data sensed by the pitot-static tube and sent to the pressure transducer. Table 3.13 represents the parameters to store the data as a digital signal. As it can easily be understood, 100 samples were taken per second while the sampling was running for 5 seconds by making a random selection of sampling quantities.

Sampling rate [Hz]	Sampling time [s]	Number of samples
100	5	500

Table 3.13: Pressure acquisition sampling parameters, decided arbitrarily for now just to be able to create a working acquisition VI code and analyze the pressure signal.

By taking the mean value of the samples, mean dynamic pressure can easily be calculated. Figure 7.3 and 7.4 shows the VI code of pressure acquisition.

First, since the offset behavior was assumed to be constant at all pressures, the pressure value at zero speed was measured and then this offset value was subtracted from the other pressure values at nonzero speed.

Under any circumstances, sampling time, sampling rate, physical channel to get the pressure voltage data, and the path to save the acquired data must be decided before running the code. Moreover, they can be modified for any specific case.

Since a 10 Torr pressure transducer was used to be able to go beyond the speed limits that a 2 Torr transducer has, the mean voltage value was multiplied by 1333.22. Thus, the dynamic pressure was obtained from the voltage value.

Moreover, to calculate the Reynolds number at the exit section, the following equation 3.14 was implemented

$$Re = \frac{\rho u d}{\mu}, \quad (3.14)$$

where:

- μ = dynamic air viscosity [$\frac{Ns}{m^2} 10^{-6}$],
- ρ = fluid density [$\frac{kg}{m^3}$],
- d = dimension of the exit section [m],
- u = flow velocity at the exit section [$\frac{m}{s}$].

The following figure 3.42 represents the front panel of the pressure acquisition. The behavior of the dynamic pressure can easily be observed from the waveform chart for a given sampling time at $Re=12299.9$.

CHAPTER 3. EXPERIMENTAL SETUP

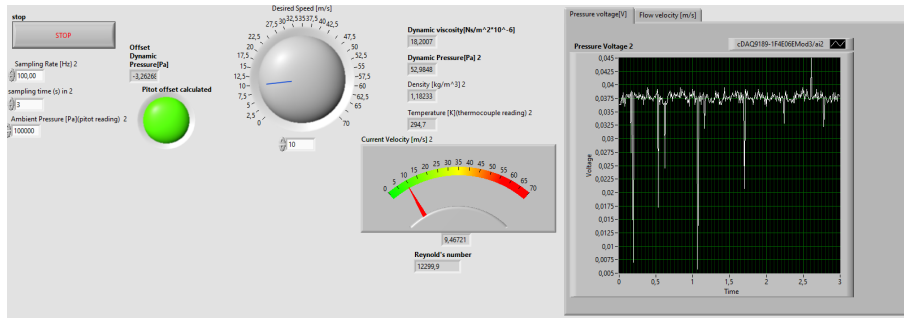


Figure 3.42: Pressure acquisition front panel. The user has to set the ambient pressure [Pa], sampling frequency [Hz], the sampling time [s], and the velocity offset [$\frac{m}{s}$] before running the code. The panel then displays the dynamic pressure [Pa] waveform, flow velocity [$\frac{m}{s}$] with a meter and a waveform graph, the density [$\frac{kg}{m^3}$], mean voltage [V], Reynolds number and elapsed time to acquire the pressure.

As it can be seen on the front panel 3.42, the offset value was first computed and then when the boolean light is on, the desired speed is set to compute the pressure and the velocity value.

Figure 3.43 represents the dynamic pressure behavior at $Re=12299.9$ for a more detailed view.

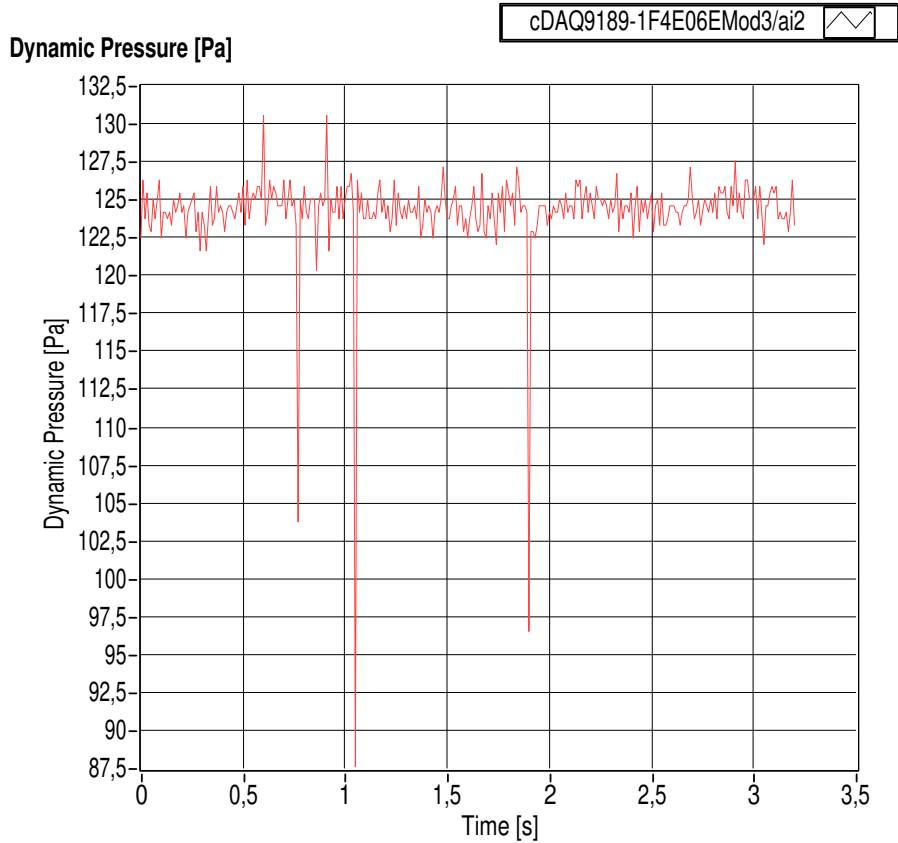


Figure 3.43: Dynamic pressure signal acquired with 100 Hz sampling frequency for 3.2 seconds of sampling time, to see the behavior. Sampling parameters were decided randomly just to see that the code is able to produce a signal in the desired form. The vertical axis is dynamic pressure [Pa] while the horizontal axis is time [s].

Temperature Acquisition

The changing temperature at the exit section was sensed by the thermocouple sensor. After the output signal was created by the transducer, it is transmitted to the computer via a serial connection. Then, a VI code was created to store, analyze and process the data by using the LabView environment. The code to acquire the temperature is a built-in block that was provided by NI itself. The following figure 7.5 shows the VI code of the most outer loop for temperature acquisition.

Moreover, one inner loop of the temperature acquisition VI code can be seen in figure 7.6.

To be able to estimate the dynamic viscosity under different conditions, air properties data[Munson, Rothmayer, and Okiishi, 2012] followed and a relationship between the temperature and the dynamic viscosity was created. By using the relation, dynamic air viscosity will be known as soon as the temperature is known.

The temperature acquisition that was done by the thermocouple and the DANTEC acquisition box was used to estimate the dynamic air viscosity at the location where the thermocouple is placed. The following plot 3.44 represents the relation between the temperature and the dynamic air viscosity at constant 1 atm atmospheric pressure. As expected physically, the viscosity of a gas increases as the temperature

increases, while the opposite is valid for a liquid.

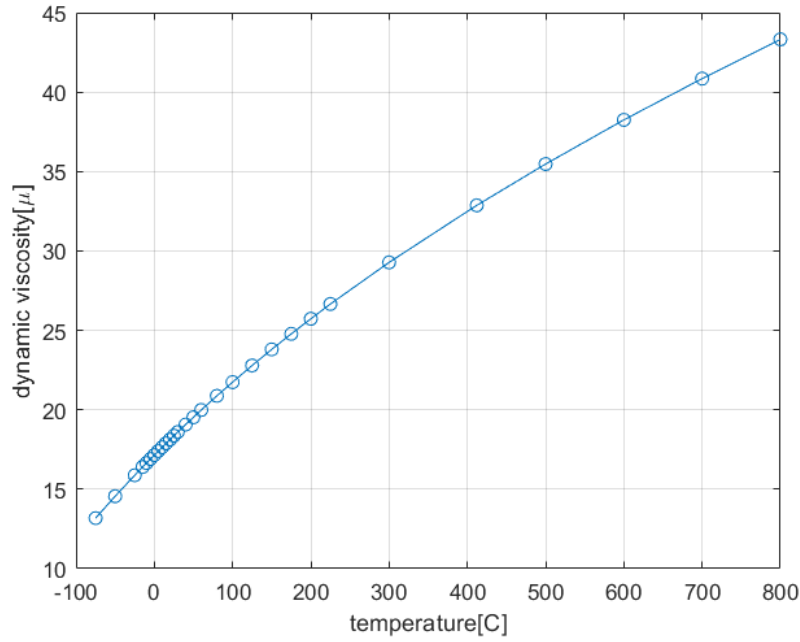


Figure 3.44: Behavior of dynamic air viscosity with respect to the temperature at a constant atmospheric pressure of 1 atm[Munson, Rothmayer, and Okiishi, 2012]. The temperature range is much wider than the operating range, but they are all included to be parallel with the data provided. Empty circles are the dynamic air viscosity values each corresponding to a temperature value.

Then, a fourth-order polynomial interpolation was performed and the following equation to relate the dynamic air viscosity to the temperature was created

$$\mu = -1.367e - 11T^4 + 3.383e - 8T^3 - 3.942e - 5T^2 + 0.04959T + 17.15, \quad (3.15)$$

where:

$$\begin{aligned} \mu &= \text{dynamic air viscosity} \left[\frac{Ns}{m^2} 10^{-6} \right], \\ T &= \text{air temperature} [C^\circ]. \end{aligned}$$

Thus, by using equation 3.15, dynamic air viscosity can be computed by just knowing the temperature.

Exit Velocity Calculation

The mean velocity at the exit section was calculated by performing pitot-static tube methodology which follows Bernoulli's equation[Qin and Duan, 2017] as shown below.

$$p_{total} = p_0 + \rho gh = p_{static} + p_{dynamic} + \rho gh = constant, \quad (3.16)$$

where:

- p_{total} = total pressure[Pa],
- $p_{dynamic}$ = dynamic pressure [Pa],
- p_0 = stagnation pressure[Pa],
- ρ = fluid density $[\frac{kg}{m^3}]$,
- g = gravitational acceleration $[\frac{m}{s^2}]$,
- h = height above the reference plane[m],
- ρgh = fluid potential energy[J],

$$p_{static} + \frac{1}{2}\rho V^2 + \rho gh = constant, \quad (3.17)$$

where:

$$V = \text{fluid speed}[\frac{m}{s}].$$

It claims that the total pressure along a streamline is constant if the flow can be said to be incompressible. Since the potential energy of the air is much less compared to p_0 , it can be neglected and the following equation 3.18 is left for Bernoulli's application

$$p_{static} + \frac{1}{2}\rho V^2 = constant. \quad (3.18)$$

Moreover, stagnation pressure can be said to be equal to the total pressure if the flow is isentropic, so

$$p_{static} + \frac{1}{2}\rho V^2 = p_{total}. \quad (3.19)$$

Thus, the following equation 3.20 allows the mean velocity to be calculated

$$\boxed{V = \sqrt{\frac{2p_{dynamic}}{\rho}}}. \quad (3.20)$$

Lastly, the ideal gas law(3.21) was used to calculate the density of the fluid as follows

$$p = \rho RT, \quad (3.21)$$

where:

- p = ambient pressure[Pa],
- R = specific gas constant = $287[\frac{J}{kg \cdot K}]$,
- T = temperature[K].

The flow path to calculate the current mean velocity at the exit section can easily be understood from figure 7.7.

Furthermore, the speed at the exit section can easily be read on the user interface as it is represented in figure 3.42. The speed is available both in meter indicator format and in the digital display to be more accurate about the digits.

3.5.2 Inverter Voltage and the Exit Velocity Relation

The program is required to be able to give the opportunity to set directly the desired velocity, instead of the voltage of the inverter. Thus, a relationship between the inverter voltage and the exit velocity was found by acquiring the exit velocity value by the pitot-static tube for different voltage input values to the inverter. The following figure 3.45 clearly shows that the relationship between the voltage and the velocity is almost linear.

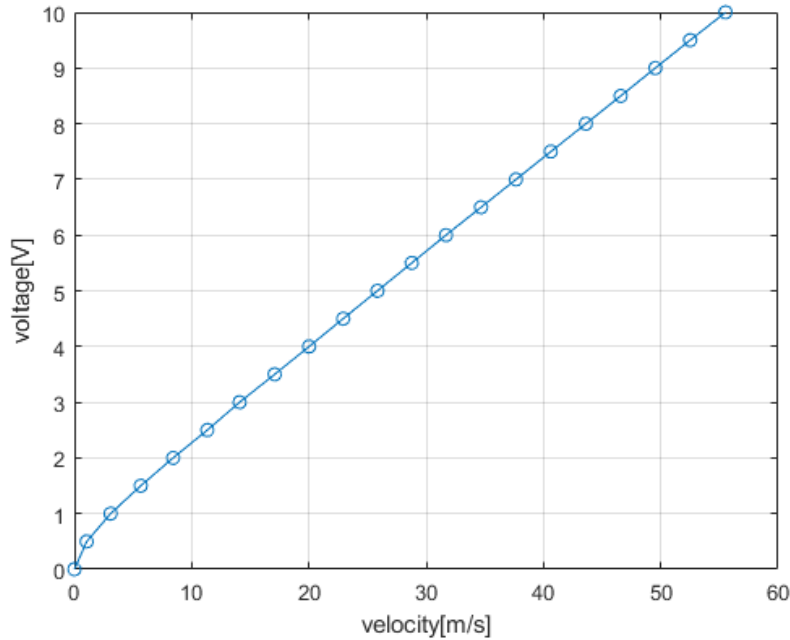


Figure 3.45: Plot to relate the velocity and the voltage, where the circles correspond to data points. The vertical axis is voltage[V] sent by the A/D board and the horizontal axis is velocity [$\frac{m}{s}$] at the exit section that was measured by the pitot-static tube. The voltage step was taken as 0.5V.

Hence, a first-order polynomial curve fitting was estimated to find the first-order relationship as follows

$$E = 0.1739V + 0.439, \quad (3.22)$$

where:

$$\begin{aligned} E &= \text{voltage[V]}, \\ V &= \text{exit velocity}[\frac{m}{s}]. \end{aligned}$$

However, equation 3.22 is built highly time and loss-dependent. Because, voltage input is given to the inverter, which transfers it to the AC motor to rotate the fan and create the flow rate inside the wind tunnel but the velocity that was related to the voltage was measured at the exit section. Thus, there are a bunch of wind tunnel components briefly explained in 3.1, which affect the flow inside and so at the exit section. Hence, the slope coefficient and the constant term will alter as the behavior of these components inside the plane air tunnel is changed.

3.5.3 Pressure Tappings

Pressure Behavior and the Exit Velocity Relation

To be able to estimate the speed at the exit section, a parameter of the flow inside the tunnel, which has a certain behavior under certain conditions, must have been related to the velocity under those certain conditions that will be analyzed during the experiments. For that purpose, pressure values at each channel were used since their behavior has a definite trend which changes their values but keeps the mean shape. Thus, pressure values were acquired at each channel for different speed values at the exit section.

The following plots were created relating the velocity at the exit section and the pressure at different locations,

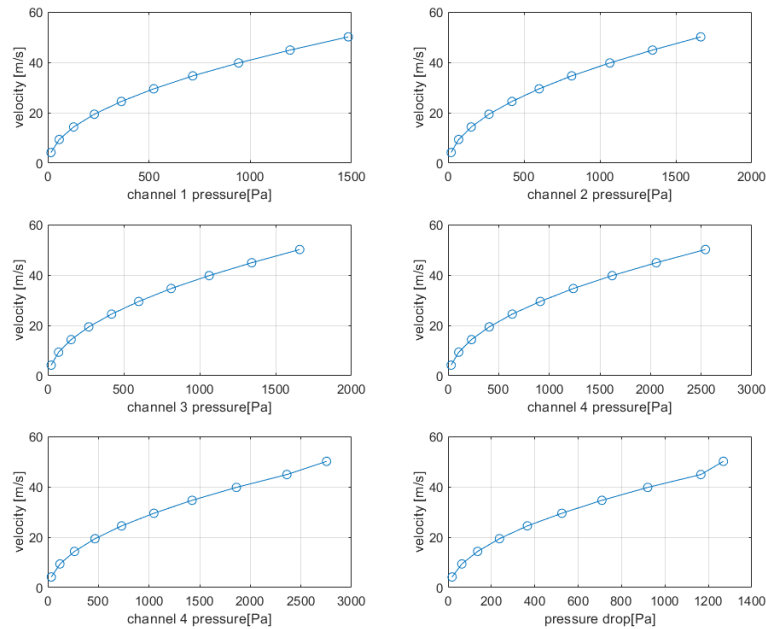


Figure 3.46: A separate investigation of the behavior of pressure at each channel placed at different locations along the plane air tunnel, reported in table 3.5, with respect to changing exit velocity. Each empty circle shows the pressure value for a specific speed value at the exit section. Pressure drop was calculated as the pressure difference between the values from channel 5 and channel 1.

where:

pressure drop = pressure difference between 5th and 1st channels.

Then, an equation for the exit section velocity is obtained as a function of pressure separately for each pressure tapping. By using the curve fitting tool of MatLab, the following fourth-order polynomials were created to relate the channel pressures to the velocity at the exit section:

Channel 1	$-2.52e - 11p^4 + 9.139e - 8p^3 - 0.0001209p^2 + 0.09163p + 3.753$
Channel 2	$-1.488e - 11p^4 + 6.086e - 8p^3 - 9.132e - 5p^2 + 0.07996p + 3.446$
Channel 3	$-1.513e - 11p^4 + 6.178e - 8p^3 - 9.248e - 5p^2 + 0.08064p + 3.318$
Channel 4	$-2.746e - 12p^4 + 1.721e - 8p^3 - 3.952e - 5p^2 + 0.05271p + 3.473$
Channel 5	$-1.434e - 12p^4 + 1.081e - 8p^3 - 2.935e - 5p^2 + 0.04562p + 3.538$
Pressure drop	$-1.266e - 11p^4 + 6.489e - 8p^3 - 0.0001031p^2 + 0.08859p + 3.413$

Table 3.14: Fourth-order polynomial interpolations that were performed with respect to the curve represented in figure 3.46. Pressure drop was calculated as the pressure difference between the values from channel 5 and channel 1. Interpolated functions will be used to estimate the exit velocity by measuring the pressure values at channels.

By using the interpolated polynomials, the velocity at the exit section can easily be estimated without using a pitot-static tube. Figure 3.47 shows the plot in which the relation between the velocity computed by pressure channels and the velocity measured by the pitot-static tube is visible

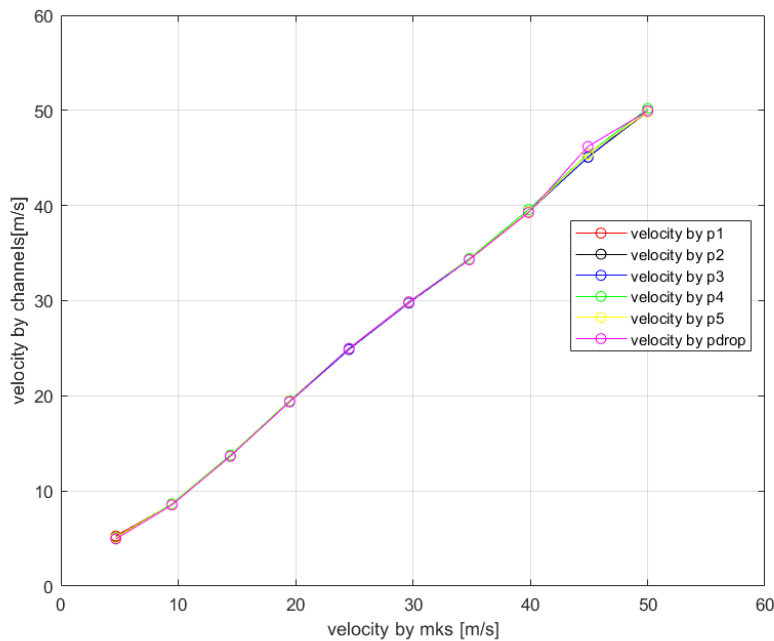


Figure 3.47: Comparison of velocity values at the exit section that were obtained by pressure tappings and pitot-static tube, **for the first experiment**. The horizontal axis represents velocity values estimated by the pitot-static tube, which uses an MKS pressure transducer. The vertical axis stands for velocity values estimated by using interpolation functions with the pressure values measured by pressure tappings. Each color corresponds to a pressure tapping and pressure drop result. Pressure drop was calculated as the difference between pressure values at channel 5 and channel 1. Each empty circle shows a data point connecting two velocity values.

where

- $p1$ = 1st pressure tapping,
 $p2$ = 2nd pressure tapping,
 $p3$ = 3rd pressure tapping,
 $p4$ = 4th pressure tapping,
 $p5$ = 5th pressure tapping,
 $pdrop$ = pressure drop calculated as $p5-p1$.

Velocity Estimation Accuracy by Pressure Tappings

Since the behavior of offset changes in time, the accuracy of pressure channels also changes. To understand which channel gives the most accurate speed value, the same experiment was performed two times in a day, and the other two times on another day. The repetition of the experiments was just for consistency of the results. Figure 3.48 shows the plot in which the relation between the velocity computed by pressure channels and the velocity measured by pitot-static tube for four different experiments is visible. Experiments were conducted for a velocity range of $[5,50] \frac{m}{s}$ with a step of $5 \frac{m}{s}$.

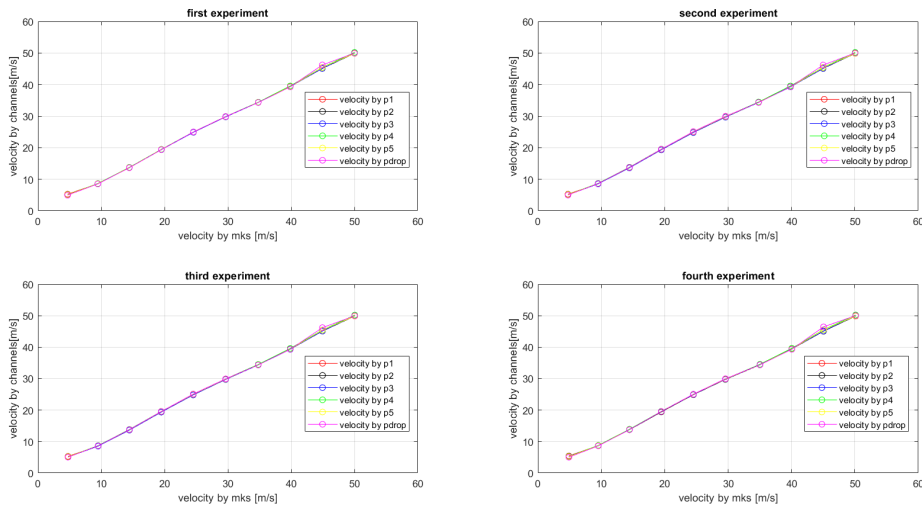


Figure 3.48: Relation between velocities that are measured by mks transducer connected to the pitot-static tube and by DSA 3217 pressure scanner that is connected to pressure tappings. $p1$ represents the results got from channel 1 and the same is valid for all p 's. $pdrop$ is the difference between the pressure at channel 5 and the pressure at channel 1. Four different plots where each was got from a different experiment, repeated to be consistent.

To see the difference between the velocities, which can also be called the error caused by velocity estimation by channels, the percentage difference between the velocity vectors was calculated as

$$\text{difference}\% = \frac{v_{pitot} - v_{channel}}{v_{pitot}} \times 100, \quad (3.23)$$

where:

CHAPTER 3. EXPERIMENTAL SETUP

v_{pitot} = vector composed by pitot velocity values,
 $v_{channel}$ = vector composed by channel velocity values.

Then, following figures 3.49, 3.50, 3.51 and 3.52, each corresponding to a different experiment, were created for all the channels to investigate the behavior of velocity deviation from the value computed by pitot-static tube.

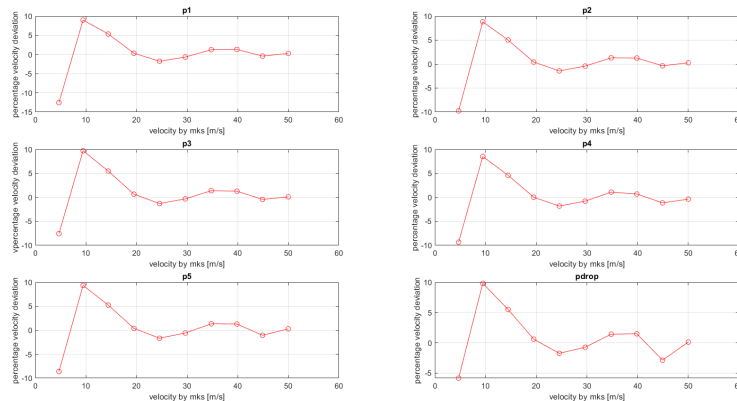


Figure 3.49: Percentage deviation of velocity values that were obtained by pressure tappings, plotted in the vertical axis, from the velocity values that were obtained by the pitot-static tube, reported in the horizontal axis, **for the first experiment**. Data were obtained for pressure drop and different channels placed along the streamwise direction of the plane air tunnel, reported in table 3.5. Each empty circle corresponds to a data point. Pressure drop was calculated as the difference between pressure values at channel 5 and channel 1.

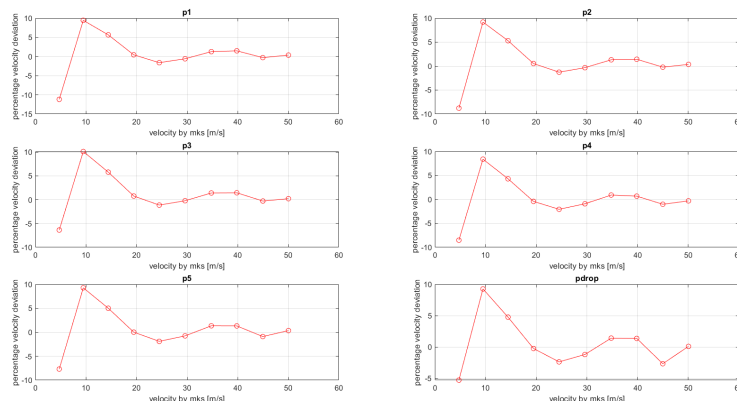


Figure 3.50: Percentage deviation of velocity values that were obtained by pressure tappings, plotted in the vertical axis, from the velocity values that were obtained by the pitot-static tube, reported in the horizontal axis, **for the second experiment**. Data were obtained for pressure drop and different channels placed along the streamwise direction of the plane air tunnel, reported in table 3.5. Each empty circle corresponds to a data point. Pressure drop was calculated as the difference between pressure values at channel 5 and channel 1.

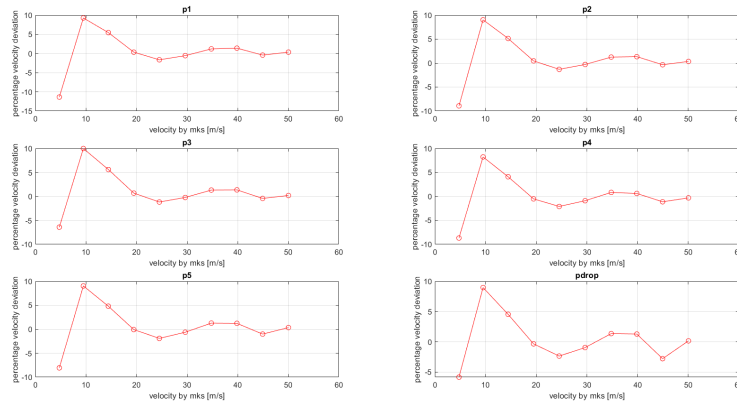


Figure 3.51: Percentage deviation of velocity values that were obtained by pressure tappings, plotted in the vertical axis, from the velocity values that were obtained by the pitot-static tube, reported in the horizontal axis, **for the third experiment**. Data were obtained for pressure drop and different channels placed along the streamwise direction of the plane air tunnel, reported in table 3.5. Each empty circle corresponds to a data point. Pressure drop was calculated as the difference between pressure values at channel 5 and channel 1.

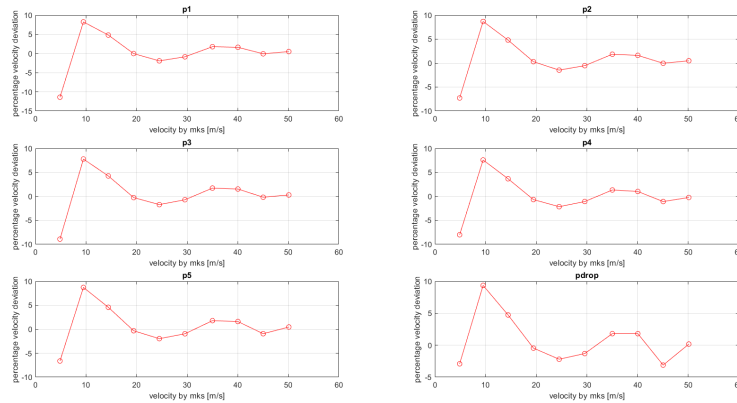


Figure 3.52: Percentage deviation of velocity values that were obtained by pressure tappings, plotted in the vertical axis, from the velocity values that were obtained by the pitot-static tube, reported in the horizontal axis, **for the fourth experiment**. Data were obtained for pressure drop and different channels placed along the streamwise direction of the plane air tunnel, reported in table 3.5. Each empty circle corresponds to a data point. Pressure drop was calculated as the difference between pressure values at channel 5 and channel 1.

Although it is not that easy to catch the most accurate channel by looking at the velocity deviation plots, it can be said that the 2nd and the 4th channels have smaller deviations compared to others.

To be able to talk about the exact results, the norm of the difference vector was computed. Norm is an operation that allows one to calculate the magnitude, or strength, of a vector. The formula to calculate the norm is

$$Norm = \sqrt{\sum_{i=1}^N d_i^2}, \quad (3.24)$$

where:

d = velocity difference vector,

$$d = v_{pitot} - v_{channel}. \quad (3.25)$$

Then, plotting the magnitude of difference for four different experiments as it is represented in figure 3.53, it was found that the 4th channel behaved as the most accurate one in all four experiments.

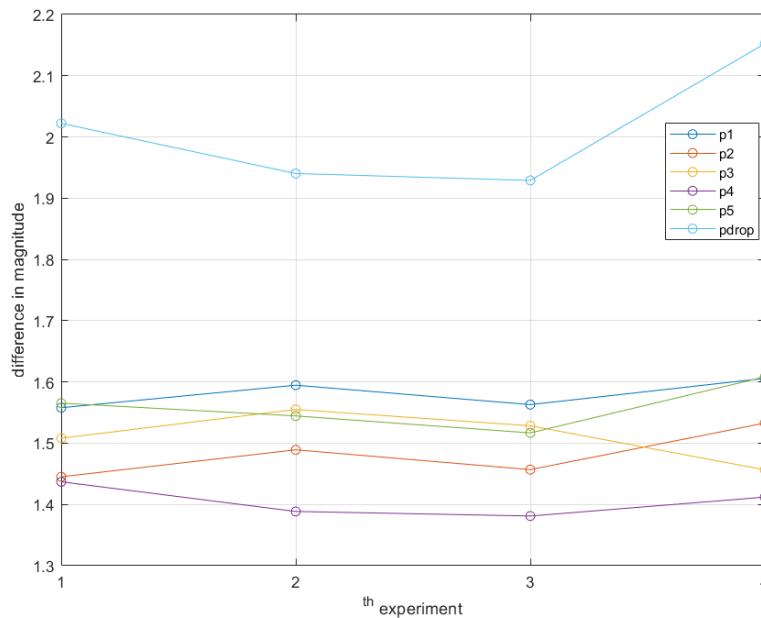


Figure 3.53: Magnitude of difference between the speed values estimated by pressure tapings and by pitot-static tube, at the exit section for four different experiments. Each color corresponds to a pressure tapping and pressure drop while each empty circle shows a data point. Pressure drop was calculated as the difference between pressure values at channel 5 and channel 1.

Hence, the 4th channel was decided to be used for any operation where there is a need to estimate the speed at the exit section without using a pitot-static tube.

3.5.4 PI Control

A proportional integral control was decided to be implemented inside a closed loop control system to be able to set the exit speed to the desired value as much as possible. In a speed control closed-loop control system, "the set point" is the desired speed value, and "the process variable" is the speed value at the exit section. The

system takes the set point input by the user, measures the speed at the exit section, sends it back to the user input as feedback, computes the error between the set point and the process variable, compensator decides the correct value to be given as input and sends it to the actuator. The loop keeps going on until the desired tolerance between the set point and the process variable is reached.

In the case that was used in PAT, the compensator was a PI controller, and the variable frequency driver giving the output to the AC motor was used as an actuator.

Firstly, in a PI controller, the speed of the correction response was decided by a proportional component. It depends only on the error value between the process variable and the set point. Increasing proportional gain results in an increment in response speed, but an excessive value makes the system unstable.

Secondly, the steady-state error is the difference between the set value and the process variable after the process variable value comes to rest. Thus, an integral component was used in the control system to allow the system to have less steady-state error. There is a continuous growth in the integral response over time as soon as the error is different than zero[“PID Theory Explained”, 2020].

The process to decide the optimal values of three constants is called ”tuning”. There are two most common ways to tune the control system. In this study, the ”guess and check” method was implemented.

With a Pitot-Static Tube

A pitot-static tube was placed at the exit section of the plane air tunnel to be able to measure the speed and send it as feedback to the controller.

After conducting multiple experiments to test the PI controller system, the values for the controller with the pitot-static tube were decided as in table 3.15 below

Proportional Gain	Integral Gain
1.4	10

Table 3.15: PI gain table that was set iteratively by trial and fail method for the case with the pitot-static tube.

Moreover, the VI code of the PI controller is shown in figure 7.9 to clarify the methodology applied for the speed control. As it can easily be seen from the code, steady state error was determined to be 4% at most.

To be more accurate on the speed value, a pressure offset was first measured at zero speed, and then it is subtracted from the next pressure values that were measured at nonzero speed values.

Due to the disturbances, errors by 1st order polynomial curve fitting that will be done by relating the inverter voltage and the velocity at the exit in section 3.5.2, lack of precision and accuracy in the measurement techniques, an offset between the desired and the measured values of the speed was observed.

Without a Pitot-Static Tube

To reach and keep the desired speed at the exit section of the plane air tunnel, a proportional integral control system was built with a pitot-static tube at the exit section to measure the pressure and then calculate the velocity to give feedback to the control loop. To get rid of the pitot-static tube for making the air tunnel exit clear and far from any disturbances, the behavior of the wind tunnel should be related to the velocity at the exit section. To achieve this, pressure tappings were used since their behavior is consistent, meaning that there is a specific trend in the behavior of pressure along the plane air tunnel. The methods that were used to relate the pressure behavior along the tunnel to the velocity measured by the pitot-static tube at the exit section were discussed in section 3.5.3.

Then, the only difference from the proportional integral speed control that was discussed in section 3.5.4 is the tool to measure the speed at the exit section, and nothing else. As it was done before, the pressure offset is again measured at the zero velocity and then it was subtracted from the pressure values at nonzero speed values.

The tuning process was performed to set the most suitable proportional and integral gains for the control system, and they were determined as reported in the following table 3.16

Proportional Gain	Integral Gain
1.4	10

Table 3.16: PI gain table that was set iteratively by trial and fail method for the case without the pitot-static tube.

As it was done the same in the version with the pitot-static tube, the stopping criterion was again taken as 4% of error. Thus, the control loop will stop when the difference between the desired and the current exit velocity becomes four percent of the desired velocity.

Moreover, the front panel to control the speed by using pressure tappings was shown in figure 4.10 in section 4.3.1.

3.6 Hot Wire Experiments

To conduct an experiment by using the theory of hot wires that was discussed in section 2.1, certain tests must be implemented for the wire and the acquisition system. Before starting to test the setup, one must ensure that all the cabling was done carefully. Firstly, the hot wire input is introduced to the acquisition board at the right channel where the wire is connected. This procedure is the start of the tests and it is done by the following user interface

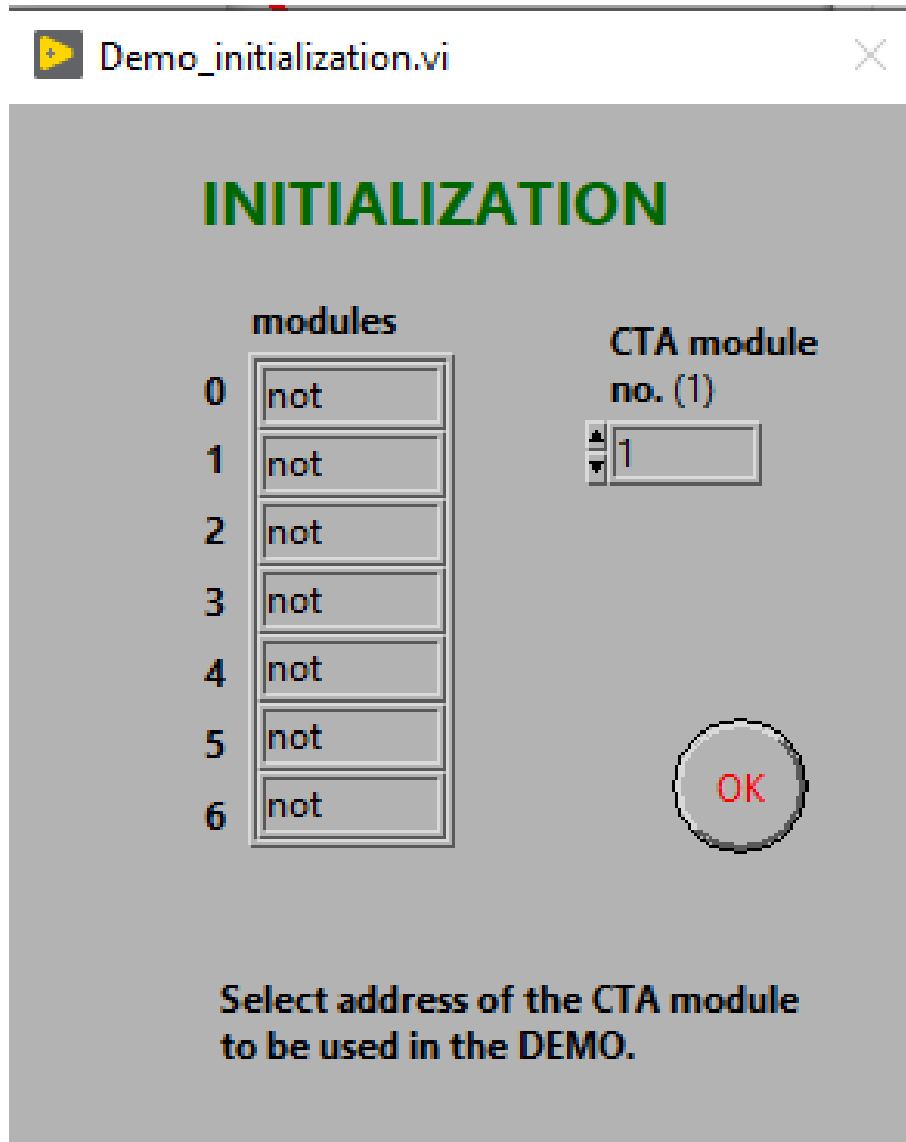


Figure 3.54: Front panel of the program in which the user introduces the hot wire connection to the acquisition board. There are 7 channels visible, 0 is for the thermocouple and 1-6 are for the hot wires. The user should select the number of the module in "CTA module no." and click ok.

The second is to adjust the overheat by measuring the current ambient temperature, wire resistance, and wire temperature, calculating the overheat ratio, and setting all of them as a decade. The user interface of the procedure can be seen in figure 3.55.

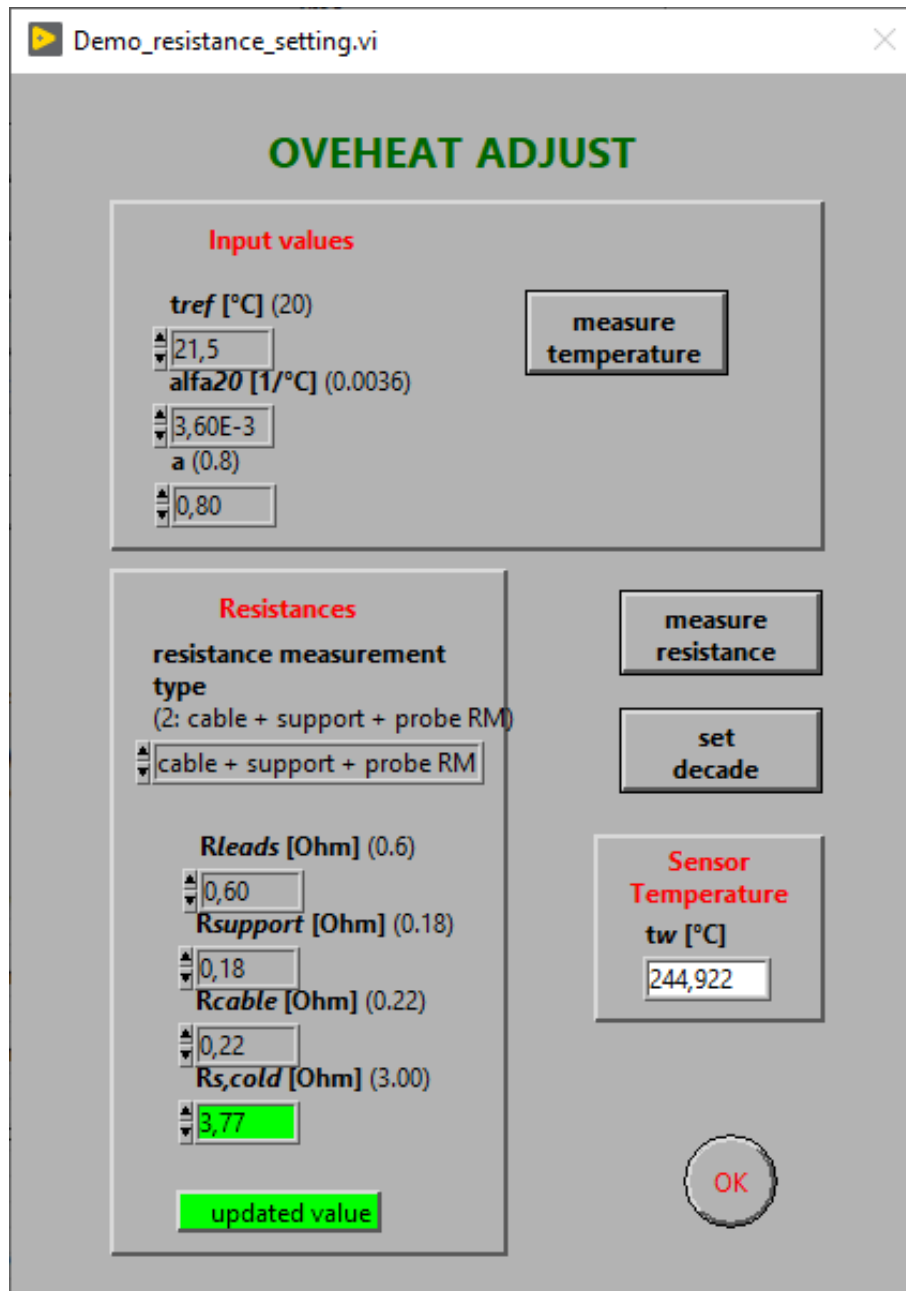


Figure 3.55: Front panel of the program in which the user adjusts the overheat for the hot wire experiment. Measured quantities are the ambient temperature, wire resistance, leads resistance, support resistance, cable resistance, cold cable resistance, and wire temperature. User should click "measure temperature", "measure temperature", "set decade" and "ok".

The next step to do is just to let the CTA system starts to operate by simply using the virtual switch as it is represented in the figure 3.56 below

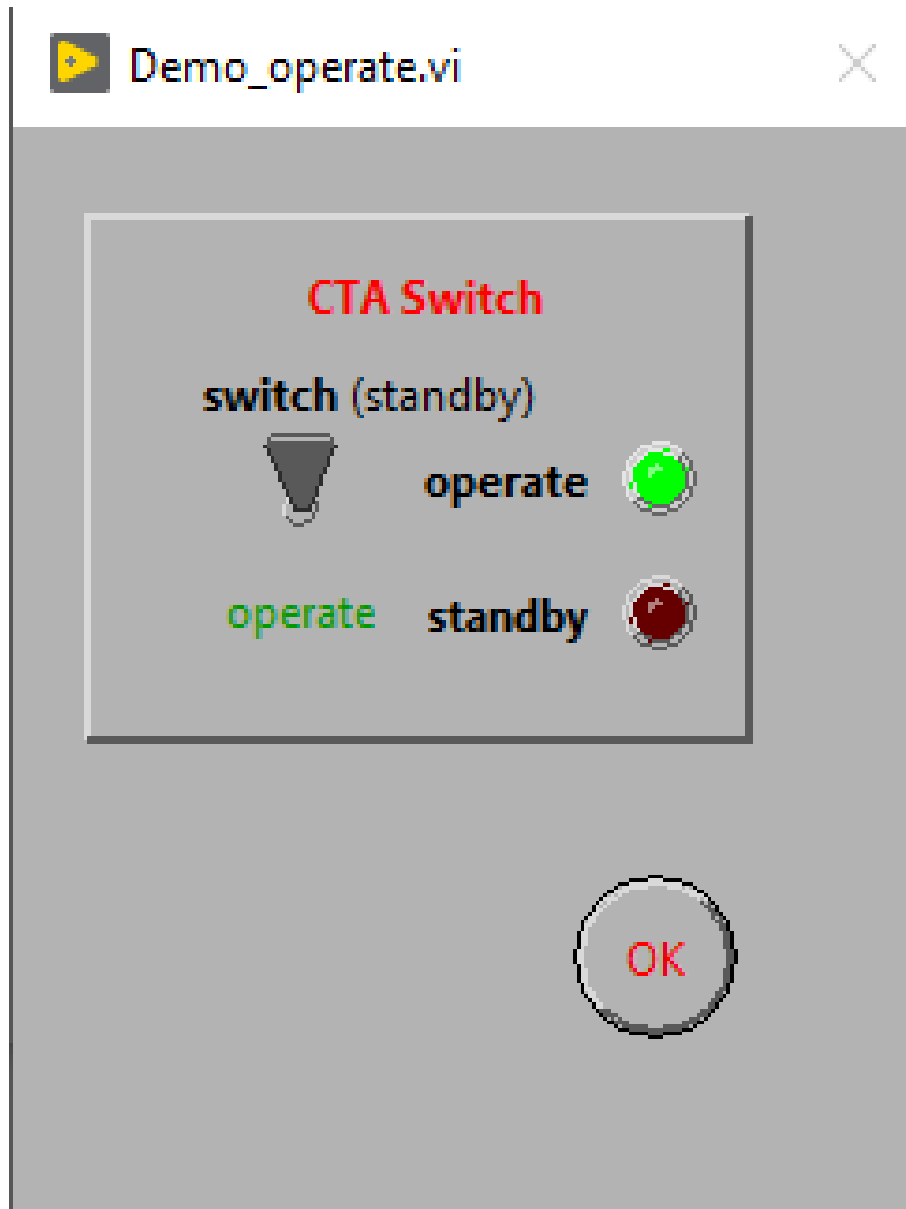


Figure 3.56: Front panel of the program in which the user simply tells the system to operate the CTA setup. The user should first click the switch above "operate" and see the green light next to "operate" and then "ok" to finish this step.

The step just before the last one is to set the parameters for the signal conditioning. If the user can guess the maximum and minimum values of the signal output with respect to the physics of the recent case, s/he can set the high-pass filtering and the low-pass filtering in this section. High-pass filtering is done to get rid of the undesired noise in the signal while the low-pass filter is needed for avoiding the aliasing(undersampling) error. Moreover, the gain and the offset for the hot wire voltage signal can be set prior to sampling in this step. The front panel used to make the conditioning visible is figure 3.57.

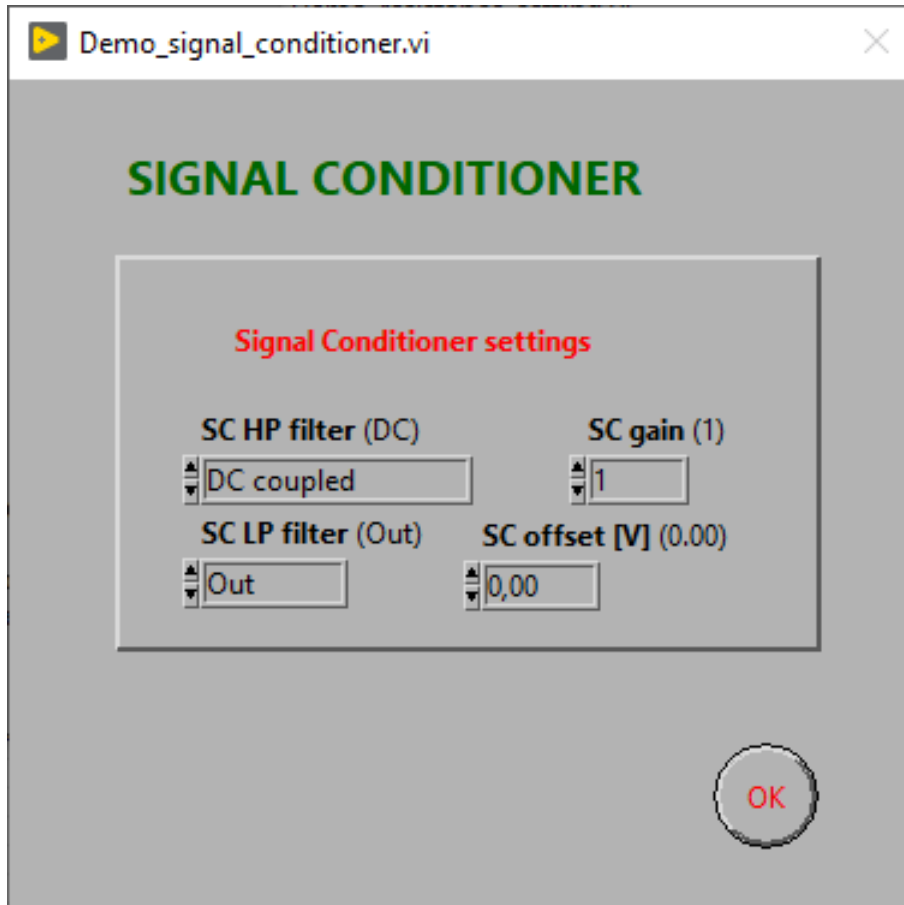


Figure 3.57: Front panel of the program in which the user sets the parameters for conditioning the hot wire signal. The high-pass filter, low-pass filter, gain, and the offset for the voltage signal are set with this front panel. The user should adjust the required parameters and click "ok".

In the last step of making the setup ready for the hot wire experiment, a square wave test is performed to test the response of the sensor. To observe the structure of the time response of the hot wire, an arbitrary voltage pulse is sent. By looking at the reaction of the wire, the performance of the sensor is estimated. The following figure 3.58 shows the user interface of the setup at which the user tests the response of the wire.

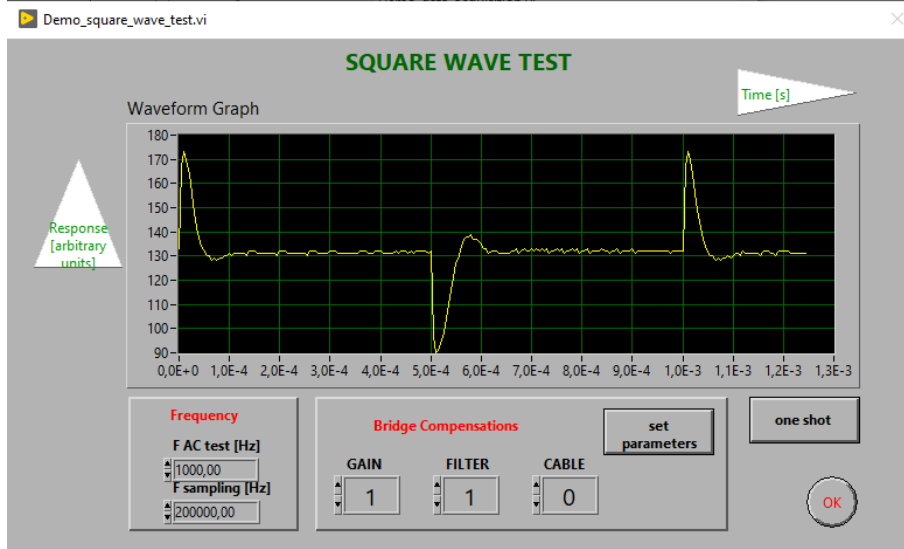


Figure 3.58: Front panel of the program in which the user tests the response of the hot wire by sending an input voltage value and observing the behavior. Frequencies of the AC test and the sampling can be changed. The vertical axis is voltage [V] and the horizontal axis is time [s]. Bridge compensations like gain, offset and the bridge can be set. The user should first click "one shot" and then "ok".

The plot visible above is a typical response of a hot wire. The feedback loop of the hot wire, including the amplifier inside the circuit, should be designed to optimize its behavior. Overshooting should be avoided while the response time is reduced as much as possible.

3.6.1 Hot Wire Sampling Time

To determine the most proper sampling time for hot wire measurements, the same methodologies that were followed in section 3.3.2 were performed again. Firstly, to be able to analyze the acquired data, the rate and the time should have been chosen in appropriate amounts. In other words, sampling parameters should be set excessively for the first time, to have data that provides a noteworthy amount of information to decide the required sampling time and the sampling frequency.

Since the turbulence intensity of the planar jet flow is different at each point of the wake, the required sampling time and the sampling frequency differ between points in space. To be able to keep the sampling parameters constant during whole hot wire signal acquisition, a location on the wake where the turbulence intensity is highest was chosen to perform the first acquisition, and then decide the required sampling parameters for that location to be on the safe side for the worst case.

To decide the location for the first acquisition, a literature review was performed. According to the plot represented in figure 2.10 in section 2.2, the velocity fluctuations seem to be the most powerful at around $\frac{x}{d} \approx 5$ streamwise location at the exit section Reynolds number $Re=8000$. Thus, the first acquisition was performed at $\frac{x}{d} = 5$ while providing the condition of $Re=8000$ for 100 seconds of sampling time with a 20 kHz sampling rate. The shape of the hot wire voltage signal can be seen in figure 3.59 below.

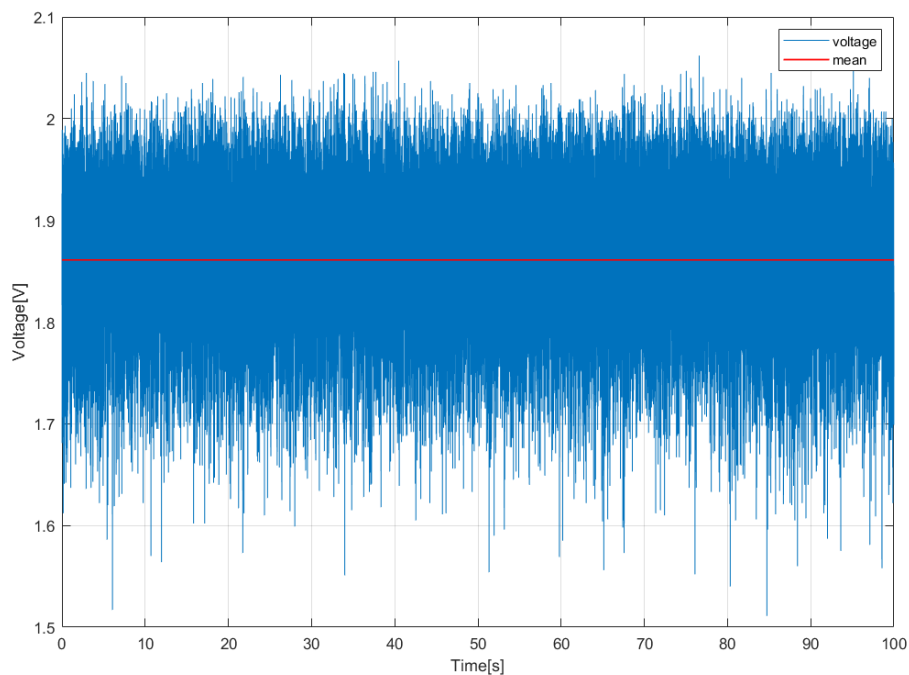


Figure 3.59: Voltage signal at $\frac{x}{d} = 5$ at exit Reynolds number $Re=8000$ that was obtained by NI DAQ acquisition board at 20000 Hz sampling rate for 100 seconds of sampling time. Blue lines represent the pressure values at the corresponding time value while the red line shows the mean value of the whole time series.

One method to analyze the sampling time is the autocorrelation of the voltage values. The process to compute the autocorrelation was discussed in 3.3.2. By using formulas 3.4 and 3.5, the autocorrelation of voltage values that are k time lag far from each other can easily be computed. Thankfully, MatLab has its own comment to automatically compute it. The autocorrelation of hot wire signal in figure 3.59 can be seen in figure 3.60. By looking at the plot, sampling time can easily be decided by determining the time lag in that the samples lose their correlation.

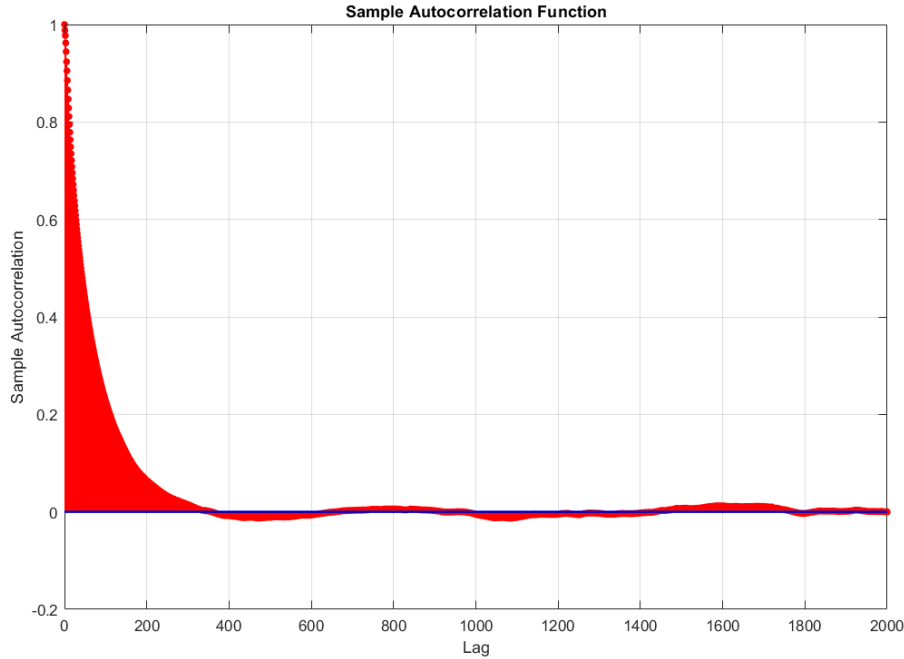


Figure 3.60: Autocorrelation between the hot wire voltage samples. The horizontal axis represents the time lag between one sample to another (number of samples) while the vertical axis shows the correlation between those samples. Each filled red circle stands for a correlation value between samples that are corresponding time lag far away from each other. The samples can be said uncorrelated when the autocorrelation goes under the horizontal blue lines

Autocorrelation of hot wire voltage signal was computed with the number of time lags that is $\frac{1}{1000}$ number of samples, then the time lag is equal 1000 times the time between each sample, which is

$$1000/f_s = 0.05s.$$

where:

$$f_s = \text{sampling frequency.}$$

As it can be understood from the figure 3.60, the autocorrelation between the voltage values starts to become insignificant after around 300^{th} time lag. To make it more clear, the following figure 3.61 represents the zoomed-in version of the autocorrelation values of the voltage signal between 100^{th} and 1000^{th} time lag.

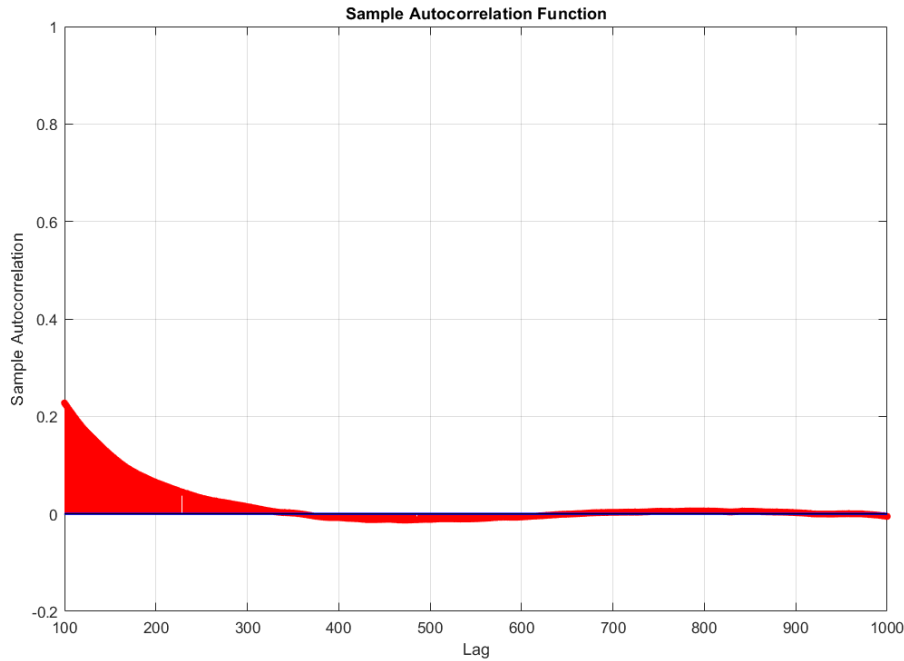


Figure 3.61: The autocorrelation of hot wire signal that is zoomed between specific values to analyze it in more detail.

As one can immediately say, the signal can be said to be uncorrelated after 350th time lag. Thus, the sampling time required with respect to the autocorrelation can be calculated as

$$350 \times 0.05 = 17.5s.$$

Another way to find the sampling time for hot wire measurements is to check the behavior of the mean values of each portion that the whole time series is divided into. As mentioned, the hot wire voltage time series that was acquired for 100 seconds with a 20 kHz sampling rate was separated into portions, where each corresponds to another sampling time. Then, the behavior of the mean values of each portion was analyzed. The following table 3.17 shows sampling time values for the corresponding number of portions that the whole time series was divided into while the mean value variation of each portion can be seen in figure 3.62 below. One can easily compare the mean values of the portions to the mean value of the whole time series.

Portions	Sampling time [s]
2	50
3	33.33
4	25
5	20
6	16.67
7	14.29
8	12.50
9	11.11

Table 3.17: Sampling time values for the corresponding number of portions that the whole hot wire voltage time series was divided to.

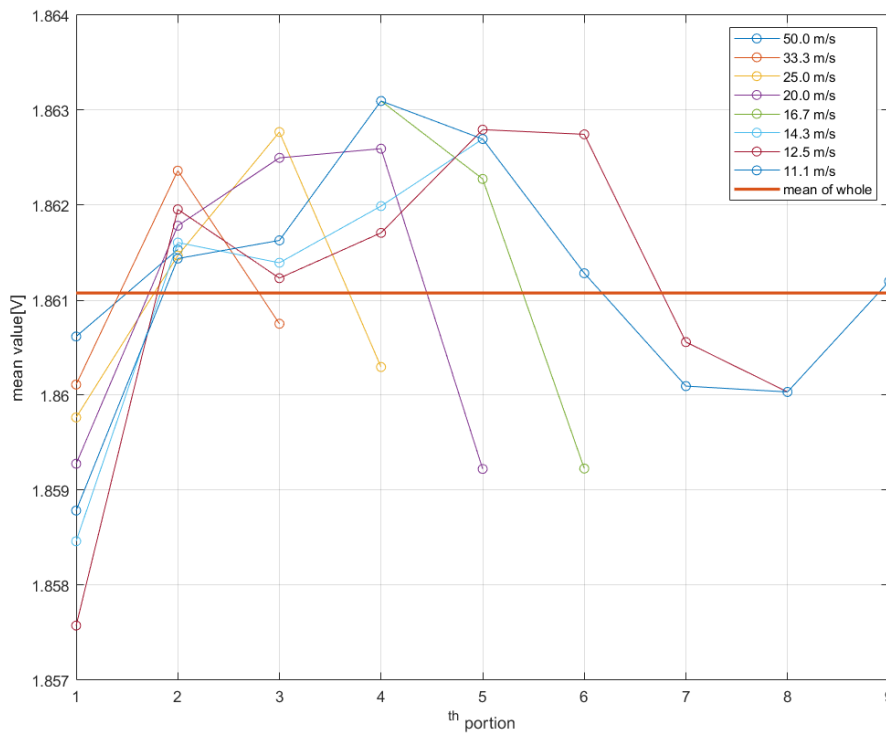


Figure 3.62: Behavior of mean values for eight different trials of sampling time. The whole hot wire voltage time series that was obtained with a 20000 Hz sampling rate for 100 seconds of sampling time, were divided into portions to see the behavior of the mean value at a corresponding sampling time. The empty circles represent the mean value of a corresponding time series portion.

To compare the performance of the mean values, there are multiple parameters to deal with. One of them was selected as the percentage range ratio whose formula was written down in equation 3.7. The figure to investigate this parameter for all sampling values (different number of portions) in a compact way is shown below.

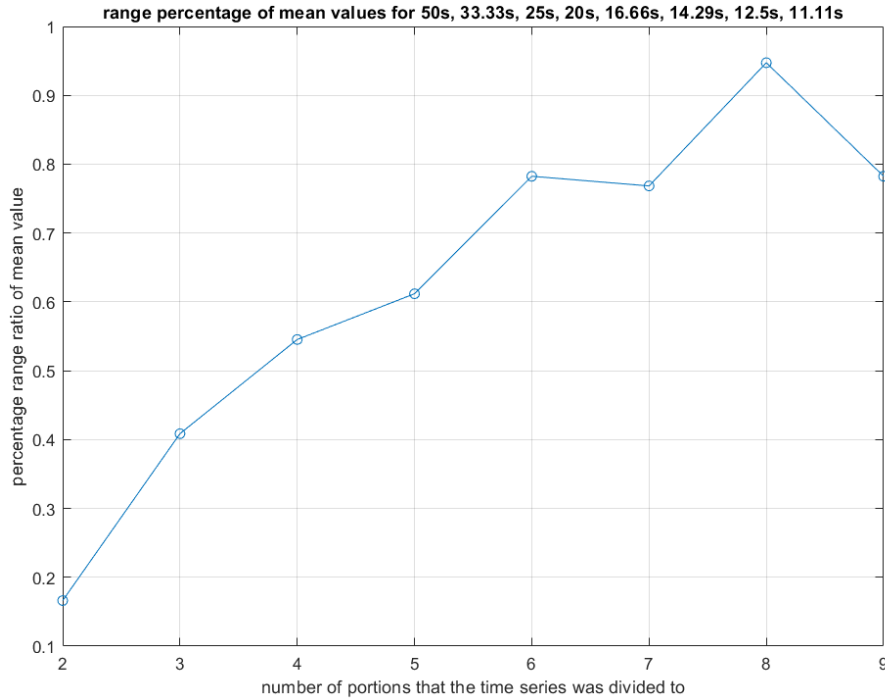


Figure 3.63: Percentage range ratios for different sampling time values that were analyzed by dividing the whole hot wire voltage time series, obtained with a 20000 Hz sampling rate for 100 seconds of sampling time, into portions. The empty circles stand for a percentage range ratio of mean values of each time series portion, implying how big the variation of mean values is with respect to the operating pressure range. Sampling time decreases as we go to the right on the horizontal axis.

As expected, there is an increasing trend in the plot of the percentage range ratio of mean values since the sampling time decreases along the positive direction on the horizontal axis. It means that the mean values become more spread as the sampling time decreases, so the result loses its reliability. Since the percentage range ratio of the mean values reaches up to 0.78 although the sampling time goes down until 11.11 seconds, we can say that 11.11 seconds of sampling time seems appropriate for this method.

Secondly, the measure of how spread the values of a series, which is called variance, was computed to compare the behavior of mean values of the portions. The formula to calculate the variance of a series was reported in equation 3.8. The following figure 3.64 stands for the variance values each corresponding to another portion's mean values.

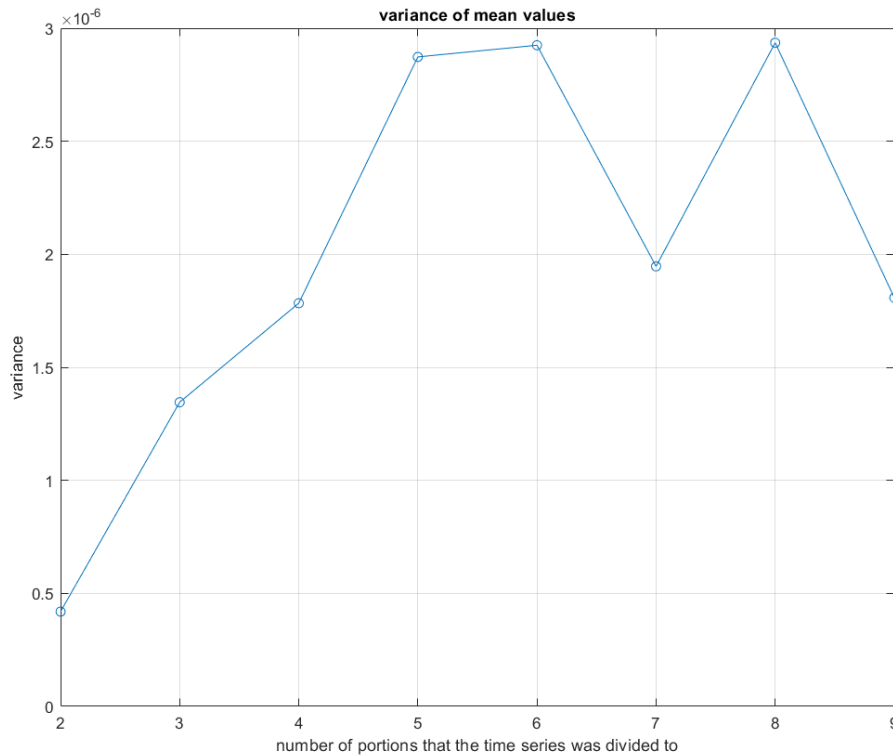


Figure 3.64: Variance of vectors formed by mean values, where each mean value corresponds to a mean of a hot wire voltage time series portion. The empty circles show the variance of mean values of corresponding portions.

One can easily comment that the increasing trend for the variance values as the sampling time decreases was completely expected. However, the maximum variance value can go up to a bit less than 2×10^{-6} even though the sampling time is reduced to 11.11 seconds. Since the range of fluctuating voltage values is 0.551, having the variance of 2×10^{-6} is completely accepted. Thus, sampling time was decided to be set as 11.11 seconds also with the variance method.

The last way chosen to check the behavior of mean values is the percentage of difference, shown in equation 3.9, between the mean values of each portion and the mean value of the whole time series signal. Since the length of each vector containing the mean values of each portion is different, the root-mean-square value of the vectors was used to analyze the cases. The formula to calculate the RMS value was written in equation 3.10. RMS of the percentage difference between the mean value of the whole hot wire voltage time series and its portions was analyzed as it is shown in figure 3.65

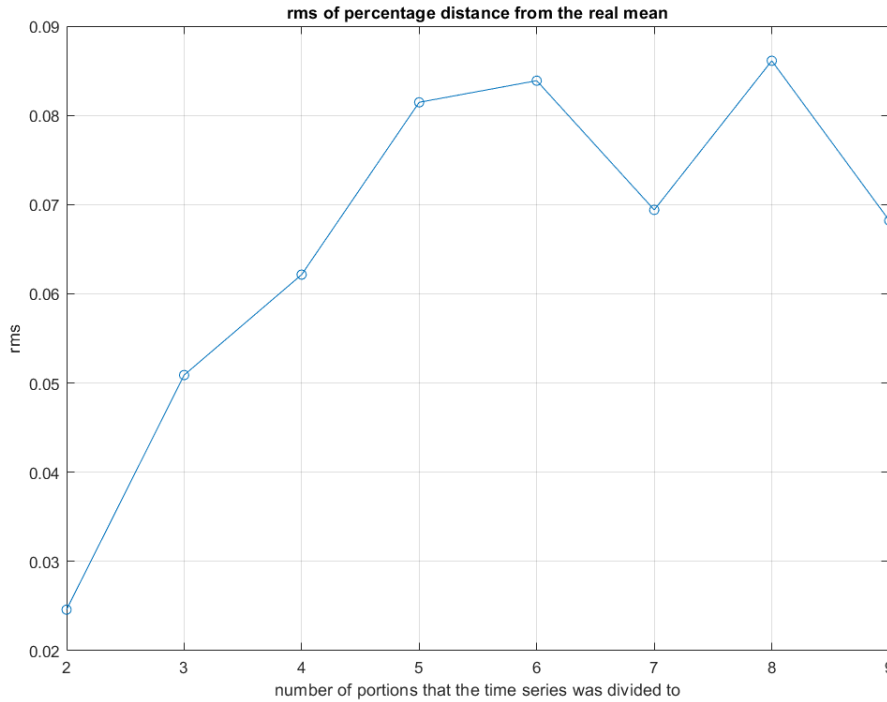


Figure 3.65: Root-mean-square of percentage difference mean value between the real and the hot wire voltage time series portions. The empty circles show an RMS % value for corresponding portions. The plot makes visible how effective is the difference between the mean values of the portions and the real mean.

From the plot, it is obvious that the behavior of the RMS values of percentage difference is genuinely similar to the behavior of variance of mean values. Thus, it can be said that the analysis is reasonable. Likely to variance values, RMS of percentage distances from the mean value can get a value of 0.068 at maximum though the sampling time is decreased to 11.11 seconds. Since this amount of percentage difference is not important for the studies, it can be said that the 11.11 seconds of sampling time is enough also from the RMS percentage difference point of view.

To sum up, the following table 3.18 lists the potential sampling time values for the hot wire acquisition selected by different methodologies.

Autocorrelation studies	17.5 s
Percentage range studies	11.11 s
Variance studies	11.11 s
Percentage difference studies	11.11 s

Table 3.18: Potential hot wire sampling time values for the NI DAQ acquisition board. The values were obtained by different methods discussed in part 3.3.2.

Therefore, not to risk the possibility of missing an important detail in velocity, the sampling time was decided as 20 seconds.

3.6.2 Hot Wire Sampling Frequency

The sampling frequency of a hot wire is one of the most important things to be decided to have a reliable set of results at the end of the experiments. The reason for that requirement is the fact that the velocity is a rapidly changing variable, resulting in the instrument that is dealing with the velocity measurement should respond as fast as possible to little quick changes in velocity. Thus, samples should be taken fast enough not to miss an important detail in velocity information.

To decide the sampling frequency, first, the maximum frequency of the signal has to be decided. Then, the sampling frequency can be determined concerning Nyquist Theorem[Colarusso et al., 1999], by taking the sampling frequency equal to or greater than two times the maximum frequency of the signal. Hence, the first thing to do is to decide the maximum frequency content of the hot wire voltage time series. To perform that, two different methods were followed to transform the voltage time series to the frequency domain, after acquiring the signal with the highest possible sampling parameters.

One of them is fast fourier transform, which requires a set of mathematical efforts represented in section 3.3.3. Thanks to the fast fourier transform, one can easily detect the maximum frequency contained inside the hot wire voltage time series by looking at the frequency versus fast fourier coefficients plot. Since the waveform of frequency versus FFT for the whole hot wire voltage signal time series is not that explanatory, the deviations from the voltage mean value were investigated. The deviation of the voltage-time series can be shown as

$$V(t) = \bar{V} + v', \quad (3.26)$$

where:

$$\begin{aligned} V(t) &= \text{instantaneous voltage signal,} \\ \bar{V} &= \text{mean voltage value,} \\ v' &= \text{fluctuating voltage value.} \end{aligned}$$

A first look to the waveform of the fluctuating voltage at exit section $Re= 8000$ at the location $\frac{x}{d} = 5$ can easily be made in following figure 3.66.

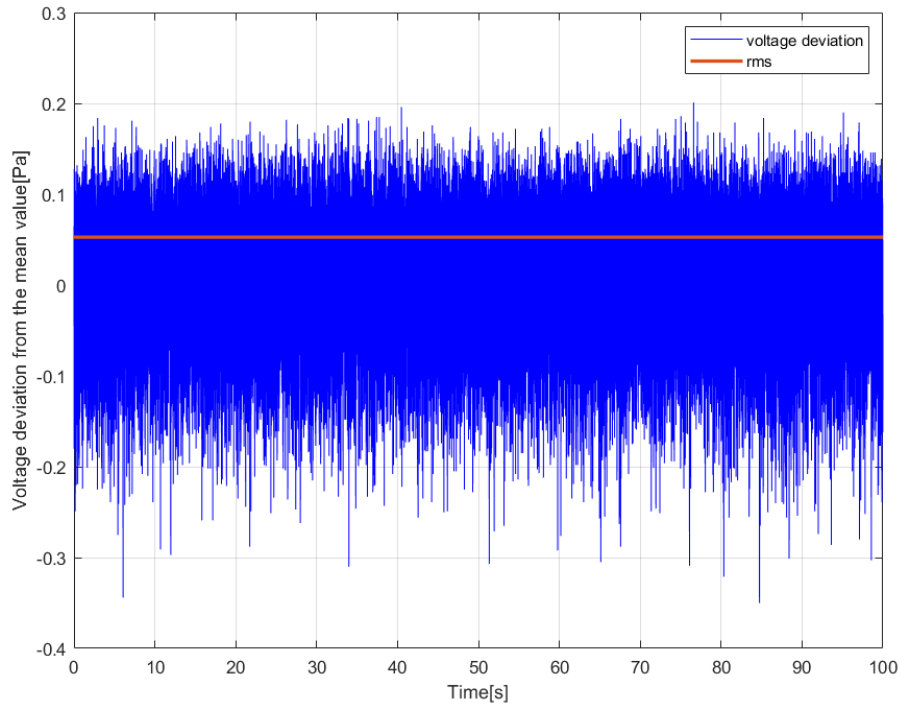


Figure 3.66: Plot of voltage deviation from the mean value at $Re= 8000$ the exit section, which is represented in blue, corresponding to each time value. Signal was obtained by NI DAQ acquisition board with 20000 Hz sampling rate for 100 seconds of sampling time. The red line shows the root-mean-square(RMS) value of the fluctuations, to be able to understand its magnitude and effectiveness. RMS value was analyzed since the mean value of the fluctuations gives 0, as expected.

After that, the fast fourier transform coefficients were plotted with respect to the frequency content of the fluctuating voltage time series as it is represented in the figure 3.67 below.

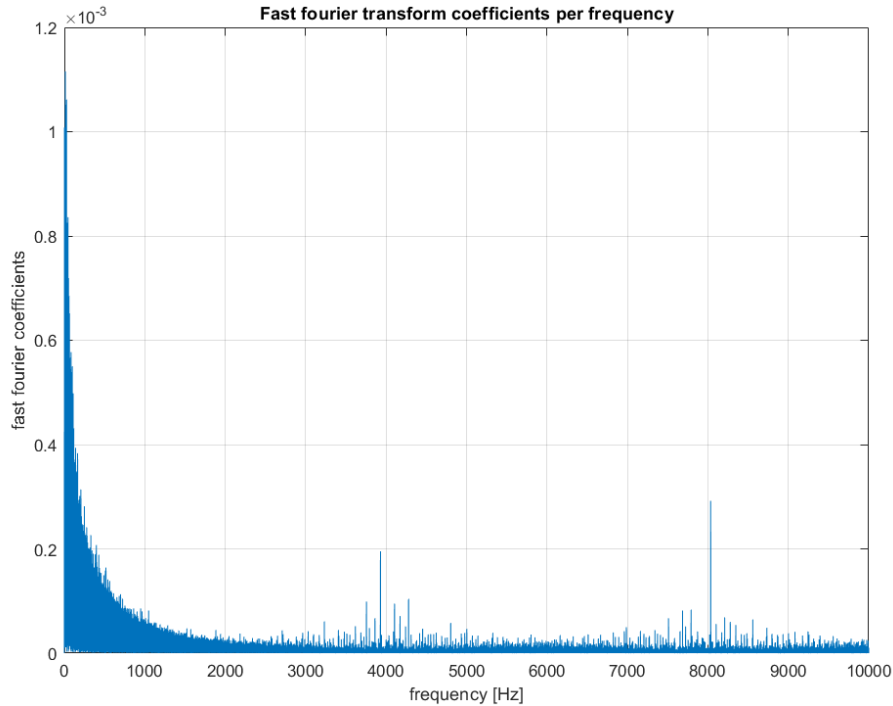


Figure 3.67: Fast fourier transform coefficients per hot wire signal frequency value that was computed with respect to the formulation discussed in section 3.3.3.

The second is power spectral density, described in section 3.3.3 and having the formula as in equation 3.11, represents the contribution of each frequency value to the power content of the time series. The reason that the PSD was preferred is that it doesn't depend on sampling time, sampling frequency, and the width of frequency bins. To make the frequency windows more visible and smooth, the number of bins was selected as

$$N_{bins} = \text{Number of samples} = f_s \times t_s = 2 \times 10^6, \quad (3.27)$$

where

$$t_s = \text{sampling time [s]}.$$

The plot of power content of the fluctuating voltage versus frequency with a sampling rate of 20 kHz can be seen in figure 3.68.

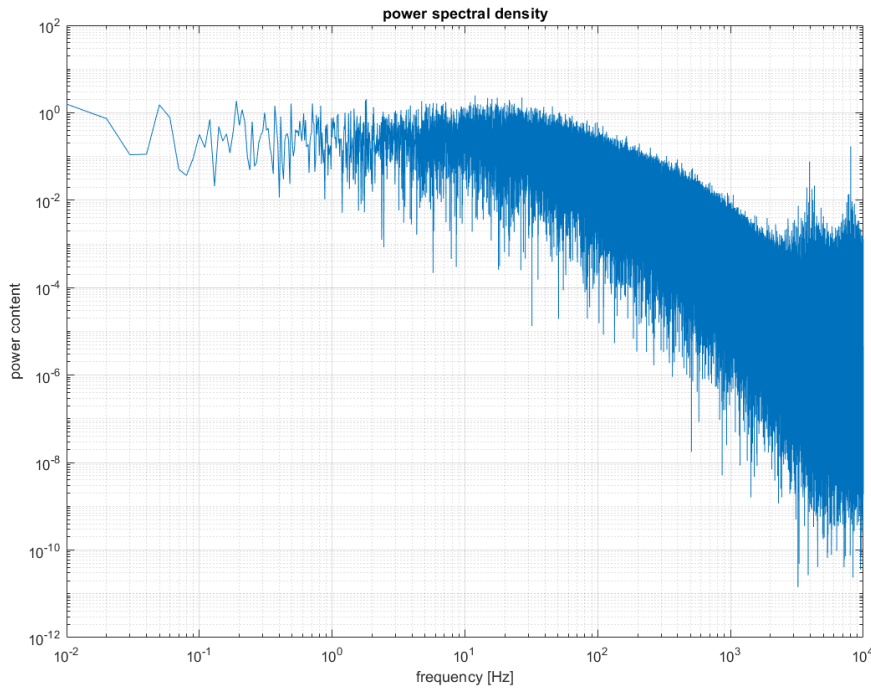


Figure 3.68: Power spectral density per hot wire signal frequency value that was computed with respect to the formulation discussed in section 3.3.3. The number of bins was selected as 2×10^6 .

In turbulent flow, the power spectra should look like a "C" shape having its highest at the lowest frequency, and its "hopefully" zero at the highest frequency content of the flow. Since the lowest frequency value corresponds to large scales and so the small scales are around the highest frequency, the ideal case of having the power zero is not usual since not all of the small scales are captured. Thus, the form that is seen in figure 3.68 is fully acceptable except for the last part which starts to oscillate after the power content stops decreasing. This part of the spectra can be treated as "noise" which is the summation of unwanted and disturbing energy from natural and sometimes man-made sources [Mishra, 2021]. Hence, without considering that part, it is obvious that the "C" shape ends at the frequency of 2 kHz, which is directly equal to

$$f_{max} = 2000Hz. \quad (3.28)$$

By applying the Nyquist Theorem and to be on the safe side, the sampling frequency for hot wire acquisition was decided as

$$f_s = 4000Hz. \quad (3.29)$$

Thus, the sampling parameters for hot wire measurement can be listed as it is in the table 3.19 below.

Sampling time [s]	20
Sampling frequency [kHz]	4

Table 3.19: Sampling parameters selected for the hot wire acquisition.

3.6.3 Single Wire Calibration

To be able to use the hot wire voltage value for velocity measurements, a certain relation between the voltage and the velocity should be created. This procedure is called calibration, which can be done in several different ways. Although the procedure is the same for all, the type of equation may differ depending on the choice of the user for the recent case.

To calibrate the hot wire, firstly it is placed inside the potential core of the jet flow, where the pitot-static tube is also placed, to be sure that the flow is not turbulent and the speed is constant. Secondly, the flow is sent and its mean velocity is measured by the pitot-static tube while the voltage acquisition from the hot wire is being performed. Having the voltage time series from the hot wire, the mean voltage is calculated and reported with the corresponding mean speed measured by the pitot-static tube. This process is repeated until the velocity range reaches the one at which the experiments will be conducted. Then, one of the methods is used to fit the curve for having an equation for velocity as a function of voltage.

To be able to calibrate the hot wire automatically, a LabView VI code was produced thanks to which any hot wire calibration can be done by just setting the desired speed values. The front panel of the VI code can be seen in figure 3.69 below.

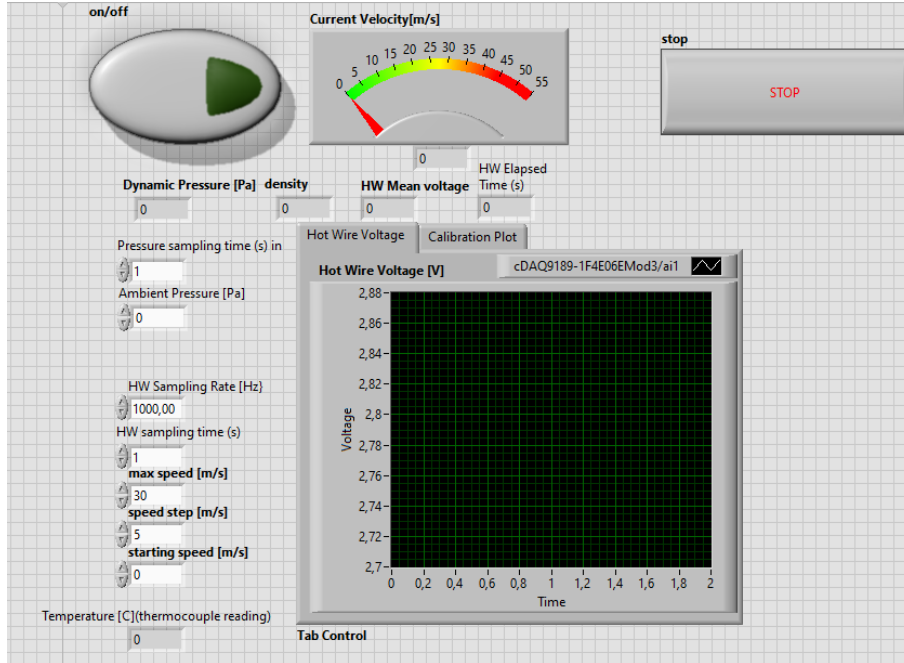


Figure 3.69: Hot wire calibration front panel in which the user can set pressure sampling time, ambient pressure, hot wire sampling rate, hot wire sampling time, maximum speed, speed step, and the starting speed. VI shows the hot wire voltage signal, calibration plot, dynamic pressure, density, hot wire mean voltage, current velocity, elapsed time for the hot wire acquisition, and temperature. The user should set on/off to true before running the VI.

To use the code shown above, the user should first set the ambient pressure [Pa], hot wire sampling time [s], hot wire sampling rate [Hz], starting speed [m/s], speed step [m/s], and the last speed [m/s] and the sampling rate for the pressure [Hz] (so for the mean velocity by pitot-static tube). After setting all the required quantities, the code is run and it basically performs the calibration by itself, plotting the curve and saving the values to a file. When the mean voltage and the last mean speed are reported, the code stops by itself.

To fit the curve obtained by plotting velocity versus voltage, one of the most common ways is 4th order polynomial curve fitting [Bruun, 1996] as represented below

$$V = C_0 + C_1E + C_2E^2 + C_3E^3 + C_4E^4, \quad (3.30)$$

where:

V = velocity [$\frac{m}{s}$],

E = voltage [V],

C_i = fitting coefficients that have to be calculated.

The other function that is widely preferred is the one that was derived from the Nusselt number, Nu by using the King's Law in section 2.1. The function can be written down as

$$E^2 = (T_w - T_a)(A + BU^n), \quad (3.31)$$

where:

- T_w = wire temperature [K],
- T_a = ambient temperature [K],
- A, B, n = constants that have to be found by fitting.

Thanks to the equation 3.31, the temperature difference is also taken into account. If the temperature of the fluid is varying a lot for the recent flow case, it is recommended to use the function reported in equation 3.31. Thus, since the temperature is varying a lot in the turbulent planar jet flow case, equation 3.31 was preferred to fit the curve.

3.6.4 Traversing System Improvement

The traversing system to be able to calibrate the x-wire that was discussed in section 3.1.2 had some missing parts before these studies. Firstly, to be capable of rotating the traversing system, a small part to fix its one end in the cross-stream direction was designed as it is shown in figure 3.70. Thanks to the part, the system is not squeezed in the z direction, so able to rotate freely.

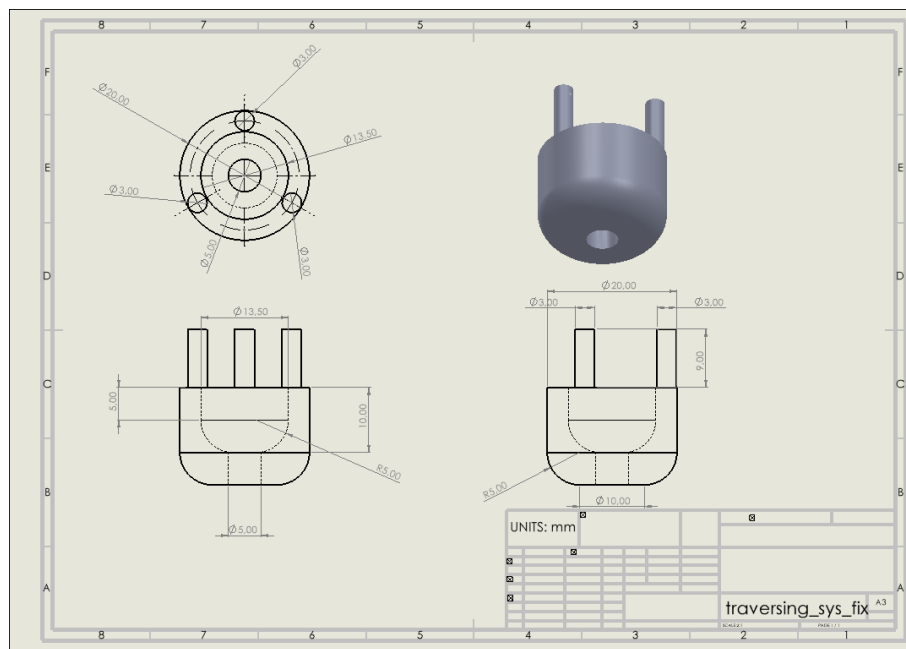


Figure 3.70: Engineering drawing of the part designed to fix one end of the traversing system. All the units are in mm.

Secondly, to achieve single and/or multiple x-wire measurements at the same time for performing two-point correlations in the jet flow, a wire holder was designed that can be seen in figure 3.71. The wire holder was designed in a way that allows the wire to be exactly at the center of rotation of the traversing system, to have the same angle as the indicator. Moreover, it can easily be moved in the z direction by sliding on the traversing system.

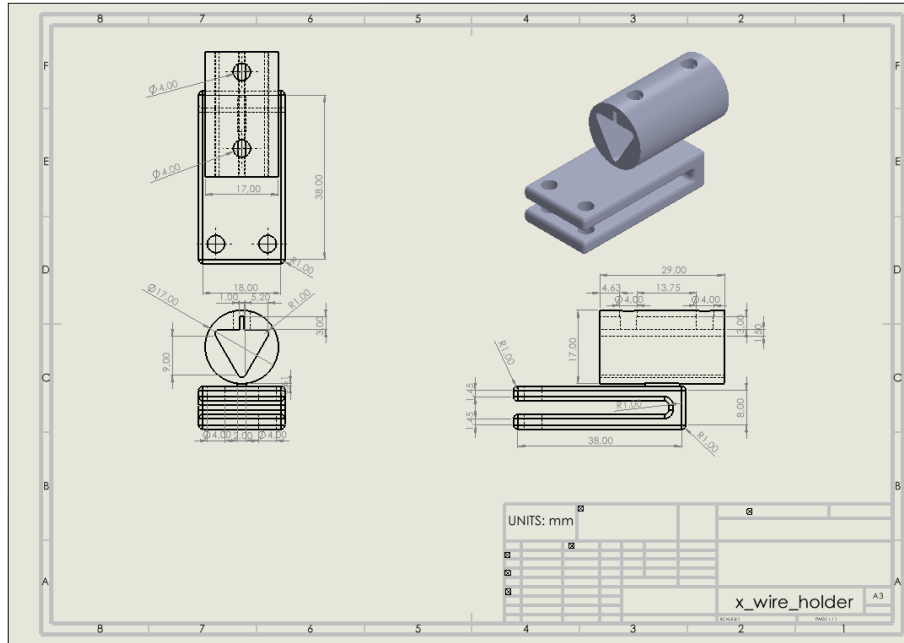


Figure 3.71: Engineering drawing of the part designed to hold the x-wire during the calibration. All the units are in mm.

After drawing the parts in the SolidWorks environment, a 3D printer was used for the production. Figure 3.72 represents the first part which is to fix one end of the traversing system while the x wire holder is shown in figure 3.73.



Figure 3.72: The product of the 3D printing process to fix one end of the traversing system for the calibration process. The part helps to fix the one end of the traversing system on the y-axis to ensure the rotation given by the stepper motor. Three legs of the part are plugged into the traversing system after drilling the holes. The material of the part is plastic.



Figure 3.73: Printed product of the x-wire holder design for the calibration process. X-wire probe is plugged in inside the holder to demonstrate the usage. X-wire is supposed to be plugged in on the right end of the probe shown in the picture. The upper two holes can be used to fix the wire probe to ensure that its location will not change during the experiments. The material of the part is plastic.

3.6.5 X-wire Calibration

Likely to single hot wire measurements, x-wire also requires a direct calibration to relate the velocity to the voltage values coming from two wires separately. After having the function for calibration, exactly the same operations that were done for the single wire have to be performed to estimate the fluctuating velocity time series, now in both streamwise and crosswise directions as it was discussed in section 3.6.7.

The highly critical point in x-wire calibration is the placement of the probes. It should be placed in a way that the two wires have 45° with the dominant flow direction. For that purpose, the x-wire stem is marked by points to be sure that the right orientation is achieved. Dots should point in the spanwise direction to have the proper orientation for the x-wires. The picture below shows the reference dots put on the x-wire stem to help the user for setting the orientation.

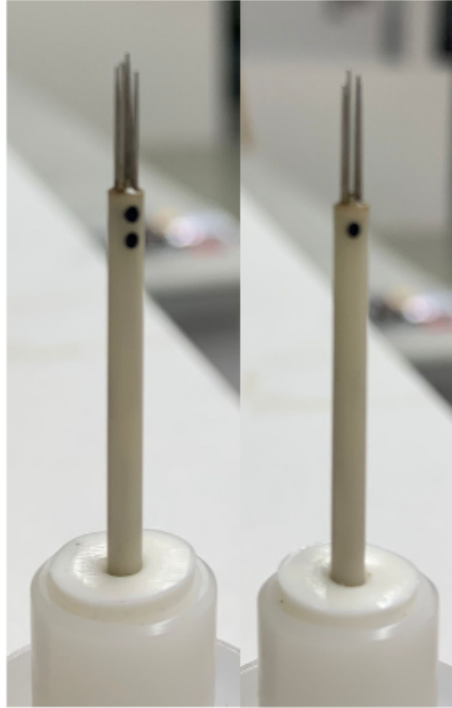


Figure 3.74: X-wire picture including the wires, probes, stem, and the dots on the stem to give a reference to the user for the proper orientation.

To calibrate the x-wire, it should be placed in a traversing system as it is shown in section 3.1.2. The x-wire should be exactly at the center of rotation of the traversing system to have the angle set by the stepper motor equal to the one for the wire. Moreover, the location of the x-wire should be inside the potential core of the planar jet flow for all the speed values that the calibration is performed. The potential core was preferred to have the speed constant and not be disturbed by the turbulence.

After placing the x-wire correctly, a range of speed and angle is chosen. The selections should be made wisely to include all the speed and angle values that the wire will face during the experiments. Two voltage values coming from two separate wires were reported for all the speed and angle values. To guarantee that the speed doesn't vary for an angle, the calibration was done by keeping the speed constant and changing the angle. Thus, the first speed value was set at the exit section, then the voltage values from two wires were acquired for different angles, and then this process was repeated for all the speed values.

To achieve a fully automatic x-wire calibration, a VI was created. The user should use the front panel, which is visible in figure 3.75, to give the desired inputs for the calibration, and then starts the process. The VI reports mean voltage values from

CHAPTER 3. EXPERIMENTAL SETUP

two wires for different angle values at different velocities and then saves it into a file that is determined by the user.

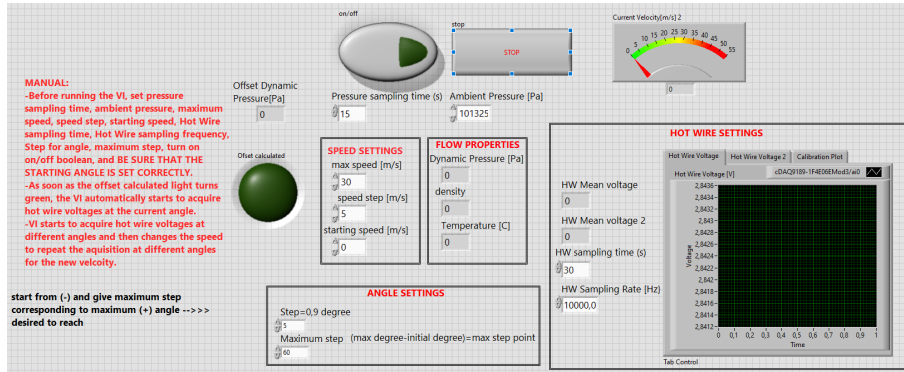


Figure 3.75: X-wire calibration front panel in which the user can set pressure sampling time, ambient pressure, hot wire sampling rate, hot wire sampling time, maximum speed, speed step, the starting speed, angle step and the maximum step corresponding to the maximum angle desired to be reached. VI shows the two hot wire voltage signals, calibration plot, dynamic pressure, density, temperature, the two hot wire mean voltage values and the current velocity. The user should set on/off to true before running the VI.

The selections for the angle and the speed values were made as they are listed in the following tables 3.20 and 3.21.

Speed values $\left[\frac{m}{s}\right]$
0
5.393
7.649
8.782
12.172
16.188
19.432
22.781
26.012

Table 3.20: Speed values chosen for the x-wire calibration.

Minimum angle value	-22.5°
Maximum angle value	22.5°
Angle step	4.5°

Table 3.21: Angle values are chosen for the x-wire calibration.

After performing the acquisition and reporting the mean voltage values for all data points in terms of velocity and angle, a look-up table was obtained, which can be seen in figure 4.15.

The aim is to have the velocity and the angle as the function of two voltage values, to be able to estimate the angle and the velocity as soon as the voltages are acquired during the experiment. To achieve that, firstly the velocity was divided into its components as

$$U = \vec{V} \cos(\theta), \tag{3.32}$$

$$V = \vec{V} \sin(\theta), \tag{3.33}$$

where:

- \vec{V} = mean velocity [$\frac{m}{s}$],
- U = mean velocity in streamwise direction [$\frac{m}{s}$],
- V = mean velocity in crosswise direction [$\frac{m}{s}$],
- θ = flow angle [$^\circ$].

After obtaining two different plots as E1 vs E2 vs U and E1 vs E2 vs V as represented in figures 4.16 and 4.17 respectively, the last step is to interpolate the data points to be able to estimate the streamwise and crosswise velocities, U and V, for arbitrary voltage values, E1 and E2, that were acquired during the experiment. To succeed in this, 2D interpolation was performed by using a MatLab command "interp2". Thanks to that, the U and V velocity time series were attained as soon as the voltage time series, E1, and E2, were acquired.

3.6.6 Single Wire Experiments

After having the velocity as a function of voltage, the voltage signal of the hot wires at any arbitrary location can easily be converted into a velocity signal, which includes the mean and the fluctuating velocity information.

To be able to perform the hot wire experiment inside the wake of the turbulent planar jet, a VI was created. The VI, that can be seen in the figure 3.76, is capable of conducting hot wire experiments fully automatically, by just getting the inputs for the step in streamwise and crosswise directions from the user.

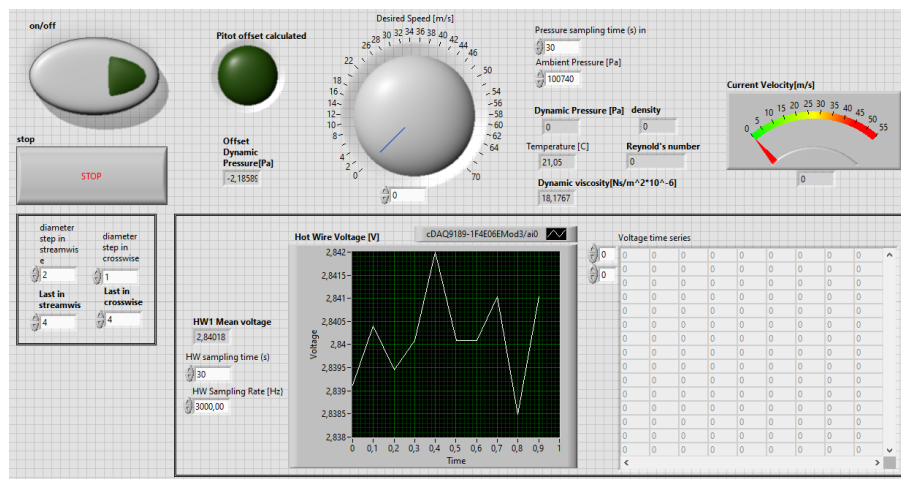


Figure 3.76: Hot wire experiment front panel in which the user can set the desired speed at the exit section, diameter step, and the last location in both stepwise and crosswise direction, hot wire sampling time and rate, pressure sampling time, and ambient pressure. VI is capable of informing the user if the offset is calculated, offset dynamic pressure, dynamic pressure, temperature, dynamic viscosity, density, Reynolds number, hot wire mean voltage, hot wire voltage signal, and the time series. The user should set on/off to true before running the VI.

The VI starts from the recent crosswise diameter and acquires the hot wire voltage at all the crosswise diameters until it reaches the maximum location specified by the user. After that, it passes to the next streamwise diameter and repeats the same process until it completes all the locations. Saving the time series to a file, the voltage values become ready to be processed easily.

By performing the methods that were discussed by writing the equation 2.64 and displayed with the figure 2.7, the fluctuations in the velocity can easily be computed by taking the difference between the whole velocity time series and their mean value.

Measurements have to be repeated at several locations along the directions where the characteristic properties of the turbulent planar jet flow are being looked for. Since the single hot wire is usually not preferred for velocity measurements in multiple directions, only one component of the properties can be achieved with the single hot wire.

3.6.7 X-wire Experiments

An x-wire, also known as cross-wire, allows the user to accomplish two-component velocity measurements depending on its orientation. The most important advantage of an x-wire is the fact that it provides two-component velocity measurements simultaneously. Two different voltage values coming from two separate wires are acquired and related to the known velocity.

As it was discussed before, the orientation of the x-wire is highly significant not only in calibration but also during the experiments. The x-wire must be placed as it was done during the experiments, in a way that the 45° angle between two wires and the dominant flow direction is provided.

To perform the x-wire experiments after the calibration, the sliding system had to be used to move the x-wire to the desired location. However, since no tool was suitable for the x-wire probe setup placement in the sliding system, an x-wire holder was designed by using the SolidWorks environment. The shape and the dimensions of the x-wire holder can be seen in figure 3.77.

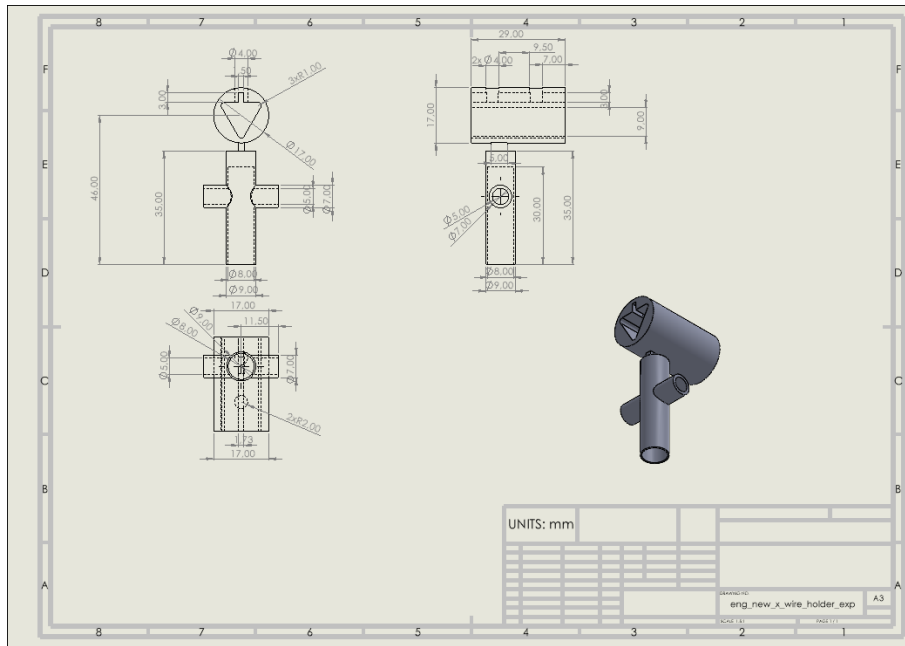


Figure 3.77: Engineering drawing of the part designed to mount the x-wire on the sliding system for the experiments. All the units are in mm.

For the x-wire experiments with the sliding system to move the x-wire in stream-wise and crosswise directions, a fully automatic VI code was created to be able to perform the acquisition at the desired points in the wake and save the data without setting the location and the speed manually. The user interface of the VI code is illustrated in figure 3.78.

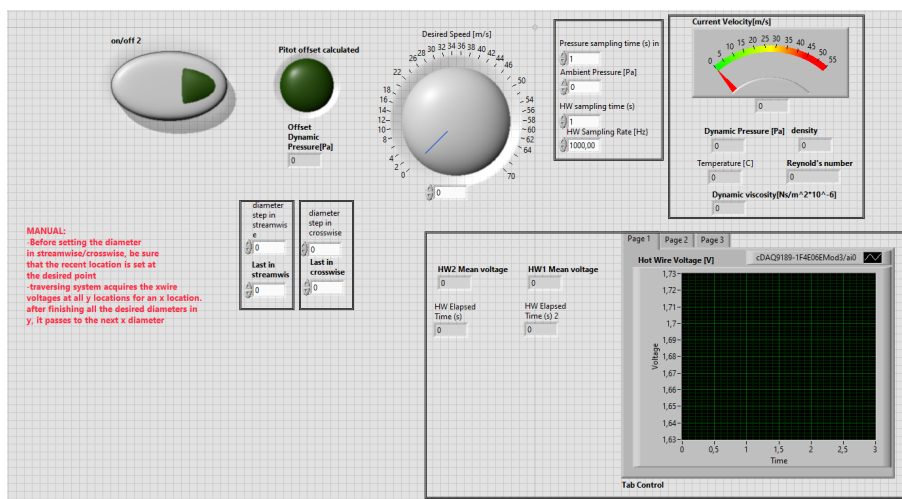


Figure 3.78: VI code for fully automatic x-wire experiments with the help of the sliding system. The user should first provide the inputs for the diameter step in the streamwise direction, diameter step in the crosswise direction, last diameter location in both directions, pressure sampling time, ambient pressure, hot wire sampling time, and the hot wire sampling rate before running the code. Measured quantities are the voltages from two wires, temperature, and dynamic pressure. The VI starts to acquire once the offset is calculated.

The code first computes the offset dynamic pressure for the pitot-static tube, then starts to acquire the x-wire voltages at the recent streamwise location after a step of indicated diameters in the crosswise direction. It acquires the voltages at all the crosswise locations, goes back to the starting crosswise location, and then passes to the next streamwise diameter location, and it repeats the same process until the last streamwise diameter is reached. After reporting the data at each point, it saves them into a file determined by the user in the block diagram.

Thanks to the calibration process, velocity in the x and y directions can easily be determined by knowing the voltage values, E1 and E2, at an arbitrary point in the wake. Thus, mean velocity profiles, fluctuating velocity profiles, turbulence intensity structure, etc. can easily be generated.

The parameters studied thanks to the x-wire experiments in turbulent planar jet flow were discussed in the next section 3.6.8.

3.6.8 Planar Jet Flow Analysis

Although the aim was not to characterize the turbulent planar jet flow, some crucial parameters were looked for to see the behavior of the flow and to ensure that the designed system is working well.

Fundamental analyses were decided on the mean and the fluctuating velocity profiles of the turbulent planar jet flow. Thanks to the hot wire anemometry, they were acquired and plotted in several different orientations to provide better visibility. Thanks to the velocity information lots of significant parameters could easily be decided.

The first parameter that was investigated is Reynolds Stress, which was shown in equation 2.65. In reality, since the turbulence is a 3D phenomenon and this results in velocity fluctuations in all three dimensions, there are six different Reynolds Stress components although the matrix contained by the Reynolds Stresses has nine elements as shown below

$$R_{ij} = \begin{bmatrix} R_{ii} & R_{ij} & R_{ik} \\ R_{ji} & R_{jj} & R_{jk} \\ R_{ki} & R_{kj} & R_{kk} \end{bmatrix} \quad (3.34)$$

where

$$R_{ij} = R_{ji}. \quad (3.35)$$

Thus, the six components are consisted of R_{xx} , R_{yy} and R_{zz} as the normal stresses, and R_{xy} , R_{xz} , R_{yz} as the shear stresses.

Since the fluctuations in the z-axis were neglected because the turbulent planar jet is homogeneous in the z direction, there are four Reynolds Stress components left to deal with.

Moreover, the so-called "jet half-width" was calculated at different streamwise locations to be able to estimate the spreading rate of the turbulent planar jet flow. The half-width is the distance from the jet centerline to the upper or lower viscous super layer discussed in section 1.1.

Furthermore, centerline velocity decay was observed to understand the behavior of the mean velocity at the jet centerline.

Lastly, to estimate where the turbulent planar jet becomes self-similar in the streamwise direction, the ratio between the mean streamwise velocity and the centerline velocity was plotted at different streamwise locations.

4

Results

4.1 Inverter Communication

In the end, the user can easily power on/off the inverter by just using a single front panel button as is represented in the figure 4.1.

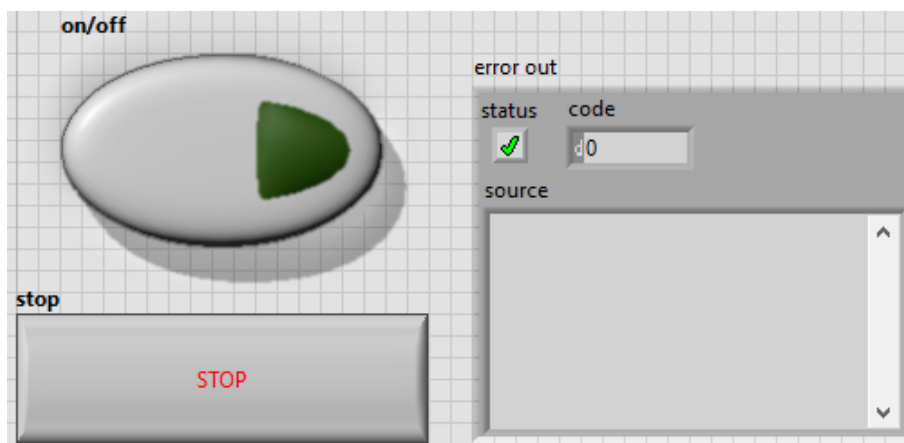


Figure 4.1: On/off command front panel where the user should use the boolean switch to power on/off the inverter. The error box on the right is there in case of any unknown error appears. If the user wants to halt the loop, it is enough to click "STOP".

The following figure 4.2 shows the user interface of the VI code, the so-called front panel.

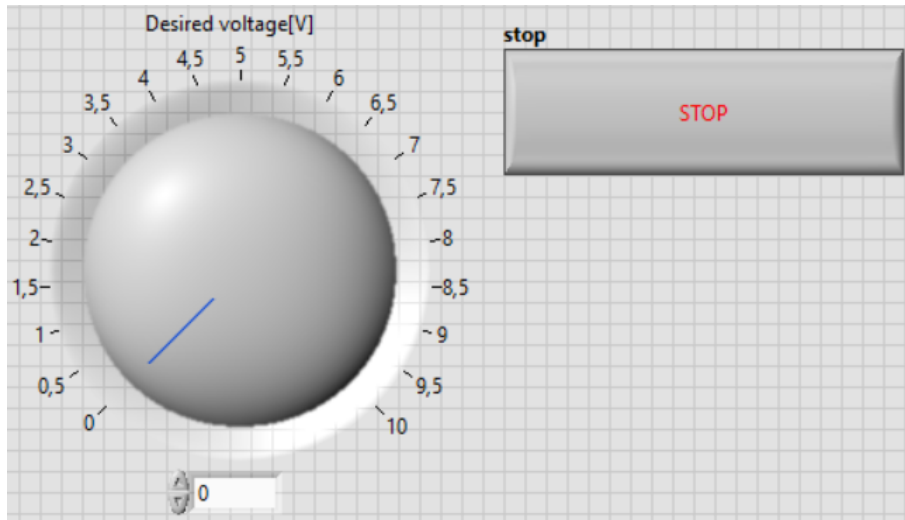


Figure 4.2: Inverter speed control front panel. The user sets the voltage either by the knob or by the digital numeric input below the knob, from the computer to control the speed of the inverter. The maximum voltage of 10V corresponds to a speed around $51 \frac{m}{s}$ at the exit section. The "STOP" button is to stop the loop.

4.2 Pressure Behavior Along the Tunnel

The behavior of the pressure from the pre-settling chamber to just before the contraction ratio was plotted as in the figure 4.3

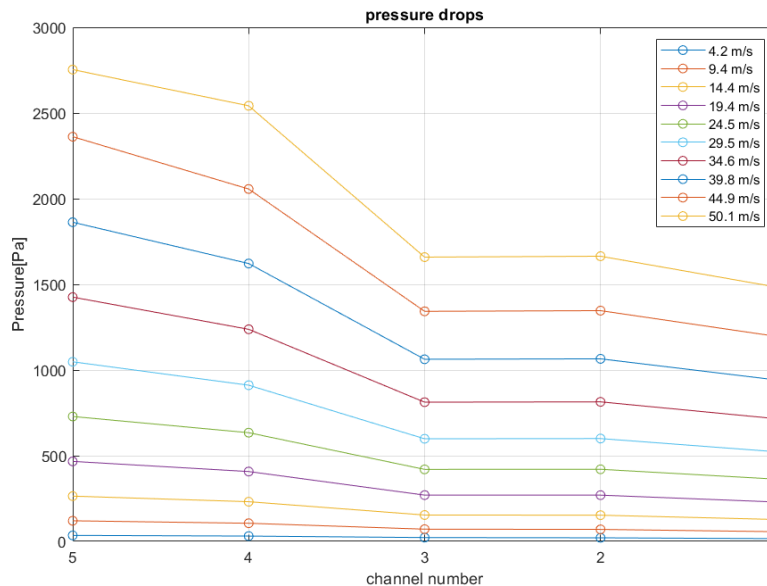


Figure 4.3: Pressure drop along PAT. Each color stands for an exit velocity and each empty circle shows the pressure value at the corresponding channel located at different locations along the plane air tunnel, reported in table 3.5. The data were obtained from DSA 3217 pressure scanner.

Moreover, the change in pressure at different locations for different speeds at the exit section can be seen more clearly in the figure 4.4 below

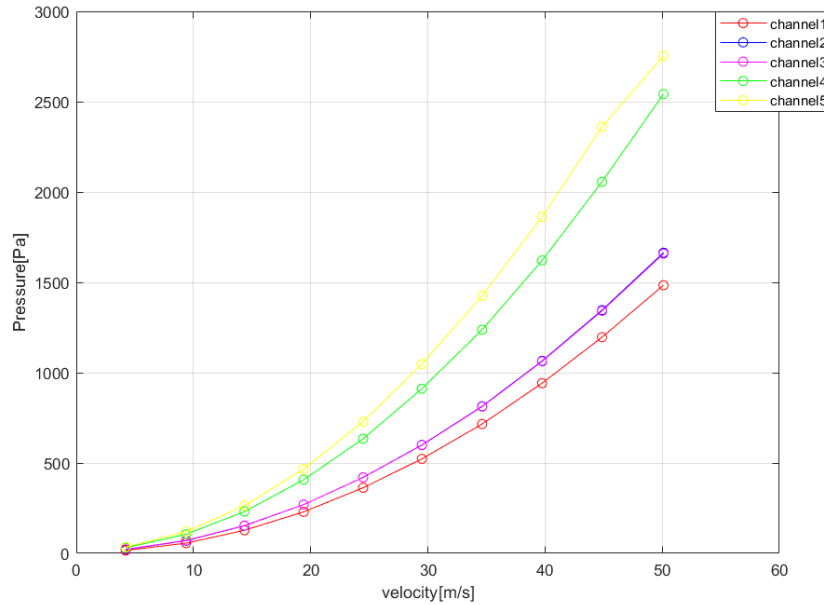


Figure 4.4: The behavior of pressure at each channel placed at different locations along the plane air tunnel, reported in table 3.5, with respect to changing exit velocity. Each color corresponds to a channel while each empty circle shows the pressure value for a specific speed value at the exit section.

As expected, the highest pressure occurs at the 5th channel, which corresponds to the pre-settling chamber, since the effect of friction is not present as intense as the next wind tunnel components. As soon as the flow conditioner wind tunnel elements are reached, friction plays a significant role and so the total pressure starts to decrease.

The pressure drop, calculated as the difference in pressure values between the 5th and 1st, pre-settling chamber and just before contraction ratio, alters if the flow speed changes. The behavior of the pressure drop related to the flow velocity is visualized in figure 4.5 below.

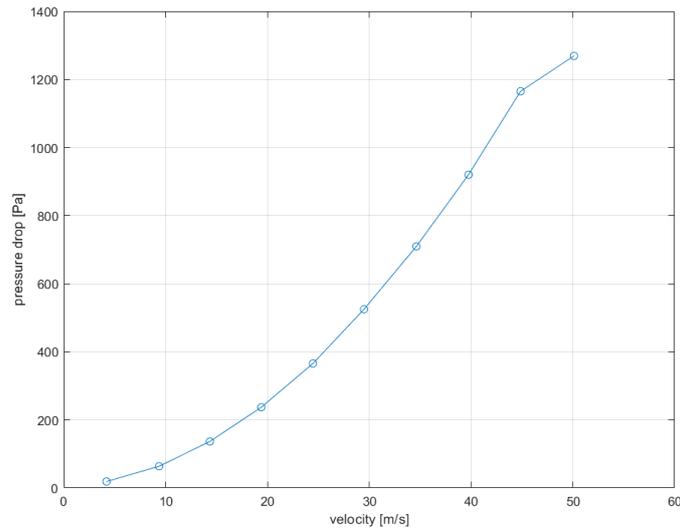


Figure 4.5: The behavior of pressure drop with respect to changing exit velocity. Pressure drop was calculated as the pressure difference between the 5th and 1st channels, where the numbers standing for the pressure tapping locations were reported in table 3.5. Each empty circle shows the pressure drop value for a specific speed value at the exit section.

As can simply be noticed from the figure above, the pressure difference between the pre-settling chamber and the point just before the contraction ratio increases as the speed at the exit section increases. This behavior can be related to the losses due to the friction caused by the wind tunnel elements, and the fact that the flow tends to become turbulent as the speed increases.

Since the friction effects are not felt in the pre-settling chamber the pressure continues to grow as the speed raises. On the other hand, since the effect of friction becomes more powerful if the speed is higher, the increase in pressure cannot be as high as it is in the pre-settling chamber. Thus, the pressure drop behavior that is seen in figure 4.5 happens accordingly.

Moreover, as well as the static pressure at the first channel, corresponding to the section just before the contraction part, dynamic pressure at the exit section was also acquired thanks to the pitot tube, by using the scanivalve multichannel pressure scanner. An interesting result of the similarity between those two pressure values can be seen in the figure 4.6 below.

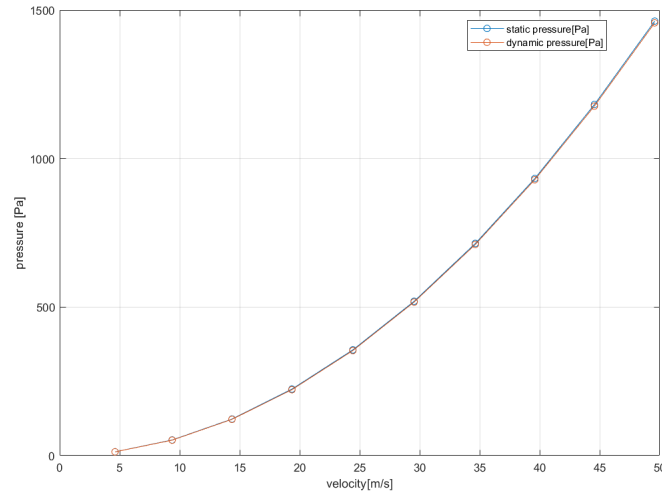


Figure 4.6: Plot of static pressure just before the contraction section and the dynamic pressure at the exit section at different exit section velocities. Each empty circle corresponds to a data point.

Moreover, the percentage difference between the two pressure values was calculated as

$$\text{difference}\% = \frac{|P_{dynamic} - P_{static}|}{\max(P_{dynamic}, P_{static})}. \quad (4.1)$$

where:

$$P_{dynamic} = \text{dynamic pressure [Pa]},$$

$$P_{static} = \text{static pressure [Pa]}.$$

By performing the equation above, the difference between the static pressure at the settling chamber and the dynamic pressure at the exit section was calculated at different speeds and plotted as can be seen in the figure 4.7.

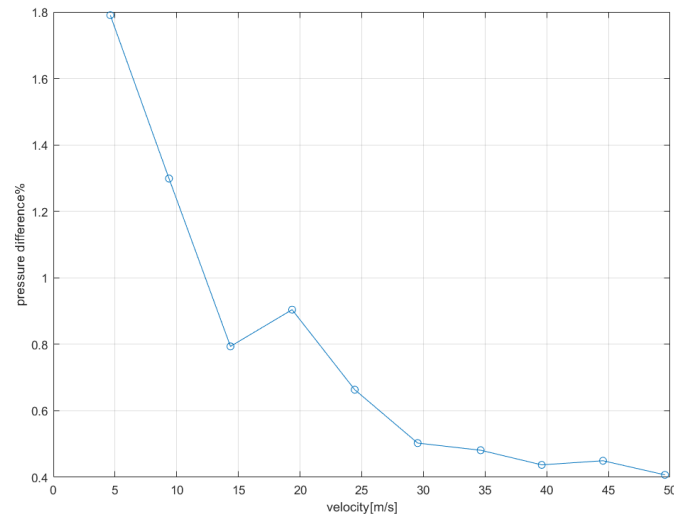


Figure 4.7: Plot of difference between static pressure at the settling chamber and the dynamic pressure at the exit section at different exit section velocities. Each empty circle corresponds to a data point.

It was made visible that the difference between the two pressures is genuinely small and it even becomes smaller as the speed increases.

4.3 Velocity Measurements

Velocity measurements were achieved both with the pitot-static tube and without the pitot-static tube thanks to the pressure tappings, to see the difference between the two and to get rid of the pitot-static tube in case it is needed. Moreover, the PI control that was discussed before was designed for both cases, whose results can be seen in the next section.

4.3.1 PI Control

Now, not only power on/off control, but also desired speed value setting at the exit of the PAT can easily be done by the user.

With a Pitot-Static Tube

The following figure 4.8 shows the user program interface of the system that is using a pitot-static tube at the exit section to measure the velocity.

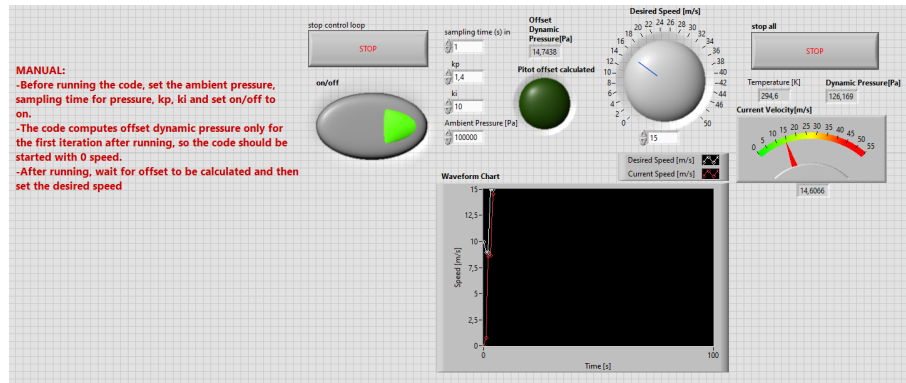


Figure 4.8: PI controller front panel using a pitot-static tube. The user has to set the ambient pressure, velocity offset, and sampling time before running the code. The sampling frequency was taken as 100 Hz which is not required to be entered every time. Moreover, the user also has to set proportional gain and integral gain, which means the behavior of the response can be controlled by the user.

As was mentioned before, the offset value in pressure was first measured and then it was subtracted from the real values to have the speed values at the exit section more accurate.

Moreover, the response of the PI controller is plotted in the front panel, which is shown below in figure 4.9 to analyze the behavior in a more detailed way.

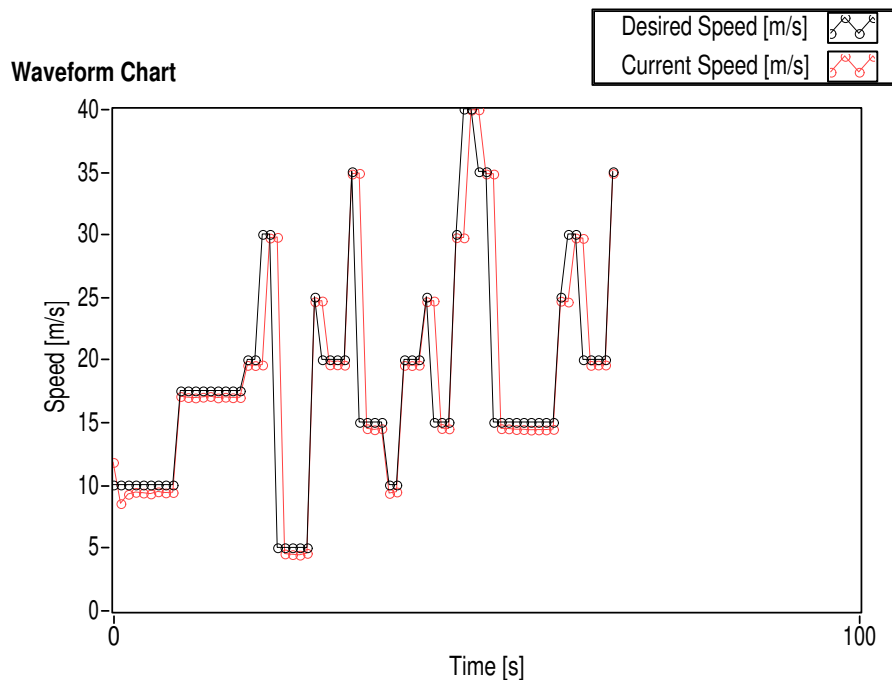


Figure 4.9: Response plot of the PI controller that was created with a pitot-static tube. The vertical axis represents the speed $\left[\frac{m}{s}\right]$ at the exit section while the horizontal one stands for the time $[s]$. Circles are data points where the speed was measured and reported. Moreover, the black line shows the behavior of the desired speed $\left[\frac{m}{s}\right]$ set by the user, on the other hand, the red line corresponds to the current speed $\left[\frac{m}{s}\right]$ measured at the exit section after the user sets the desired speed.

As it is obvious in the figure 4.9, the response of the PI controller is robust for the speeds that are higher than $20 \frac{m}{s}$. However, its performance decreases as the desired speed decreases since the high range, 10 Torr, the transducer was preferred for the pressure acquisition. Thus, to be able to become more precise at lower speeds, it is suggested to use the lower range, 2 Torr, transducer. The comparison of the resolutions of the two different range transducers is given in the table 4.1 below

Range [Torr]	Resolution [Pa]
2	0.0027
10	0.013

Table 4.1: Comparison of resolutions of two different range MKS transducers, which were calculated by using equation 3.2.

Without a Pitot-Static Tube

The speed control at the exit section without using a pitot-static tube to measure the speed at the exit section was achieved using the pressure tappings along the streamwise direction of the plane air tunnel. Following figure 4.10 represents the VI code user interface to set the desired speed at the exit section

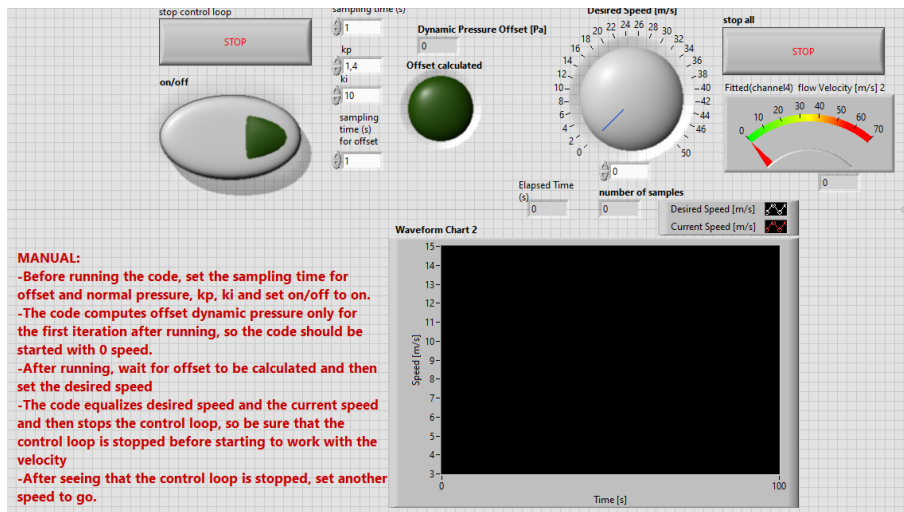


Figure 4.10: PI controller front panel without using a pitot-static tube. The user has to set the ambient pressure, velocity offset, and sampling time before running the code. Moreover, the user also has to set proportional gain and integral gain, which means the behavior of the response can be controlled by the user.

To set the sampling rate of the pressure acquisition by DSA 3217 pressure scanner, the user should follow the steps reported in 3.3.3.

As it can directly be understood from the front panel, first the offset pressure was measured to be more accurate with respect to the real value. Then, this value is subtracted from the pressure values at a nonzero speed at the exit section.

In figure 4.11 below, the response of the speed controller with the pressure tappings for velocity measurement can be seen.

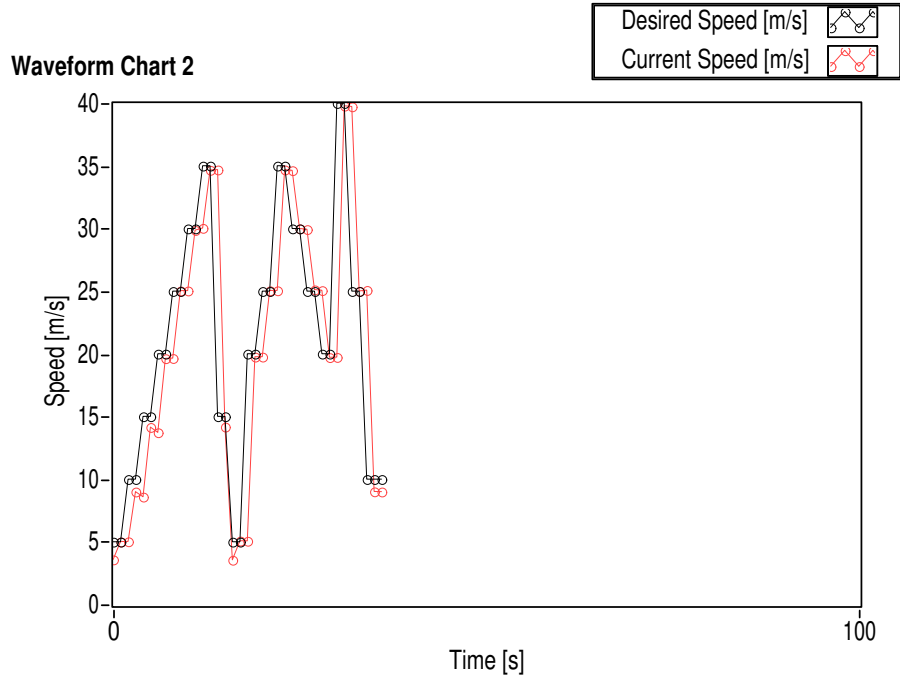


Figure 4.11: Response plot of the PI controller that was created without a pitot-static tube. The vertical axis represents the speed [$\frac{m}{s}$] at the exit section while the horizontal one stands for the time[s]. Circles are data points where the speed was measured and reported. Moreover, the black line shows the behavior of the desired speed [$\frac{m}{s}$] set by the user, on the other hand, the red line corresponds to the current speed [$\frac{m}{s}$] measured at the exit section after the user sets the desired speed.

By looking at the plot above, it is easy to say that the behavior of the controller is much more accurate at speed values higher than 20 [$\frac{m}{s}$]. One of the reasons for this kind of behavior is the resolution of the pressure scanner used to convert the change in sensor status to a signal. Since the resolution of the pressure scanner is 0.04 Pa, it can create some accuracy problems in some situations.

Another reason is the error caused by the interpolation function created to relate the pitot velocity to the pressure values at tappings in section 3.5.3. However, since the steady-state error is still below 10%, it can be said that the automatic speed control system without the pitot-static tube can be used.

4.4 Hot Wire Experiments

Thanks to the automatic calibration and experiment VI codes designed in the LabView environment, the hot wire experiments were conducted with respect to the sampling parameters decided in sections 3.6.1 and 3.6.2. However, experiments were advanced by increasing the sampling parameters to ensure that enough information is reached. Sampling parameters used during both single wire and the x-wire experiments are reported in the following table 4.2

Sampling time [s]	40
Sampling frequency [kHz]	10

Table 4.2: Sampling parameters preferred during the hot wire experiments.

Single Wire Calibration

The following figure 4.12 shows the curve obtained for the hot wire calibration thanks to the VI.

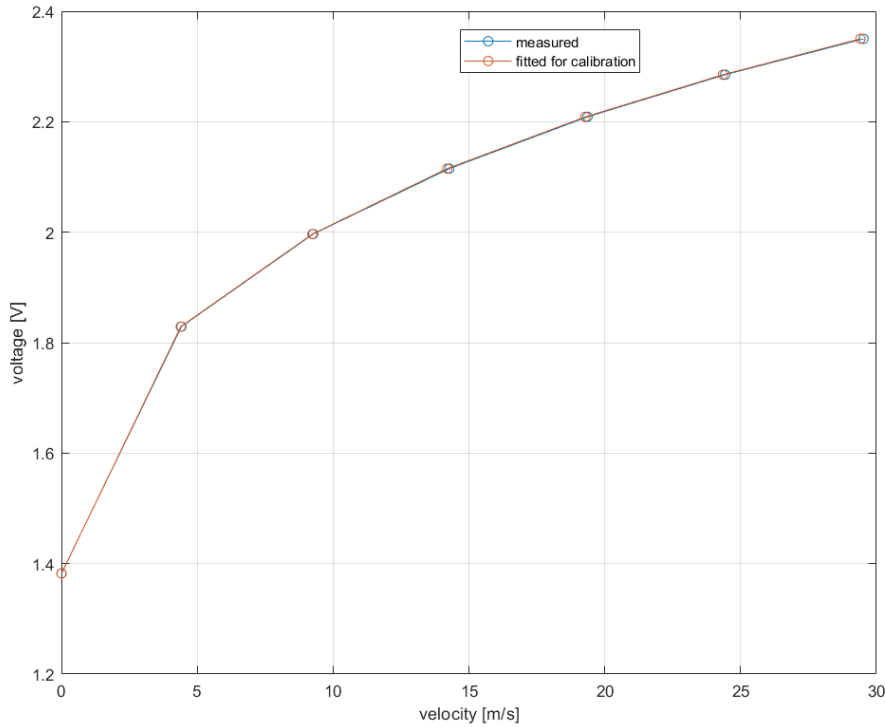


Figure 4.12: Hot wire calibration curve obtained at the exit section of plane air tunnel. Each empty circle corresponds to a data point.

The curve was fitted by using equation 3.31, and the calibration equation can be written as

$$E^2 = (T_w - T_f)(0.008522 + 0.003126U^{0.4808}). \quad (4.2)$$

where:

E = voltage[V],

$T_w - T_f$ = vector composed of the temperature difference between the wire and the flow[C°].

Thanks to the fact that there is a direct relationship between the voltage and the velocity, velocity can be written as a function of voltage and the temperature difference.

$$U = \left\{ \left[\left(\frac{E^2}{T_w - T_f} \right) - 0.008522 \right] \frac{1}{0.003126} \right\}^{\frac{1}{0.4808}}. \quad (4.3)$$

Then, the velocity can easily be computed for any arbitrary voltage and temperature difference value at any location.

For example, behavior of the velocity at $\frac{x}{d} = 10$ having $Re=8000$ at the exit section can be seen in below figure 4.13

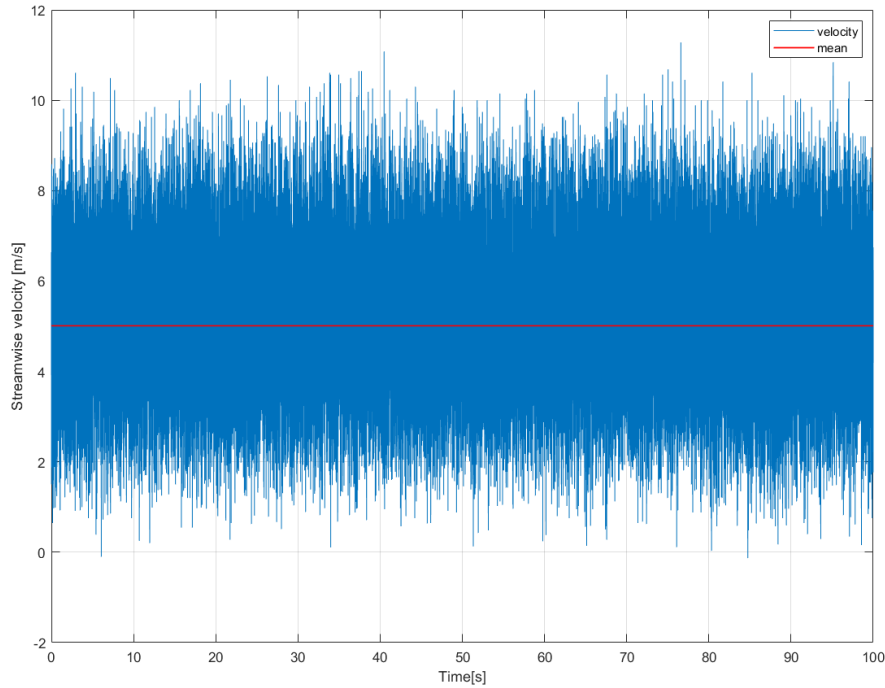


Figure 4.13: Velocity behavior of the planar jet flow at $\frac{x}{d} = 10$, $\frac{y}{d} = 0$ and with exit section Reynolds number, $Re=8000$. The plot was obtained thanks to the hot wire voltage signal and the calibration function relating the velocity to the voltage. The acquisition was performed for 100 seconds at a sampling rate of 20 kHz.

By performing the velocity decomposition, fluctuating velocity behavior can be computed as mentioned before. The plot seen in figure 4.14 represents the behavior of fluctuating velocity at $\frac{x}{d} = 10$ with $Re=8000$.

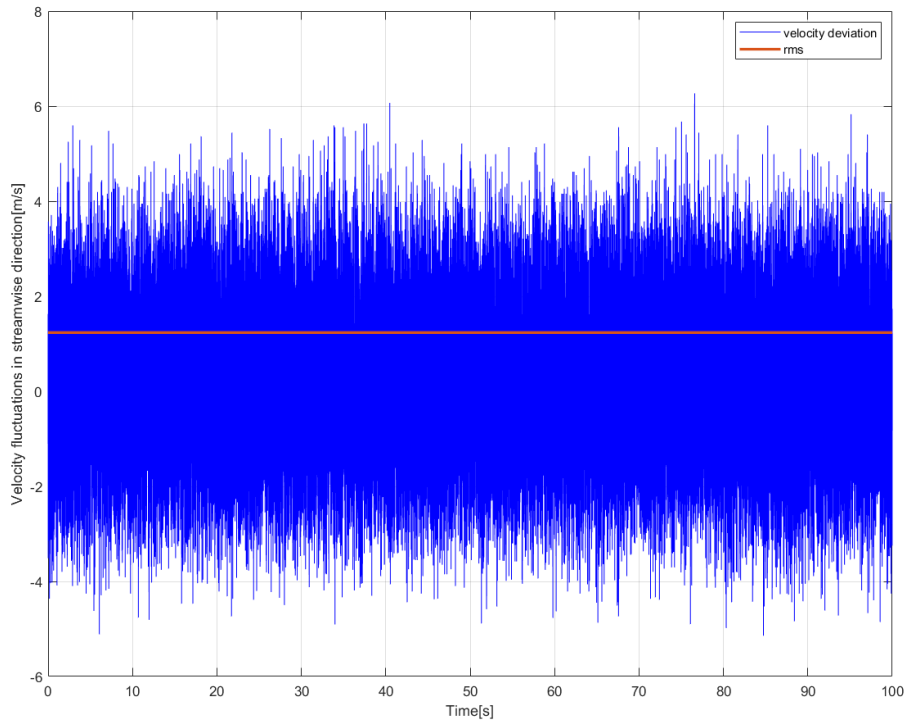


Figure 4.14: Fluctuating velocity behavior of the planar jet flow at $\frac{x}{d} = 10$, $\frac{y}{d} = 0$ and with exit section Reynolds number, $Re=8000$. The plot was obtained thanks to the hot wire voltage signal and the calibration function relating the velocity to the voltage and the formula represented in equation 2.64. The acquisition was performed for 100 seconds at a sampling rate of 20 kHz.

X-wire Calibration

The look-up table, which was procured by reporting the voltage data at different angles for different speeds, can be seen in the figure 4.15 below.

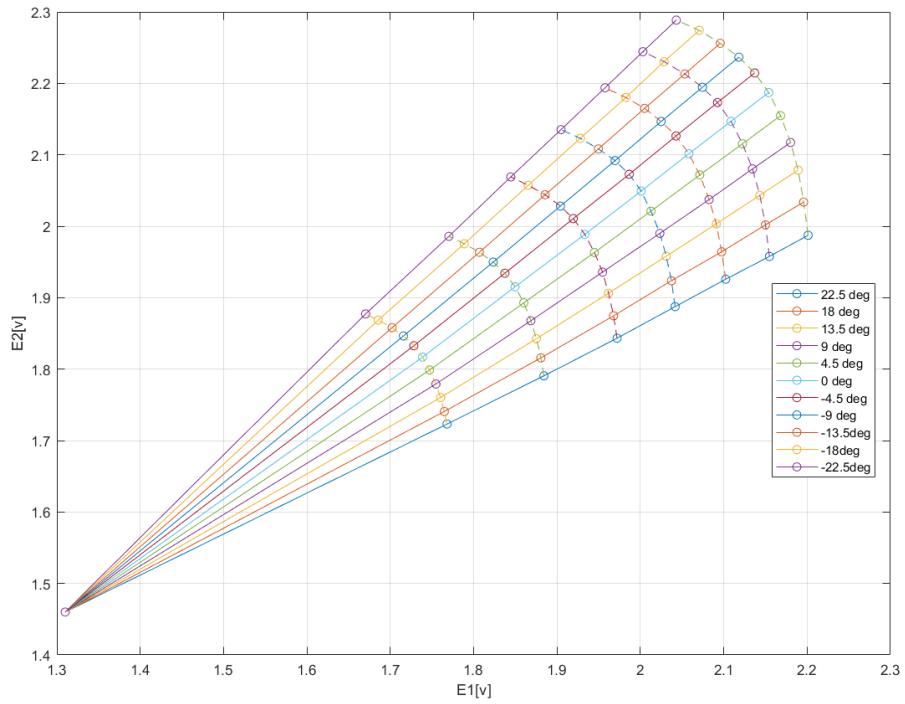


Figure 4.15: Look-up table obtained by reporting the mean voltage values of two wires at the corresponding velocity and the angle values. E1 is the mean voltage value of wire 1 while the mean voltage of wire 2 is denoted as E2.

Then, since the mean velocity, \vec{V} and the angle, θ are known, voltage values E1 and E2 can be plotted with respect to U and V separately as can be seen in figures 4.16 and 4.17.

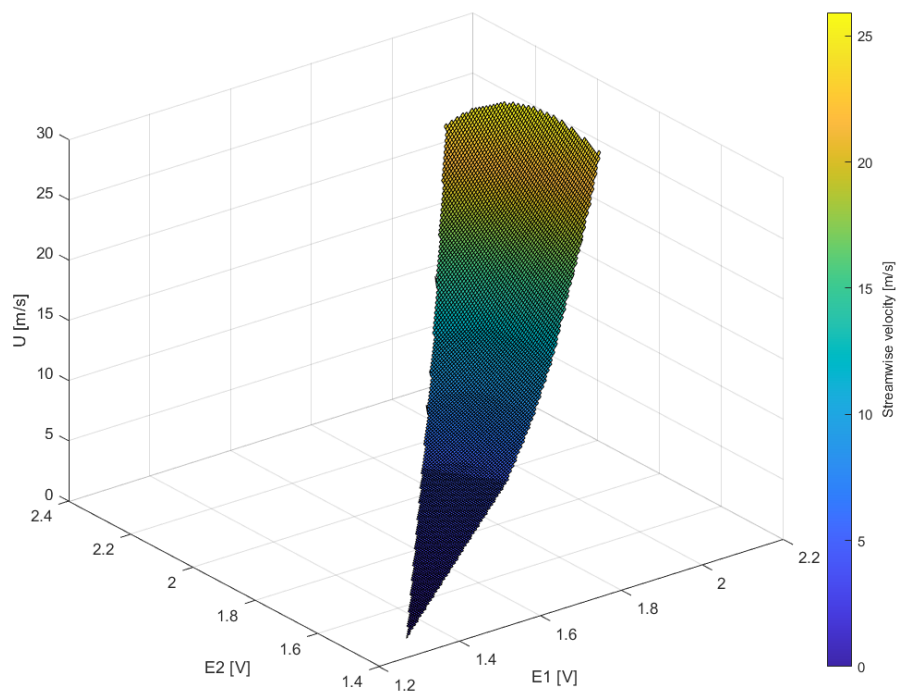


Figure 4.16: The surface formed by the data points at which the voltage values from the calibration correspond to a streamwise velocity calculated by the equation 3.32. The grid was created with 1001 points.

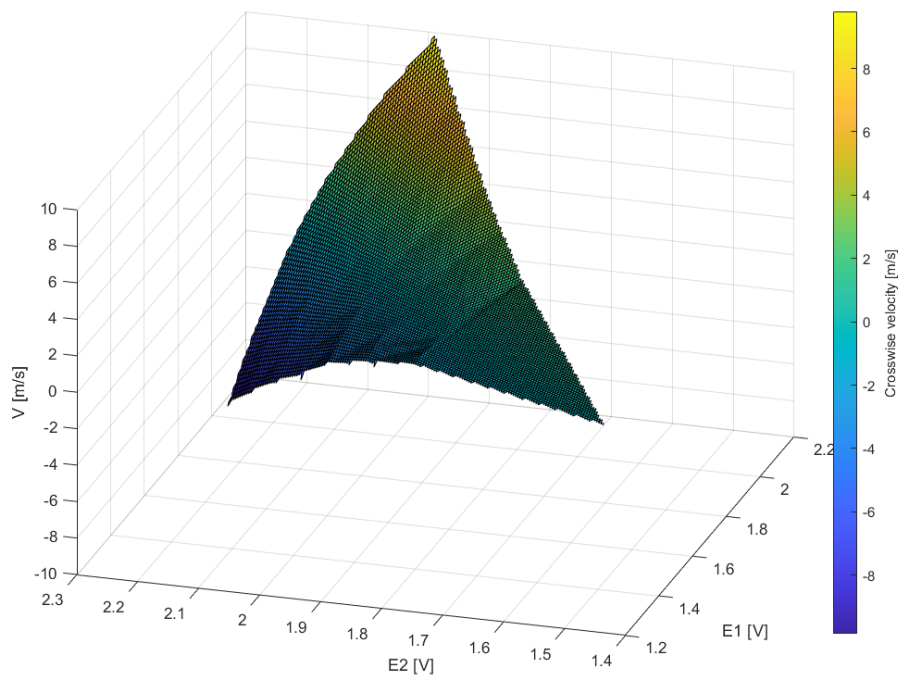


Figure 4.17: Surface formed by the data points at which the voltage values from the calibration correspond to a crosswise velocity calculated by the equation 3.32. The grid was created with 1001 points.

Surfaces were created by using a grid consisting of 1001 points. By interpolating the plots as discussed in section 3.6.5, any arbitrary velocity information can easily be reached.

4.4.1 Mean Velocity Profile

The mean velocity profiles in both streamwise and crosswise directions determined by using hot wire anemometry, thanks to both the single wire and the x-wire. Since the single hot wire was used only for the streamwise velocity profile, the comparison for the mean and fluctuating velocity profiles obtained by the single hot wire and the x-wire was performed. The acquisition for a wire was performed for 40 s having a sampling rate of 10 kHz.

The distance in both streamwise and crosswise directions was normalized by dividing the distance values by the exit section height, denoted by "d". The first velocity acquisition was obtained at the streamwise location $x/d=1.5$, and the measurements continued by performing experiments at $x/d=3$, $x/d=4.5$, $x/d=6$, $x/d=8$, $x/d=10$, and $x/d=15$, $x/d=20$, respectively.

To accomplish a proper grid for the measurements at each streamwise location, a preparatory experiment was performed. The grid points at each streamwise location can be listed as

x/d	y/d
1.5	2.50, 1.25, 1, 0.75, 0.65, 0.50, 0.45, 0.35, 0.25, 0, -0.25, -0.35, -0.45, -0.55, -0.65, -0.75, -1, -1.25, -2.50
3	3, 1.50 1.25, 1, 0.85, 0.75, 0.60, 0.50, 0.25, 0.10, 0, -0.10, -0.25, -0.50, -0.60, -0.75, -0.85, -1, -1.25, -1.50, -3
4.5	3.75, 2.75, 2.25, 1.75, 1.50, 1.25, 1.1, 0.95, 0.80, 0.65, 0.50, 0.35, 0.20, 0, -0.20, -0.35, -0.50, -0.65, -0.80, -0.95, -1.1, -1.25,, -1.50, -1.75, -2.25, -2.75, -3.75
6	4, 3.25, 2.75, 2.25, 2, 1.75, 1.50, 1.25, 1, 0.75, 0.50, 0.25, 0, -0.25, -0.50, -0.75, -1, -1.25, -1.50, -1.75, -2, -2.25, -2.75, -3.25, -4
8	4.75, 3.50, 2.50, 2.25, 2, 1.75, 1.50, 1.25, 1, 0.75, 0.50, 0.25, 0, -0.25, -0.50, -0.75, -1, -1.25, -1.50, -1.75, -2, -2.25, -2.50, -3.50, -4.75
10	5, 3.50, 3, 2.50, 2.25, 2, 1.75, 1.50, 1.25, 1, 0.75, 0.50, 0.25, 0, -0.25, -0.50, -0.75, -1, -1.25, -1.50, -1.75, -2, -2.25, -2.50, -3, -3.5, -5
15	6, 4.50, 4, 3.50, 3, 2.50, 2.25, 2, 1.75, 1.50, 1.25, 1, 0.75, 0.50, 0.25, 0, -0.25, -0.50, -0.75, -1, -1.25, -1.50, -1.75, -2, -2.25, -2.50, -3, -3.50, -4, -4.50, -6
20	8.5, 7, 5.5, 4.5, 3.75, 3.25, 3, 2.75, 2.50, 2.25, 2, 1.75, 1.50, 1.25, 1, 0.75, 0.50, 0.25, 0, -0.25, -0.50, -0.75, -1, -1.25, -1.50, -1.75, -2, -2.25, -2.50, -2.75, -3, -3.25, -3.75, -4.5, -5.5, -7, -8.5

Table 4.3: Points at which the hot wire measurements were performed. x/d is the normalized distance in streamwise directions and the y/d is the normalized distance in the crosswise direction.

Streamwise Mean Velocity Profile

To be able to compare the velocity profiles, the first thing to do was to perform the single hot wire measurements in the wake of turbulent planar jet flow. The following figure 4.18 shows the mean streamwise velocity profiles at different locations, which were all obtained by performing single hot wire measurements at the positions listed above.

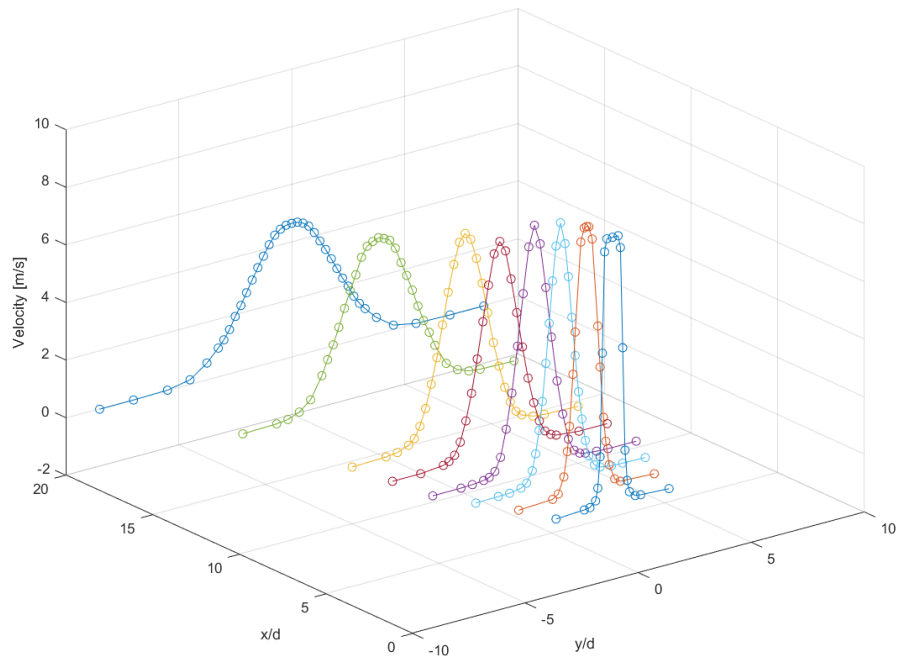


Figure 4.18: 3D plot of mean streamwise velocity profiles measured at different streamwise locations with single hot wire at exit Reynolds number $Re=12235.8$. Each empty circle corresponds to a data point. Dimensions both crosswise and streamwise are normalized with the exit section length, which is represented by "d". The acquisition for a wire was performed for 40 s having a sampling rate of 10 kHz.

As one can easily understand, each color corresponds to a different streamwise location.

Secondly, figure 4.19 represents the fluctuating velocity profiles in different streamwise directions, which were obtained by the single hot wire.

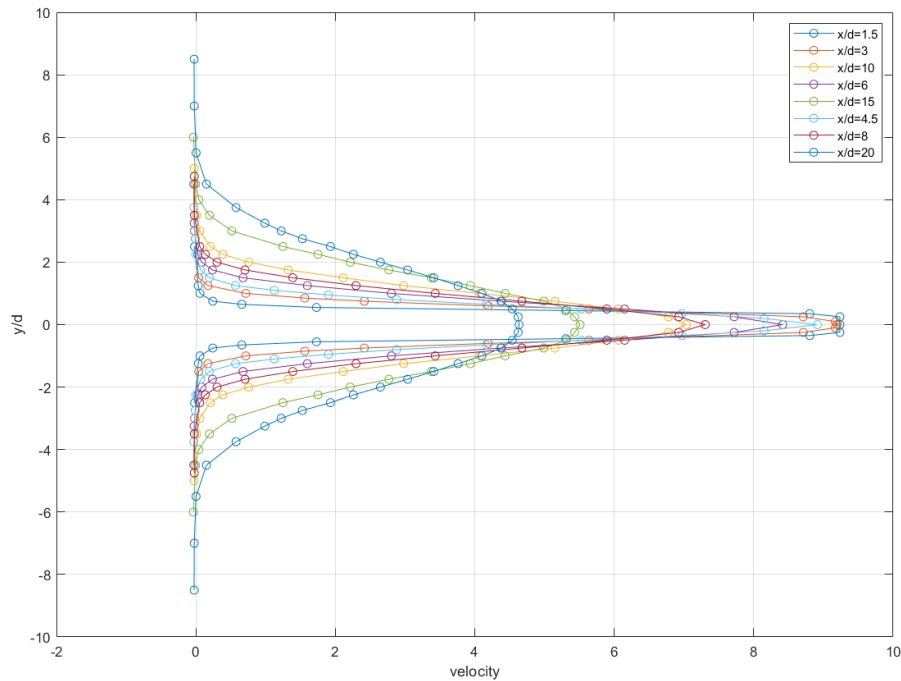


Figure 4.19: 2D plot of mean streamwise velocity profiles measured at different streamwise locations with single hot wire at exit Reynolds number $Re=12235.8$. Each empty circle corresponds to a data point. Dimensions both crosswise and streamwise are normalized with the exit section length, which is represented by "d". The acquisition for a wire was performed for 40 s having a sampling rate of 10 kHz.

Thanks to plotting every velocity profile to visualize them together from one aspect, it is easy to see the difference between each other.

After performing the calibration of the x-wire as discussed in section 3.6.5, the voltage-time series were acquired at the grid points shown above and the mean streamwise velocity profiles were created to compare the results with the ones from the single hot wire. The plots obtained can be seen in the following figures 4.20 and 4.21.

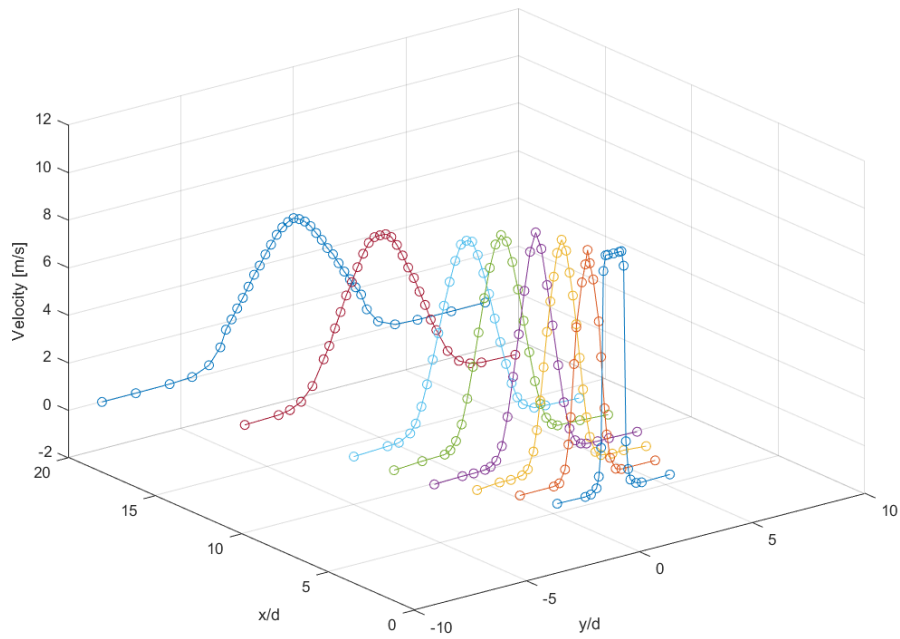


Figure 4.20: 3D plot of mean streamwise velocity profiles measured at different streamwise locations with x-wire at exit Reynolds number $Re=11506.6$. Each empty circle corresponds to a data point. Dimensions both crosswise and streamwise are normalized with the exit section length, which is represented by "d". The acquisition for a wire was performed for 40 s having a sampling rate of 10 kHz.

The 3D figure above represents the mean streamwise velocity profiles where each color corresponds to another acquisition point in the streamwise direction, denoted by x/d .

To visualize the streamwise velocity profile in the streamwise direction, they were plotted in the same plane as follows.

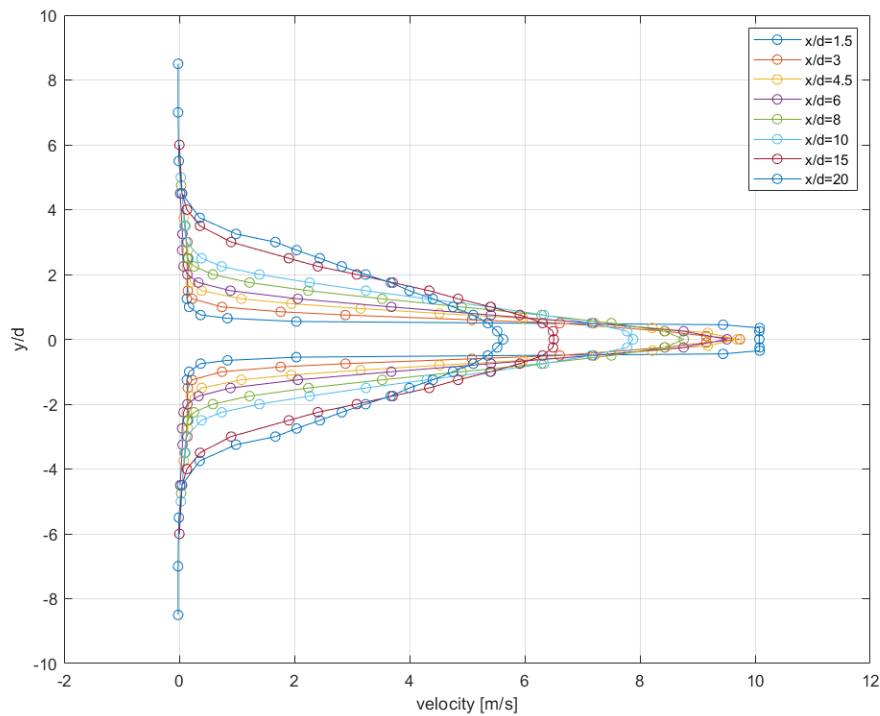


Figure 4.21: 2D plot of mean streamwise velocity profiles measured at different streamwise locations with x-wire at exit Reynolds number $Re=11506.6$. Each empty circle corresponds to a data point. Dimensions both crosswise and streamwise are normalized with the exit section length, which is represented by "d". The acquisition for a wire was performed for 40 s having a sampling rate of 10 kHz.

The behavior of the turbulent planar jet flow velocity in the streamwise direction can easily be observed by just looking at the plot above.

The comparison between the velocity profiles acquired by the single hot wire and the x-wire can easily be done by analyzing the figures 4.18, 4.19, 4.20 and 4.21 above.

Crosswise Mean Velocity Profile

To see the structure of the flow not only in the streamwise direction but also in the crosswise direction, the following figure 4.22 was plotted thanks to the x-wire experiments. Due to the lack of equipment performance, the acquisition was performed only in five different streamwise locations.

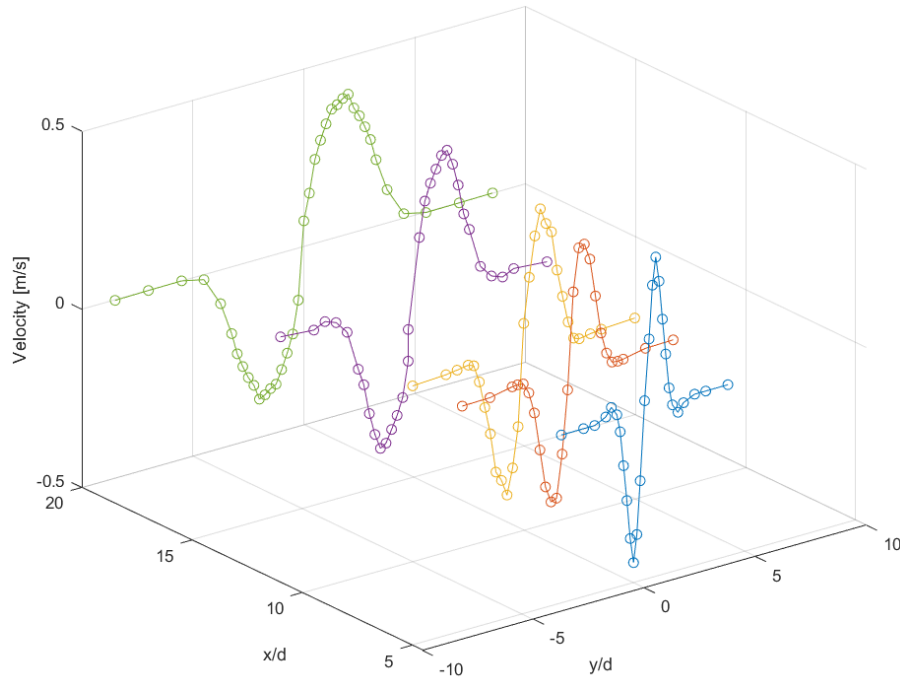


Figure 4.22: 3D plot of mean crosswise velocity profiles measured at different streamwise locations with x-wire at exit Reynolds number $Re=12833.47$. Each empty circle corresponds to a data point. Dimensions both crosswise and streamwise are normalized with the exit section length, which is represented by "d". The acquisition for a wire was performed for 40 s having a sampling rate of 10 kHz.

The mean crosswise velocity profiles at different streamwise locations were plotted in the same plane to be able to analyze more easily the difference between the profiles. Figure 4.23 below represents the velocity profiles plotted together.

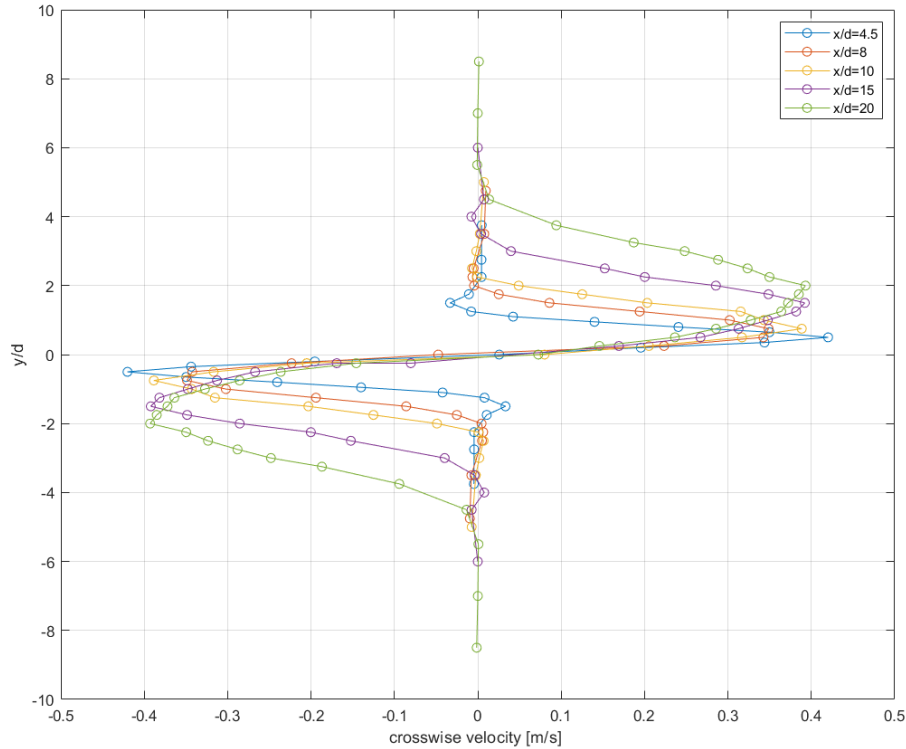


Figure 4.23: 2D plot of mean crosswise velocity profiles measured at different streamwise locations with x-wire at exit Reynolds number $Re=12833.47$. Each empty circle corresponds to a data point. Dimensions both crosswise and streamwise are normalized with the exit section length, which is represented by "d". The acquisition for a wire was performed for 40 s having a sampling rate of 10 kHz.

4.4.2 Fluctuating Velocity Profile

Fluctuating velocity profiles in both streamwise and crosswise directions were obtained by conducting experiments with both a single hot wire and the x-wire. After having the relationship between an arbitrary hot wire voltage value and the velocity value thanks to the calibration procedure, fluctuations were computed by decomposing the velocity into its components. Since the single hot wire can determine the fluctuations in the streamwise direction, a comparison of the streamwise fluctuations was achieved between data obtained by the single hot wire and the x-wire.

The acquisition for a wire was performed for 40 s having a sampling rate of 10 kHz.

Again, as it was mentioned in section 4.4.1, the grid points to perform the acquisition were decided as they were reported in table 4.3.

Streamwise Fluctuations

Velocity fluctuations in the streamwise direction that were estimated by using the single hot wire are shown in the figures 4.24, 4.25 below. The 3D figure allows one to observe the profiles at different streamwise locations which also helps in visualizing the distance between the locations.

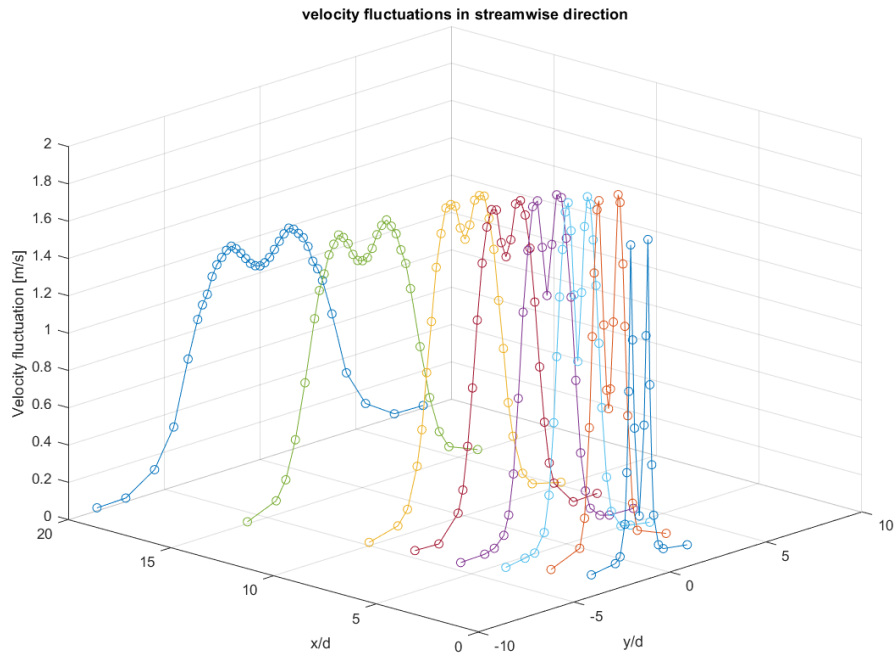


Figure 4.24: 3D plot of fluctuating streamwise velocity profiles measured at different streamwise locations with single hot wire at exit Reynolds number $Re=12235.8$. Each empty circle corresponds to a data point. Dimensions both crosswise and streamwise are normalized with the exit section length, which is represented by "d". The acquisition for a wire was performed for 40 s having a sampling rate of 10 kHz.

To reach a better comparison between the profiles at different locations, all of them were plotted in the same plane as they can be seen in the figure (ref).

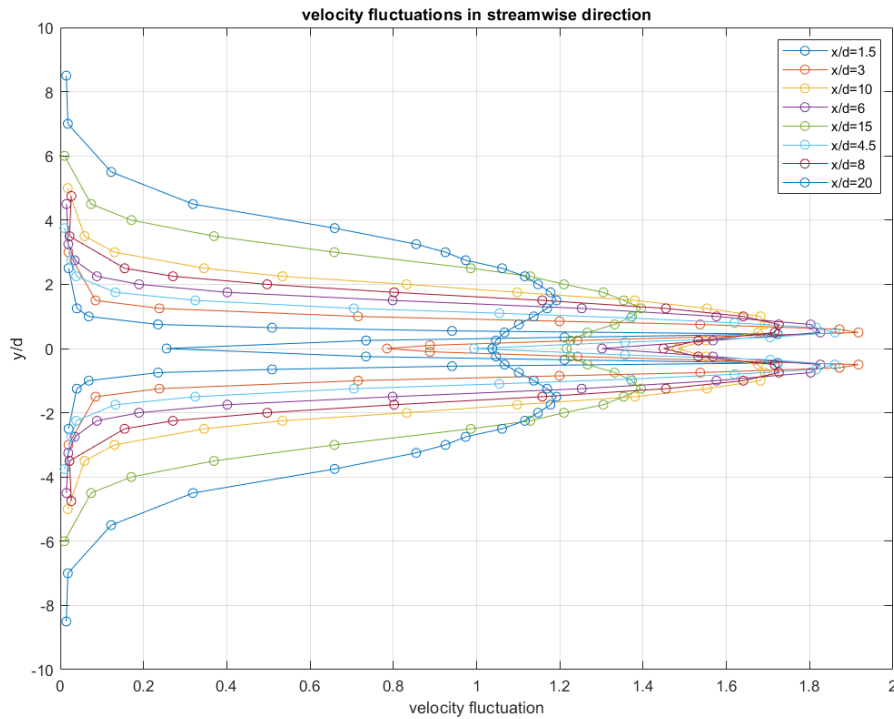


Figure 4.25: 2D plot of fluctuating streamwise velocity profiles measured at different streamwise locations with single hot wire at exit Reynolds number $Re=12235.8$. Each empty circle corresponds to a data point. Dimensions both crosswise and streamwise are normalized with the exit section length, which is represented by "d". The acquisition for a wire was performed for 40 s having a sampling rate of 10 kHz.

Having obtained the streamwise velocity fluctuation profiles by using the single hot wire, the next step is to perform the same process with an x-wire to compare the results. Thus, the 3D velocity fluctuations at different streamwise locations can be seen in figure 4.26 while the 2D plot collecting all the profiles in the same plane is visible in figure 4.27.

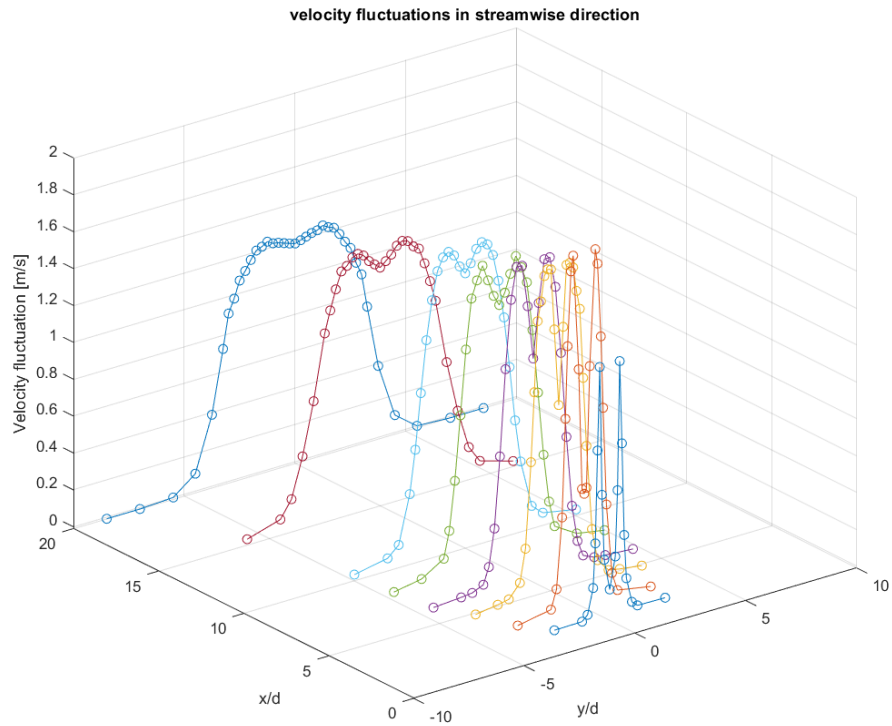


Figure 4.26: 3D plot of fluctuating streamwise velocity profiles measured at different streamwise locations with x-wire at exit Reynolds number $Re=11506.6$. Each empty circle corresponds to a data point. Dimensions both crosswise and streamwise are normalized with the exit section length, which is represented by "d". The acquisition for a wire was performed for 40 s having a sampling rate of 10 kHz.

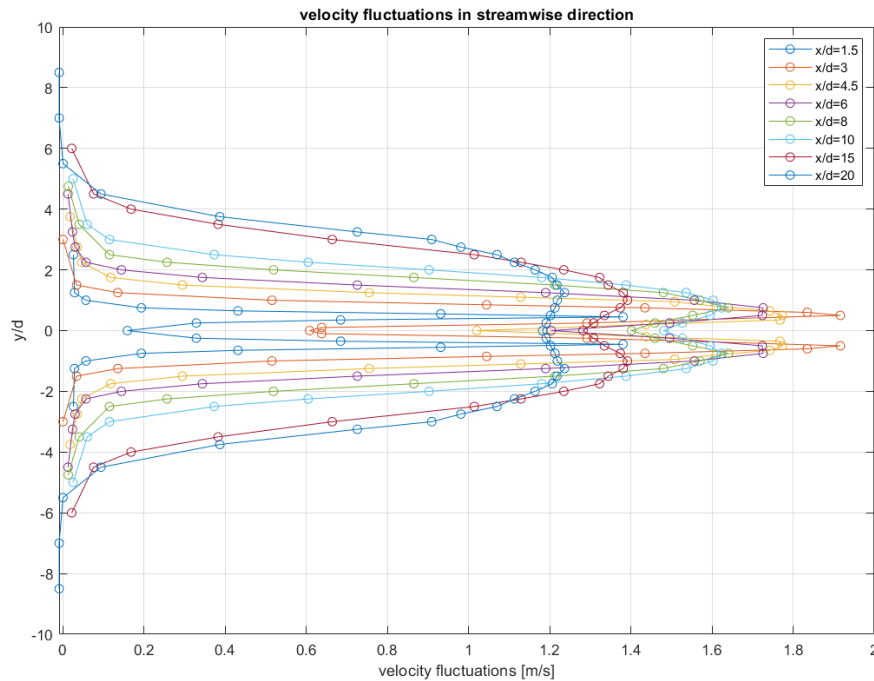


Figure 4.27: 2D plot of fluctuating streamwise velocity profiles measured at different streamwise locations with x-wire at exit Reynolds number $Re=11506.6$. Each empty circle corresponds to a data point. Dimensions both crosswise and streamwise are normalized with the exit section length, which is represented by "d". The acquisition for a wire was performed for 40 s having a sampling rate of 10 kHz.

Crosswise Fluctuations

By conducting the x-wire experiments by placing the wire at five different locations in a streamwise direction fully automatically thanks to the improvements in the wind tunnel, the following figure 4.28 was obtained to have a 3D visualization of the fluctuating velocity in the crosswise direction.

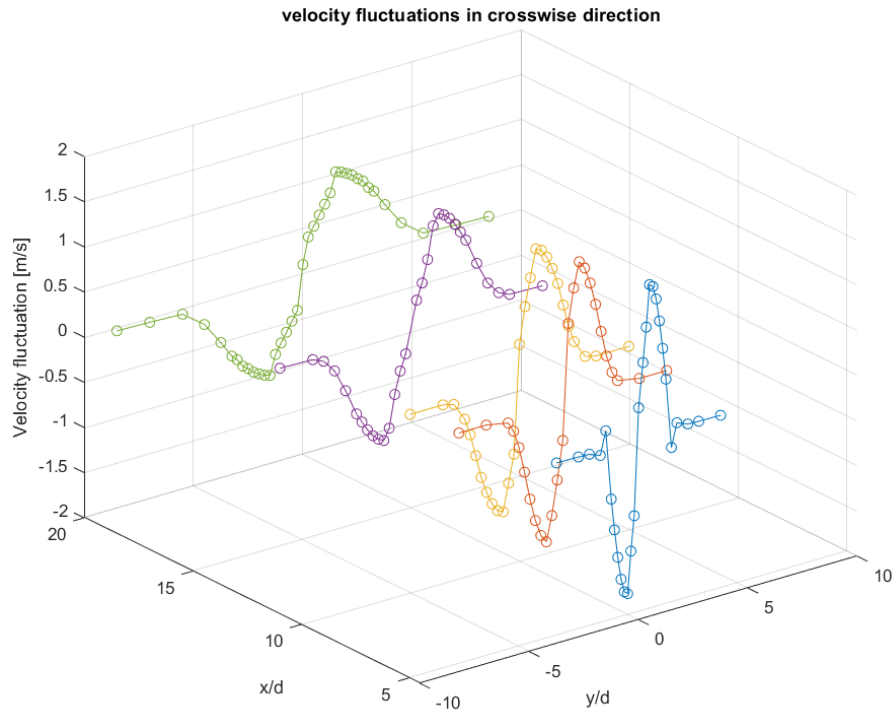


Figure 4.28: 3D plot of mean streamwise velocity profiles measured at different streamwise locations with x-wire at exit Reynolds number $Re=12833.47$. Each empty circle corresponds to a data point. Dimensions both crosswise and streamwise are normalized with the exit section length, which is represented by "d". The acquisition for a wire was performed for 40 s having a sampling rate of 10 kHz.

To be able to analyze the behavior of the fluctuations and see the variation with respect to the distance from the exit section, the following plot 4.29, which represents all the profiles in the same plane, was created.

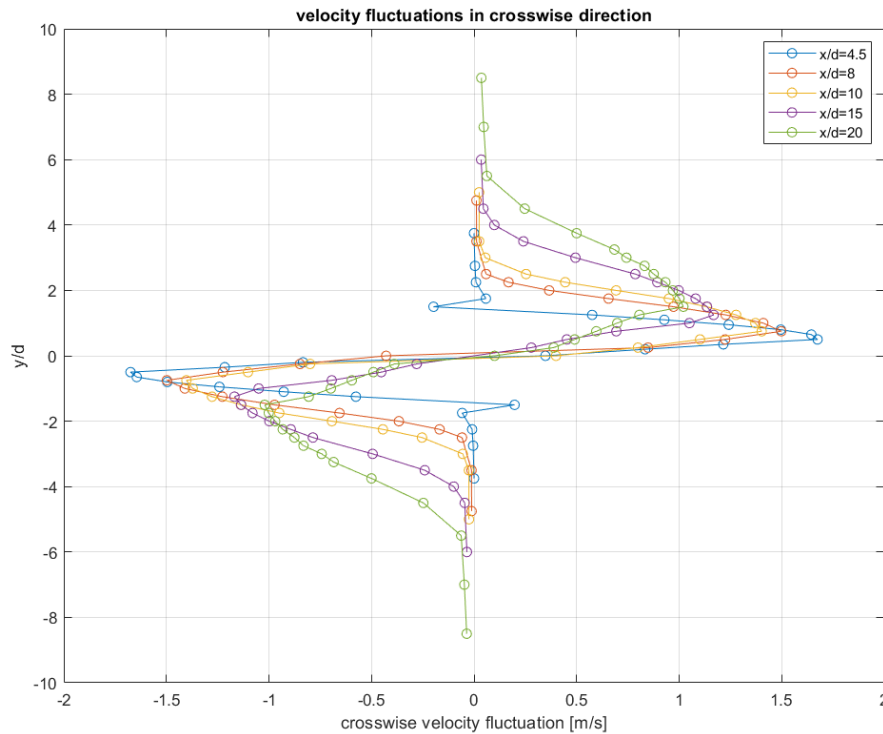


Figure 4.29: 3D plot of mean streamwise velocity profiles measured at different streamwise locations with x-wire at exit Reynolds number $Re=12833.47$. Each empty circle corresponds to a data point. Dimensions both crosswise and streamwise are normalized with the exit section length, which is represented by "d". The acquisition for a wire was performed for 40 s having a sampling rate of 10 kHz.

4.4.3 Reynolds Normal Stress

Reynolds normal stresses in streamwise direction were computed thanks to the single hot wire experiments to study the fluctuation variation and to compare the plane air tunnel jet with the results from the literature.

The following figure 4.30 shows the Reynolds normal stresses at eight different streamwise locations, normalized by the exit section height, d. As expected, the behavior is very similar to the fluctuating velocity structure.

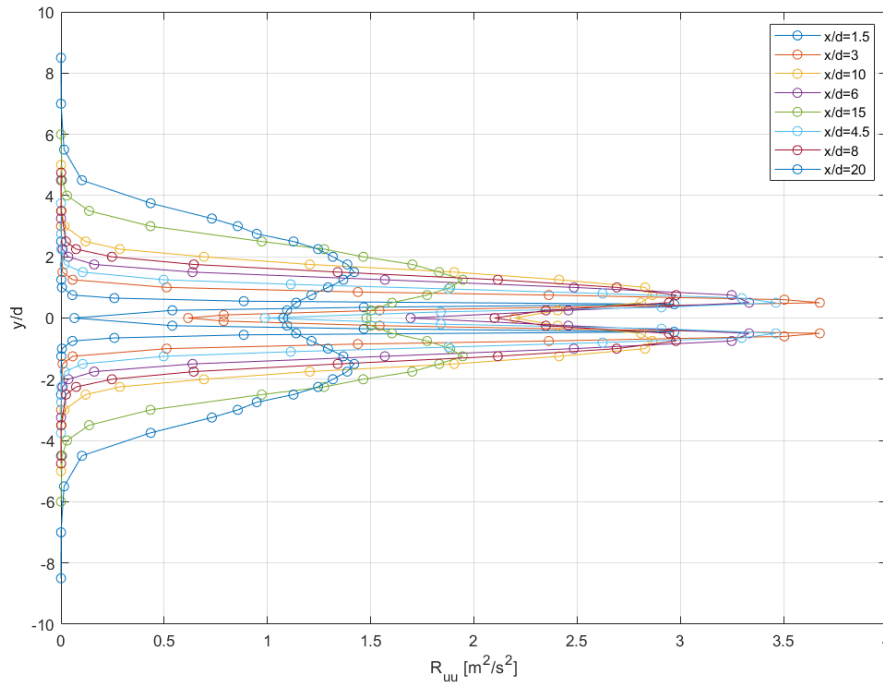


Figure 4.30: Variation of Reynolds normal stresses along the crosswise direction at different streamwise locations. Each empty circle corresponds to a data point. Experiments were conducted with the single hot wire at 10 kHz for 40 seconds at the exit section Reynolds number $Re=12235.8$.

To visualize the decay in Reynolds normal stress on the centerline along the streamwise direction, the following plot was obtained.

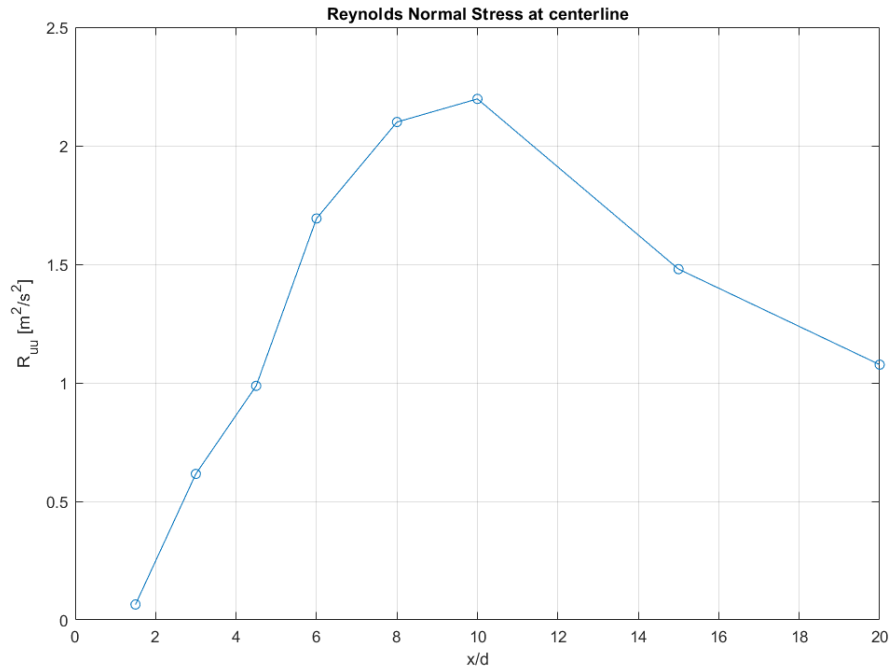


Figure 4.31: Variation of Reynolds normal stresses along the centerline at different streamwise locations. Each empty circle corresponds to a data point. Experiments were conducted with the single hot wire at 10 kHz for 40 seconds at the exit section Reynolds number $Re=12235.8$.

Moreover, the Reynolds normal stress was normalized with the square of the centerline mean velocity at the corresponding location, to have a more universal result and a better comparison with the literature. Figure 4.32 shows the behavior of normalized Reynolds normal stress along the crosswise direction at different streamwise locations.

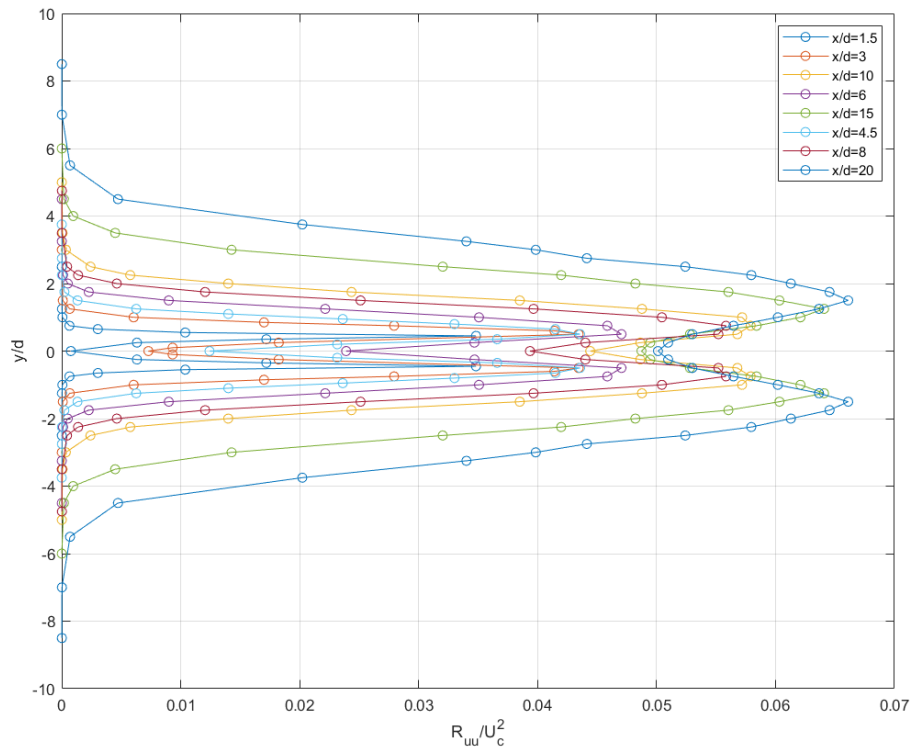


Figure 4.32: Variation of Reynolds normal stresses, normalized by the squared centerline velocity at the corresponding location, along the crosswise direction at different streamwise locations. Each empty circle corresponds to a data point. Experiments were conducted with the single hot wire at 10 kHz for 40 seconds at the exit section Reynolds number $Re=12235.8$.

5

Discussion

5.1 Velocity Measurements by the Pitot-Static Tube and Pressure Tappings

As was always the case for all experimental studies, the accuracy can be and should be improved from all aspects of the phenomena. According to most experimental studies, there is always a degree of the error caused by the accuracy. Here in this study, the speed was measured in two different ways, where one is a pitot-static tube and the other is pressure tappings. Hence, there are two main sources of accuracy error, where one is related to another since pressure tappings are used with respect to the results taken by the pitot-static tube.

The inaccuracy in pitot readings can be caused by external disturbances, the resolution of the pressure transducer and the thermocouple transducer, and noise in data. Since the external disturbances are not in higher order due to the placement of the pitot-static tube at the exit section, and the noise in pressure data can be assumed as negligible, the resolution of the pressure transducer is the key parameter to determine the accuracy errors in pressure measurements. The resolution, which is sometimes called also as uncertainty, of a transducer is determined as

$$\delta U = \frac{U_{range}}{Numberofintervals}, \quad (5.1)$$

where,

$$Numberofintervals = 2^N - 1, \quad (5.2)$$

δU = uncertainty,
 U_{range} = Range of the signal value,
 N = number of bits.

As it can be understood from the equations 5.1 and 5.2, the resolution is the minimum detectable value of the measured quantity. Thus, the lower it is, the more accurate measurements can be reached.

Three different MKS pressure transducers are available for the setup. One of them has a range of 2 Torr, the other has a range of 10 Torr while the last one has a range of 100 Torr, where the relation between the Torr and the Pascal is in equation

5.3 and the resolution of a corresponding MKS transducer can be calculated by using equation 3.2

$$1 \text{ Torr} = 133.322 \text{ Pa}. \quad (5.3)$$

To be most accurate and to catch all the small changes in pressure, a 2 Torr transducer has to be used to have the resolution smaller. However, since its range is small, it cannot go further than the exit velocity of $22 \frac{m}{s}$ which corresponds to $Re=27796.1$. Therefore, the selection of transducer should be made carefully with respect to what is being dealt with.

Another significant source of error that can be faced while measuring the mean velocity at the exit section is the resolution of another pressure scanner, which is used for pressure tappings. The Scanivalve DSA3217 pressure scanner has $10'' H_2O$, which corresponds to

$$1'' H_2O = 249.089 \text{ Pa}. \quad (5.4)$$

Thus, the case is again the same, the lower the range the lower the accuracy error due to small changes in pressure, but the lower the values that can be detected.

The last important error source is the error that can be caused by the fourth-order polynomial interpolation done to relate the pressures at tappings to the velocity measured by the pitot-static tube. No matter how accurate the fittings are, there is always an error between a fitted function and the real one. Moreover, the real curve formed by the pitot velocity also changes with time, which means the fitting should be created and repeated each time before starting the test. Nevertheless, the fitting was kept constant as it was done for the first time, but another accuracy analysis was performed to ensure the consistency of the pressure tappings.

The temperature acquisition is not really a source of error since the temperature itself is a slow varying quantity.

Furthermore, since the pressure transducer is not fast enough and the pressure is not really a fast varying quantity, neither of the two are able to catch the fluctuations although the velocity is a fast varying quantity, which means that only the mean velocity field could be measured by using these two methods. In other words, the dynamic range, represented in the equation 5.5, of the pitot-static tube is not high enough, but it is wanted to be as high as possible since the turbulence level is higher than 1%.

$$DR = \frac{U_{range}}{\Delta u_{min}}, \quad (5.5)$$

where,

DR = dynamic range,

Δu_{min} = minimum detectable fluctuation of a measured signal.

5.2 PI control

The proportional integral control, used in many applications, is preferred to have better control in a closed-loop control system. There are multiple variables that determine its performance.

Two of them are the proportional and integral gains. They have to be tuned very carefully for the recent specific task since they differ with respect to the mission. The proportional and integral gains are determined for this task as they are represented in the table 5.1

Proportional Gain	Integral Gain
1.4	10

Table 5.1: PI gain table that was set iteratively by trial and fail method.

The user is free to play with the gains to change the response of the control system. An increase in proportional gain will result in a system that goes to a steady state value in a shorter time. On the other hand, an increase in the integral gain causes a lower steady-state error value. However, the system goes unstable if the gain values are so high depending on the task.

In this study, it was made visible that the desired level of response of the control system was achieved with the shown gain values. However, there is another source of weakness in the system behavior, which is again the accuracy of speed measurement. Since the control system takes the measured speed and proceeds with that value, it should be able to accurate enough, meaning that a high resolution is required especially in lower speed values. By looking at the figure 4.9, it can easily be commented that the response of the system is much better when the speed at the exit section is higher than $20 \frac{m}{s}$. The reason for this behavior is the range, and so the resolution, of the transducer used to measure the pressure. As was discussed in the mean velocity section, the speed value is not that accurate at low speeds if the resolution of the transducer is not high enough. Thus, it could be much better to use a low-range transducer while the control loop is being forced to set the speed at low values, and the opposite for high-speed values.

Since the use of case structures is not allowed inside the control and simulation loop feature of the LabView environment, the control loop was put inside an event structure, flat sequence, while loop respectively, and the loop itself is a heavy application, it takes a bit of time to reach an equilibrium after setting the desired speed. Moreover, due to the fact that there are so many operations inside and outside the control loop, it sometimes skips stopping even if the criterion is met for the first time. This issue is not that practical to be solved since the use of any structure is not allowed inside the loop. It is not really a problem from an accuracy point of view because the speed value doesn't diverge once it reaches the stopping criteria. However, it requires more time to ensure that the loop stopped after reaching the desired speed and that the speed is no more being changed by the loop.

These problems that are caused by the control and simulation loop were ignored since it was the most practical way to accomplish a speed controller by command-

ing the inverter automatically. Thus, a suggestion may be to use another way of controlling the speed, preferably including the effects of proportional and integral gains, to get rid of the drawbacks of the control loop faced during this application.

Furthermore, to compare the behavior of two different automatic speed controllers with and without using the pitot-static tube at the exit section, the following figure 5.1 was created by combining the response of two cases to make the visibility more compact.

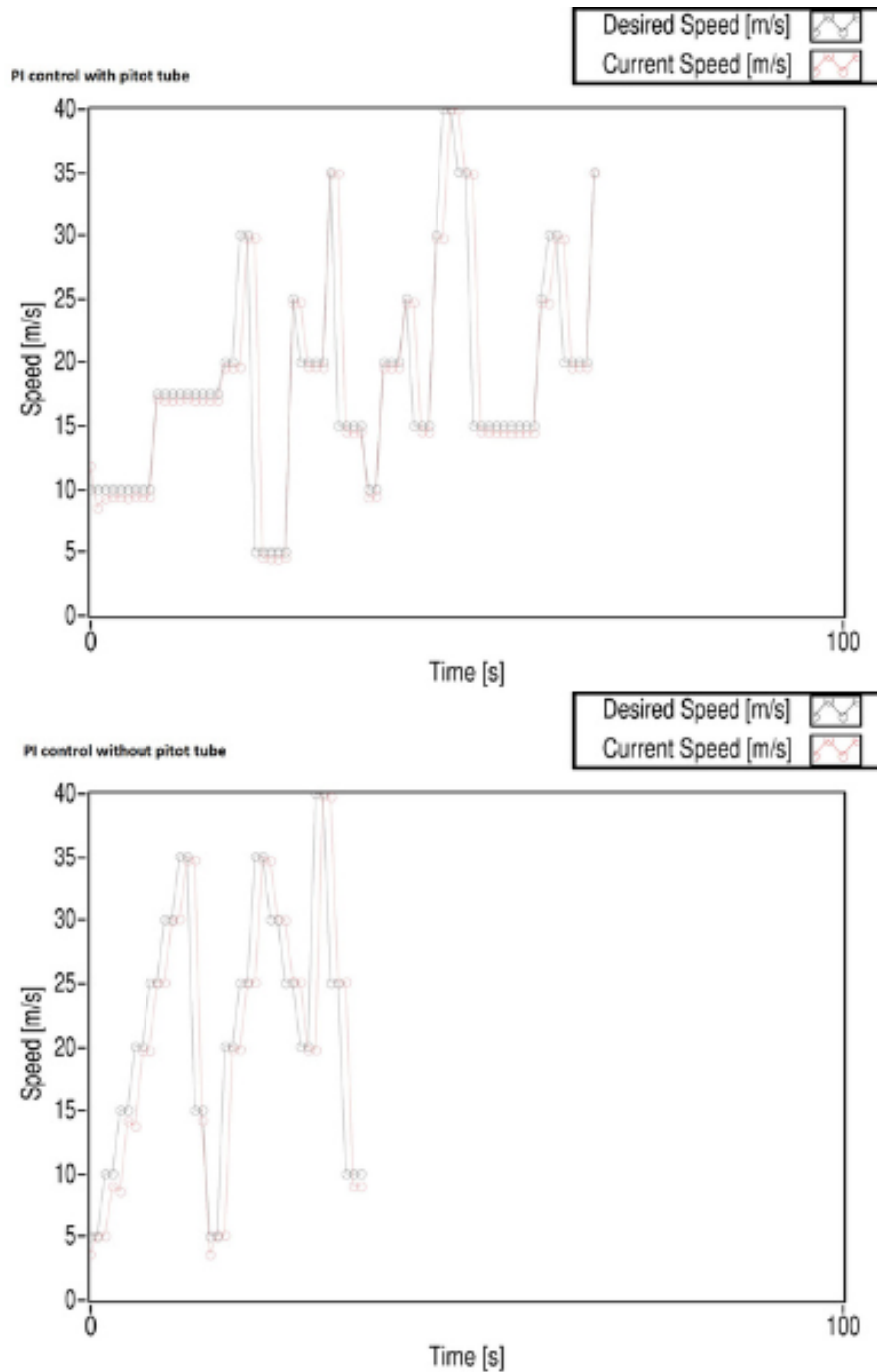


Figure 5.1: Response plots from two different control loops, where one is with the pitot-static tube at the exit section and the other is without the pitot-static tube. Empty circles correspond to a data point where each stands for a different type of speed at the exit section.

As one can easily see, both control loops behave poorly under the exit section velocity $20 \frac{m}{s}$ since the resolution of the transducers is not the most proper one, and the losses inside the wind tunnels are bigger at low speeds. The behavior of both control loops is close to each other at exit velocity values higher than $20 \frac{m}{s}$. However, the one with the pitot-static tube differs from the one without the pitot-static tube in terms of the steady-state error at lower speeds at the exit section. The

reason for this kind of result could be said to be the resolution difference between two transducers, one for the pitot-static tube and the other for the pressure tapping. The following table 5.2 represents the resolutions of the transducers.

Transducer	Resolution [Pa] %
MKS for pitot-static tube	0.013
DSA 3217 for pressure tapplings	0.04

Table 5.2: Resolution, minimum detectable pressure value in Pascals, values by two different pressure transducers where one was used for the pitot-static tube (MKS) and the other was used for pressure tapplings (DSA 3217).

By looking at the table above, it is obvious that the MKS transducer will behave more accurately to the small pressure changes since it is capable to measure pressure changes which are in smaller amounts compared to DSA 3217 pressure scanner. Thus, the steady-state error can go smaller with the MKS pressure transducer.

In addition, as it can be seen from the figures 3.49, 3.50, 3.51 and 3.52, the deviation of the speed value by pressure tapplings is much bigger at low speeds. Hence, the steady-state error of the control loop with the pressure tapping for velocity measurement is higher at low speeds.

In addition, although it is not visible in the comparison plot since the horizontal axis is just the moment that the velocity is fixed, but not the real-life time, the response speed of the controllers was investigated manually. It was observed that the control loop with the pitot-static tube was much faster in stopping the control loop after hitting the desired speed.

5.3 Pressure behavior

There is a well-known phenomenon called pressure drop, also called pressure loss, which is caused by the velocity increment, turbulence, or friction. Although there are empirical formulas for the pressure drop, it should be analyzed for the recent specific cases, by taking into account the effect of wind tunnel components. In PAT, the speed is almost constant between the glass spheres and the contraction part. Moreover, since the components like honeycomb and screens were used to decrease the turbulence, the turbulence level is also not that high. However, there is a really high level of friction caused by the components as well as the walls of the wind tunnel. Thus, the pressure drop was expected along the tunnel.

The following figure 5.2 shows the pressure drop percentage for different exit section velocity values. It is obvious that although the amount of pressure drop increases a lot with the speed increment as was shown in figure 4.5, the percentage pressure drop decreases as the speed increases.

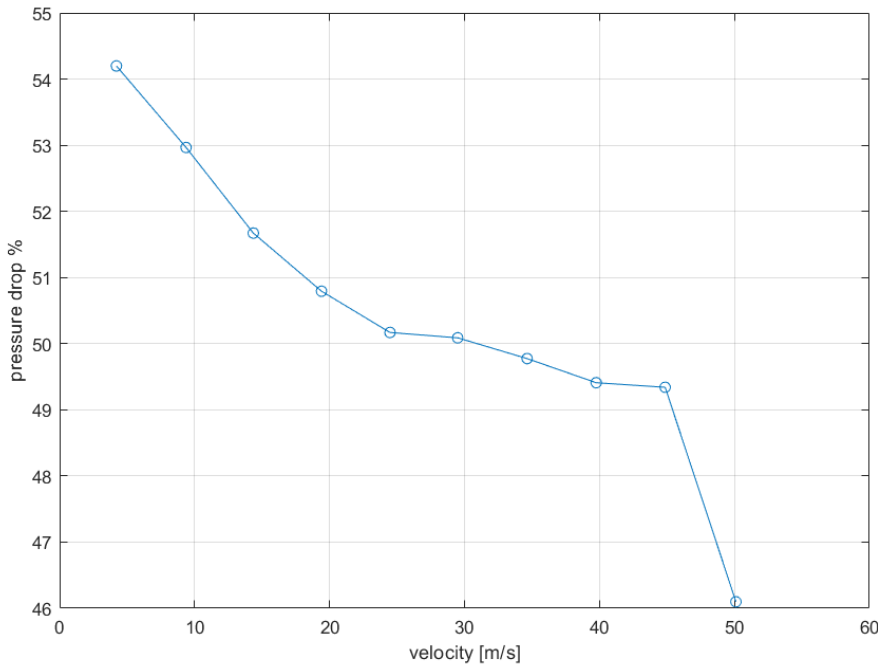


Figure 5.2: Percentage pressure drop calculated at different exit section velocity values. Pressure drop is the difference between the pressure at the pre-settling chamber and the settling chamber just before the contraction part. Each empty circle corresponds to a data point.

This behavior can be interpreted by the theory of the fact that the aerodynamic efficiency of the wind tunnel components increases if the speed increases.

The pressure that was measured by the pressure tapings is the total pressure in principal. However, since there is no flow inside the cavity where the tapping was mounted, the dynamic pressure was said to be 0. Thus, the pressure values acquired at channels can be said to be static pressure. The behavior of static pressure along plane air tunnel was visualized in figure 4.3.

By having a look at figure 4.3, it is obvious that the lowest pressure decrease happens between channels 3 and 2, which correspond to the honeycomb. As it was discussed before, since the main reason behind the pressure drop inside the plane air tunnel is the friction and the friction is mainly caused by the area of the wind tunnel components, the cross-sectional area of the honeycomb was compared with the other components' cross-sectional area. To make this comparison, analyses were performed on the porosity values of each component, which can be written as

$$\beta = \frac{A_f}{A_t}, \quad (5.6)$$

where,

A_c = free tunnel cross-sectional area,
 A_t = total tunnel cross-sectional area.

Listing the porosity of each component as

Component	Porosity, β
Glass spheres	0.58
Honeycomb	0.9669
Screens	0.58

Table 5.3: Porosity values for three different wind tunnel components.

Since the porosity value is almost 1 for the honeycomb, it can be said that the free area in the honeycomb section is much higher than the other components, so resulting in the least friction. The less the friction is, the smaller the pressure drop value is.

Moreover, going into more detail in the figure 4.3, the pressure drop becomes negative after a certain velocity value. The behavior of pressure drop along the honeycomb for different speed values is represented in figure 5.3 below.

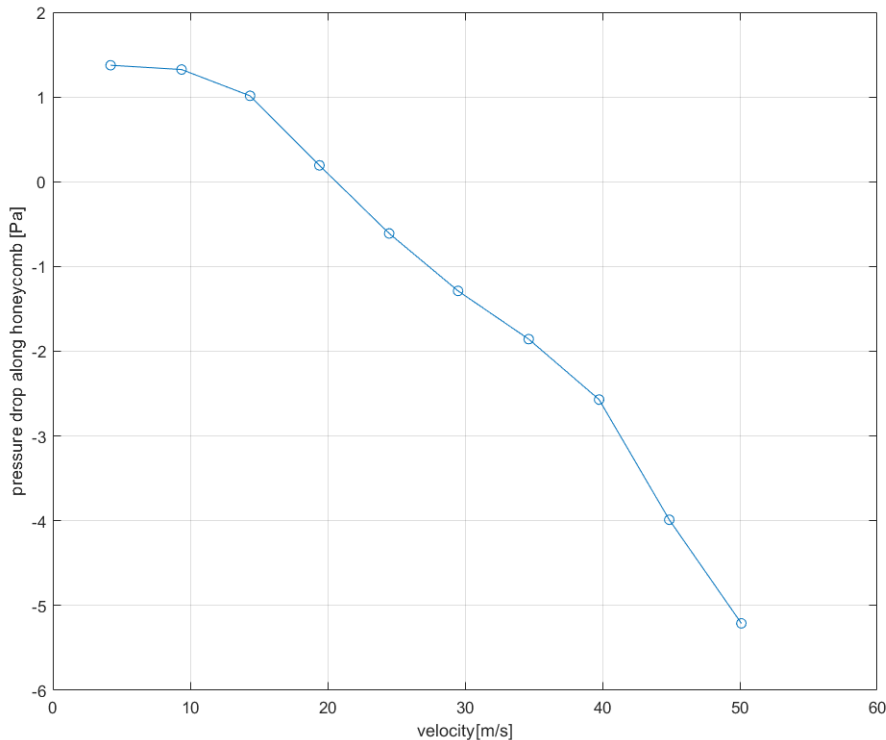


Figure 5.3: Pressure drop along the honeycomb for different speed values at the exit section of the plane air tunnel. Each empty circle corresponds to a data point.

It was displayed that the pressure drop has a decreasing behavior as the speed increases, which is the direct opposite of the expectations considering the physics of the flow inside the plane air tunnel. After a certain value of velocity, which is different for every experiment, the static pressure stops decreasing and starts increasing along the honeycomb.

The behavior seen in figure 5.3 can be explained by referring to the analysis performed in section 3.3.1. As was discussed before, the offset values for the channels

of the Scanivalve pressure scanner were assumed to be constant although literally, they were not. By focusing on the behavior of channel 3 and channel 2 in figures 3.24 and 3.25, which were represented with the numbers in tables 3.6 and 3.7 respectively, it can be said that the offset increment in channel 2 is much higher than the one in channel 3. However, the first offset values for all of the channels were considered constant. Thus, as soon as the difference between the current and the first offset values of channel 2 becomes greater than the one for channel 3, inaccuracy starts to appear for the pressure behavior along the honeycomb also because the values at channel 3 are almost equal to the ones at channel 2. Therefore, a more accurate investigation of the offset behavior should be performed to be able to catch small changes in pressure values.

Lastly, as was shown in figure 4.6 before, it was realized that the values of static pressure at the settling chamber and the dynamic pressure at the exit section are almost equal to each other. The difference between the two pressures is 1.8% at maximum when the speed at the exit section is $4.61 \frac{m}{s}$ and starts to decrease with the increasing speed at the exit section as it can be observed thanks to the figure 4.7. The reason behind this behavior is actually the main goal of the converging shape of the exit section. Considering the conservation of mass flow rate [Hall, 2021a]

$$\dot{m} = \rho U A = \text{constant}, \quad (5.7)$$

where,

\dot{m} = mass flow rate,
 ρ = fluid density,
 U = velocity,
 A = section area,

once the area of the section that the fluid goes through decreases, the fluid velocity increases to keep the total fluid mass flow rate constant.

As the velocity increases, the dynamic pressure increases due to its definition, which is directly proportional to the square of the velocity. Taking into account the Bernoulli theorem represented in equation 3.17, the static pressure decreases as the dynamic pressure increases. Thus, it can be said that the static pressure at the settling chamber is almost fully converted into the dynamic pressure at the exit section since the total pressure was said to be constant.

The efficiency of the contraction part could be decided by simply computing the amount of static pressure drop. The following figure 5.4 represents the static pressure difference between the exit and the settling chamber.

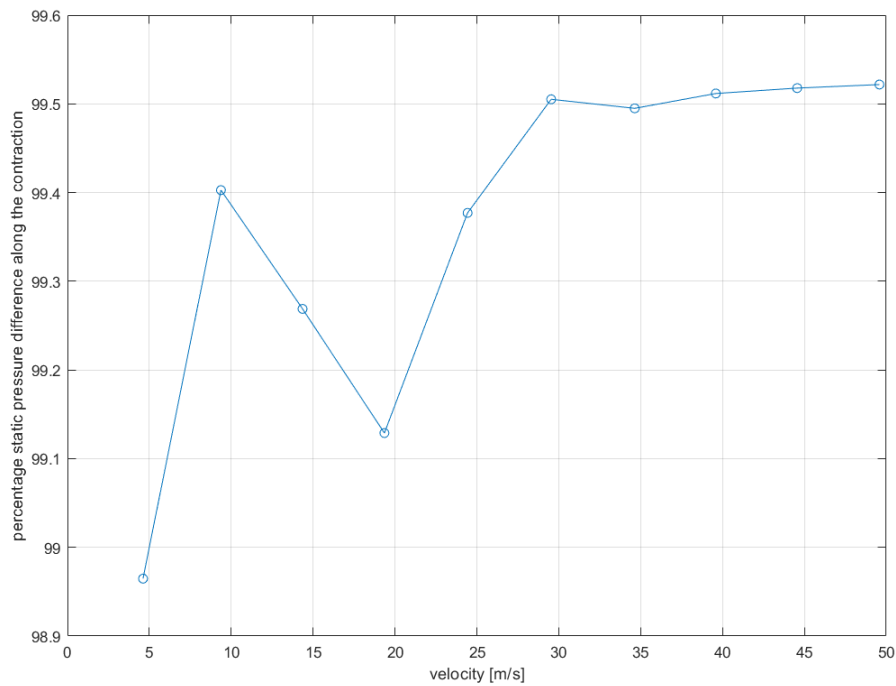


Figure 5.4: Percentage static pressure decrement along the contraction part for different exit section velocity values. Each empty circle corresponds to a data point.

As it is obvious from the figure, the static pressure drop along the contraction part has a minimum value of 98.96% when the velocity is at its lowest value, $4.61 \frac{m}{s}$, and it reaches up to its maximum value of 99.52% when the exit section velocity is increased to $49.58 \frac{m}{s}$. So, the higher the exit section velocity, the higher the static pressure drop, thus the more efficient the contraction part.

Moreover, the last figure 5.5, which can be seen below, represents static pressure at the settling chamber and the static pressure drop along the contraction part. One can easily tell that the values are extremely close to each other.

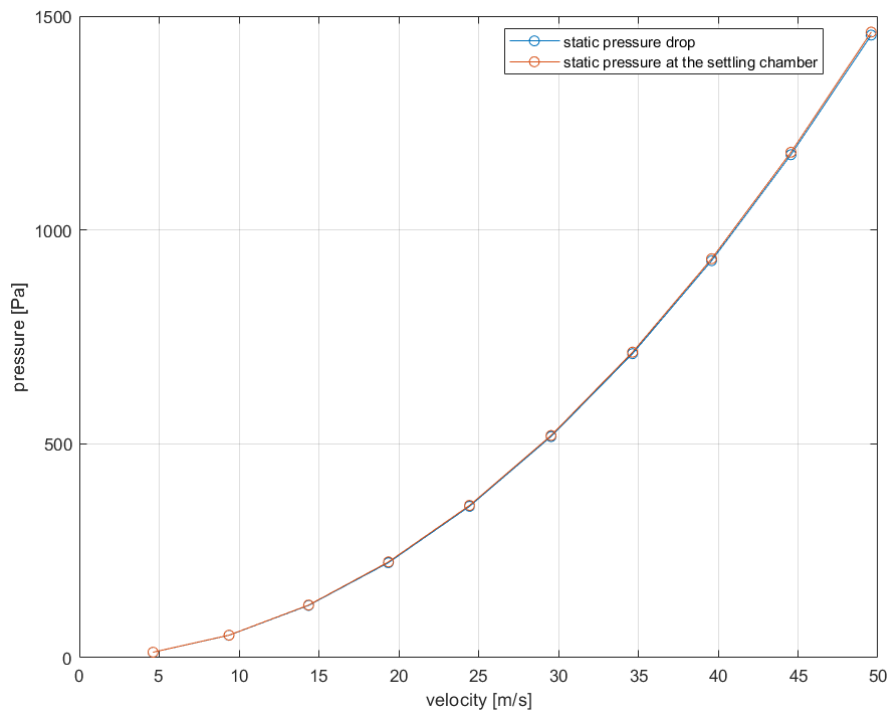


Figure 5.5: Similarity between the static pressure at the settling chamber and the static pressure drop along the contraction part. Each empty circle corresponds to a data point.

Thus, it can be said that the contraction part has a genuinely high efficiency at all of the speed values although there are still some losses. Even more, its efficiency increases directly proportional to the speed increment, meaning that the losses become smaller as the exit velocity is increased.

5.4 Hot wire experiments

As it was discussed in section 3.6.2 and 3.6.1, the sampling time was decided as 20 s while the sampling frequency was chosen as 4 kHz. However, after performing literature research about the hot wire experiments, the sampling time and the frequency were decided as that is reported in the following table 5.4 to ensure that enough details of fluctuations will be caught.

Sampling time	40 s
Sampling frequency	10 kHz

Table 5.4: Sampling parameters for the hot wire experiments

By analyzing the mean streamwise velocity profile estimated by both the single hot wire and the x-wire, the first idea for the velocity profile of a turbulent planar jet was reached. The results for the mean streamwise velocity profile from the single hot wire and the x-wire can be compared by analyzing the following figure 5.6.

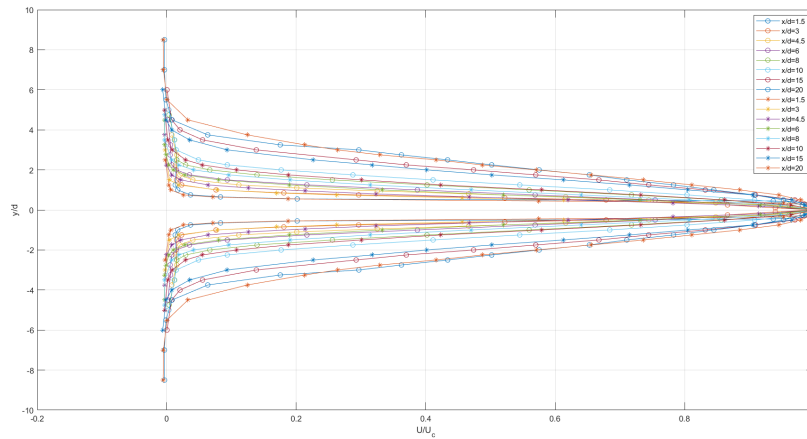


Figure 5.6: Normalized mean velocity profile variation along the streamwise direction. The horizontal axis shows the normalized velocity where the U_c refers to the centerline mean velocity. Each symbol corresponds to a data point. The data points marked with the "o" belong to x-wire while the ones shown with "*" are from the single wire experiments.

In the figure above, the horizontal axis shows the normalized velocity where the U_c refers to the centerline velocity. The data points marked with the "o" belong to x-wire while the ones shown with "*" are from the single wire experiments. As it can be understood from the figure, the velocity profiles are almost the same for the two types of hot wire.

It was observed that the mean velocity profiles obtained by both of the wires are reasonable. Since the first diameter is still inside the potential core, there is a drastic speed increment as soon as we go between the $y/d=1$, and the maximum speed is almost constant since there is no dissipation yet. Moreover, as we get far from the plane air tunnel exit section, the velocity profile starts to have a hat-shape since the dissipation, and so the entrainment starts to change the velocity, especially at the outer locations.

Moreover, to compare the fluctuating velocity in the streamwise direction, the following figure 5.7 was plotted after estimating the normalized fluctuating velocity values.

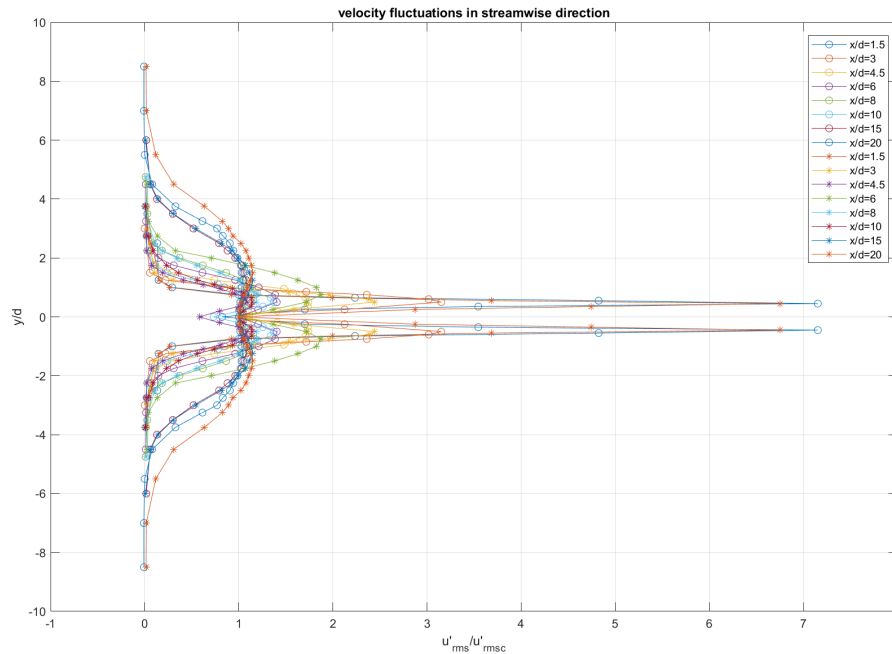


Figure 5.7: Normalized fluctuating velocity profile variation along the streamwise direction. The horizontal axis shows the normalized velocity where the u_{rms} refers to the centerline fluctuating velocity. Each symbol corresponds to a data point. The data points marked with the "o" belong to x-wire while the ones shown with "*" are from the single wire experiments.

As one can easily say, velocity fluctuations reach their maximum value where the entrainment starts since they are one of the most important parameters included in the entrainment theory. Due to the fact that there is the dominant flow oriented through the streamwise direction, the fluctuations cannot appear close to that region so it decreases hitting their minimum value. Thus, the shape of the fluctuating velocity profiles obtained by two types of hot wires was totally reasonable.

Lastly, to see the change in fluctuating velocity, so does the turbulence intensity and the Reynolds normal stress along the streamwise direction, following figure 5.8 was obtained by normalizing the fluctuating velocity with the mean velocity at the centerline.

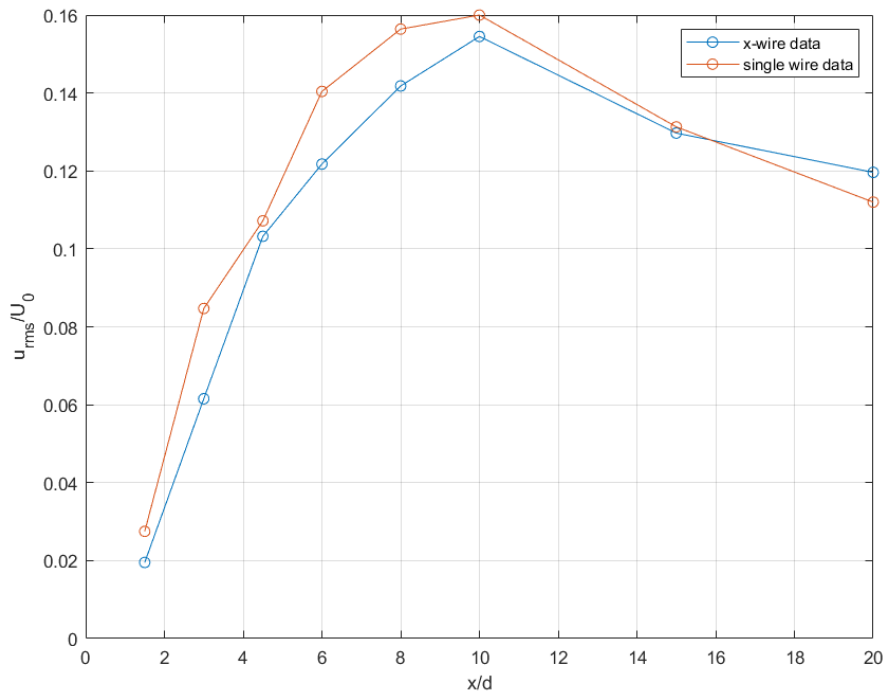


Figure 5.8: Normalized fluctuating velocity by the centerline velocity at $y/d=0$ plotted at different streamwise locations. Each symbol corresponds to a data point. The data points marked with the "o" belong to x-wire while the ones shown with "*" are from the single wire experiments.

As expected, the intensity of fluctuations first starts to increase where the potential core ends, due to the fact that the mixing is the highest at the end of the potential core. Then, a decrement, as mixing slows down, occurs.

Considering the crosswise velocity structure that was evaluated thanks to two different x-wires and represented in figures 4.22, 4.23, 4.28, and 4.29, an expected behavior was observed. By looking at the figures, it is obvious that the velocity first increases as one goes from the center to the borders of the jet, due to a high amount of entrainment, and then decreases as it leaves the entrainment region going through the ambient air. Moreover, the maximum velocity location in the vertical direction goes up as the streamwise location increases resulted by the spreading of the jet.

Although the shape of the mean velocity profiles and the fluctuating velocity behavior computed by the x-wire is reasonable, since the acquisition for $x/d=4.5$ streamwise location was performed a day before with another x-wire than the other locations, it has been realized that there is a small amount of drift between the crosswise velocity behaviors although the calibration was repeated for each experiment, resulting in unrealistic velocity values. Therefore, it is highly suggested that the experiments are better be performed on the same day with pre and post-calibration without changing the wire.

5.4.1 Literature comparison

As was mentioned in section 2.2, the first comparison was made by investigating the self-similarity of the turbulent planar jet. The following figure 5.9 was created

to compare the self-similarity profiles.

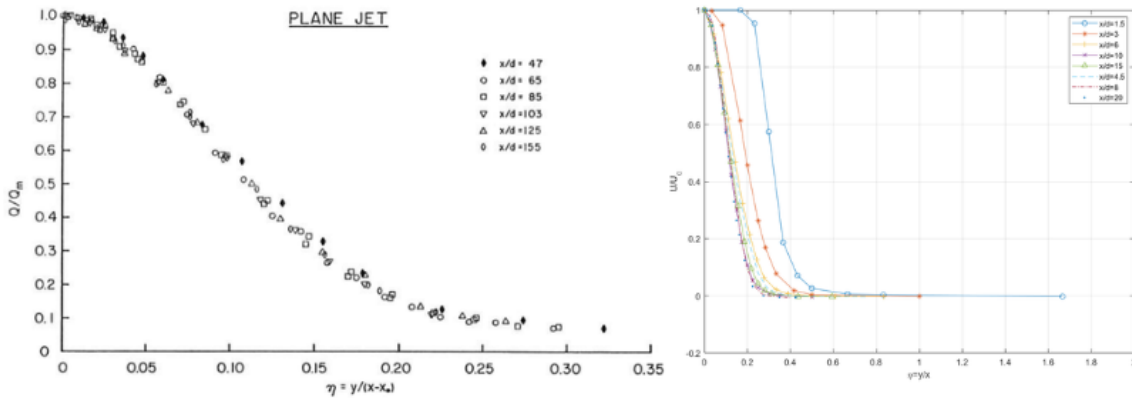


Figure 5.9: Comparison between the literature(left)[Heskestad, 1965] and the experimental results(right) for the mean velocity value normalized by the mean centerline velocity value at the corresponding streamwise location. The horizontal axis is the ratio between the crosswise and the streamwise direction while the vertical axis is the normalized velocity.

As it is obvious in the figures, the behavior of the velocity profiles is almost identical. However, since the experimental setup was limited in the streamwise directions in which the acquisition could be performed. Thus, the streamwise locations reported in the figure on the left couldn't be reached. Nevertheless, it was observed that the turbulent planar jet that is created by the plane air tunnel becomes self-similar after around $x/d=5$ and starts to act very similarly to the one on the left.

Secondly, the turbulence intensity, calculated by the formula 2.66, was analyzed to check the similarity between the literature and the experiments conducted in the plane air tunnel. As it can be seen from the plot on the right in figure 5.10, the turbulence intensity starts to increase as we move away from the exit, and it hits its maximum value where the potential core ends. Completely identical behavior was observed in the results found in the literature, which can be seen on the left with the green dots corresponding to the rectangular jet exit section. As discussed previously, the reason for this kind of behavior is the fact that the mixing process increases the fluctuating velocity components, and so also the turbulence intensity. Since the mixing is the highest at the end of the potential core, it increases until that point, reaches its peak, and starts to fall down as it gets away from the potential core.

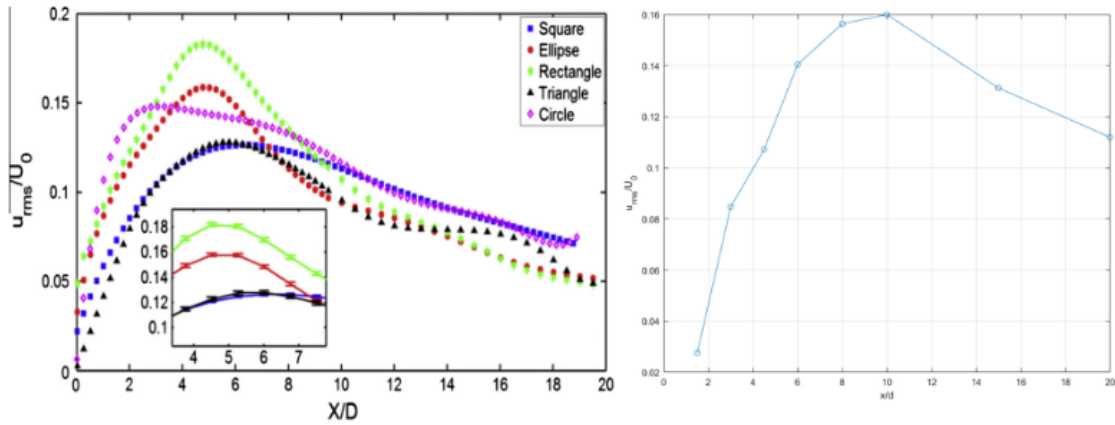


Figure 5.10: Comparison between the literature(left)[Hashiehbfaf and Romano, 2013] and the experimental results(right) for the fluctuating velocity value normalized by the mean exit velocity value at the corresponding streamwise location. The horizontal axis is the streamwise location while the vertical axis is the normalized velocity, also called turbulent intensity. Each empty circle corresponds to a data point on the right.

6

Conclusion

To conclude, communication between the inverter and the computer was the first achievement reached in this study. The commands for on/off as well as the desired voltage input were achieved. After accomplishing the speed measurement with the offset calculation thanks to a pitot-static tube, an automatic control system was designed for the speed at the exit section of a facility named plane air tunnel. While designing the controller, the responses of the control loops and the resolutions of the pressure transducers were taken into account. Moreover, the tuning process was performed carefully considering the performance of the LabView environment. It was observed that the control loop response is much more robust at higher speeds depending on the resolution of the transducer.

Secondly, pressure behavior along the plane air tunnel was studied by inserting pressure tappings at five different locations that were listed in table 3.5. A VI was created to report the pressure values at each location after taking into account the constant offset values at each channel. It was observed that there is a pressure drop decreasing from 54% to 46% as the speed is increased. Moreover, it was understood that almost all of the static pressure was converted into dynamic pressure along the contraction ratio, making the exit part highly efficient.

Then, the velocity at the exit section was related to the pressure behavior to estimate it by avoiding the usage of the pitot-static tube at the exit section. The accuracy of the estimated values was analyzed. After being able to guess the speed at the exit section, the automatic control was implemented without using a pitot-static tube at the exit section. It was pointed out that the automatic speed controller is working poorly at low speeds due to the resolution of the pressure scanner and the deviation from the real speed values at the exit section. To go into more in detail about the sampling parameters, the required sampling time and the frequency for the pressure acquisition were estimated.

Comparing the response of the two different control systems, it was realized that the steady-state error of the control loop, which is using the pressure tappings, is higher than the other one due to low accuracy in speed estimation and the resolution of the pressure scanner. Moreover, it is much slower than the one which is using the pitot-static tube.

Thirdly, a literature review was performed to become familiar with the physics of the turbulent planar jet flow, and the analogy of the hot wire anemometry before starting the experiments. After understanding the planar jet flow behavior from

some aspects, the sampling parameters were decided by operating certain methods such as autocorrelation, variance for the sampling time, and Fast Fourier Transform, power spectral density for the sampling frequency for the hot wire anemometry. Moreover, the acquisition chain of the plane air tunnel was studied to be able to understand the source of problems and uncertainties.

Having decided the sampling parameters and what is being looked for, the first procedure was to calibrate the hot wire with the fully automatic VI code in the LabView environment. Thanks to having the velocity as a function of voltage, velocity signals were acquired at different locations inside the wake of the turbulent planar jet. Both the fluctuating and the mean velocity profiles in the streamwise direction were acquired. Thanks to that, the Reynolds Normal Stress, centerline velocity decay, and the self-similarity of the wake structure were analyzed. The results were compared with the literature and it was observed that the behavior of the turbulent planar jet created by the plane air tunnel is almost the same as the ones found in the literature. According to the outcomes of the velocity profiles, the streamwise fluctuating velocity is the maximum at the y/d location where the upper boundary of the exit corresponds, and it is the minimum at the centerline. On the other hand, the streamwise mean velocity is maximum at $\frac{y}{d} = 0$ and it goes to zero in the positive and negative vertical directions.

After that, to compare the results also with the x-wire and analyze the behavior of the flow also in the crosswise direction, a completely automatic VI code was designed in the LabView environment. Thanks to the code, the user has to just set the angle and the speed values and run the VI. Forming the look-up table with two voltage values from two wires, a known angle, and the known mean velocity, the calibration process was performed. Conducting the experiments at exactly the same points where the single hot wire experiments were performed, results were compared with the single hot wire data. It was detected that the structure of the wake is almost identical to the one that was obtained by the single hot wire. Moreover, the turbulence intensity was calculated by neglecting the fluctuations in the spanwise direction. In addition, the Reynolds Shear Stress was also reached in the XY plane. Comparing the results with the literature, it was realized that the values and the structure obtained by the x-wire experiments were reasonable.

Bibliography

- Alziadeh, M. (2017). *Flow-sound interaction mechanism of a single spirally finned cylinder in cross-flow* (Doctoral dissertation). doi:10.13140/RG.2.2.12457.65123
- AMSO. (2012). *Reynolds stresses*. AMSO. Retrieved from [https://glossary.ametsoc.org/wiki/Reynolds_stresses#:~:text=The%20mean%20forces%20\(per%20unit,mean%20flow%20by%20turbulent%20fluctuations](https://glossary.ametsoc.org/wiki/Reynolds_stresses#:~:text=The%20mean%20forces%20(per%20unit,mean%20flow%20by%20turbulent%20fluctuations)
- Anderson, J. D. (1992). Governing equations of fluid dynamics. In J. F. Wendt (Ed.), *Computational fluid dynamics: An introduction* (pp. 15–51). doi:10.1007/978-3-662-11350-9_2
- Astakhov, V. (2012). 4 - environmentally friendly near-dry machining of metals. In V. Astakhov & S. Joksch (Eds.), *Metalworking fluids (mwfs) for cutting and grinding* (pp. 135–200). doi:<https://doi.org/10.1533/9780857095305.135>
- Banerjee, S. (2014). *Compressible turbulence in space and astrophysical plasmas : Analytical approach and in-situ data analysis for the solar wind* (Doctoral dissertation).
- Bergman, T., Bergman, T., Incropera, F., DeWitt, D., & Lavine, A. (2011). *Fundamentals of heat and mass transfer*. Wiley. Retrieved from <https://books.google.it/books?id=vvyIoXEywMoC>
- Bruun, H. H. (1996). Hot-wire anemometry: Principles and signal analysis. *Measurement Science and Technology*, 7(10). doi:10.1088/0957-0233/7/10/024
- Burattini, P. (2008). The effect of the x-wire probe resolution in measurements of isotropic turbulence. *Measurement Science and Technology*, 19(11), 115405. doi:10.1088/0957-0233/19/11/115405
- Je-Chin Han, L. M. W. (2020). *Experimental methods in heat transfer and fluid mechanics*. doi:<https://doi.org/10.1201/9781003021179>
- Colarusso, P., Kidder, L. H., Levin, I. W., & Neil Lewis, E. (1999). Raman and infrared microspectroscopy. In J. C. Lindon (Ed.), *Encyclopedia of spectroscopy and spectrometry* (pp. 1945–1954). doi:<https://doi.org/10.1006/rwsp.2000.0402>
- COMSOL. (2018). *Fluid flow: Conservation of momentum, mass, and energy*. COMSOL. Retrieved from <https://www.comsol.com/multiphysics/fluid-flow-conservation-of-momentum-mass-and-energy>
- Corp., S. (2016). *Dsa3217/3218 ethernet pressure scanner*. Scanivalve Corp. USA, WA: Scanivalve Corp.
- DEMPSTER, J. (2001). Chapter six - signal analysis and measurement. In J. DEMPSTER (Ed.), *The laboratory computer* (pp. 136–171). doi:<https://doi.org/10.1016/B978-012209551-1/50039-8>
- Enjalbert, N., Galley, D., & Pierrot, L. (2009). An entrainment model for the turbulent jet in a coflow. *Comptes Rendus Mécanique*, 337(9), 639–644. doi:<https://doi.org/10.1016/j.crme.2009.09.005>
- Farouk, B., Lin, Y., & Lei, Z. (2010). Acoustic wave induced flows and heat transfer in gases and supercritical fluids. In Y. I. Cho & G. A. Greene (Eds.), *Advances in heat transfer* (Vol. 42, pp. 1–136). doi:[https://doi.org/10.1016/S0065-2717\(10\)42001-8](https://doi.org/10.1016/S0065-2717(10)42001-8)
- Gentle, R., Edwards, P., & Bolton, B. (2001). 3 - fluid mechanics. In R. Gentle, P. Edwards, & B. Bolton (Eds.), *Mechanical engineering systems* (pp. 112–168). doi:<https://doi.org/10.1016/B978-075065213-1/50003-9>
- George, W. K. (1985). The measurement of turbulent fluctuations: An introduction to hot-wire anemometry and related transducers. by a. v. smol'yakov and v. m. tkachenko (translated by s. chomet, edited by p. bradshaw). springer, 1983. 298 pp. dm.98.00. *Journal of Fluid Mechanics*, 152, 502–503. doi:10.1017/S0022112085230808
- Gramer, L., Gramer@noaa, L., & Gov. (2007). Kelvin-helmholtz instabilities.
- Hall, N. (2021a). *Conservation of mass*. NASA. Retrieved from <https://www.grc.nasa.gov/www/k-12/airplane/mass.html>
- Hall, N. (2021b). *Navier stokes equations*. NASA. Retrieved from <https://www.grc.nasa.gov/www/k-12/airplane/nseqs.html>

- Hashiehbaf, A., & Romano, G. (2013). Particle image velocimetry investigation on mixing enhancement of non-circular sharp edge nozzles. *International Journal of Heat and Fluid Flow*, *44*, 208–221. doi:10.1016/j.ijheatfluidflow.2013.05.017
- Hassan, H., Guo, T., & Vlachos, P. (2019). Flow field evolution and entrainment in a free surface plunging jet. *Physical Review Fluids*, *4*. doi:10.1103/PhysRevFluids.4.104603
- Heskestad, G. (1965). Hot-Wire Measurements in a Plane Turbulent Jet. *Journal of Applied Mechanics*, *32*(4), 721–734. doi:10.1115/1.3627309. eprint: <https://asmedigitalcollection.asme.org/appliedmechanics/article-pdf/32/4/721/5446858/721\1.pdf>
- Jones, A. Z. (2019). *Understanding what fluid dynamics is*. ThoughtCo. Retrieved from <https://www.thoughtco.com/what-is-fluid-dynamics-4019111>
- Kashi, B., Weinberg, E., & Haustein, H. (2018). Analytical re-examination of the submerged laminar jet's velocity evolution. *Physics of Fluids*, *30*, 063604. doi:10.1063/1.5028560
- Kramers, H. (1946). Heat transfer from spheres to flowing media. *Physica*, *12*(2), 61–80. doi:[https://doi.org/10.1016/S0031-8914\(46\)80024-7](https://doi.org/10.1016/S0031-8914(46)80024-7)
- Mathieu, J., & Scott, J. (2000). *An introduction to turbulent flow*. Cambridge University Press. Retrieved from <https://books.google.it/books?id=nVA53NEAx64C>
- Measuring Turbulent Flows*. (2022). JoVE, Cambridge, MA, retrieved from <https://www.jove.com/v/10450/measuring-turbulent-flows>
- Mishra, D. (2021). *Noise in a dataset*. Madras Scientific Research Foundation. Retrieved from <https://www.madrasresearch.org/post/noise-in-a-dataset#:~:text=What%20is%20Noise%20in%20a,prediction%20of%20any%20meaningful%20information.>
- MKS Instruments, I. (1999). *Mks baratron type 627b absolute pressure transducer*. MKS Instruments, Inc. USA, MA: MKS Instruments, Inc.
- Morris, A. S., & Langari, R. (2012). Chapter 16 - flow measurement. In A. S. Morris & R. Langari (Eds.), *Measurement and instrumentation* (pp. 425–459). doi:<https://doi.org/10.1016/B978-0-12-381960-4.00016-4>
- Munson, B., Rothmayer, A., & Okiishi, T. (2012). *Fundamentals of fluid mechanics, 7th edition*. Wiley. Retrieved from <https://books.google.it/books?id=GQMCAAQAQBAJ>
- NASA. (2011). *What is aerodynamics?* Retrieved from <https://www.nasa.gov/audience/forstudents/k-4/stories/nasa-knows/what-is-aerodynamics-k4.html>
- Patil, A., Radle, M., & Shome, B. (2015). One-dimensional solar heat load simulation model for a parked car. (Vol. 2015). doi:10.4271/2015-01-0356
- PID Theory Explained*. (2020). National Instruments. Retrieved from <https://www.ni.com/it-it/innovations/white-papers/06/pid-theory-explained.html>
- Qin, R., & Duan, C. (2017). The principle and applications of bernoulli equation. *Journal of Physics: Conference Series*, *916*, 012038. doi:10.1088/1742-6596/916/1/012038
- Quartapelle, L. (2013). *Numerical solution of the incompressible navier-stokes equations*. Birkhäuser Basel. Retrieved from <https://books.google.it/books?id=k775BwAAQBAJ>
- Rathakrishnan, E. (2020). *Instrumentation, measurements, and experiments in fluids*. doi:10.1201/9781315365619
- Sample autocorrelation*. (2022). MathWorks. Retrieved from <https://it.mathworks.com/help/econ/autocorr.html>
- Sheikholeslami, M., & Ganji, D. D. (2017). Chapter 3 - nanofluid forced convection heat transfer. In M. Sheikholeslami & D. D. Ganji (Eds.), *Applications of nanofluid for heat transfer enhancement* (pp. 127–193). doi:<https://doi.org/10.1016/B978-0-08-102172-9.00003-4>
- Shekhter, Y. (2011). *Hot-wire and hot-film anemometers*. doi:10.1615/AtoZ.h.hot-wire_and_hot-film_anemometers
- Shires, G. L. (2011). *Grashof number*. doi:10.1615/AtoZ.g.grashof_number
- Siemens. (2013). *Siemens sinamics v20 inverter*. Siemens. GERMANY, NÜRNBERG: Siemens.
- SimScale. (2021). *What is turbulent flow?* Retrieved from <https://www.simscale.com/docs/simwiki/cfd-computational-fluid-dynamics/what-is-turbulent-flow/>
- Smith, G. M. (2020). *Data acquisition (daq) - the ultimate guide*. DEWESoft. Retrieved from <https://dewesoft.com/daq/what-is-data-acquisition>
- STANLEY, S. A., SARKAR, S., & MELLADO, J. P. (2002). A study of the flow-field evolution and mixing in a planar turbulent jet using direct numerical simulation. *Journal of Fluid Mechanics*, *450*, 377–407. doi:10.1017/S0022112001006644

BIBLIOGRAPHY

- Taveira, R., & Silva, C. (2014). Characteristics of the viscous superlayer in shear free turbulence and in planar turbulent jets. *Physics of Fluids*, 26. doi:10.1063/1.4866456
- Wendt, J. (2008). *Computational fluid dynamics: An introduction*. Springer Berlin Heidelberg. Retrieved from https://books.google.it/books?id=P%5C_wrvhjiFWIC
- WU, N., SAKAI, Y., NAGATA, K., SUZUKI, H., TERASHIMA, O., & HAYASE, T. (2013). Analysis of flow characteristics of turbulent plane jets based on velocity and scalar fields using dns. *Journal of Fluid Science and Technology*, 8(3), 247–261. doi:10.1299/jfst.8.247
- Zhao, J., Chen, Q., Chen, Z., Chen, C., Liu, Z., & Zhao, G. (2021). *Impact of the structure on the thermal burnout effect induced by microwave pulses of pin limiter diodes*. doi:10.21203/rs.3.rs-622735/v1

7

Appendices

7.1 Fast fourier transform

$$f(x) = \int_0^{\Lambda} \hat{f}_k e^{2\pi j k x / \Lambda} dx. \quad (7.1)$$

where:

- Λ = period[s],
- k = number of fourier coefficients [Pa],
- \hat{f}_k = fourier coefficient,
- j = imaginary coefficient.

By identifying the discretization parameters as

$$\Delta x = \Lambda / N, \quad (7.2)$$

where:

- N = number of data points,
- i = recent point indicator, $i=1,2,\dots,N+1$,
- $x_i = i\Delta x$.

Applying the discretization to fourier transform formula, discrete fourier transform formula was derived as

$$f_i = \sum_{k=-N/2}^{N/2} \hat{f}_k e^{2\pi j k i / N}, \quad (7.3)$$

where:

- \hat{f}_k = discretized fourier coefficients.

So, the discrete fourier coefficients can be computed as

$$\hat{f}_k = \frac{1}{N} \sum_{i=1}^N f_i e^{-2\pi j k i / N}, \quad (7.4)$$

where:

$$\omega_n = e^{-2\pi j/N}.$$

Thus, the form of the solution resulted by the formula 7.4 is

$$\begin{bmatrix} \hat{f}_1 \\ \hat{f}_2 \\ \cdot \\ \cdot \\ \hat{f}_N \end{bmatrix} = \frac{1}{N} \begin{bmatrix} 1 & 1 & \cdot & \cdot & \cdot & 1 \\ 1 & \omega_N & \omega_N^2 & \cdot & \cdot & \omega_N^{N-1} \\ 1 & \omega_N^2 & \omega_N^4 & \cdot & \cdot & \omega_N^{2(N-1)} \\ \cdot & \cdot & \cdot & \cdot & \cdot & \cdot \\ \cdot & \cdot & \cdot & \cdot & \cdot & \cdot \\ 1 & \omega_N^{(N-1)} & \omega_N^{2(N-1)} & \cdot & \cdot & \omega_N^{(N-1)^2} \end{bmatrix} \begin{bmatrix} f_1 \\ f_2 \\ \cdot \\ \cdot \\ f_N \end{bmatrix} \quad (7.5)$$

$$\hat{f} = F_N f, \quad (7.6)$$

The solution system 7.5 has an $N \times N$ matrix to be solved, which includes complex numbers and requires N^2 operations. In reality, this matrix is not that easy to solve, so the technique called "fast fourier transform" is used to solve the system. The system can be written in the form below, by using the fast fourier transform technique.

$$\hat{f} = \begin{bmatrix} I_{N/2} & -D_{N/2} \\ I_{N/2} & -D_{N/2} \end{bmatrix} \begin{bmatrix} F_{N/2} & 0 \\ 0 & F_{N/2} \end{bmatrix} \begin{bmatrix} f_{even} \\ f_{odd} \end{bmatrix} \quad (7.7)$$

where:

- $I_{N/2}$ = $N/2 \times N/2$ identity matrix,
- $D_{N/2}$ = $N/2 \times N/2$ diagonal matrix including ω_n ,
- $F_{N/2}$ = $N/2 \times N/2$ coefficient matrix,
- f_{even} = even indices f vector,
- f_{odd} = odd indices f vector.

This operation of reducing the size of the system to be solved can be performed until it reaches a reasonable size to be solved easily like

$$F_N \rightarrow F_{N/2} \rightarrow F_{N/4} \rightarrow F_{N/8} \rightarrow F_{N/16} \rightarrow \dots$$

7.2 VI block diagrams

7.2.1 Inverter communication

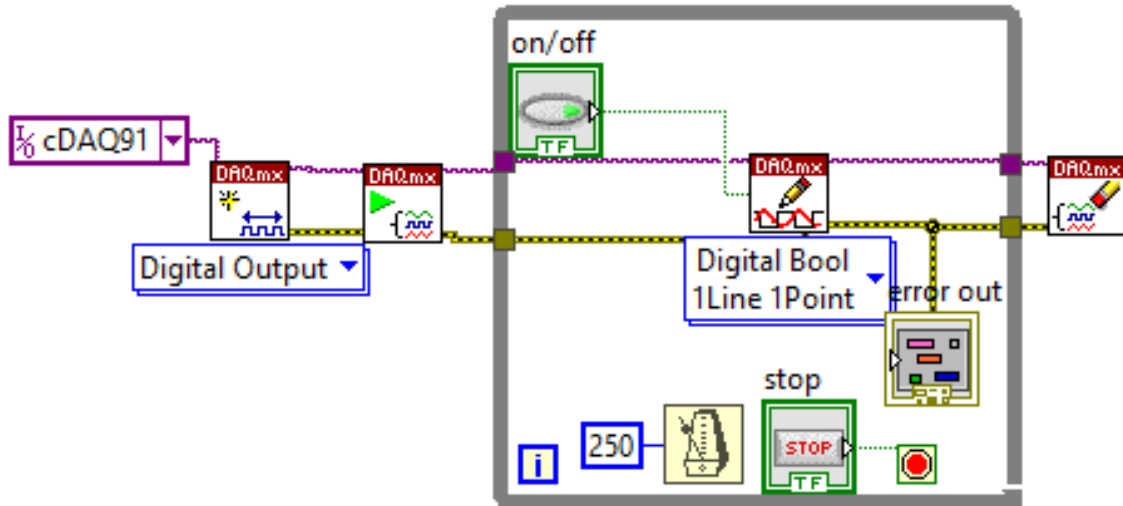


Figure 7.1: On/off command VI code

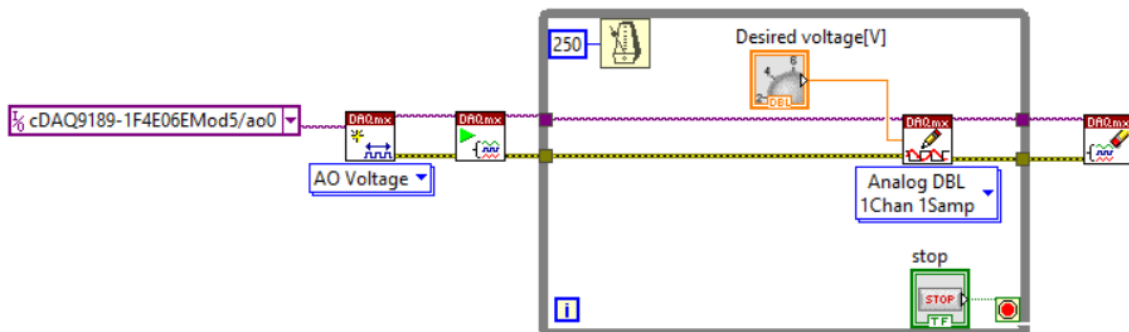


Figure 7.2: Inverter control VI code

Pressure acquisition with mks transducer

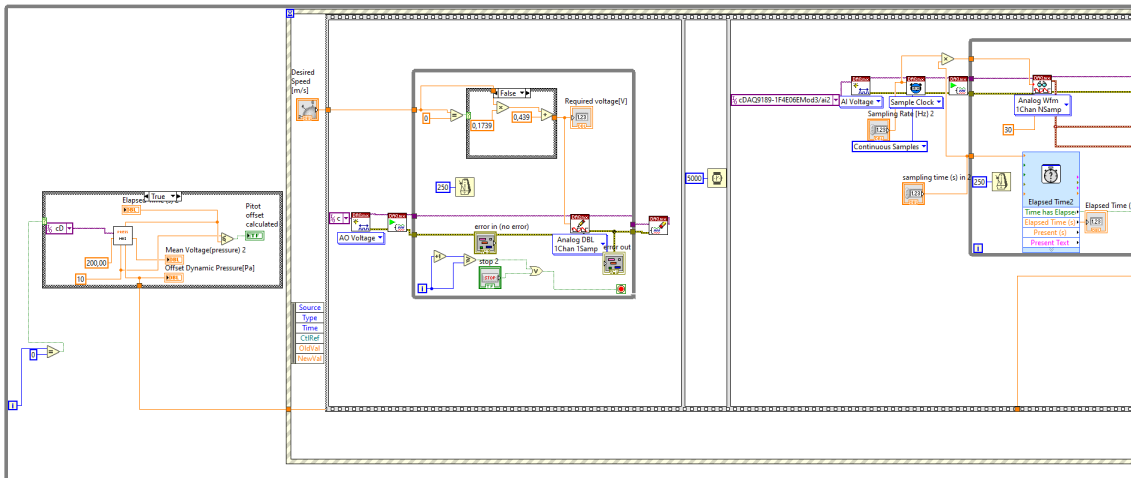


Figure 7.3: Pressure acquisition VI code for mks transducer

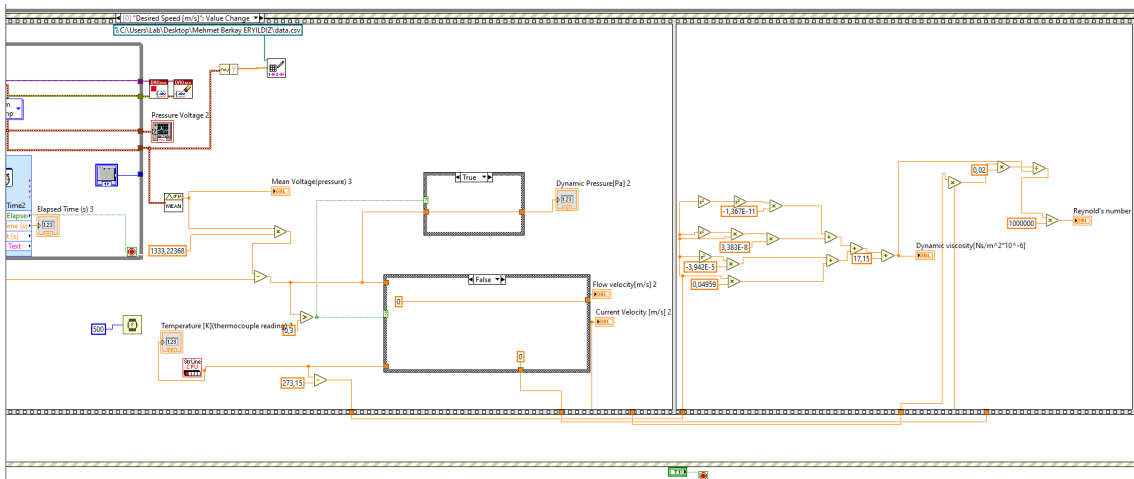


Figure 7.4: Pressure acquisition VI code for mks transducer

7.2.2 Temperature acquisition

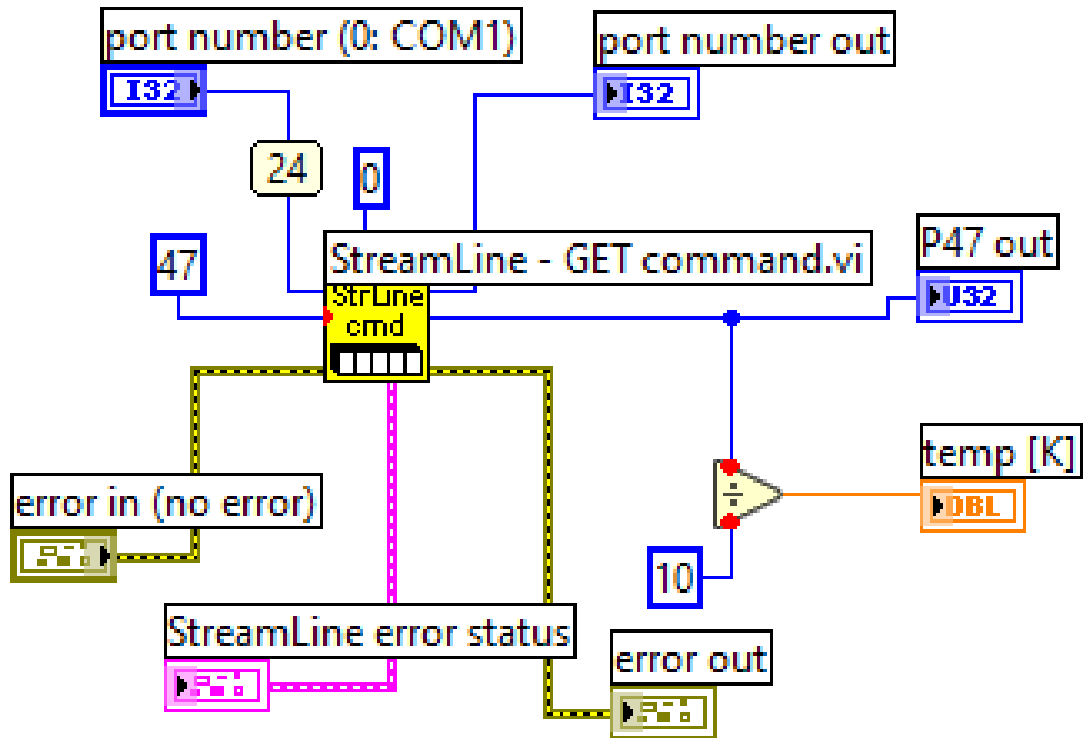


Figure 7.5: Temperature acquisition VI code

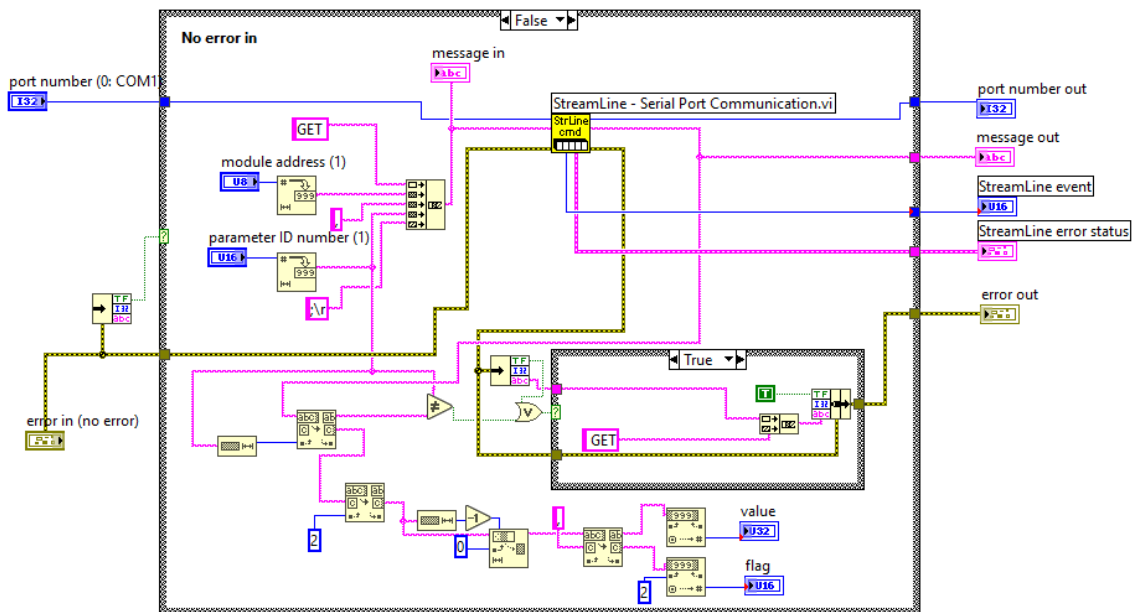


Figure 7.6: Inner loop of temperature acquisition VI code

7.2.3 Exit velocity calculation

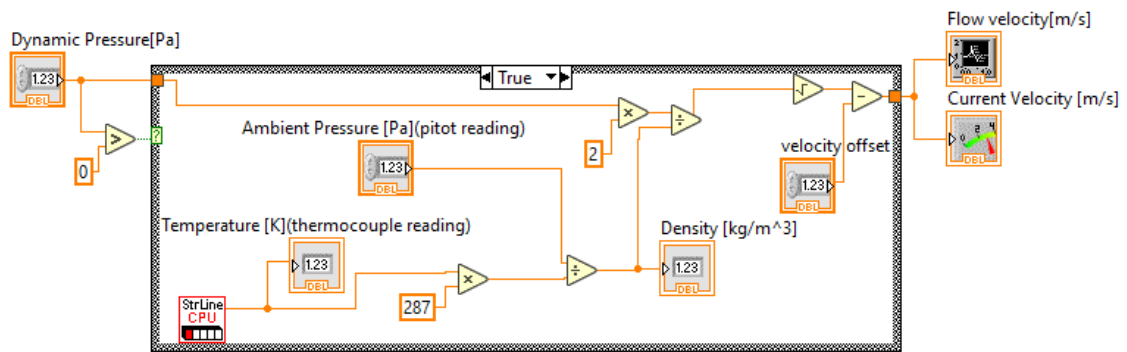


Figure 7.7: Velocity calculation VI code

7.2.4 Stepper motor

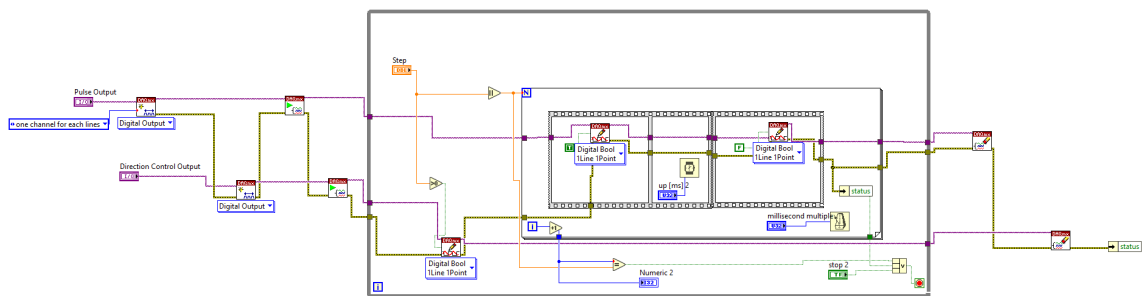


Figure 7.8: Block diagram of the VI to control the rotation of the stepper motor used for the traversing system for x-wire calibration.

7.2.5 PI controller with a pitot-static tube

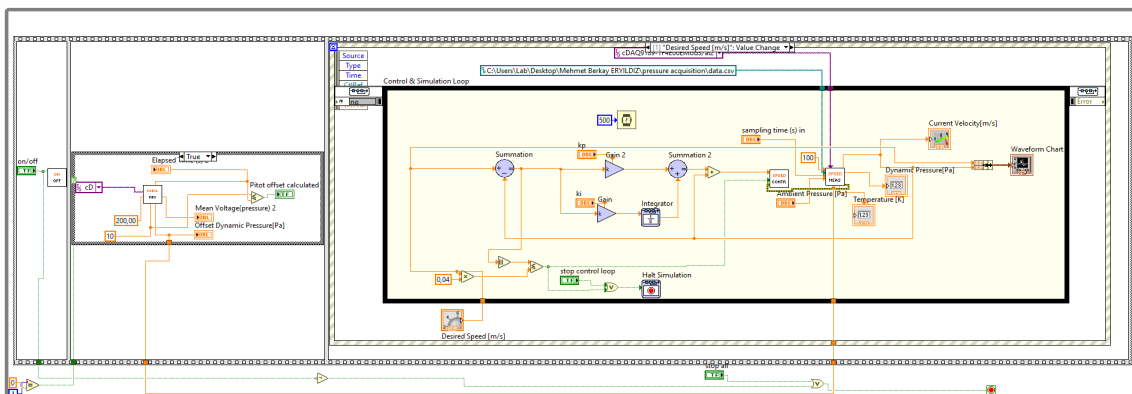


Figure 7.9: PI controller with a pitot-static tube VI code

7.2.6 PI controller without a pitot-static tube

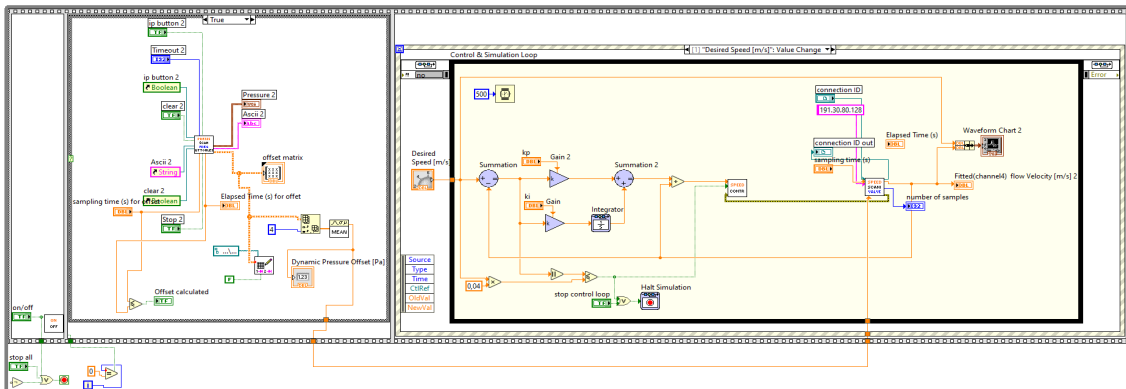


Figure 7.10: PI controller without a pitot-static tube VI code

7.2.7 Pressure acquisition for Scanivalve pressure scanner

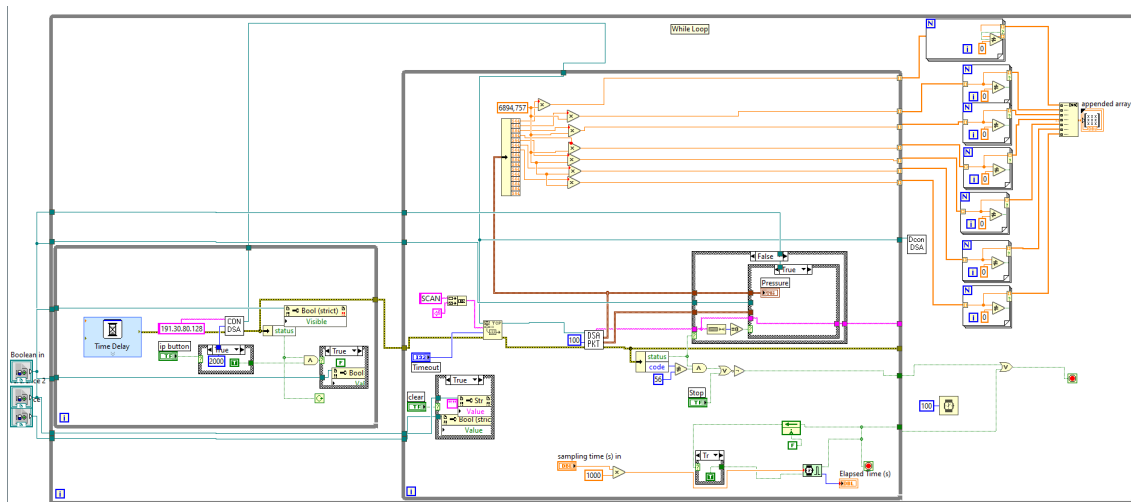


Figure 7.11: Adjustable frequency pressure scanner VI

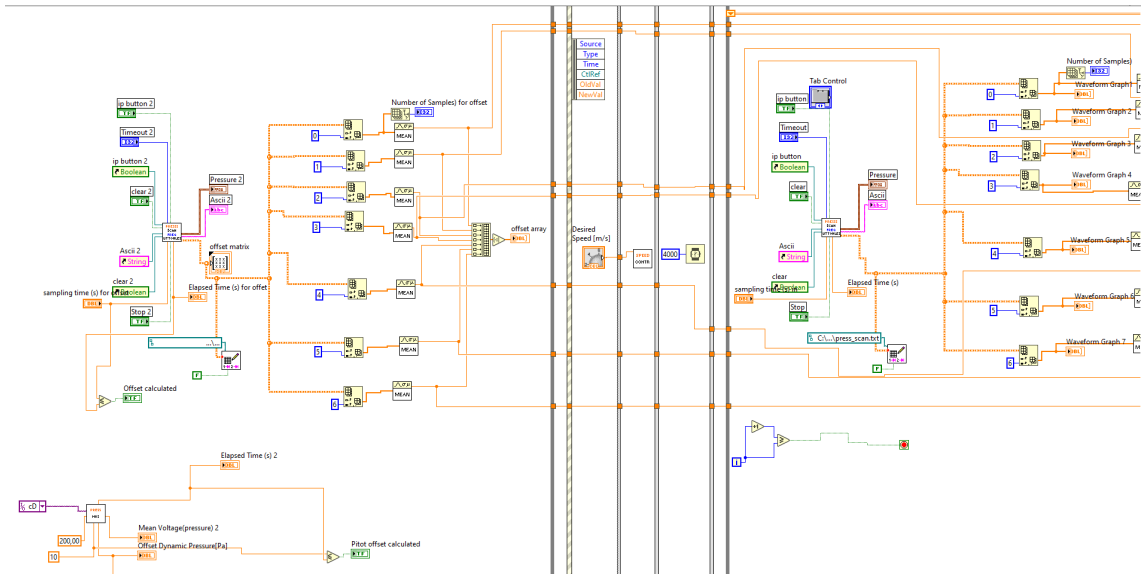


Figure 7.12: Pressure scanner block diagram 1

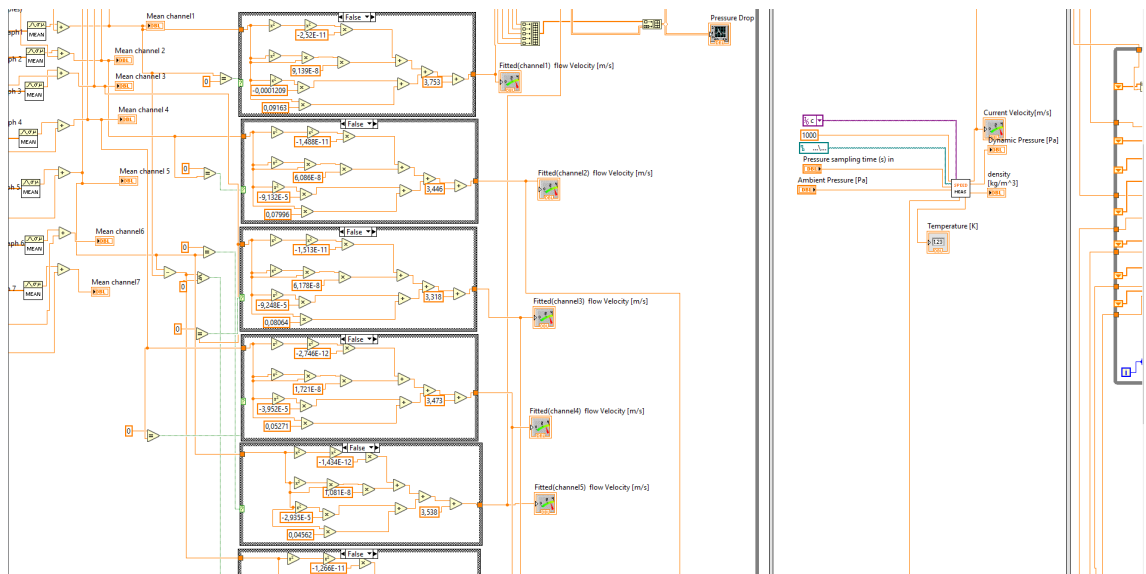


Figure 7.13: Pressure scanner block diagram 2

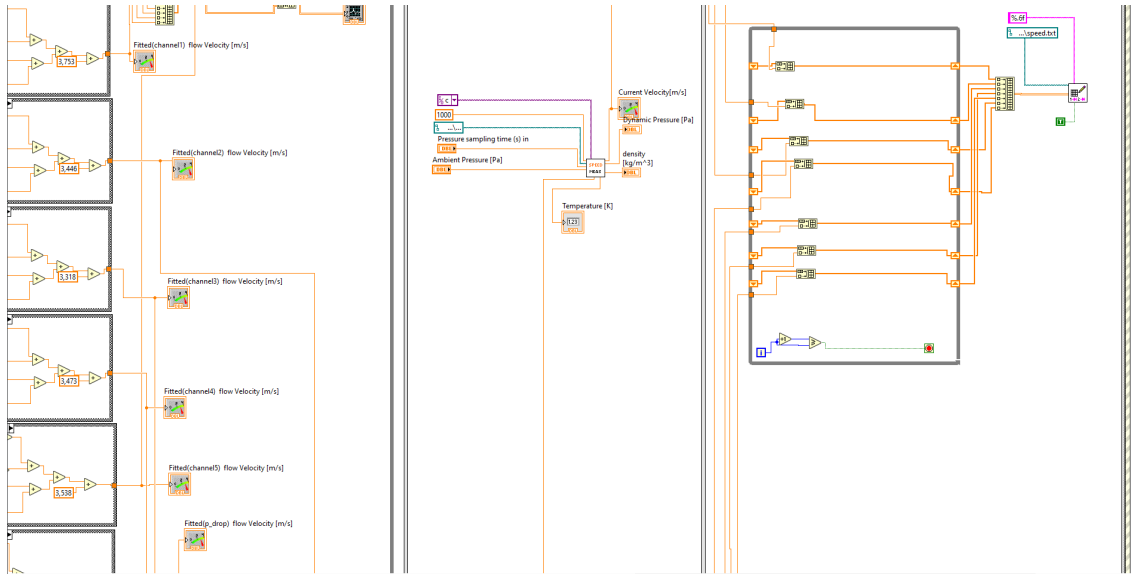


Figure 7.14: Pressure scanner block diagram 3

7.2.8 Hot wire calibration

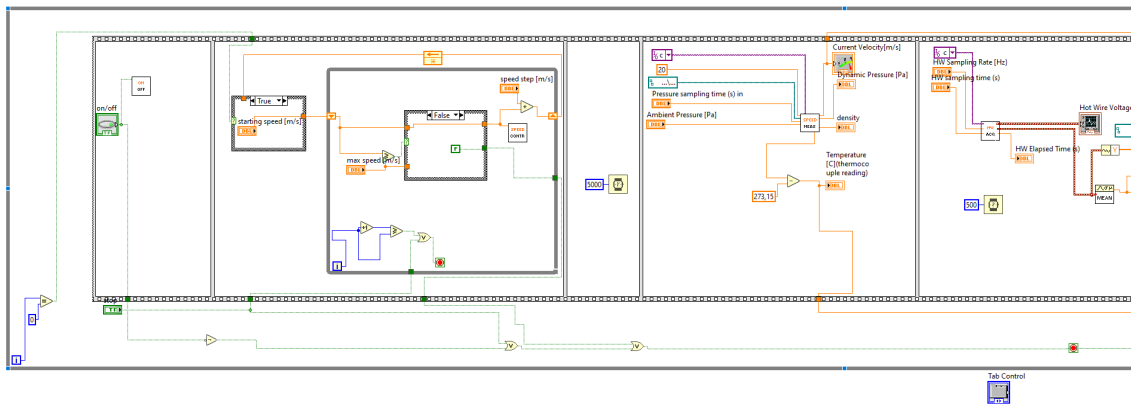


Figure 7.15: Hot wire calibration fully automatic VI block diagram 1

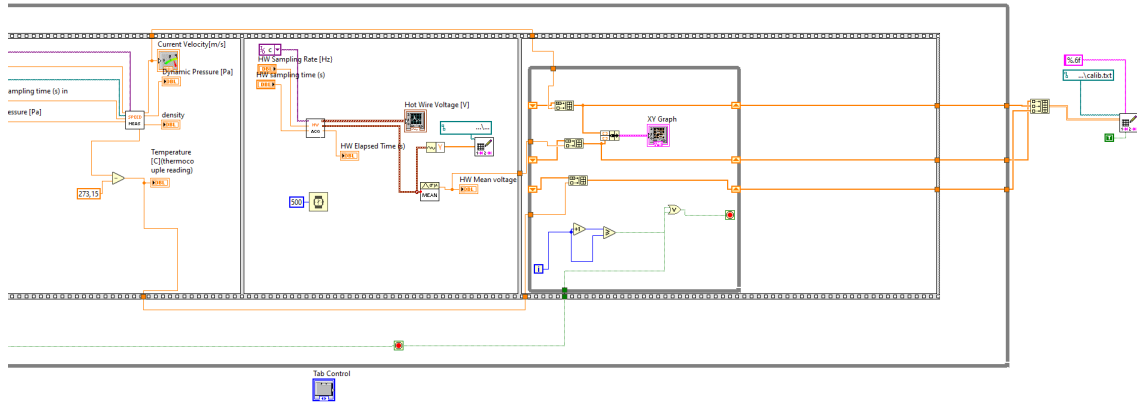


Figure 7.16: Hot wire calibration fully automatic VI block diagram 2

7.2.9 Hot wire experiment

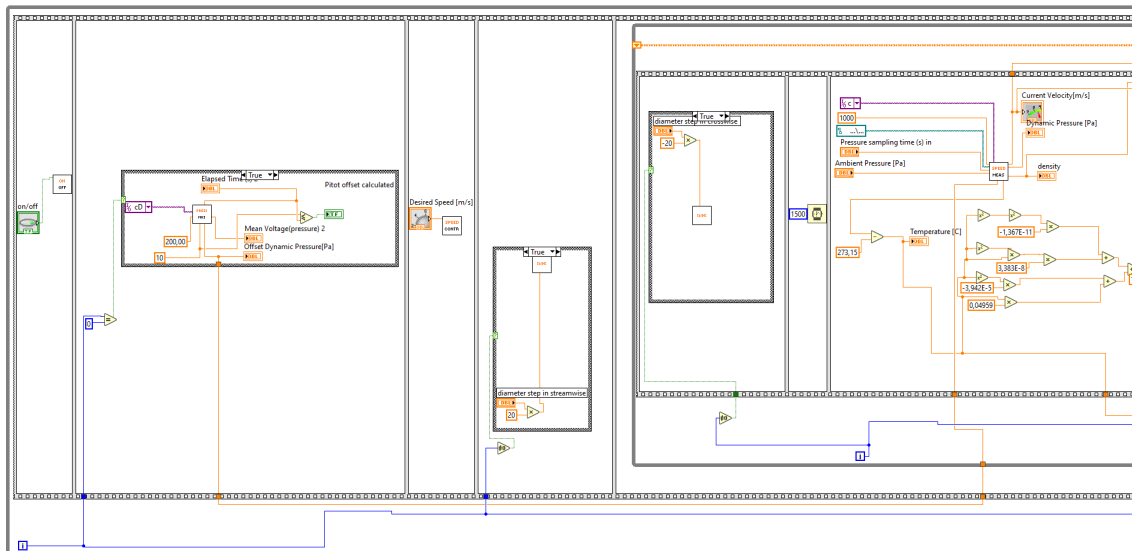


Figure 7.17: Hot wire experiment fully automatic VI block diagram 1

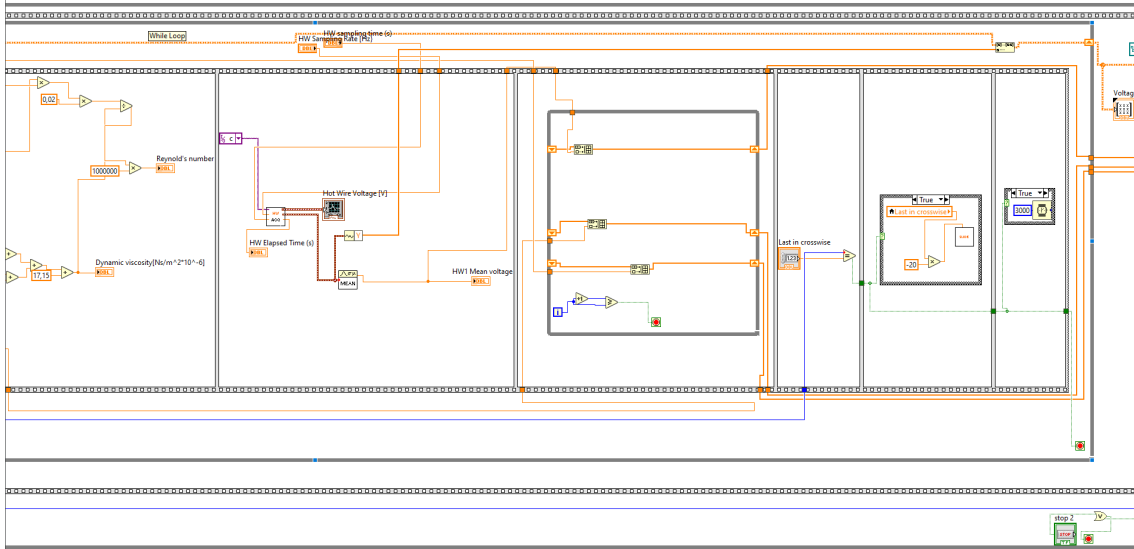


Figure 7.18: Hot wire experiment fully automatic VI block diagram 1

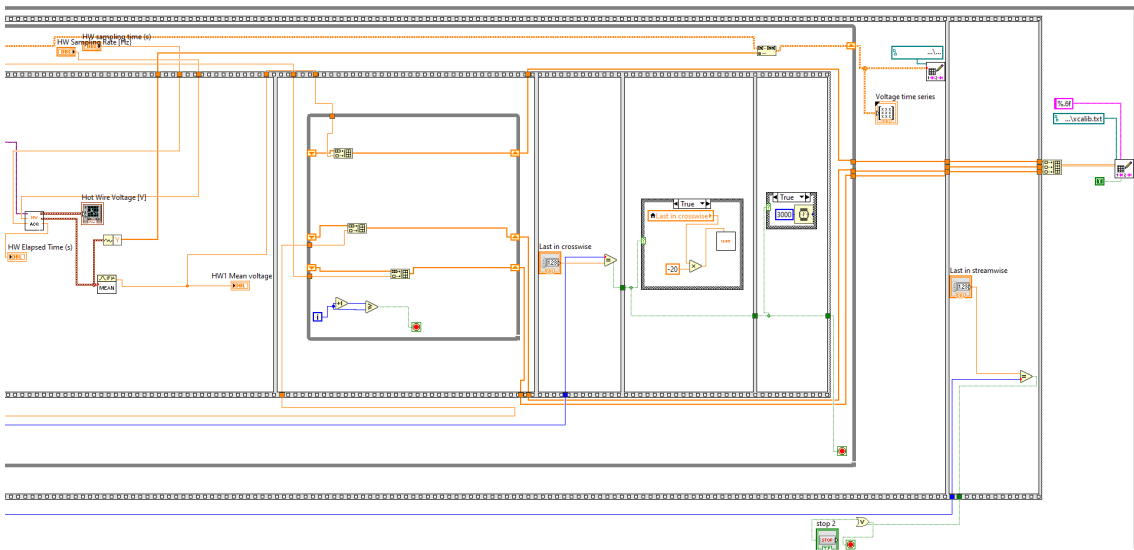


Figure 7.19: Hot wire experiment fully automatic VI block diagram 3

7.2.10 X-wire calibration

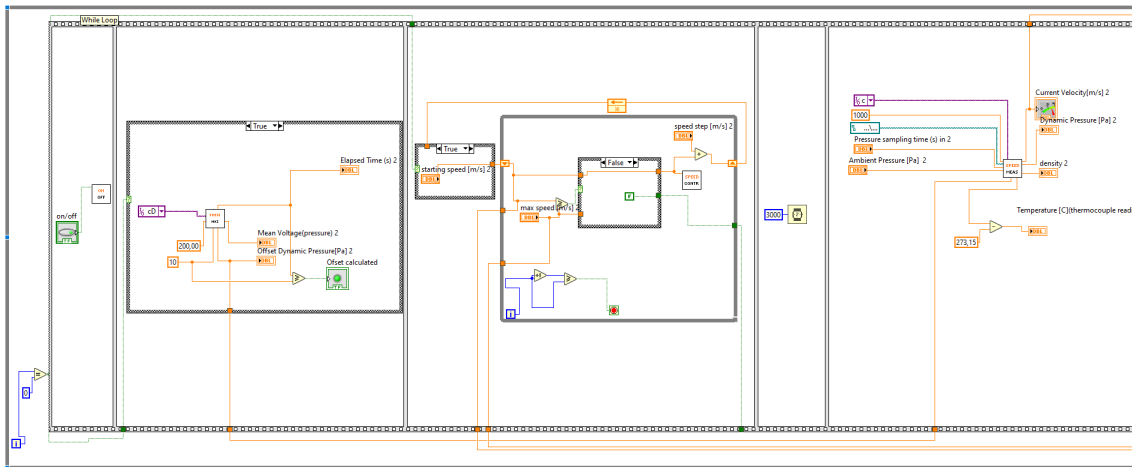


Figure 7.20: X-wire wire calibration fully automatic VI block diagram 1

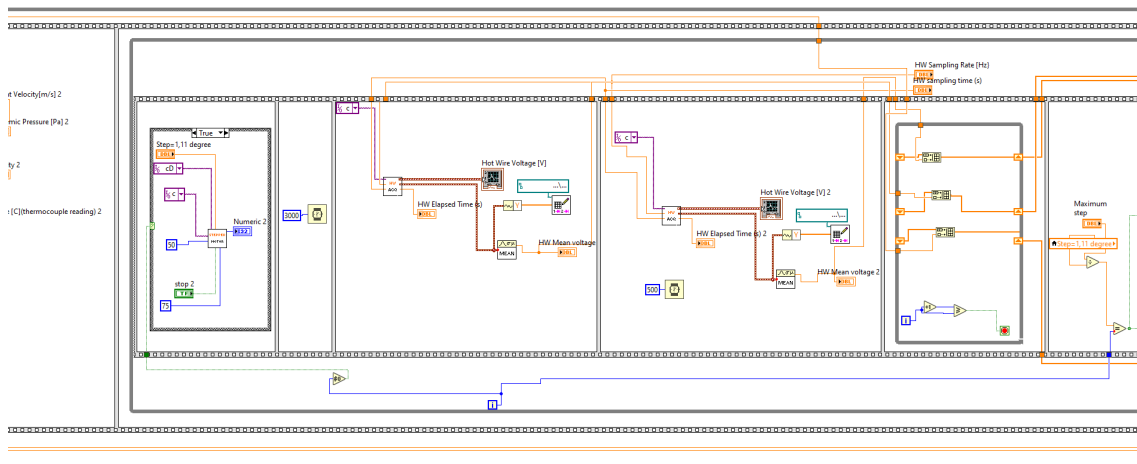


Figure 7.21: X-wire wire calibration fully automatic VI block diagram 2

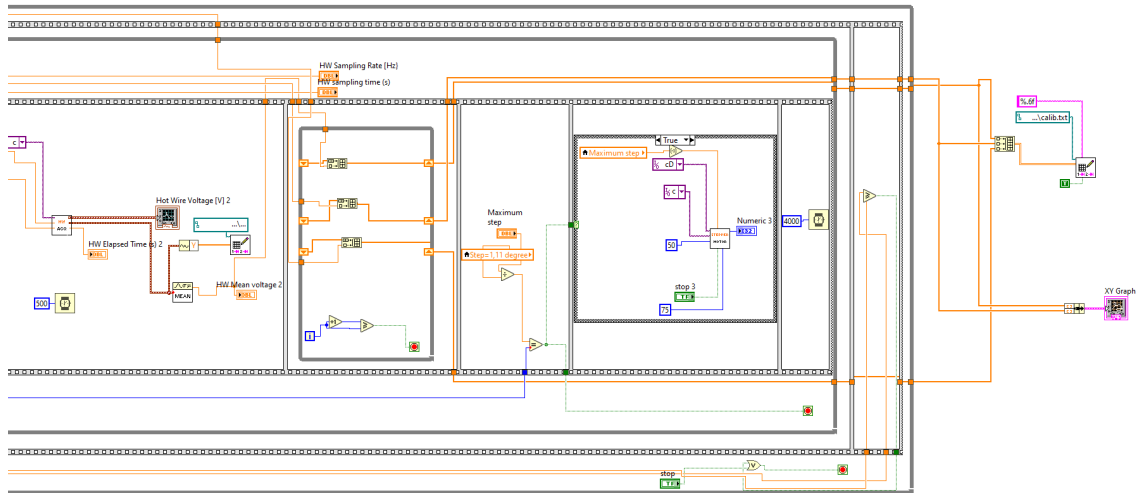


Figure 7.22: X-wire wire calibration fully automatic VI block diagram 3

7.2.11 X-wire experiments

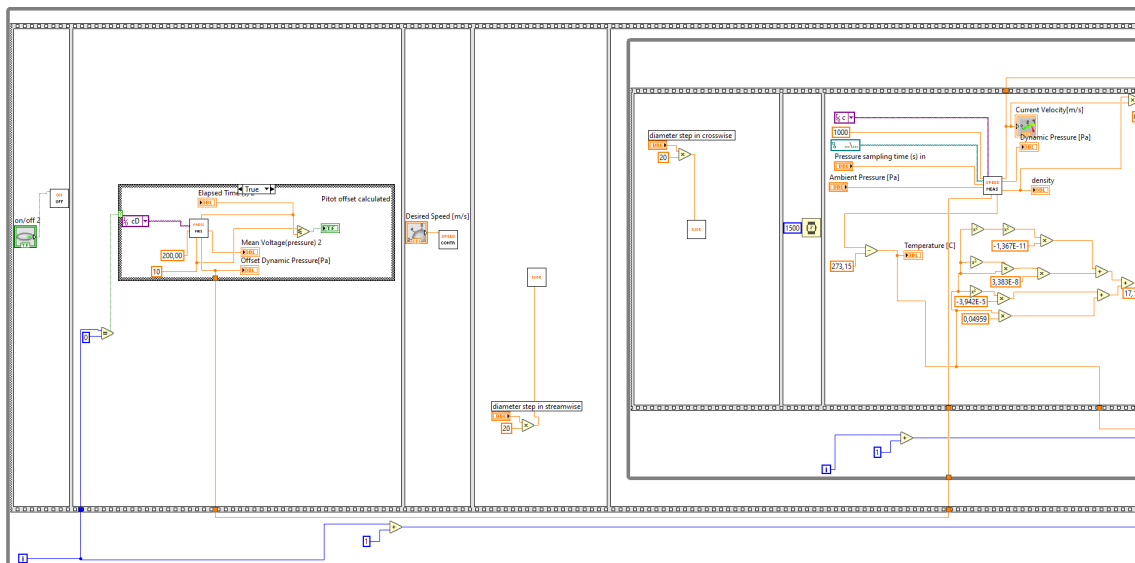


Figure 7.23: X-wire experiment fully automatic VI block diagram 1

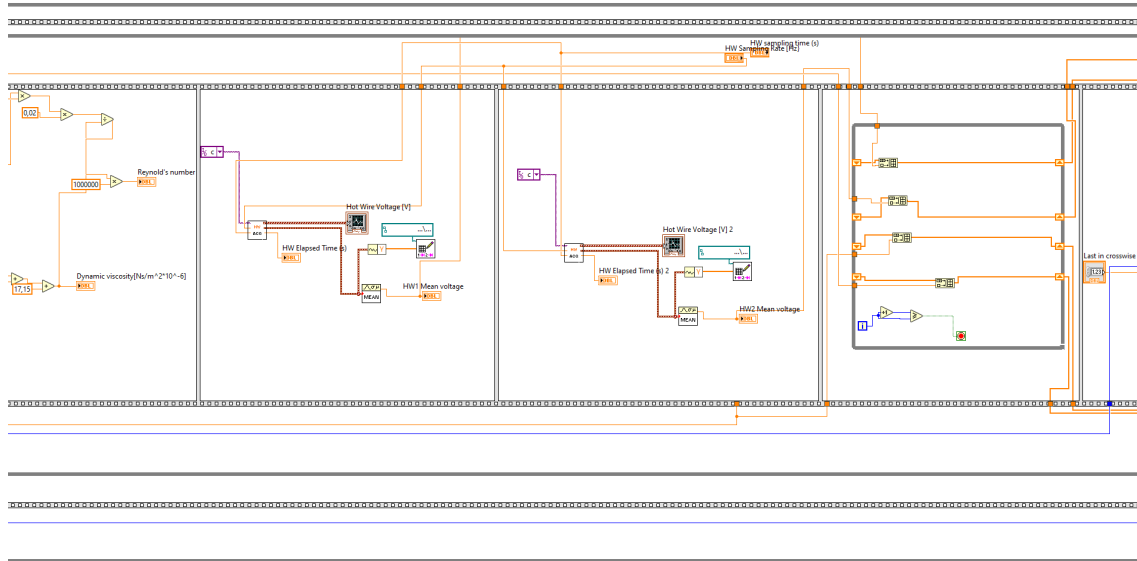


Figure 7.24: X-wire experiment fully automatic VI block diagram 2

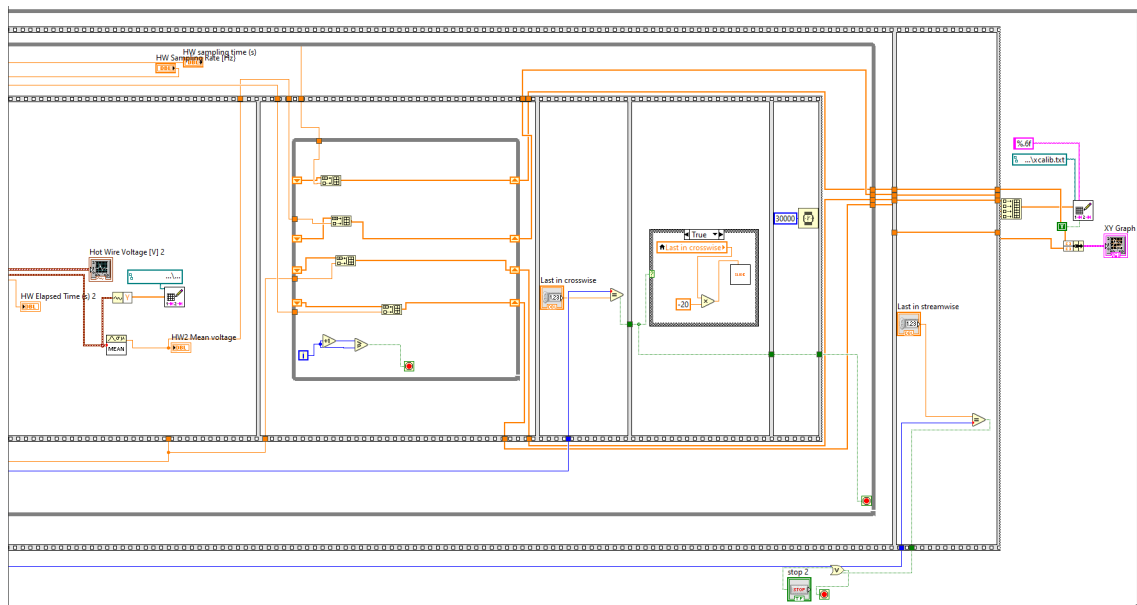


Figure 7.25: X-wire experiment fully automatic VI block diagram 3